BEHAVIOUR OF FOOTINGS FOR OFFSHORE STRUCTURES UNDER COMBINED LOADS

by

Paulo Eduardo Lima de Santa Maria

A thesis submitted for the
degree of Doctor of Philosophy at
the University of Oxford

Magdalen College

Trinity Term, 1988

ABSTRACT

BEHAVIOUR OF FOOTINGS FOR OFFSHORE STRUCTURES UNDER COMBINED LOADS

A thesis submitted for the degree of Doctor of Philosophy

P.E.L. de Santa Maria
Magdalen College, Oxford
Trinity Term, 1988

The lack of knowledge about the behaviour of footings for jack-up rigs under storm loads poses a design problem which can be tackled by model testing. The areas of prime concern are the ultimate loads on footings under combined loading, which affects the safety of the rig, and the rotational stiffness, which affects the interaction between the foundation and the structure.

A programme of loading tests was performed on model footings on clay, and was divided into two stages: monotonic loading and cyclic loading. The clay samples were obtained by consolidating Speswhite kaolin slurry in cylindrical tanks 450 mm in diameter. The strength and compressibility characteristics of the samples were verified by means of standard laboratory tests.

The model footings were 50 mm and 100 mm in diameter and several shapes were tested: circular flat plate, cones of various angles and model spud-cans. Loads and displacements were monitored using appropriate instrumentation and a data logger.

A series of central vertical loading tests provided data for comparison with existing bearing capacity theories. Combined loading tests were performed applying a displacement controlled horizontal load at a fixed height above the footing which was also subjected to a fixed vertical load. The main series of tests involved a parametric study of the relevant variables. Special tests allowed the assessment of the effect of embedment of the footing and the interaction of a flexible leg with the foundation.

Cyclic loading tests were carried out using a load controlled system which applied a sinusoidal load simulating wave action. Effects of currents were investigated by introducing an offset to the loading cycle. The influence of amplitude and period of loading as well as the influence of vertical load were also investigated. Special tests were carried out to cover some peculiarities of real loading conditions.

Fitting of a three-parameter hyperbola to the test results provided a systematic and accurate method of analysis of monotonic loading tests, leading to valuable information involving stiffness and ultimate loads.

Analysis of cyclic loading tests yielded useful qualitative information regarding the progress of settlement and the variation of rotational stiffness and damping ratio with the number of cycles.

"The outcome of any serious research can only be to
make two questions grow where only one grew before"

T.B. Veblen (1857-1929)

To
Silma,
Adriana, Alessandro and Igor

ACKNOWLEDGEMENTS

First of all I would like to express my appreciation to my supervisor, Dr. G.T. Houlsby, for his most valuable judgement, advice and suggestions throughout all the stages of this research. Dr. Houlsby has always been present and I much appreciated his dedication and constant willingness to offer help.

It has been a great privilege to be a member of the Oxford Soil Mechanics Group, which under the leadership of Prof. C.P. Wroth has provided a highly intellectual and most friendly environment for the realization of this work. I wish to thank all its members for the many stimulating discussions and extremely beneficial exchange of information.

For sponsoring the research thanks are due to:

Agip (UK) Ltd, American Bureau of Shipping, ARCO Oil and Gas Company, Department of Energy (United Kingdom), Elf UK plc, Exxon Production Research Company, Far East Levingston Shipbuilding Ltd, Friede & Goldman Ltd, Gusto Engineering b.v., Marathon Le Tourneau Marine Company, Mitsui Engineering & Shipbuilding Co. Ltd, Mitsui Ocean Development & Engineering Co. Ltd, Petroleo Brasileiro S.A., Reading & Bates Drilling Company, Santa Fe Drilling Company, Shell U.K. Exploration and Production, Sonat Offshore Drilling Inc., Transworld Drilling Company and Science and Engineering Research Council (SERC).

I am particularly grateful to Mr. M.J. Reardon of Noble Denton and Associates who carried out much of the coordination of the joint industry study.

I am greatly obliged to Conselho Nacional de Desenvolvimento Cientifico e Tecnologico (CNPq), of Brazil, for granting me the scholarship to carry out postgraduate study at Oxford University.

I am particularly indebted to Mr. R. Earl and Mr. C. Donnelly for their invaluable assistance in the development and construction of part of the equipment employed in the experiments.

I must also praise the Brazilian community in Oxford for their highest sense of brotherhood. My deepest appreciation in particular to Deusa and Ennio Palmeira for their friendship and readiness to help, especially during the period of my adaptation in Oxford.

I wish to express my thanks to Mr. N. Knight for kindly revising the text of the thesis and to Magda Rodrigues for her invaluable assistance with the photography of some parts of the equipment.

My special thanks also to those who, in one way or another, unselfishly helped me with my interests in Brazil. Personal mention should be made of Luiz A. L. de Santa Maria and Selma C. Pires.

I would like to record my profound gratitude to my parents for their continuous support, encouragement and interest in my education and professional achievements. I am eternally thankful to them.

Finally, but by no means least, I am deeply indebted to my wife Silma who sacrificing herself in numerous ways has unfailingly devoted her love, kindness, companionship and understanding which provided me with persevering courage and constant stimulation.

Paulo Eduardo Lima de Santa Maria

LIST OF SYMBOLS

A	cross-sectional area of a footing
A	$= M_a \Delta\theta/8$ (see figure 9.7)
B	Skempton's pore pressure parameter
B	width of a footing
D	diameter of a circular footing
E	Young's modulus
E_u	Young's modulus for undrained loading in terms of total stresses
EC	index related to the amount of clay displaced during a cyclic loading model test
G	elastic shear modulus
G	specific gravity of soil particles
G_{33}	secant shear modulus corresponding to a third of the failure stress on the stress-strain curve
G_{50}	secant shear modulus corresponding to a half of the failure stress on the stress-strain curve
H	horizontal load
I	2nd moment of area
I_r	$= G/s_u$ (rigidity index)
K	bulk modulus
K_o	coefficient of lateral earth pressure at rest
LL	liquid limit
M	moment loading
M	slope of critical state line in p':q space
M_a	peak-to-peak amplitude of cyclic moment loading
M_f	failure moment
M_o	offset of cyclic moment loading
N	geometric scale of a model

N	number of cycles of loading
OCR	overconsolidation ratio for one dimensional compression
PI	plasticity index
PL	plastic limit
R	overconsolidation ratio for isotropic compression
R	radius of a circular footing
T	period of cyclic loading
V	vertical load
V_f	vertical central failure load
W	rotational energy dissipated during a complete cycle of loading
a,b,c	hyperbola parameters
a_u	undrained adhesion of a clay to a surface
c_v	coefficient of consolidation
d	initial depth of installation of a model footing in a clay sample (embedment)
e	eccentricity of vertical load
e	voids ratio
$(e_\lambda)_{1-D}$	voids ratio at p′ = 1 kPa
h	height of application of horizontal load
k	coefficient of permeability
k	non-dimensional stiffness
k_1	non-dimensional initial stiffness
k_2	non-dimensional plastic stiffness
k_3	non-dimensional unloading stiffness
l	length of a model leg
p	contact pressure for a rigid footing
p′	mean normal effective stress

p'_o	mean normal effective stress at the beginning of a triaxial test
q	deviator stress
r	correlation coefficient
r	radial coordinate
r	spacing ratio
r_s	ratio between the average values of the undrained shear strength at the depths of 140 mm and 60 mm (in the present research)
s_o	undrained shear strength at the soil surface
s_u	undrained shear strength
t	thickness of a model leg
t	time
v	specific volume
w	ground heave
w	water content
y	horizontal displacement of a rigid footing
z	depth
z	vertical displacement of a rigid footing
α	$= a_u/s_u$ (roughness of a footing surface)
β	cone apex angle or enveloping angle for spud-cans
Δu	excess pore pressure
$\Delta\theta$	variation of rotation angle corresponding to peak-to-peak amplitude of moment loading
δ	deflection of a model leg when subjected to a bending moment
ε	strain
η	damping ratio (see figure 9.7)
θ	rotation angle of a rigid footing
θ_c	cumulative rotation angle
κ	slope of swelling line in e:ln p′ space

Λ	plastic volumetric strain ratio
λ	$= \sqrt{V/EI}$
λ	slope of consolidation line in e:ln p′ space
ν	Poisson's ratio
ν_u	Poisson's ratio for undrained loading
ρ	gradient of a linearly increasing undrained shear strength with depth
$\sigma_1, \sigma_2, \sigma_3$	principal stresses
σ_v	consolidation pressure
σ'_{vo}	vertical effective stress at the beginning of a triaxial test
ϕ'_{tc}	angle of shearing resistance (triaxial compression)

CONTENTS

CHAPTER 10 CONCLUDING REMARKS

CHAPTER 1

INTRODUCTION

About sixty percent of the world's offshore oil and gas exploration is accomplished by about 440 jack-up mobile drilling platforms, some of which can operate in water depths in excess of 100 m and under severe weather conditions involving extreme wave heights of the order of 30 m.

These rigs are floatable drilling units provided with legs (usually 3 or 4) which can be jacked up and down. This feature introduces great mobility to the rig as it can be propelled or towed from one location to another, although dry transportation employing heavy lift vessels has recently become a common practice.

After arriving at the exploration site, the legs of the jack-up are lowered until contact and a slight penetration into the seabed is obtained just to prevent horizontal movements. The rig is termed "pinned" and is kept at that position until the location is confirmed and accepted. Then, before beginning drilling, a three stage operation must be carried out:

* jacking the hull clear of the water;
* adding a surcharge weight or preload;
* jacking the platform to the required airgap for operation.

Jack-up rig foundations can be classified into two categories: (i) individual circular or polygonal footings called "spud-cans" and (ii) a

single large mat. The present research concerns only the former type of foundation.

Unlike offshore production units (fixed platforms or gravity structures) jack-up rigs are not designed for a specific site and therefore the footings must penetrate into the seabed until a safe foundation is achieved. Sometimes, however, the foundation is unstable and the structure collapses during a severe loading condition. According to Young, Remmes, and Meyer (1984), among all types of mobile offshore drilling units, jack-up rigs experienced the worst accident rate during the period from 1955 to 1982, one third of which is believed to be related to foundation misbehaviour.

In contrast with most onshore foundation design problems, where generally the footing depth is fixed and the dimensions calculated, one of the basic aims of the geotechnical study for a jack-up rig foundation is the assessment of the footing penetration into the seabed. The importance of this analysis is easily understood if one bears in mind that the sum of the airgap below the hull, the water depth and the footing penetration must not exceed the maximum available leg length. Usually this analysis is performed by means of charts of bearing capacity versus penetration prepared for the relevant geometry of footing and the soil profile.

Although the loads on jack-up foundations include a dynamic component, the footing penetration analysis is normally carried out as if the loading condition were solely static. In fact, cyclic loads are mainly caused by storm waves and tend to cause additional footing penetrations. The amount of additional penetration depends on the magnitude of the fixed load, the magnitude of the cyclic load and the number of cycles.

Besides the problem concerning the stability and penetration of the spud-can into the seabed, foundation fixity also requires attention. Foundation fixity is defined as the ability of the soil to restrain the rotational movement of a footing due to a moment loading.

When a jack-up rig experiences a storm loading, the footings have to respond to combined vertical loads, horizontal loads and moments. The conventional procedure in the design of the legs is based on the assumption that the footing offers no restraint to moment loading and therefore behaves as a pinned support, disregarding any moment fixity. Under this assumption the maximum bending moment occurs at the top of the leg. This bending moment proves to be critical in many designs. This approach is clearly conservative and, if any restraint actually can be accounted for (Figure 1.1), the ultimate load capacity of the whole structure under wave loading may increase substantially. In particular, any moment at the footing reduces the moment at the top of the leg. This would allow the utilization of the rig under more severe loading conditions than those assumed formerly and, consequently, the operational area could be extended with commercial benefits. Also, the fixity reduces the structural stress range, resulting in a lengthening of the fatigue life of the rig.

The trend of design of larger jack-up rigs to reach greater depths results in their natural periods of oscillation approaching the excitation period of the waves. An additional benefit of fixity would be the reduction of the natural period of the rig.

The mechanisms related to collapse loads of circular flat and conical footings on clay under vertical central loading are quite well understood. However, only a little is known about bearing capacity of these footings

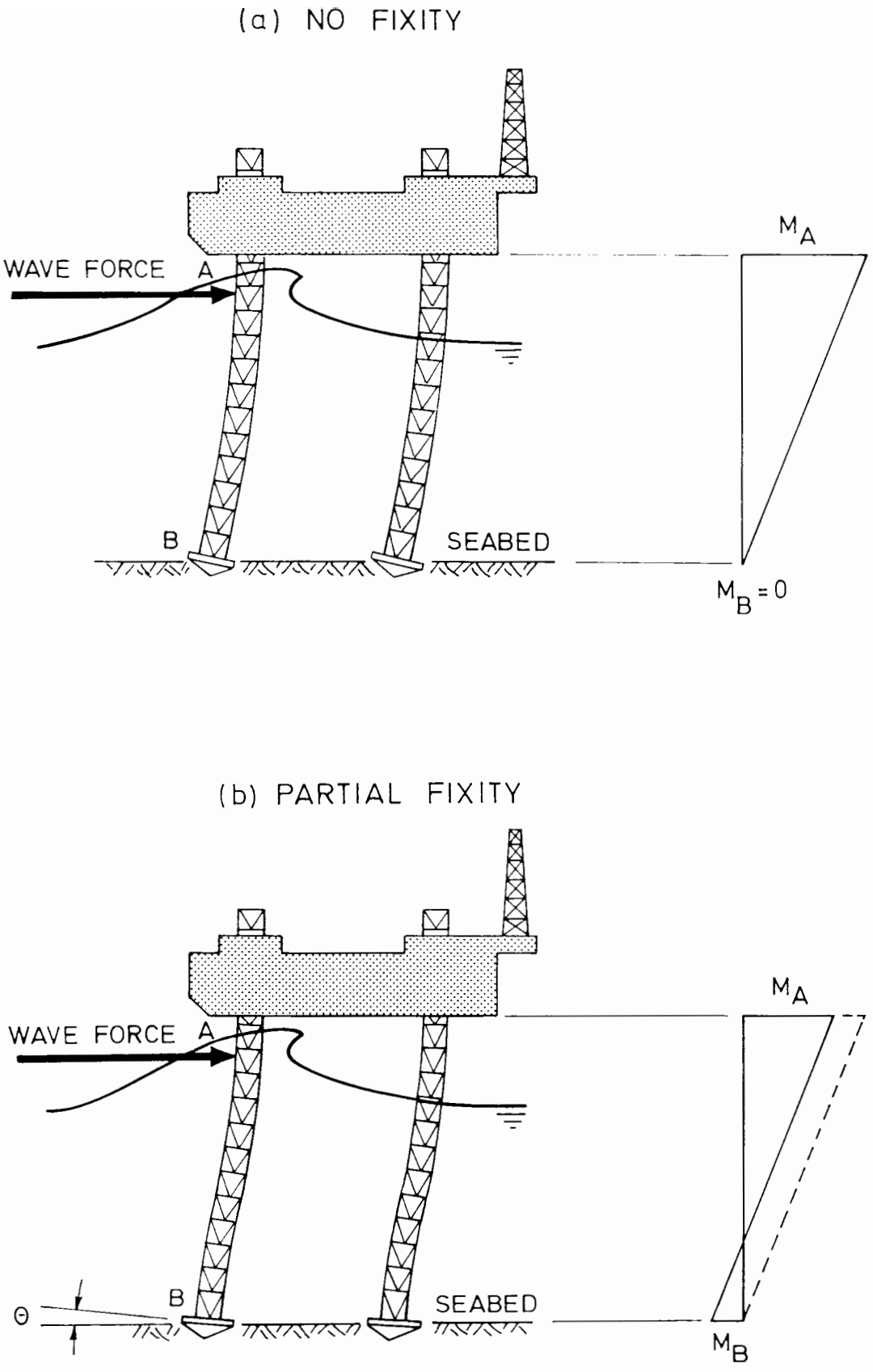

Figure 1.1 Bending moment distribution along a jack-up leg with no fixity (a) and partial fixity (b) at the footing

when subjected to combined loading. Such a knowledge is essential if fixity of jack-up foundation is to be assessed.

Another area requiring research concerns the rotational behaviour before failure of axisymmetric footings on clay under combined loading. For reasons already stated, a knowledge regarding the rotational stiffness of conical shaped footings is of paramount importance in the design and operation of jack-up rigs.

Although the understanding of the behaviour of footings under monotonic loading is unmistakably an important step in the analysis of this problem, it is also necessary to take account of the fact that a train of waves reaches the rig under storm conditions, causing cyclic loading.

The economic importance of the above problems motivated this research project, the purpose of which is the investigation of the behaviour of circular footings on clay under combined loading by means of physical models. As far as the loading is concerned, the study is divided into two stages:

* monotonic loading;
* cyclic loading.

In the first stage, involving monotonic loading and undrained behaviour, the modelling is believed to be quite realistic. The second stage involves some unavoidable scaling imperfections and therefore the results must be treated carefully and with good sense.

CHAPTER 2

LITERATURE REVIEW

2.1 Introduction

This chapter presents a brief review of previous works related to this research. A survey of the properties of the kaolin clay is initially presented, including results obtained in recent research works carried out at Oxford University. The value rigidity index G/s_u is then reviewed. This parameter is believed to be of major importance in the analysis of the behaviour and design of foundations, and some of its peculiarities are sometimes misunderstood. Considerable use of this quantity will be made later in this thesis.

The behaviour of circular footings on clay under monotonic loading has been extensively studied for many years and is presented in this chapter under two distinct headings: elastic behaviour and bearing capacity. Recent and important contributions related to limit analysis of footings with axial symmetry are believed to be of importance in offshore engineering applications.

Although much attention has been given to soils under cyclic loading, most of the works available in the literature are related to the fundamental behaviour of soils, either theoretical (constitutive models of various formulations and their numerical treatment) or experimental (triaxial tests, simple shear tests, etc.). Unfortunately only a small number of analytical

and experimental studies dealing with the overall behaviour of foundations under slow cyclic loading have been carried out.

2.2 Kaolin Clay

Kaolin clay has been extensively and successfully used as a model clay soil for both fundamental and applied soil mechanics research. Spestone Kaolin, now unavailable, was used for about twenty years in experimental works at Cambridge University. Speswhite Kaolin is now in current use by soil mechanics researchers and fortunately its geotechnical properties are similar to those of the Spestone Kaolin, as reported by Steenfelt, Randolph and Wroth (1981). This clay has been employed at Oxford University for the last seven years by several investigators, namely Love (1984), Gue (1984), Fannin (1986) and May (1987).

Table 2.1 shows the mechanical properties of the Speswhite Kaolin as obtained by Steenfelt, Randolph and Wroth (1981), Martins (1983), Gue (1984)

Table 2.1 Mechanical properties of the Speswhite Kaolin

property	symbol	value			
		(1)	(2)	(3)	(4)
plasticity index	PI	31	30	31	31
plastic limit	PL	38	32	34	31
liquid limit	LL	69	62	65	62
specific gravity of solids	G	2.61	-	2.60	2.61

Notes
(1) Steenfelt, Randolph and Wroth (1981)
(2) Martins (1983)
(3) Gue (1984)
(4) Fannin (1986)

and Fannin (1986). The consolidation and strength properties reported by Steenfelt, Randolph and Wroth (1981), Martins (1983) and Fannin (1986) are indicated in Table 2.2.

Martins (1983) found that the slope of the virgin consolidation line varied with ln p′ in e (voids ratio):ln p′ (logarithm of the mean effective stress)

Table 2.2 Consolidation and strength properties of the Speswhite Kaolin

property	symbol	values		
		(1)	(2)	(3)
slope of critical state line (tc)	M	0.9	0.9	0.88
angle of shearing resistance (tc)	ϕ'_{tc}	$\simeq 23^o$	$\simeq 23^o$	22.6^o
slope of consolidation line	λ	0.25	0.23 to 0.25 (p′=5 to 50kPa) 0.21 to 0.23 (p′=50 to 200kPa) 0.18 to 0.21 (p′=200 to 350kPa)	0.247
slope of swelling line	κ	0.05	0.04 (p′=10 to 350kPa)	0.04
voids ratio at p′ = 1 kPa	$(e_\lambda)_{1-D}$	2.58	2.52 (p′=50 to 100kPa)	2.51
coefficient of "at rest" earth pressure	K_o	-	0.65 ± 0.01	0.64 ± 0.05

Notes

(1) Steenfelt, Randolph and Wroth (1981)
(2) Martins (1983)
(3) Fannin (1986)
(4) tc = triaxial compression

space, the value decreasing slightly with increasing p'. Butterfield (1979), calling attention to this problem, proposes an alternative approach suggesting a linear relationship between log v and log p' where v is the specific volume.

2.3 Rigidity Index

The elastic deformation analysis of soils requires the knowledge of any two out of the four constants from linear isotropic elasticity, namely Young's modulus E, Poisson's ratio ν, shear modulus G and bulk modulus K. Since G is the only deformation modulus which is not affected by the type of analysis being undertaken (total stress or effective stress), either the pair G,ν or G,K is preferable as representative of the soil elastic behaviour.

In the case of saturated clays under undrained loading conditions, the only modulus required is G (since $\nu_u = 1/2$ and $K \rightarrow \infty$). This parameter can be conveniently related to the undrained shear strength of the clay s_u, resulting in a dimensionless ratio called rigidity index I_r:

$$I_r = G/s_u \ . \qquad [2.1]$$

Wroth, Randolph, Houlsby and Fahey (1984) present a number of important considerations associated with the evaluation and behaviour of G/s_u, summarized as follows:

(i) As G (secant modulus) obviously varies with the amplitude of strain, then it is necessary to decide over which range of strain the stiffness must be determined. This range varies significantly among many practical problems in Soil Mechanics.

(ii) It is very difficult to determine the ratio G/s_u accurately because it involves the measurement of the modulus G, notoriously difficult to measure with accuracy, and the undrained shear strength s_u, which is by no means a unique property of a particular soil. As pointed out by Wroth (1984), the latter parameter is dependent on the type of test and on the intermediate principal stress σ_2, which is not taken into account in its definition.

(iii) For normally consolidated clays, the rigidity index corresponding to 50 % of the shear strength of the clay (G_{50}/s_u) decreases with increasing plasticity index, confirming a similar trend previously observed by D'Appolonia, Poulos and Ladd (1971) for the ratio E_u/s_u.

(iv) For the same type of test and consolidation (isotropic or one-dimensional), there is a well defined pattern of behaviour between the rigidity index and the overconsolidation ratio OCR for samples originally consolidated to the same maximum stress level, described by the following semi-empirical expression:

$$\frac{\left(\frac{G}{s_u}\right)}{\left(\frac{G}{s_u}\right)_{nc}} = (1 + C \ln OCR)\ OCR^{-\Lambda} , \qquad [2.2]$$

where:

$(G/s_u)_{nc}$ = rigidity index for normally consolidated clay;

C = a soil constant, in the range between 0 and about 2;

OCR = overconsolidation ratio;

$\Lambda = \frac{\lambda - \kappa}{\lambda}$ (plastic volumetric strain ratio).

(v) The values of the rigidity index obtained from triaxial tests are significantly lower than those produced by in-situ tests such as the pressuremeter or plate loading test.

Houlsby and Wroth (1985) present an alternative expression relating the rigidity index to the isotropic overconsolidation ratio R:

$$\frac{\left(\frac{G}{s_u}\right)}{\left(\frac{G}{s_u}\right)_{nc}} = R^{(n-\Lambda)}, \qquad [2.3]$$

where n is a constant that should lie between 0 and 1. The above expression [2.3] comes from a proposed equation, supported by experimental data, involving the quantity G/p′, the value of this quantity for a normally consolidated soil and the overconsolidation ratio. It also assumes that isotropic elasticity is applicable during the initial stages of an undrained shear test. The authors conclude that values of n may typically be about 0.5 and, considering the value of Λ as being about 0.75, the exponent $(n-\Lambda)$ may be around -0.25.

2.4 Circular Footings on Clay under Monotonic Loading

2.4.1 Elastic Behaviour

The analysis of the elastic behaviour of circular footings resting on the ground level of an isotropic elastic continuum can be subdivided into two different approaches:

* analysis of flexible footings;
* analysis of rigid footings.

The first approach is normally adopted for structural design of footings and also for stress and strain analysis in the soil medium if the stiffness of the foundation body is comparable to the soil stiffness.

The second approach, assuming that the plate is infinitely rigid, is a particular simplified case of the first one. It is appropriate for many design problems.

For the case of rigid footings, the general solution can be formulated in terms of Airy's strain potential function $\Psi(r,z)$ which satisfies the biharmonic equation:

$$\nabla^2 \nabla^2 \Psi(r,z) = 0 \ , \qquad [2.4]$$

where:

∇^2 = Laplace operator referred to a system of cylindrical polar coordinates;

r,z = cylindrical coordinates.

The contact pressure p(r) can be evaluated from (Poulos and Davis, 1974):

$$p(r) = \frac{2Gz}{\pi (1 - \nu) R} \frac{1}{\sqrt{[1 - (r/R)^2]}} \ , \qquad [2.5]$$

where:

G = shear modulus of the soil mass;

ν = Poisson's ratio of the soil mass;

z = settlement of the footing;

R = radius of the footing;

r = radial coordinate.

The total load V can be represented by the following expression:

$$V = \frac{4GzR}{1 - \nu} \, . \qquad [2.6]$$

Poulos and Davis (1974) record a number of elastic solutions for particular cases of rigid loaded circular area of radius R or circular area subjected to uniform displacements, derived by various authors:

(i) Bycroft obtained the following expression relating the horizontal displacement y to the horizontal load H applied to a rigid circular footing:

$$H = \frac{32G\ (1 - \nu)\ Ry}{7 - 8\nu} \, . \qquad [2.7]$$

(ii) Gerrard and Harrison derived the following equation for the same problem:

$$H = \frac{8GRy}{2 - \nu} \, , \qquad [2.8]$$

where H is the lateral load applied.

It is worth pointing out that there is an inconsistency between the two solutions [2.7] and [2.8]. The ratio between the displacements evaluated from equations [2.7] and [2.8], for the same horizontal force, the same elastic soil medium and the same circular area varies from 1.00, for $\nu = 0.5$, to 0.88, for $\nu = 0$.

(iii) Borowicka obtained the expression relating the rotation angle θ of a circular rigid footing to the loading moment M:

$$M = \frac{8GR^3\theta}{3\,(1 - \nu)} \quad . \qquad [2.9]$$

The formula [2.9] is referenced in API RP2A (AMERICAN PETROLEUM INSTITUTE, 1984, "API Recommended Practice for Planning, Designing and Constructing Fixed Offshore Platforms").

Sneddon (1965) derived expressions for the load-deflection response and contact pressure distribution beneath rigid foundations of arbitrary axisymmetric profiles. The general form of the load-deflection expression is:

$$V = \frac{4GR}{1 - \nu} \int_0^1 \frac{x^2\, f'(x)\, dx}{\sqrt{(1 - x^2)}} \quad , \qquad [2.10]$$

by means of which the total load V necessary to produce the vertical displacement z of a rigid footing whose profile is defined by the function f can be calculated. In the special case of cones, expression [2.10] becomes:

$$V = \frac{4G\,\cot(\beta/2)}{\pi\,(1 - \nu)}\, z^2 \quad , \qquad [2.11]$$

$$\text{for} \qquad z \leq \frac{R}{\tan(\beta/2)} \quad ,$$

where:

β = angle of the cone;

R = maximum radius of the cone.

The results of a finite element study carried out to analyse the elastic rotational behaviour of cones and spud-cans can be found in Noble Denton & Associates (1987). In this study, the rotational stiffness M/θ of a rigid cone on a no-tension elastic soil is established in the form:

$$\frac{M}{\theta} = GR^3 f_1(\beta, \frac{e}{R}, \nu) \ , \qquad [2.12]$$

where:

R = radius of the cone at the soil surface;

β = cone angle;

e = eccentricity of vertical load.

The form of function f_1 depends on the adhesion between the soil and the cone surface. Figure 2.1 shows the variation of f_1 with cone angle, when $\nu = 0.495$, for both perfectly smooth and perfectly rough cones. It is worth mentioning that rotational stiffness of circular plates ($\beta = 180^o$) is about the same for either a smooth or a rough surface.

The results for elastic behaviour of the spud-can represented in Figure 2.2

Table 2.3 Values of non-dimensional stiffnesses of a spud-can and its limiting cones (after Noble Denton and Associates, 1987)

$\nu = 0.495$	spud-can	cones		surface
		$\beta = 150^o$	$\beta = 137.5^o$	
$\frac{M}{\theta GR^3}$	5.431	5.417	5.486	rough
	3.613	1.347	1.459	smooth

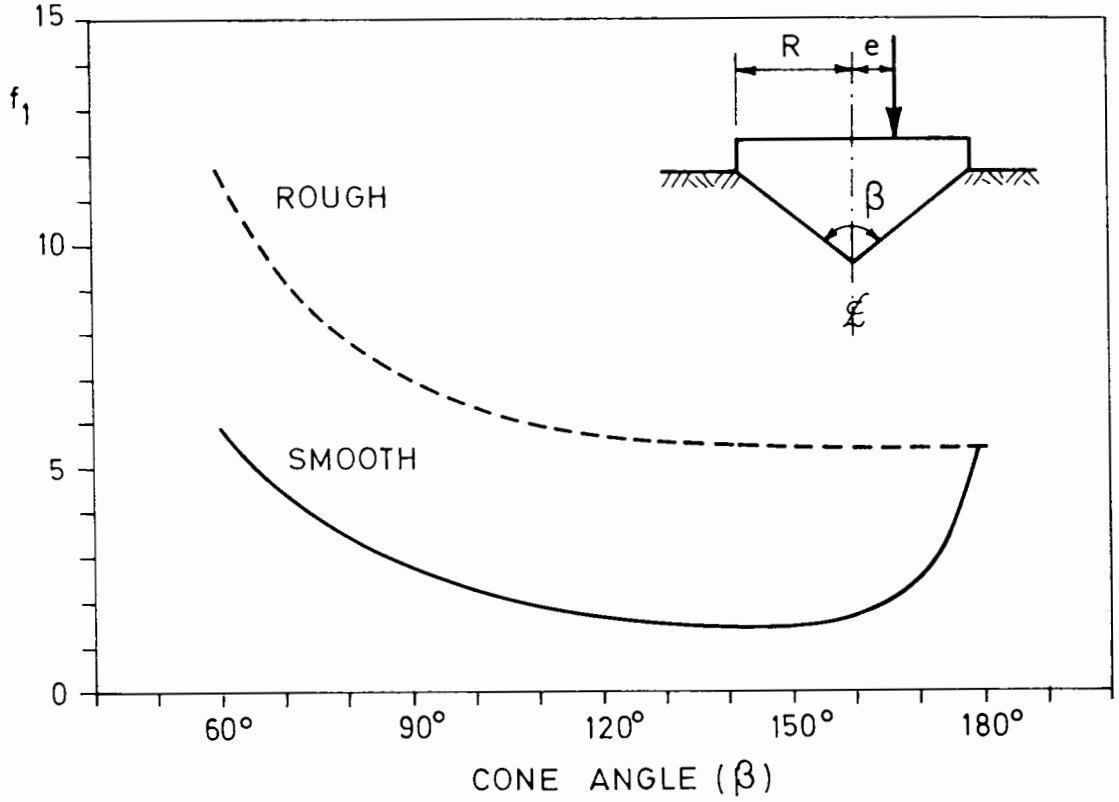

Figure 2.1 Variation of the elastic rotational function $f_1(\beta, e/R, \nu)$ with cone angle (after Noble Denton and Associates, 1987)

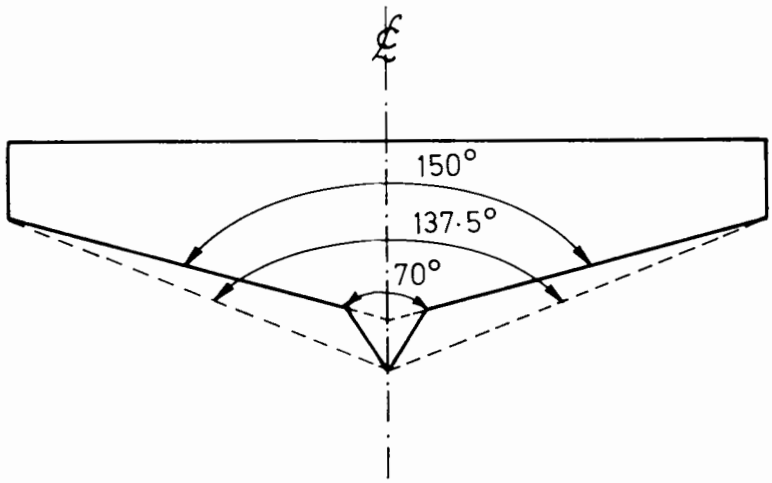

Figure 2.2 Spud-can geometry (after Noble Denton and Associates, 1987)

are shown in Table 2.3 for both fully smooth and fully rough cases and $\nu = 0.495$. The values of $M/\theta GR^3$ for the bounding cones (Figure 2.2) are also presented for comparison. It can be seen that the rough spud-can has

approximately the same rotational stiffness as the rough bounding cones while the smooth spud-can is on average 2.6 times stiffer than the smooth bounding cones.

2.4.2 Bearing Capacity

The first closed form solution to a bearing capacity problem was achieved by Prandtl in 1920, using plasticity theory, for an infinitely long smooth flat strip on the surface of a weightless medium. Since then, only a few exact solutions for particular cases of loading and geometry have been obtained, while a significant number of approximate formulae have become available in the technical literature, among which Terzaghi's formula (1943) stands out for its pioneering and historical value. Apart from Terzaghi, the following authors have also provided relevant contributions to this subject: Brinch Hansen (1961 and 1970), Meyerhof (1951, 1953, 1961 and 1963), Skempton (1951) and Vesic (1973 and 1975).

The approximate solutions proved to be very attractive to the foundation engineer, mostly because of their intrinsic simplicity and versatility. In many cases, correction factors were introduced to extend the formulae to cover almost any conceivable situation of design involving the geometry of the footing, its position with respect to the ground surface and the combination of loads applied. Obviously, for some of these cases the assumptions regarding the theoretically based part of the formulae become unrealistic.

Meyerhof (1961) presents an extension of his previous theory to wedge-shaped bases and cones, providing charts for bearing capacity factors for perfectly smooth and perfectly rough cones (cone angles varying from about 10^{o} to 180^{o}) and for various angles of internal friction of the soil. For

intermediate roughness Meyerhof recommends linear interpolation.

Cox, Eason and Hopkins (1961), using the method of the characteristics, obtained the exact solution for the maximum load applied to a semi-infinite region of soil, bounded by a plane surface, by means of a flat-ended, smooth, rigid, circular cylinder for both frictionless and frictional materials. The bearing capacity factor for the former case of soil is 5.69.

Houlsby and Wroth (1983), also employing the method of the characteristics, studied the problem of shallow penetration of cones into a cohesive soil. They presented the results (Figure 2.3) in terms of variation of bearing capacity factor N_c with cone angle β and roughness α (defined as a_u/s_u where a_u is the undrained adhesion of the clay to the cone surface). For perfectly smooth cones the bearing capacity factor is 5.69 when $\beta = 180^o$ (the same value previously obtained by Cox et al), decreasing then with β up to a minimum value of about 4.44 at β of about 54^o, slightly increasing when β decreases to 30^o. For perfectly rough cones the bearing capacity factor is 6.05 for circular plates ($\beta = 180^o$), slightly increasing with decreasing β until approximately 90^o. Then, for sharper cones, the bearing capacity factor increases abruptly.

One of the most common cases of non-homogeneity observed in normally consolidated deposits of clay is an increasing undrained shear strength with depth. This variation can often be satisfactorily assumed as linear and may have a significant effect on the bearing capacity of large footings. As seabed soils frequently exhibit this kind of non-homogeneity, such a problem cannot be ignored in the analysis and design of foundations of offshore structures.

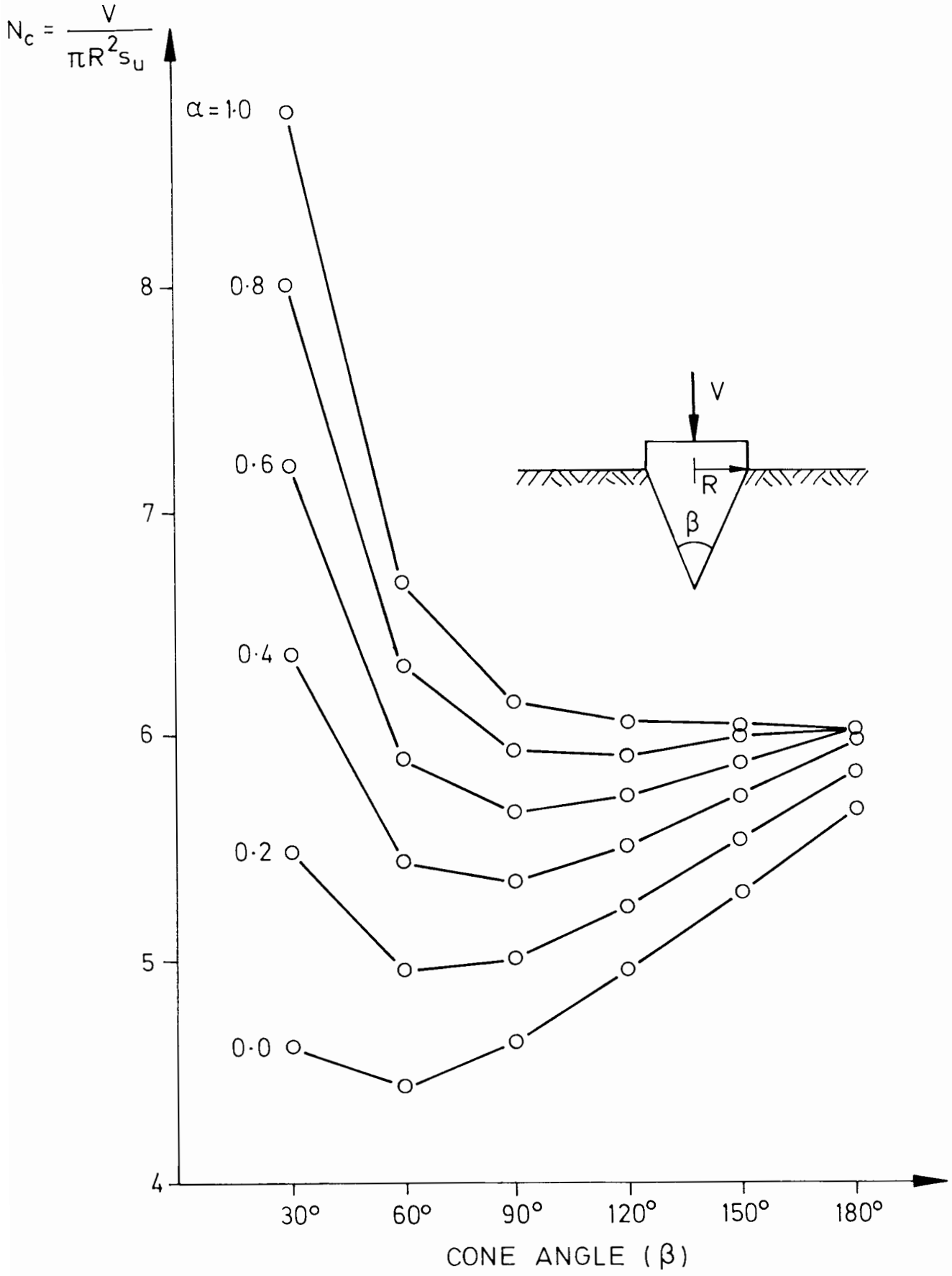

Figure 2.3 Theoretical variation of bearing capacity factor N_c with cone angle β and cone roughness α (after Houlsby and Wroth, 1983)

Davis and Booker (1973) achieved solutions to the problem of bearing capacity of clay which is non-homogeneous in the vertical direction, for the case of smooth and rough footings in plane strain.

Houlsby and Wroth (1983), using the same technique of integration along characteristics previously mentioned, obtained bearing capacity factors for smooth and rough circular flat footings on the surface of a clay soil with strength increasing with depth in the form:

$$s_u = s_o + \rho z \ , \qquad [2.13]$$

where:

s_o = undrained shear strength at the soil surface;

ρ = a soil constant;

z = depth.

One of the interesting conclusions brought about by this work is that the ratio between the bearing capacity factors N_{cas} and N_{cps} (defined as V/s_oA where V is the load and A the area of the footing) for axially symmetric and plane strain footings respectively, usually referred to as shape factor, is not equal to the conventional value of 1.2 even for homogeneous material, as shown in Figure 2.4. For values of $\rho B/s_o$ (B represents the width of a plane strain footing or diameter of a circular footing) higher than about 2 this ratio is less than 1 for both smooth and rough footings.

The Noble Denton & Associates (1987) shows the results of a finite element analysis carried out to study the failure conditions of perfectly rough cones on clay under combined loading. Figure 2.5 shows the ultimate loads of 120^o cone, 150^o cone and circular plate ($\beta = 180^o$) by means of two sections

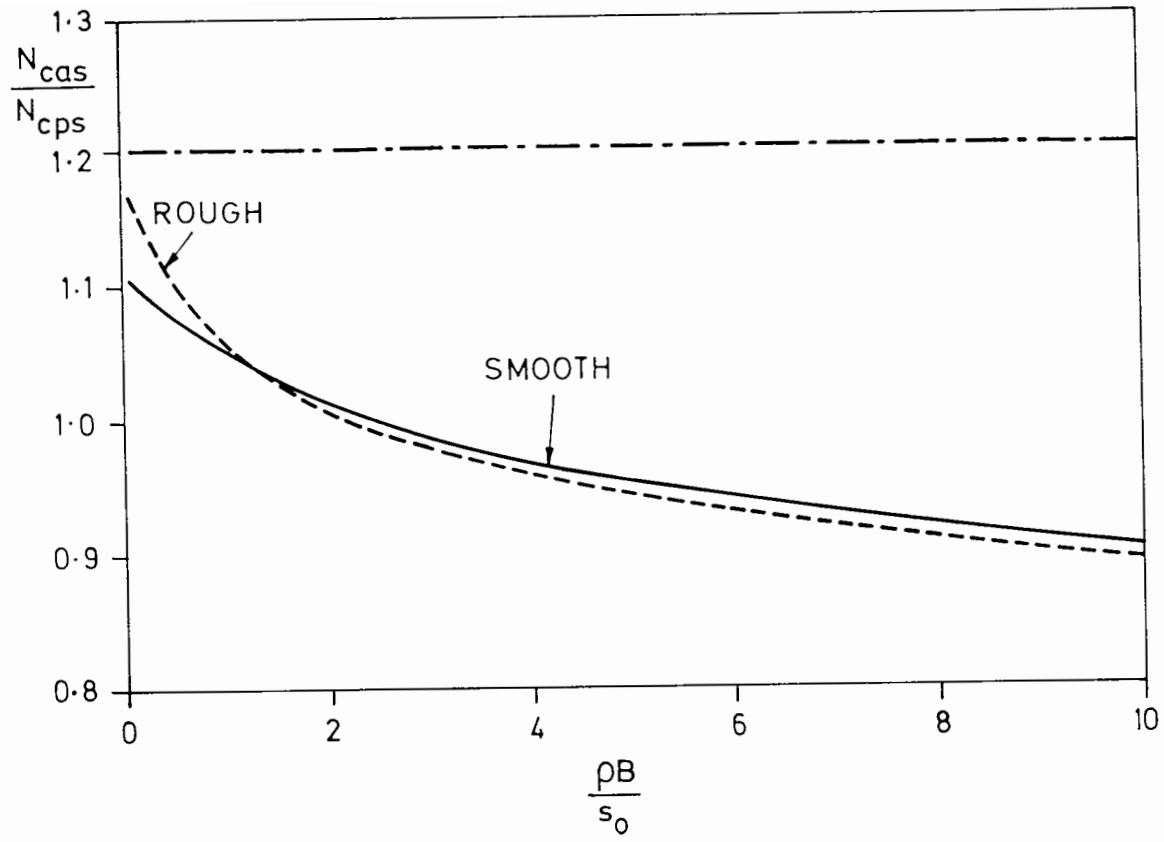

Figure 2.4 Variation of the ratio between the bearing capacity factors for axially symmetric and plane strain footings with the quantity $\rho B/s_o$ (data from Houlsby and Wroth, 1983)

in the $V/s_uA:H/s_uA:M/s_uAR$ space, one corresponding to $M/s_uAR = 0$ (a) and the other to $V/s_uA = 3.6$ (b), where:

V = vertical load;

H = horizontal load;

M = moment;

A = cross-sectional area of the footing at soil surface.

The results obtained demonstrate that the horizontal load does not significantly affect the ability of the footing to resist moment loading until that load approaches its ultimate value.

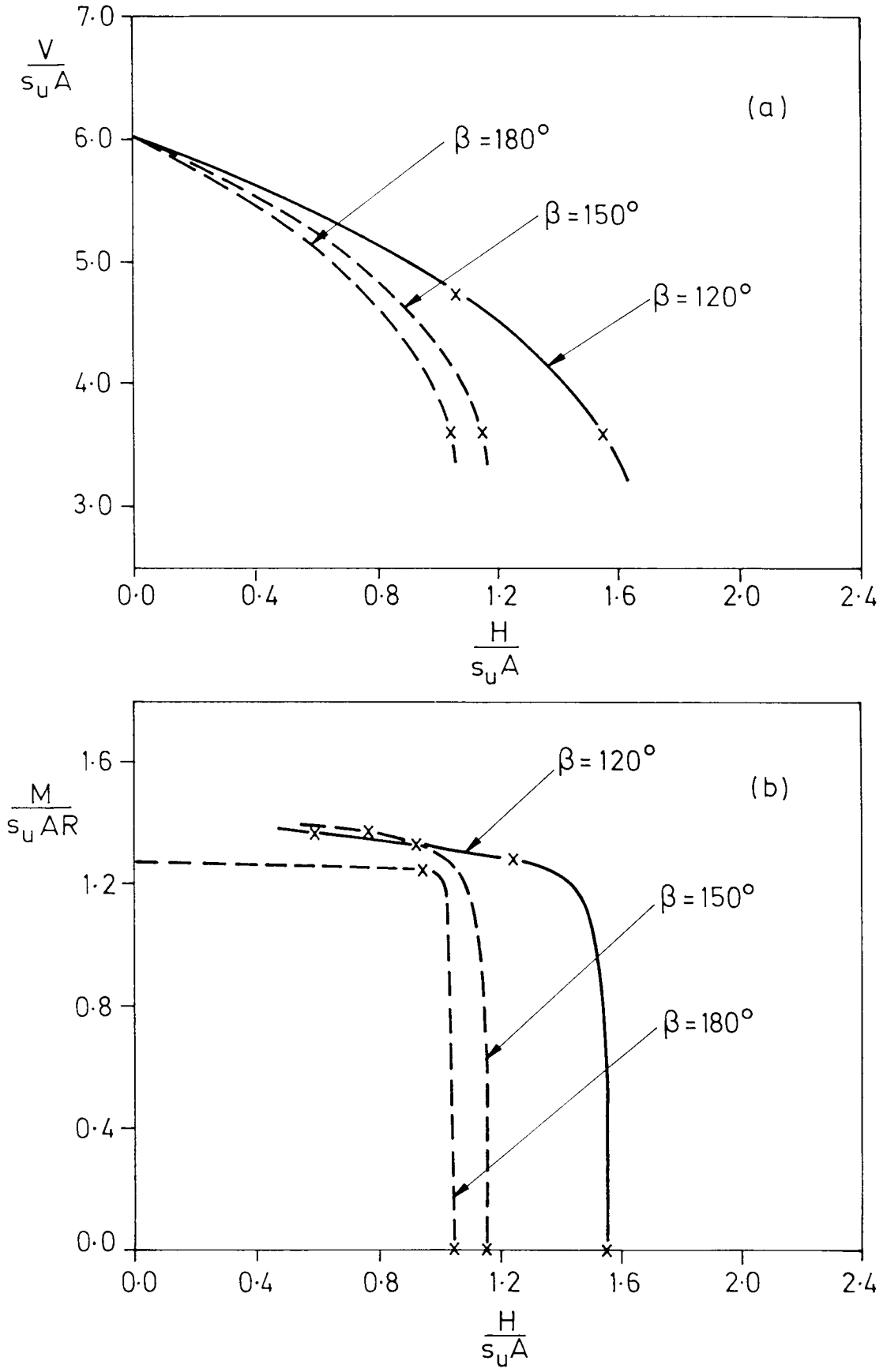

Figure 2.5 Ultimate loads for conical footings in V/s_uA:H/s_uA:M/s_uAR space corresponding to $M/s_uAR = 0$ (a) and $V/s_uA = 3.6$ (b) (after Noble Denton and Associates, 1987)

2.5 Footings on Clay Under Cyclic Loading

Andersen (1976) sets out a method for predicting clay behaviour under storm loading producing varying shear stresses. This method has been successfully used in design of offshore gravity platforms and is based on data corresponding to cyclic shear strain and pore pressures versus number of cycles, acquired from laboratory tests with constant two-way cyclic shear stress. By means of plots produced with laboratory data, cyclic shear strain and permanent pore pressure can be obtained at the end of a storm loading. In the case of clays the procedure must be repeated for a series of consecutive storms, when the reduction in undrained shear strength (and safety) may then be evaluated.

Pande (1982) proposes the use of the shakedown theorems to determine the upper and lower bound on the shakedown load for ideal elasto/plastic materials. These theorems, of which the collapse theorems are particular cases, have been neglected in the Soil Mechanics literature until recently. The first shakedown theorem was proved by Melan in 1936 and the second by Koiter in 1956. Pande emphasises that precise determination of shakedown loads leads to mathematical programming problems of great magnitude, involving excessive computing costs, and suggests alternative and simplified rules for analysis of situations related to geotechnical engineering, assuming the material as linear elastic and ideally plastic.

Rowe (Rowe and Smith, 1982) reports that a gravity platform model placed on saturated uniform overconsolidated clay and subjected to an increasing oscillatory lateral force ΔH, having no static component, exhibits an amplitude of lateral displacement increasing to an unacceptably large value. It was observed that the layer of weakened clay just below the model was progressively displaced, causing settlement.

Smith (Rowe and Smith, 1982), using finite element analysis, modelled Rowe's model gravity platforms on overconsolidated clay and obtained a correlation between vertical displacement and horizontal load in good agreement with the experimental data, although the magnitudes of the settlements were overpredicted. Also, the shape of the curve of vertical displacement versus number of cycles, predicted at various values of vertical load, qualitatively agreed with the test data, but the number of cycles was two orders of magnitude less than in the test.

CHAPTER 3

EQUIPMENT

3.1 Introduction

Except for the consolidation apparatus, which already existed in the Soil Mechanics Laboratory before the beginning of this work, all the mechanical equipment used in the tests was conceived, designed and built or ordered specially for this research. A microcomputer equipped with a data logging system was also acquired, in cooperation with another project being carried out in the laboratory.

Most of the equipment used in the first stage of this research, dealing with monotonic loading, was also employed in the second stage, when cyclic loading was applied. Although the loading system was initially designed for use in the first stage, it was also designed to apply cyclic loading with only minor alteration required.

3.2 Consolidation Apparatus

There are three consolidation frames, all connected to the same pressurization system, allowing simultaneous preparation of three clay samples, as illustrated in Figures 3.1 and 3.2.

Each apparatus, designed by Gue (1984), consists of a reaction frame and a double action hydraulic ram attached to the top of the frame. A loading platen is bolted to the lower end of the piston and the sealing between the

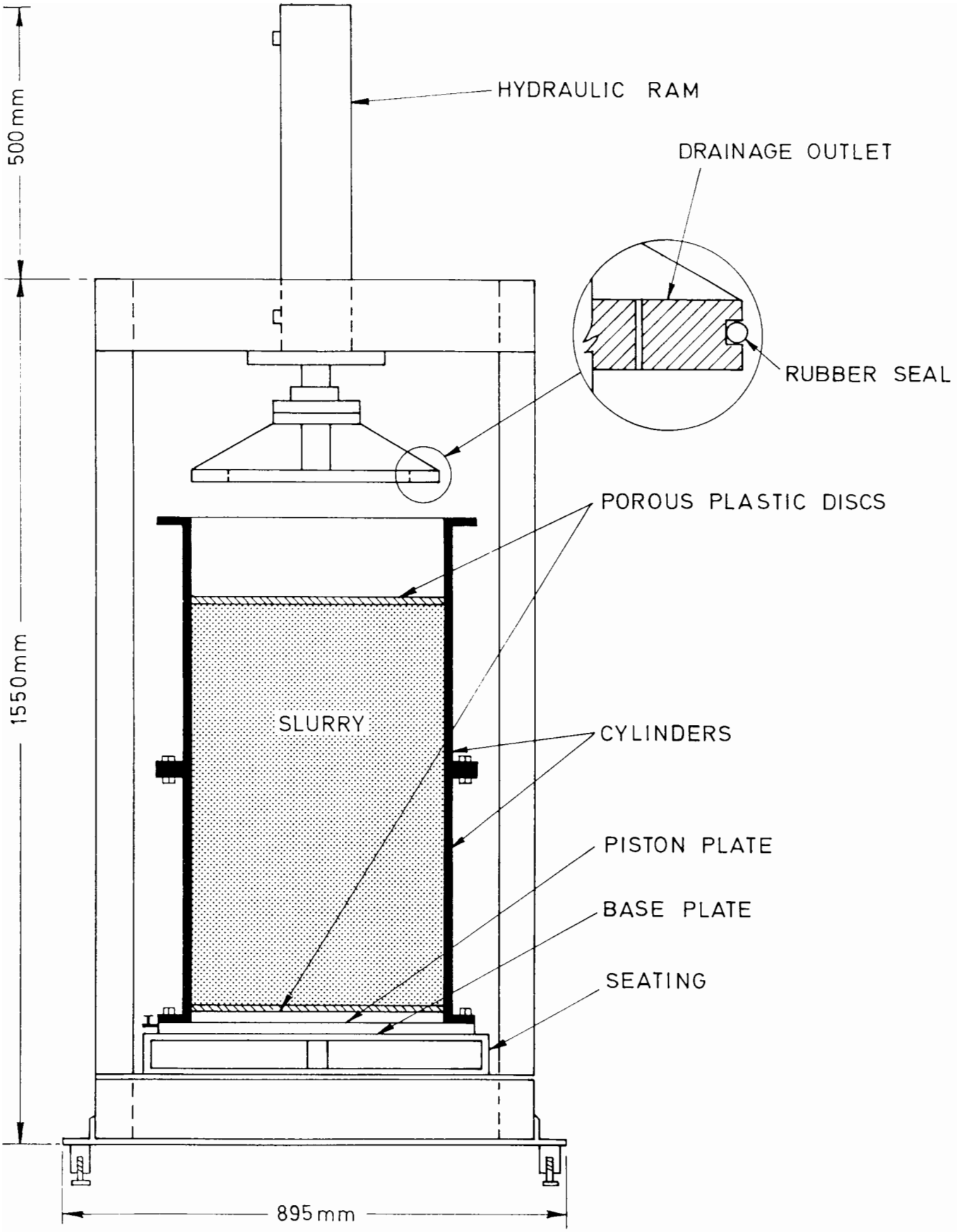

Figure 3.1 Consolidation apparatus

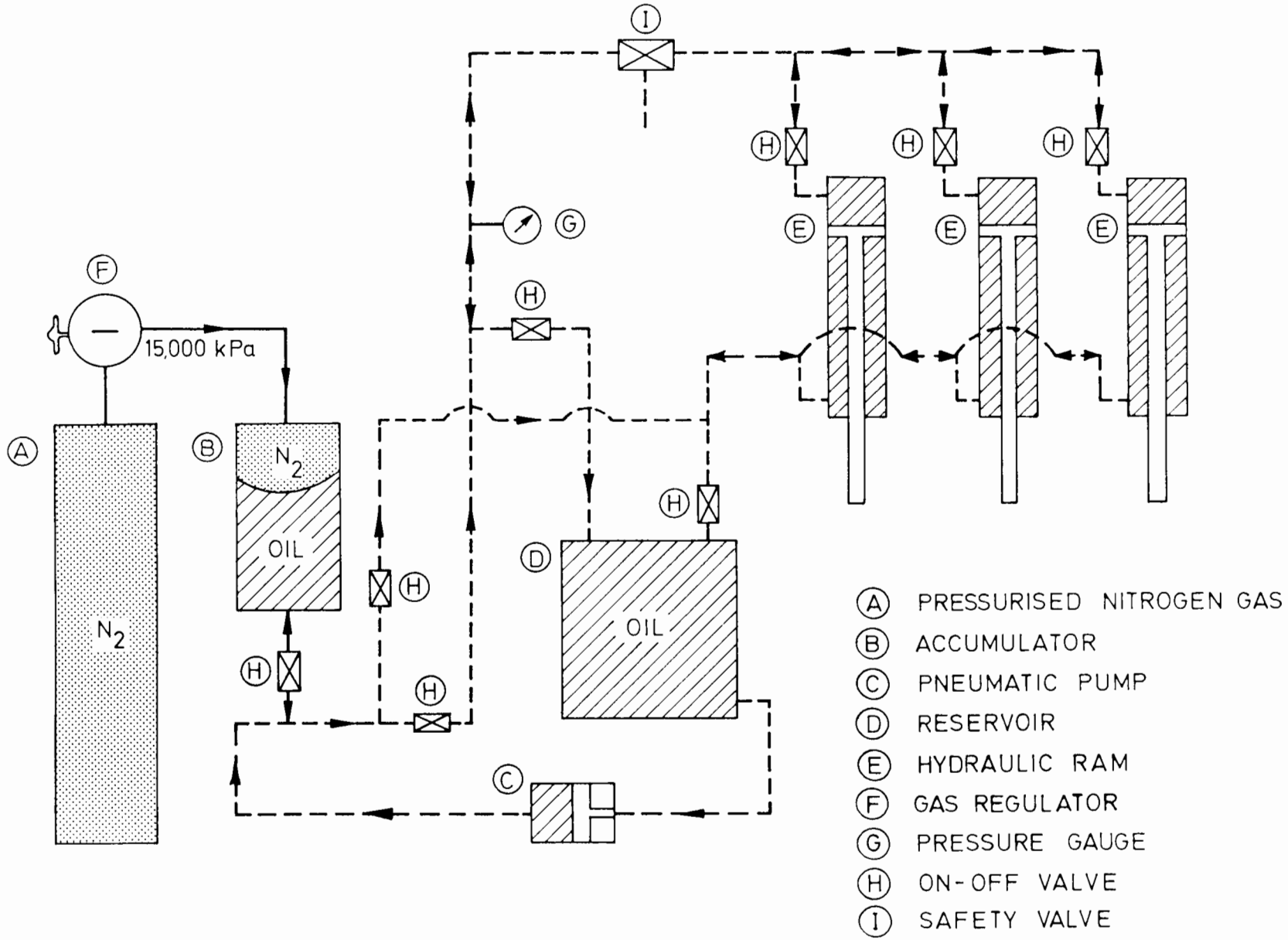

Figure 3.2 Diagram of the hydraulic system

platen and the tank wall is achieved by means of a flexible rubber hose placed into a groove around the platen.

The slurry tank consists of 2 cylinders and a circular base plate, all bolted together and sealed by rubber gaskets. The cylinders are 450 mm in inner diameter, 450 mm in height and 6 mm in wall thickness, provided with 2 flanges 10 mm thick and 50 mm wide.

Inside the lower cylinder and lying on the base plate is set a piston designed to push part of the clay block out of the cylinder, allowing a second testing stage. The same sealing method adopted for the loading platen was repeated for the lower piston. In order to push the piston up, four 20 mm diameter and 275 mm long rods are attached to it through four holes in the base plate. A 20 mm thick 318 mm square plate fixes the lower ends of the rods in their respective positions. Four 20 mm thick and four 15 mm thick triangular plates are used to separate the square plate from the circular base plate. Figure 3.3 shows the accessories employed in the pushing up operation.

During the consolidation process, the circular base and the piston are fixed together by four plugs, fitted with "O" rings, attached to the piston, closing and sealing the holes in the base plate.

The apparatus allows both top and bottom drainage. Top drainage occurs through two holes in the loading platen and bottom drainage is carried out through grooves and channels existing in the piston plate and in the circular base. A small tap attached to the bottom outlet, providing control to the bottom drainage, is connected to a plastic hose leading to the top cylinder. Two porous discs are placed at the top and bottom of the slurry tank.

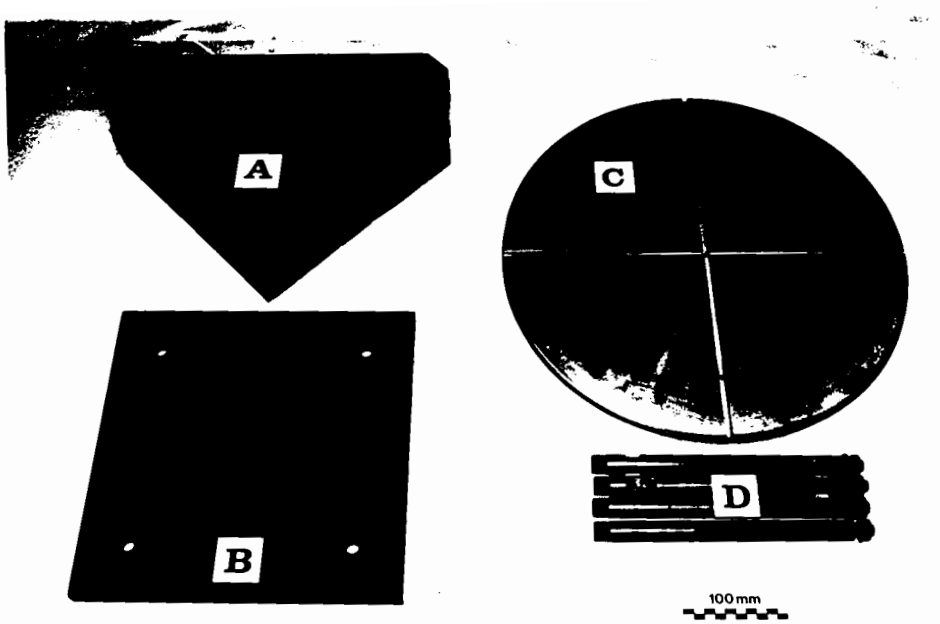

A = triangular plates
B = square plate
C = piston
D = rods

Figure 3.3 Accessories employed in the pushing up operation

The pressure needed to consolidate the clay samples is supplied by an hydraulic system, which is represented in the diagram of Figure 3.2. Pressurized nitrogen gas, controlled by a regulator, transmits an input gas pressure to an accumulator, which acts as a gas-oil interface, producing the same output oil pressure. A set of eight valves are arranged so that the system can be operated in different ways. A pneumatic pump is used to raise or lower the platen by pumping oil from the reservoir into one or other section of the ram and to fill the accumulator before it is pressurized. This pump can also be used to apply small pressures in the system. An adjustable maximum pressure safety valve, placed in the oil circuit, prevents any overpressure on the clay under consolidation in case a fault occurs in the gas regulator.

The main structure of the consolidation apparatus is made of mild steel channels, while the loading platen, cylinders, base plates and the lower pistons are of duralumin, a nonferrous alloy which has the same mechanical strength as the mild steel and good corrosion resistance. It is also convenient for handling since its unit weight is about a third that of mild steel.

The three hydraulic rams were calibrated against a 199.3 kN (20 tonf) capacity load cell and the loads obtained were on average 99.2 % and 97.5 % of the loads inferred from the cross-sectional area of the pistons, in loading and unloading respectively.

3.3 Loading Device

The loading device, shown in Figure 3.4 and illustrated in Figure 3.5, was designed to produce axial linear displacements either at a pre-set constant speed or at a pre-defined function of time. The whole system is assembled on a rectangular duralumin plate 335 mm x 200 mm x 9.5 mm and weighs 39.1 N.

To provide support for the motor, another rectangular plate 200 mm x 60 mm x 9.5 mm is firmly attached to the rear of the first one, forming a right angle. The power unit is a geared d.c. servo tacho motor, which transmits a rotary motion to a ballscrew. Two motors with different specifications were used during the research so that the best performance of the loading system could be achieved in each stage:

monotonic loading, when torque was an important feature for the system to reach the maximum load without dropping the pre-set speed: motor GM1562/T24 (full load speed: 10 rpm; full load torque: 45 Ncm);

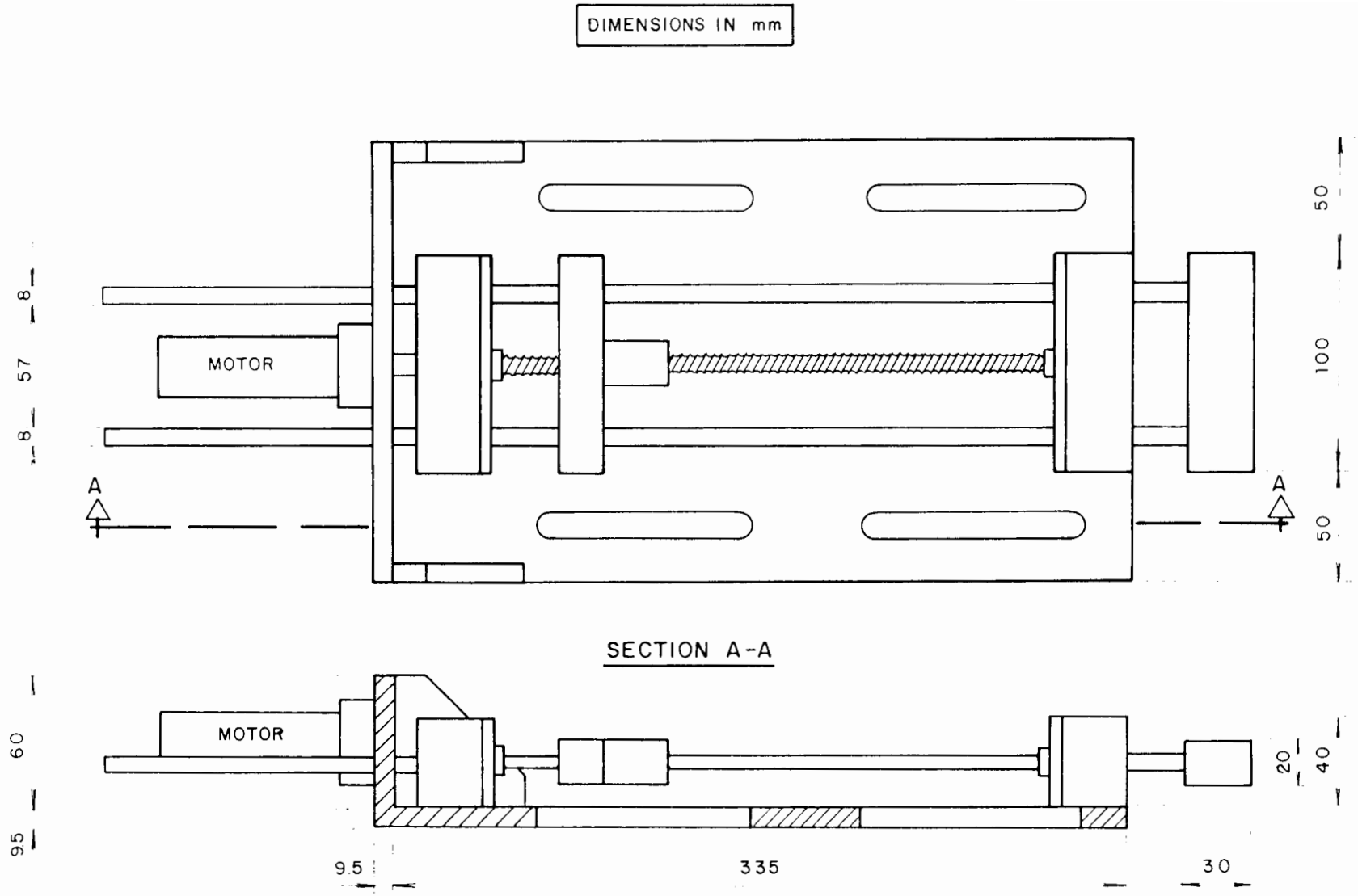

Figure 3.4 Loading device

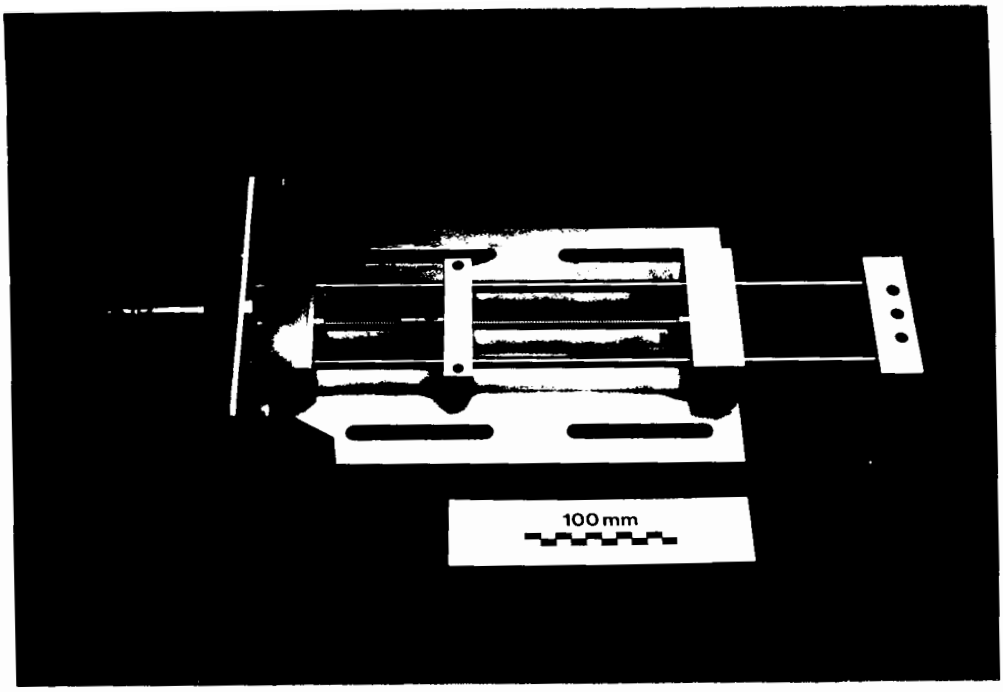

Figure 3.5 Photograph of the loading device

cyclic loading, when loads were only a fraction of the maximum value required in the previous stage, but swiftness was imperative to allow the system to follow loading and unloading patterns in a short period of time: motor GM1552/T24 (full load speed: 30 rpm; full load torque: 40 Ncm).

The nut fitted to the screw is fixed to two linear bearing shafts supported by four ball bushings so that it cannot rotate and so a linear movement is provided. A thrust ball bearing and a single row radial ball bearing support the ballscrew on each extremity. Two housings accommodate the ball bearings and the ball bushings.

The motor is assisted by a servo amplifier system allowing the device to be operated in three different modes of interest:

(a) manual velocity control;

(b) pre-set load control;

(c) pre-set displacement control.

The diagrams in Figure 3.6 show the connections for (a) manual velocity control mode and (b) pre-set load controlled mode, used in monotonic and cyclic loading stages respectively.

When motor GM1562/T24 is installed, the maximum load capacity of the system is 1000 N, with a limit linear speed of ± 20 mm/minute. Otherwise, with motor GM1552/T24, the maximum load reduces to 850 N while the speed may reach ± 60 mm/minute. In both cases, the maximum stroke is 165 mm. The device can be easily fixed to the reaction frame by means of four bolts placed through four slots 12 mm wide and 150 mm long existing in the assembling plate.

3.4 Reaction Frame

The reaction frame is the structure to which the loading device is attached. It also provides support for part of the instrumentation and any additional accessories needed during the test. It consists of two columns and one beam made from 8" x 3" x 5/16" x 1/2" duralumin channel (Figure 3.7). The columns are 1638 mm long and each one has two 16 mm thick and 409 mm long duralumin bars welded to it at the bottom, provided with oval holes, to fix it to the flanges of the testing tanks. There are also pairs of slots 100 mm long and 12 mm wide (except for one pair which is only 50 mm long) along the length. Through these holes the loading device is attached to the columns. The arrangement of slots is different on the two columns so that the loading device can be located horizontally at any position along the frame.

(a) MANUAL VELOCITY CONTROL

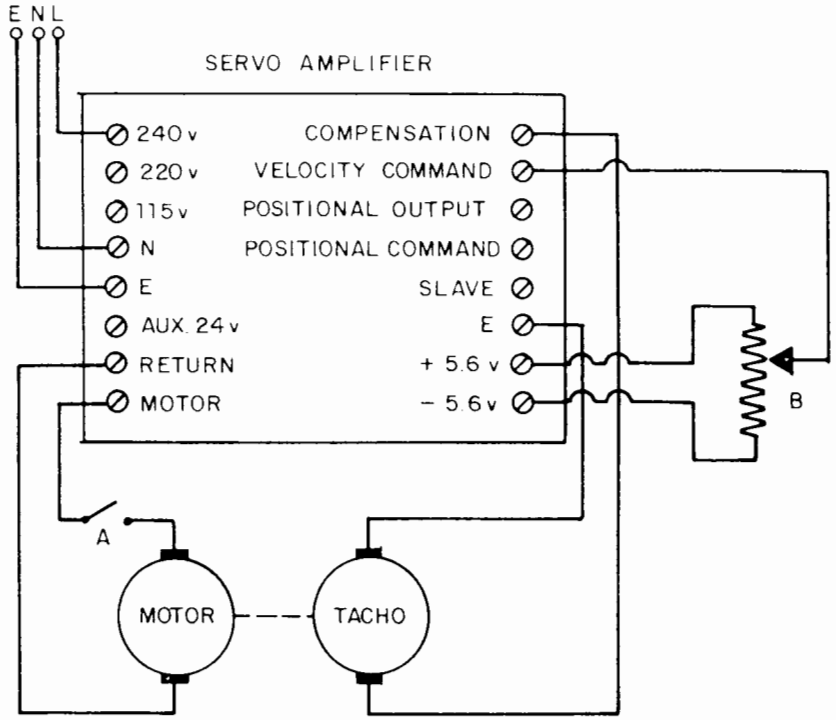

(b) PRE-SET LOAD CONTROLLED

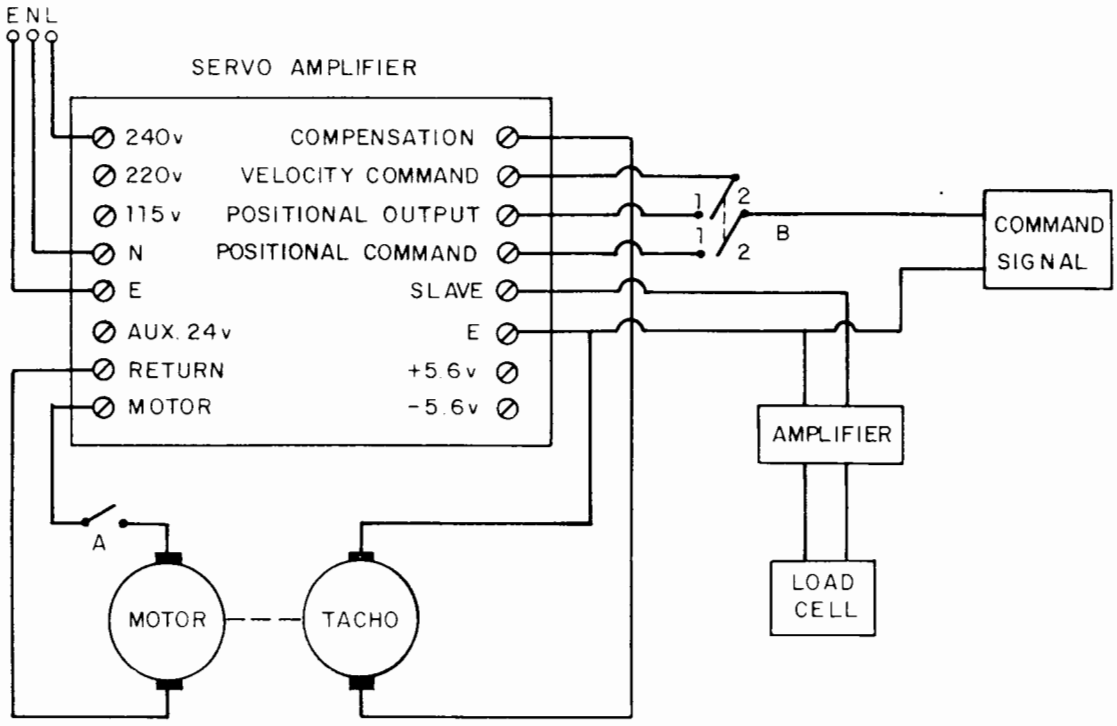

Figure 3.6 Diagrams showing the connections for manual velocity control mode and pre-set load controlled mode

The beam can be positioned at any height from the top of the tank up to a maximum clearance of 1093 mm. It is also provided with pairs of slots so that the loading device can be fixed vertically on it at some positions. The double slot bolting attachment allows rotation of the loading direction relative to the frame member axis (Figure 3.7).

3.5 Model Footings and Model Legs

Two sets of duralumin model footings were employed in this work: one set 50 mm in diameter including a flat circular plate, a 150^{o} cone, a 120^{o} cone, a 90^{o} cone, a 60^{o} cone, a 120^{o} spud-can and a 130^{o} spud-can, and another 100 mm in diameter including a flat circular plate, a 120^{o} cone, a 60^{o} cone, a 120^{o} spud-can and a 130^{o} spud-can (Figure 3.8). Each model footing is provided with a threaded hole in the centre of the upper face through which the loading arm (vertical loading tests), a bar (combined loading tests) or a leg (leg tests) can be screwed to it.

The 100 mm diameter model footings also have hemi-spherical depressions diametrically located at 37.5 mm distance from the centre, to position the two identical (but smaller in radius) spherical tips of the hanger used to apply vertical dead loads.

The leg models, shown in Figure 3.8, are basically duralumin rectangular bars 665 mm long and 20 mm wide with a threaded pin at one end and a spherical depression at the other. In order to prevent any rotation at its top during the horizontal loading, the leg was held between two stiff duralumin plates which the loading device moves by means of two parallel arms. Two legs were available for testing: 9.0 mm and 14.3 mm in thickness.

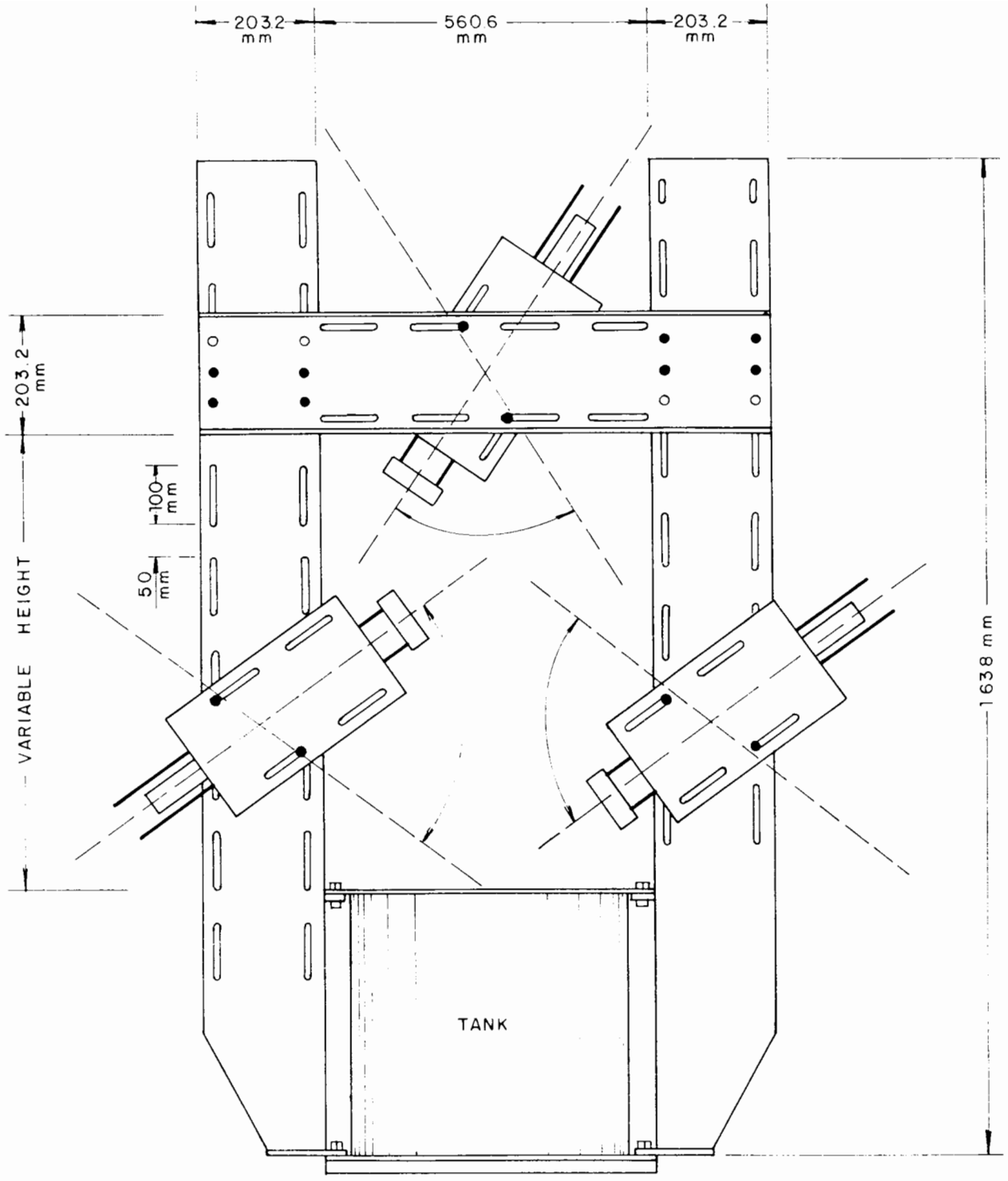

Figure 3.7 Reaction frame with the loading device attached at various possible positions

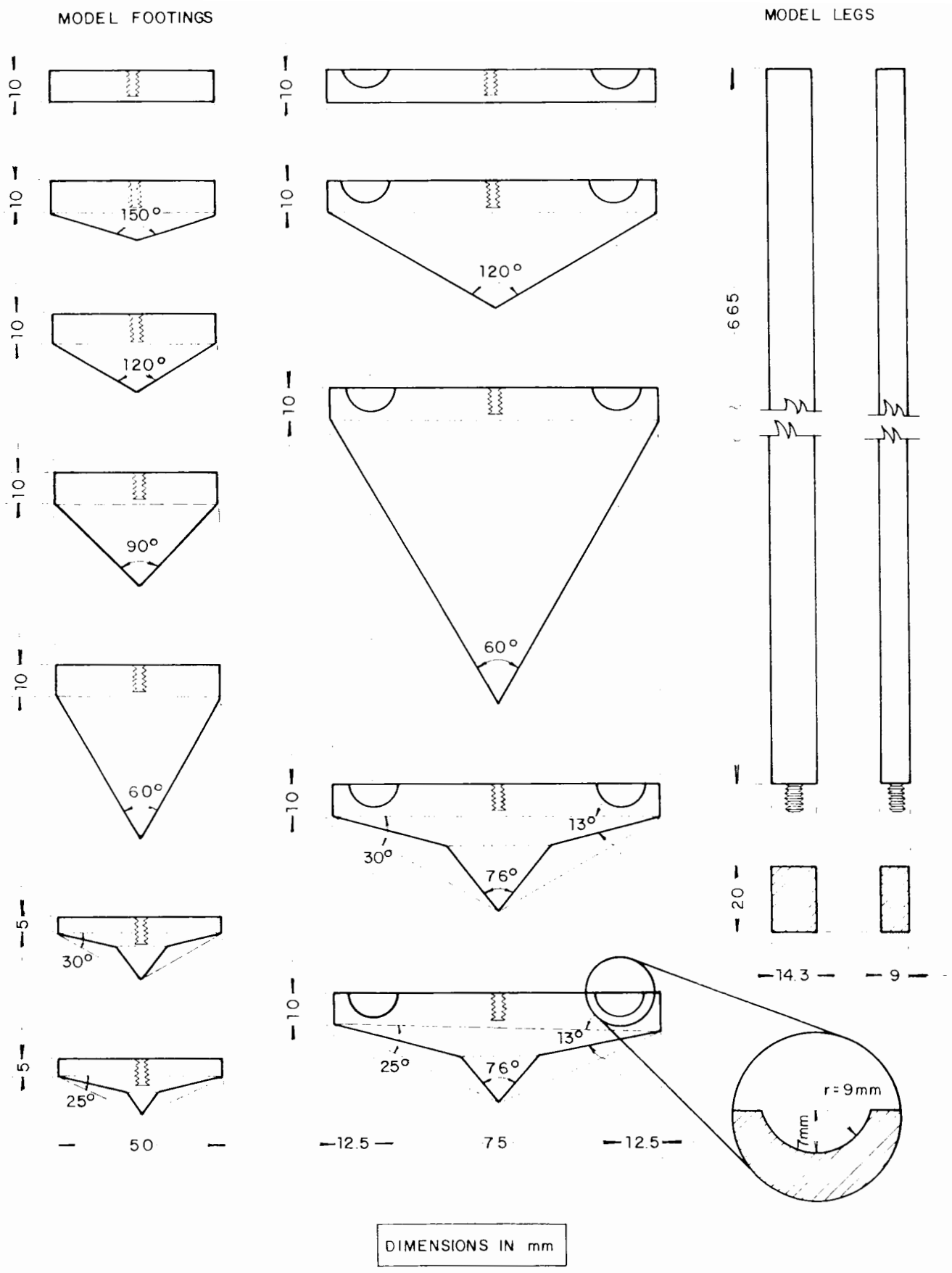

Figure 3.8 Model footings and model legs

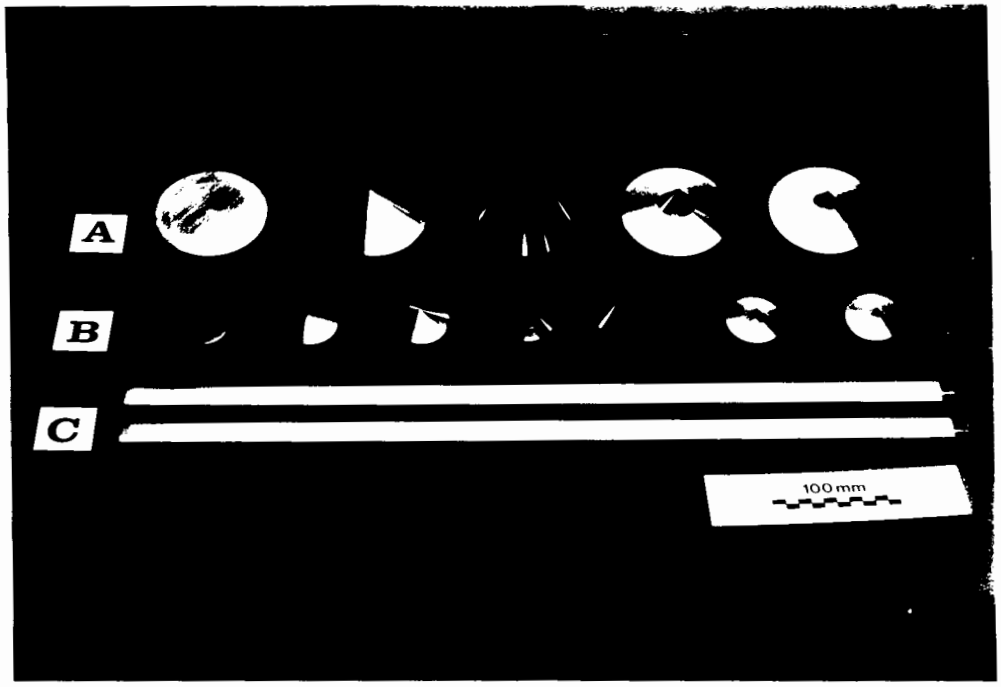

A = 100 mm diameter model footings
B = 50 mm diameter model footings
C = model legs

Figure 3.9 Photograph of the model footings and model legs

They were machined from a wider bar and special precautions were taken to guarantee their straightnesses. Figure 3.9 illustrates the model footings and the model legs.

3.6 Test Accessories

All the accessories used in this work are described in the following sections and displayed in Figure 3.10.

(a) LVDT Holders

The LVDTs were attached to the fixed parts of the test assembling by means of holders. There are two kinds of LVDT holder: one consisting of a duralumin bar provided with a slot at one end and a hole with a plastic

screw at the other, where the LVDT's body is attached, and another which is a duralumin plate provided with two slots and bolted at right angles to a small bar having also a hole with a plastic screw to fix the instrument. The first type was used to set up LVDTs in a vertical positions and was attached to the tank flange, and the second for the horizontal LVDT and was usually bolted to the columns of the reaction frame.

(b) Hanger

The hanger is used to apply vertical dead loads to model footings or legs. It is made of duralumin and the load can be transmitted either by two parallel rods symmetrically disposed, for combined loading tests, or by a shorter central rod, for leg tests. In both cases the rods have a ball bearing attached at the end.

(c) Hanger Winch

A small hand-operated winch is provided to allow the hanger to be lowered gently onto the model footing or model leg. It is bolted to the horizontal beam of the reaction frame and the hanger is suspended from it by a 1.5 mm diameter wire.

(d) Loading Arms

The loading arms are used to link the loading device and the model footing or model leg. The load cell forms part of the arm. There are two different types of loading arms:

* for vertical central loading tests, with both ends threaded for fixing to the loading device and to the model footing;

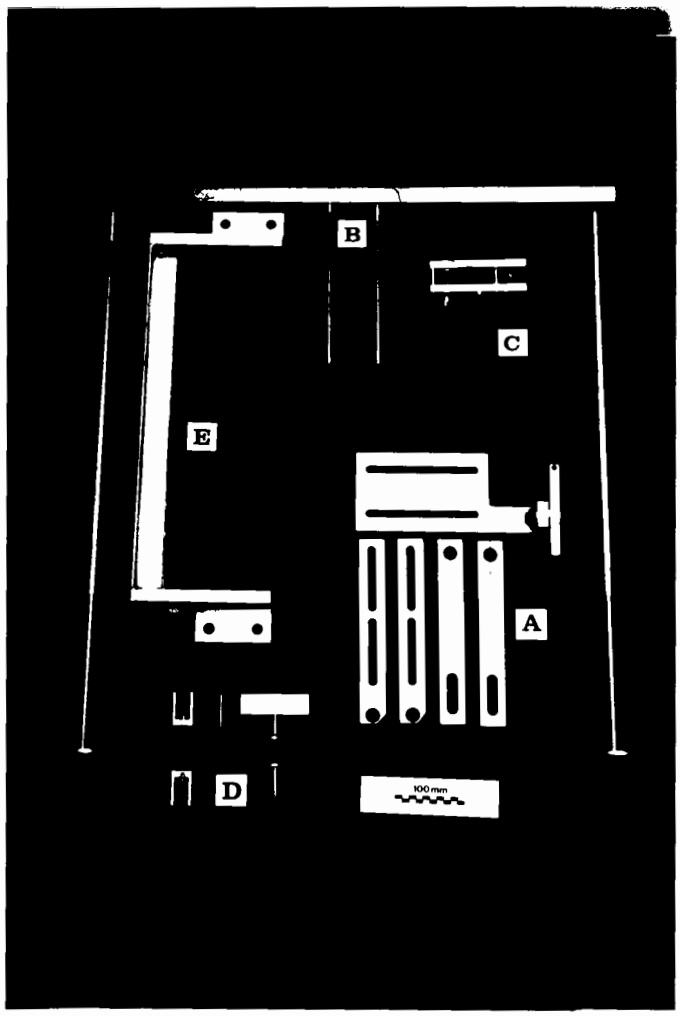

A = LVDT holders
B = hanger
C = hanger winch
D = loading arms
E = leg test guide

Figure 3.10 Test accessories

* for combined loading and leg tests, with forked ends to allow pinned joints with the loading device and with the rod of the model footing or the head plate of the model leg;

(e) Leg Test Guide

In order to avoid lateral instability during leg tests, a guide consisting of two duralumin 1.5" x 1.5" angles separated by a 48 mm gap and welded to supporting plates at their ends, was fixed to the reaction frame. Two smooth perspex strips were stuck to the inner faces of the guide so that the friction between it and the head plate was minimized.

3.7 Instrumentation and Data Logging

Linear Variable Differential Transformers (LVDTs) were used to measure all the relevant displacements during the tests as well as to monitor the consolidation process. Five LVDTs type D5/1000A (Figure 3.11), with captive spring return armature, and one D5/2000, with free unguided armature, were used to compute the model footing displacements. Three LVDTs type D5/100H, with free unguided armature, were used to measure the ground heave in the first test carried out while one LVDT type D5/10000C, with captive guided armature and monitored by a chart recorder, was used to register the clay sample height during the consolidation. The LVDTs have infinite resolution and the rated accuracies are 0.1 % of the full stroke for the D5/100H and lower than 0.3 % for the other types employed. The specifications of the LVDTs are shown in Table 3.1.

All the LVDTs used in this work are a.c. devices and therefore require some special electronics, consisting of signal conditioning modules (one for each LVDT), which are self contained, d.c. energised carrier amplifier with a transducer energisation output of 5 volts r.m.s. at 5 kHz.

Load cells of different ranges (TCLZ-10KA, TCLZ-20KA and TCLZ-100KA) were employed to measure the loads applied to the model footings (Figure 3.11).

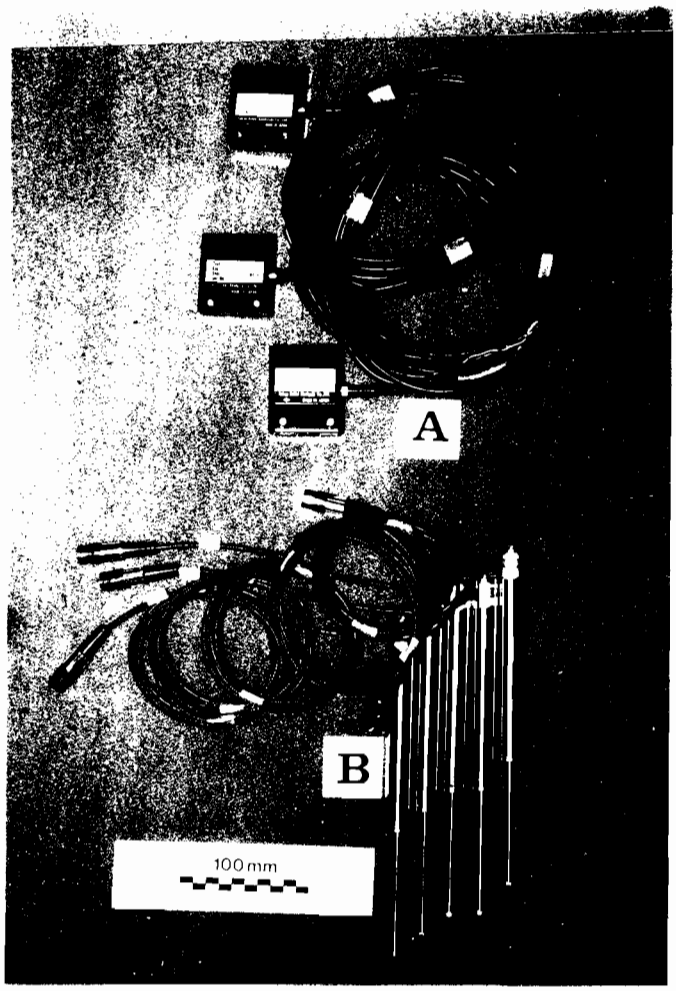

A = load cells
B = D5/1000A LVDTs

Figure 3.11 Load cells and some LVDTs employed

Two amplifiers were used in connection with these load cells to provide the necessary amplification of the output signals and also to deliver the transducer excitation voltage of 10 volts. The accuracy of these transducers is 0.3 % of the full range. Table 3.2 shows the load cells specifications.

All the transducers were calibrated before first use and their calibration constants checked regularly. It was observed that their values remained practically the same over the duration of the research.

The short stroke LVDTs were calibrated using a micrometer while a vernier caliper was employed in the calibration of the long stroke LVDT.

Because of the low capacity of load cells TCLZ-10KA and TCLZ-20KA, their calibration could be performed using a set of weights. Load cell TCLZ-100KA, however, had to be calibrated against a proving ring of 1 kN capacity.

The data logging system consists of an IBM XT equipped with a DASH-8 datalogger, which is an 8 channel 12 bit high speed A/D converter and counter/timer board. The full scale input of each channel is ± 5 volts with a resolution of 0.00244 volts. A machine language I/O driver (DASH8.BIN) software is provided for control of A/D, timer and digital I/O channel functions via BASIC CALLs. Using the facility of the CALL routine, seven programs were written in BASIC to monitor the tests, four for monotonic loading and three for cyclic loading, and also to store the channel voltages read in every scanning.

A second microcomputer, an Olivetti M19 also equipped with a DASH-8 datalogger, was used in the cyclic loading tests. In these tests the IBM XT was employed to generate a sinusoidal output voltage as a reference for the driving system. For this purpose a D/A converter, consisting of 2 separate double buffered 12 bit multiplying channels, was installed and a BASIC program written.

Table 3.1 LVDTs specifications

type	working range (mm)	linearity	typical sensitivity (mV/V/mm)
D5/100H	± 2.5	B.S.I. Grade A1	70.0
D5/1000A	± 25.0	B.S.I. Grade A	35.0
D5/2000	± 50.0	B.S.I. Grade A	35.0
D5/10000C	± 250.0	B.S.I. Grade A	7.0

Table 3.2 Load cells specifications

type	working range (N)	rated output (μV/V)	non-linearity (% of RO)	hysteresis (% of RO)
TCLZ-10KA	± 98	1499.9 (c) 1499.9 (t)	0.03	0.03
TCLZ-20KA	± 196	1501.2 (c) 1501.4 (t)	0.03	0.03
TCLZ-100KA	± 980	2000.9 (c) 2001.2 (t)	0.03	0.03

Notes

(1) RO = rated output
(2) c = compression
(3) t = tension

CHAPTER 4

SAMPLE PREPARATION AND CLAY PROPERTIES

4.1 Introduction

Modelling a soil is always the most difficult part in a programme of model tests in foundation engineering. In this work a clay soil model was produced to allow the testing of circular model footings under various loading configurations. For monotonic loading tests, when undrained conditions hold, the modelling is quite realistic, while for cyclic loading tests, performed over much longer intervals of time, the results must be understood with attention to the possibility of drainage.

As clay generally takes a long time to reach a steady state during consolidation or swelling processes, the testing programme had to be a compromise between a minimum time required for sample preparation and the necessary number of tests to be carried out to accomplish a parametric study in a limited period of time.

Monitoring of consolidation of the clay samples was carried out for all the fourteen series. A total of 698 vane tests, 2 consolidation tests and 9 triaxial tests provided data for analysis of the clay model.

The consolidation tests were to compare with the compressibility parameters found in the literature and for comparison with data obtained from preparation of the clay samples in the consolidometers.

Because the index properties of Speswhite kaolin clay are reasonably well-known, no index tests were performed in this research.

4.2 Preparation of the Clay Sample

4.2.1 Kaolin Clay

The choice of the Speswhite Kaolin for the clay samples was made mainly because of the following reasons:

(a) It is easily obtainable.

(b) It has been extensively used in research and therefore its geotechnical properties are well known.

(c) For a clay, it has a high permeability, allowing consolidation of large clay samples in a relatively short period of time. However, this is disadvantageous when undrained behaviour it sought and long intervals of loading are required.

4.2.2 Setting up the Consolidometers

For each consolidometer the first step was to attach loosely the base plate to the piston plate using the plugs designed for this purpose so that the plates could move relatively a few millimetres. The bottom cylinder was then bolted to the base plate with the piston inserted in it and with greased rubber gasket between its flange and the base. At this stage the plugs were fastened and the top cylinder bolted to the bottom one with another greased rubber gasket placed between them.

Silicon grease was spread all over the inner surface of the tanks' walls (approximately 0.10 l of grease per consolidometer) to minimize friction between them and the clay during consolidation. In each consolidometer a plastic hose was attached to the tap in the base plate and fixed to the top cylinder so that the water coming from the bottom drainage could be collected and transferred to the free surface of water.

After being assembled, the consolidation tanks were carefully centred with respect to the apparatus rams and filled up with water to check for leaks.

Because double drainage was allowed during consolidation, two porous discs were used at the top and bottom of the consolidometers. They were made up by cutting discs 449 mm in diameter from a sheet of 4.75 mm thick porous plastic (Vyon "F"). They were chamfered to reduce friction when placed at the top and always positioned with the smooth face in contact with the slurry. To guarantee complete saturation, they were soaked in clean water for at least 24 hours before they were used.

4.2.3 Mixing the Slurry

The clay samples were prepared by consolidating from a kaolin slurry obtained through continuous mixing of water and kaolin powder in a mechanical mixer powered by a 2 H.P. geared motor. The mixer operates under vacuum and is equipped with a slurry pump and a vacuum gauge. Gue (1984) describes the mixer in more detail.

The output valve of the mixer, placed between it and the slurry pump, was initially closed and a volume of about 67 l of water was poured into the trough. A weight of kaolin powder was then added to the water to produce about 88 l of slurry at 120 % water content (about twice the liquid limit).

At this stage special attention had to be paid to ensure that there was no free powder on the surface of the water or dry kaolin cakes stuck to the trough wall. The lid was closed, a vacuum of about 90 kPa (about 30 ft H_2O) applied by means of a vacuum pump and the mixing started. Although the lid was firmly fastened using "G" clamps, some problems were experienced with sealing. A minimum vacuum of 80 kPa (about 27 ft H_2O) was maintained. The mixing was carried out for 2 hours and in the last 15 minutes the vacuum was slowly released. At the end of the mixing the motor was switched off, the lid was opened and water content specimens were collected for control purposes. The slurry was then pumped into the tanks in each consolidation apparatus until a pre-set height was met. This height was derived from the compressibility characteristics of the clay so that the upper face of the sample was about 15 mm below the top of the bottom tank at the end of the consolidation process.

4.2.4 Consolidation and Swelling

Having filled the three consolidometers, the porous discs were placed in their respective positions, the loading platens lowered and a small pressure applied to check any leak of slurry past the sealing tubing existing around them. The slurry under pressure squeezes up if the platen is not accurately centred with respect to the cylinder.

With the long stroke LVDT installed in tank 1 and connected to a chart recorder through a signal conditioning module, and the bottom drainage tap open, the clay was then consolidated up to the maximum pressure of 200 kPa in four stages of loading (25 kPa, 50 kPa, 100 kPa and 200 kPa). The excess pore pressure was not allowed to dissipate entirely during the two initial stages, the next stage being applied when displacement rate dropped to about 1 mm/hour. The last two stages were allowed to reach the end of primary

consolidation, which was found to correspond approximately to the rate of settlement of 0.1 mm/day.

It usually took three to three and a half weeks to consolidate a batch of clay samples. After the end of consolidation, the pressure on the samples was released in three stages of unloading (100 kPa, 50 kPa and 0 kPa) with the bottom drainage closed to prevent air entering the clay sample. Unloading stages larger than 100 kPa must be avoided because it induces cavitation, affecting the clay strength, as reported by Mair (1979). The two first stages lasted one day each, approximately, and the last one the minimum period of one and a half days before starting testing. This timing was initially thought to be enough to allow full dissipation of the suction inside the clay sample. Gue (1984), using the same clay, the same consolidometers and the same procedures observed by means of pore pressure transducers installed near the bottom of the tank that the suction developed when the clay sample was unloaded from 200 kPa to 100 kPa dissipated in about 3 hours, and on unloading from 100 kPa to 33.3 kPa dissipation occurred within a period of 17 hours.

4.3 Miniature Site Investigation

A miniature site investigation was carried out on the clay sample after the end of every test performed. It consisted of eight laboratory shear vane tests and water content measurements. The vane tests were performed using a miniature Pilcon vane with 33 mm by 50 mm vane in four different locations on the surface, 70 mm from the tank's wall and on two perpendicular lines passing through the centre of the sample (Figure 4.1). The strength was measured at two depths, 60 mm and 140 mm, measured from the surface of the clay to the mid height of the blades.

The vane was slowly and carefully inserted into the sample up to the first level and then a torque was applied by manually rotating the handle at a rate of approximately one revolution per minute, as recommended by the manufacturer. When the four tests at the level of 60 mm had been completed, four 80 mm deep holes were augered at these locations so that the second level vane tests could be carried out with the same shaft embedment as in the first level. The tests at the depth of 140 mm were performed following the same procedures as before.

Water content specimens were collected from a vertical diametrical section of the sample, 70 mm from each side and at depths of 60 mm and 140 mm, approximately, and determined in accordance with B.S. 1377. In order to cut the sample and obtain the specimens (Figure 4.1), the clay block had to be removed from the cylinder either by being pushed up (first half) or disassembling the tank set-up (second half). In both cases the operation took a few hours, and these samples were usually not taken until 3 to 12 hours after the end of testing.

4.4 Standard Laboratory Tests

Batch 14 was used for standard laboratory tests. Initially a volume of slurry was collected from the mixer, at the time of the mixing, for two oedometer tests. After consolidation and swelling, five half samples were used for strength and water content measurements in accordance with the plan represented in Figure 4.2.

(a) Oedometer Tests

Oedometer tests were done using a standard consolidation cell with a fixed ring, as specified in B.S. 1377, extended by a cylinder of perspex with the

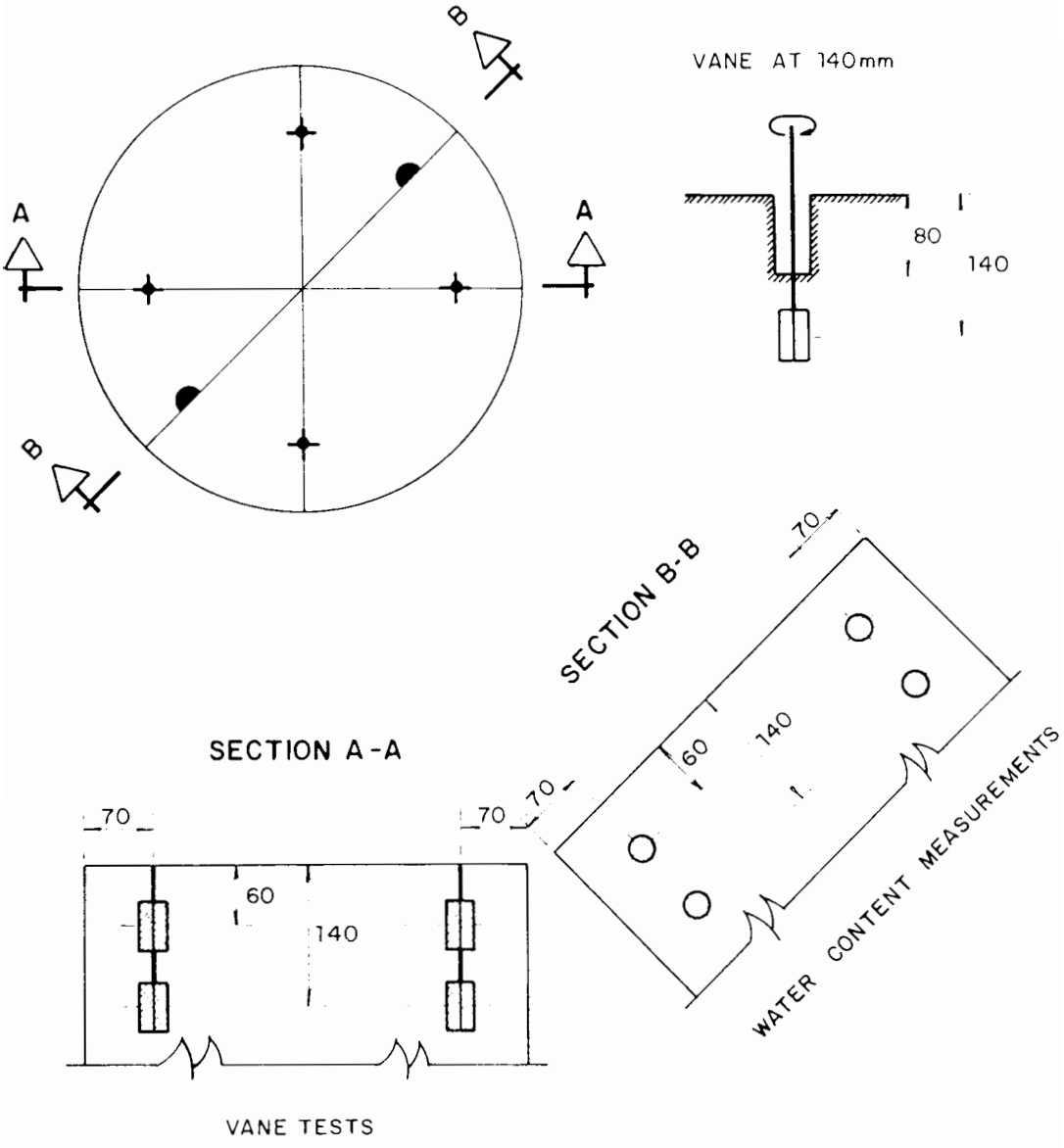

Figure 4.1 Miniature site investigation lay-out

same inner diameter as the cell and 90 mm high. Silicone grease was spread over the inner surface of the cell to minimize friction. Porous discs were placed at the bottom and at the top of the consolidometer so that double drainage could be allowed. To avoid the slurry squeezing up when loaded, a perspex disc with a number of tiny holes (to allow drainage) and an "O" ring laterally fitted was placed between the porous disc and the loading plate. The cell was set up in a consolidation press and an LVDT type D5/1000A installed to measure the vertical displacement.

The initial height of the sample was carefully measured before the beginning of each test and later checked through back calculation using the values of initial and final voids ratios and the total settlement. The loads were applied in four stages of loading (12 kPa, 36 kPa, 90 kPa and 190 kPa) and removed in three stages of unloading (113 kPa, 60 kPa and 12 kPa).

Before each test the compressibility of the assembling was determined and the friction between cell wall and perspex disc measured. A quite good repeatability was observed. The pressures were corrected for the friction.

The final water content specimen was weighed no longer than two minutes after the end of the test.

(b) Vane Tests and Water Content Measurements

The aim of these tests was to supplement the strength and water content data obtained during the model testing. Vane shear tests were carried out along a diameter to define a horizontal profile of strength, and also at depths of 100 mm and 180 mm in addition to the standard 60 mm and 140 mm. Water content specimens were also taken at these depths (Figure 4.2).

Vane tests were performed following the same procedure as in Section 4.3 and water content specimens were taken about 2 hours after the vanes and weighed within the period of 1 to 2 minutes after collection. Remoulded shear strength was obtained by shearing the sample at normal rate after it had been sheared for three revolutions at a much faster rate.

(c) Triaxial Tests

A group of undrained triaxial tests with measurement of pore pressure were carried out as part of the investigation programme on batch 14.

The samples were taken from tank 2, first half, and tank 3, first half, as shown in Figure 4.2, using cylindrical brass samplers 38 mm in diameter and 1 mm wall thickness, slightly oiled to reduce friction and minimize disturbance. With the clay surface covered with a layer of water, the samplers were carefully driven into the clay until the top reached the water level. At this point the water enclosed by the sampler wall was replaced by a layer of silicon grease overlain with a coating of wax. After the vane tests and collection of water content specimens, the block of clay was taken apart so that the samplers could be freed without any disturbance. The other extremity of each sampler was covered with layers of grease and wax and finally they were individually wrapped in cling film. The tests were carried out in an ELE Tritest 50 triaxial apparatus equipped with a proving ring to measure axial loads, an LVDT to measure vertical displacements and a pore pressure transducer. Specimens 38 mm in diameter were prepared with a height of 76 mm, accurately measured and weighed, placed on the pedestal and then, very carefully, fitted with a rubber membrane. Precautions were taken at this stage to ensure that the base porous stone and the paper filter to be placed between it and the specimen were fully saturated with de-aired water and no air bubbles were entrapped either inside the specimen or in the

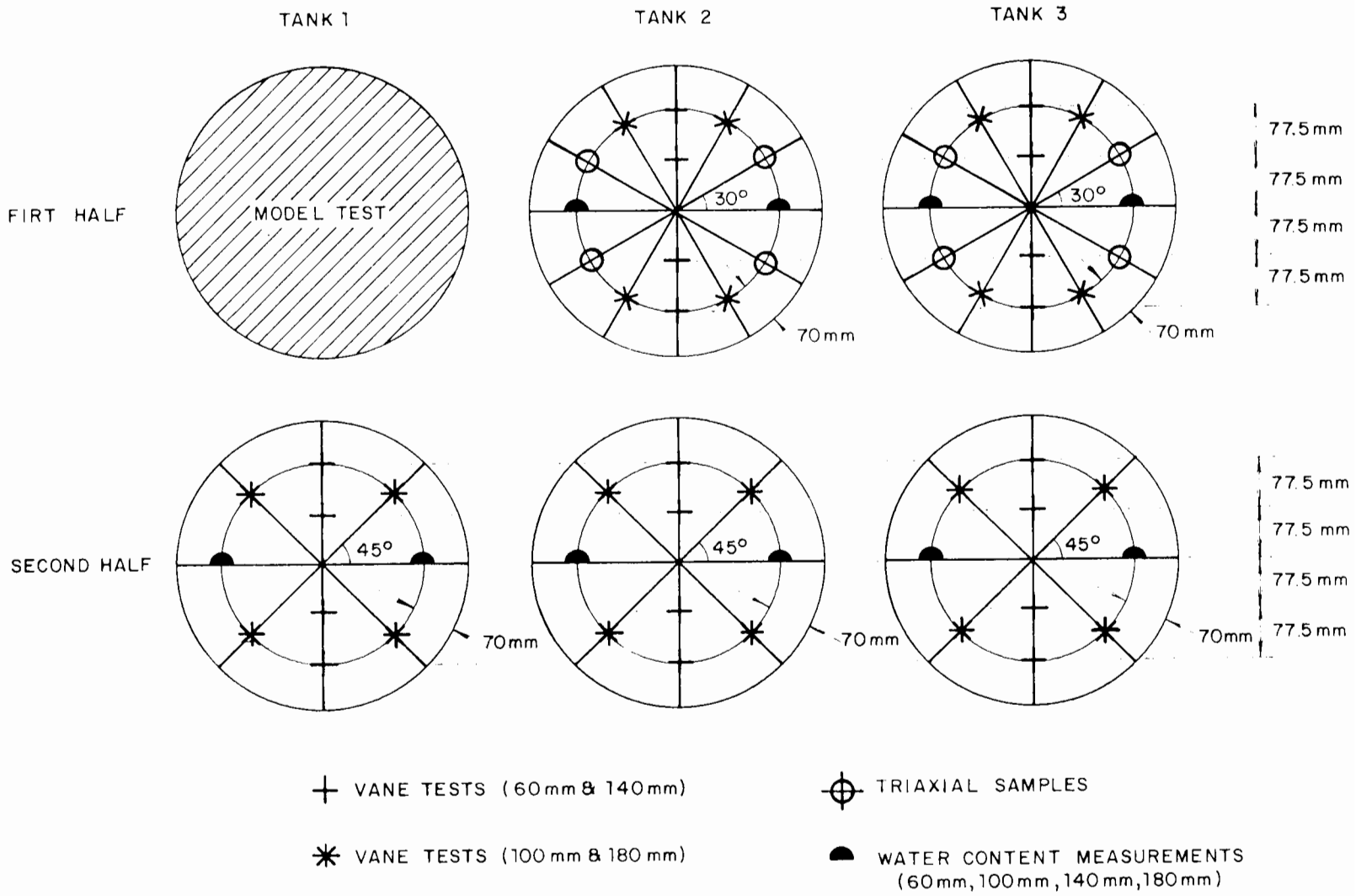

Figure 4.2 Batch 14 – plan view of the measurement locations

system that measures the pore water pressure at its bottom.

A cell pressure of 400 kPa was applied in four stages (100 kPa, 200 kPa, 300 kPa and 400 kPa), each stage being held for about 1 hour and the pore pressure read at intervals. The ratio between the increments of pore pressure and cell pressure (Skempton's parameter B) was always higher than 0.90 in the second stage and higher than 0.95 in the third and fourth stages.

The tests were undrained and were run at a constant vertical displacement rate of 0.08 mm/minute. This value was derived using the method introduced by Bishop and Henkel (1962) assuming 95 % of equalization of pore pressure throughout the specimen and the coefficient of consolidation c_v of 14 m^2/year.

4.5 Compressibility of the Kaolin Clay

Results of oedometer tests 1 and 2 are plotted in Figure 4.3 as voids ratio versus vertical pressure in logarithmic scale. In the same figure are shown points obtained from consolidation of batches 5, 7, 9, 13, and 14 (two final stages), Gue's results (1984) and Fannin's results (1986). Despite the scatter, the agreement is good.

Considering only the points corresponding to oedometer tests, the best fit for the slope of the compression line λ is 0.22 and for the swelling line κ is 0.03. The plastic volumetric strain ratio Λ calculated is 0.85. Assuming K_o = 0.64 (Fannin, 1986), the value of $(e_\lambda)_{1-D}$ is 2.34, which is slightly lower than the values obtained from the literature review (Table 2.2).

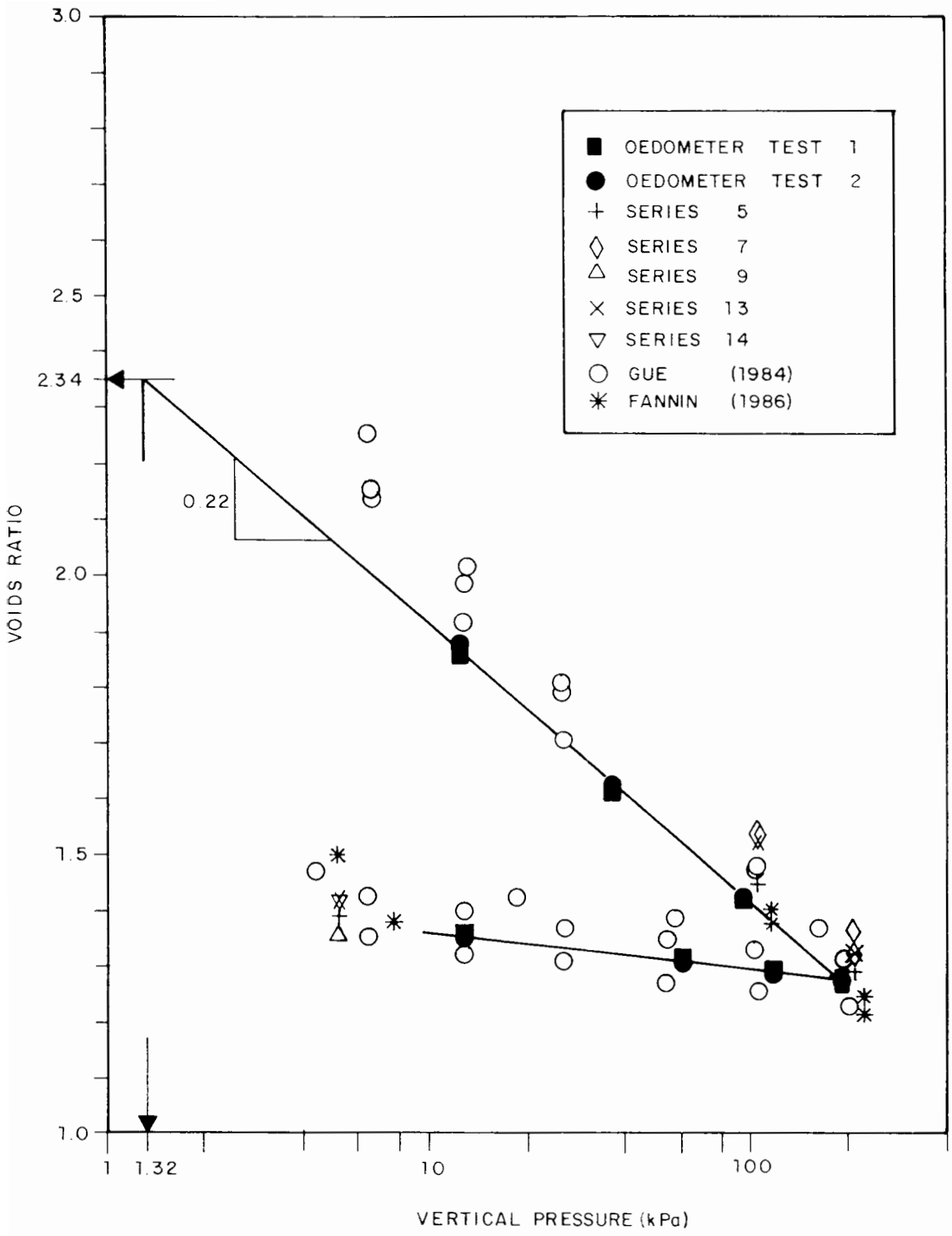

Figure 4.3 Variation of voids ratio with consolidation pressure

It can be noticed, however, that the compression line is not absolutely straight, as previously reported by Butterfield (1979) and Martins (1983). If two straight lines are fitted through the points obtained, the slopes are 0.23, for vertical pressures up to 50 kPa, and 0.21, for higher pressures, being in good agreement with the literature reviewed.

Figure 4.4 shows the variation of the coefficient of consolidation c_v calculated for each increment of pressure, with vertical pressure in a logarithmic scale. The figure includes results of oedometer tests 1 and 2, the last two stages of consolidation of batches 5, 7, 9, 13 and 14 as well as points obtained by Gue (1984), Love (1984) and Fannin (1986).

A good agreement between the existing and new data is observed with a little scatter. Results from oedometer tests seem to confirm an approximately linear relationship between c_v and the logarithm of the vertical pressure.

Using the c_v values obtained in each stage of loading for oedometer tests and from the last two stages for consolidation of batches 5, 7, 9, 13 and 14, the coefficient of permeability could be derived for each increment of pressure, as presented in Figure 4.5. For the increment from about 100 kPa to about 200 kPa , the coefficient of permeability is of the order of 3.0×10^{-9} m/s.

4.6 Strength of the Clay Sample

4.6.1 Vane Tests

A total of 84 model tests were performed on 76 half clay samples in fourteen batches. In each half sample eight vane shear tests were carried out at two

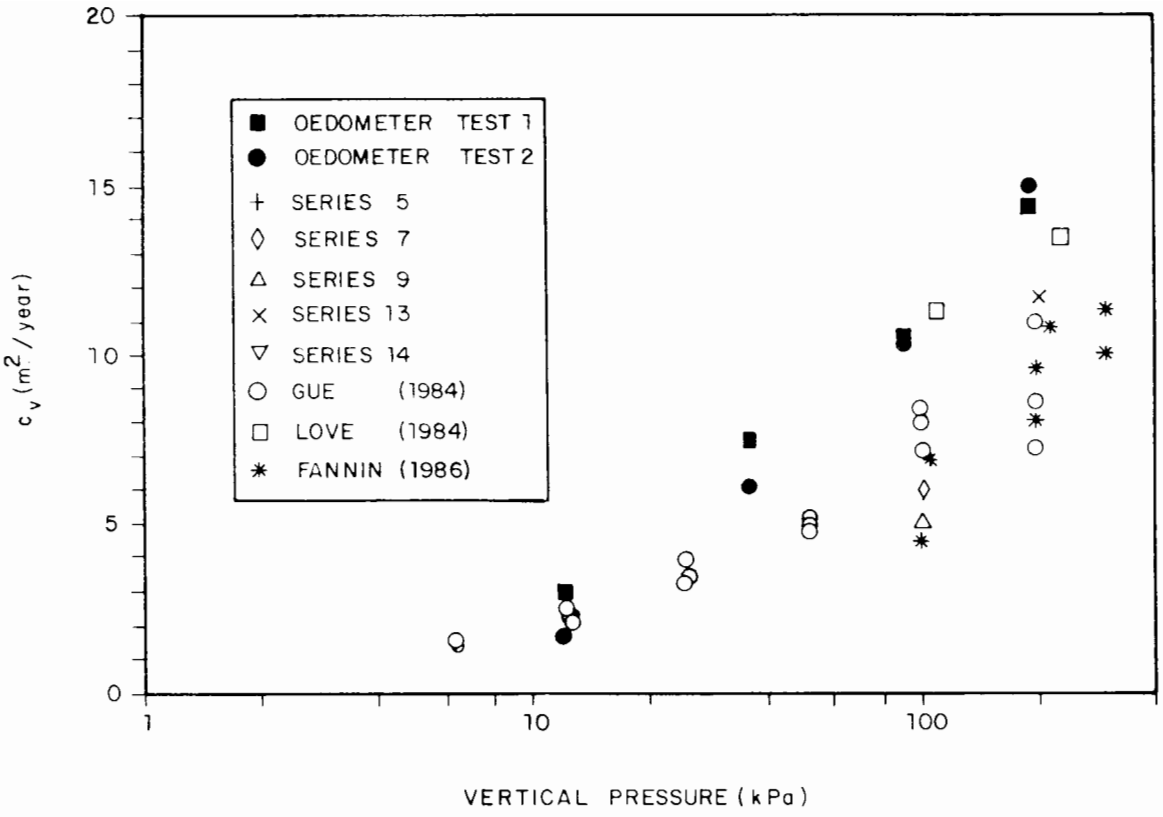

Figure 4.4 Variation of coefficient of consolidation with consolidation pressure

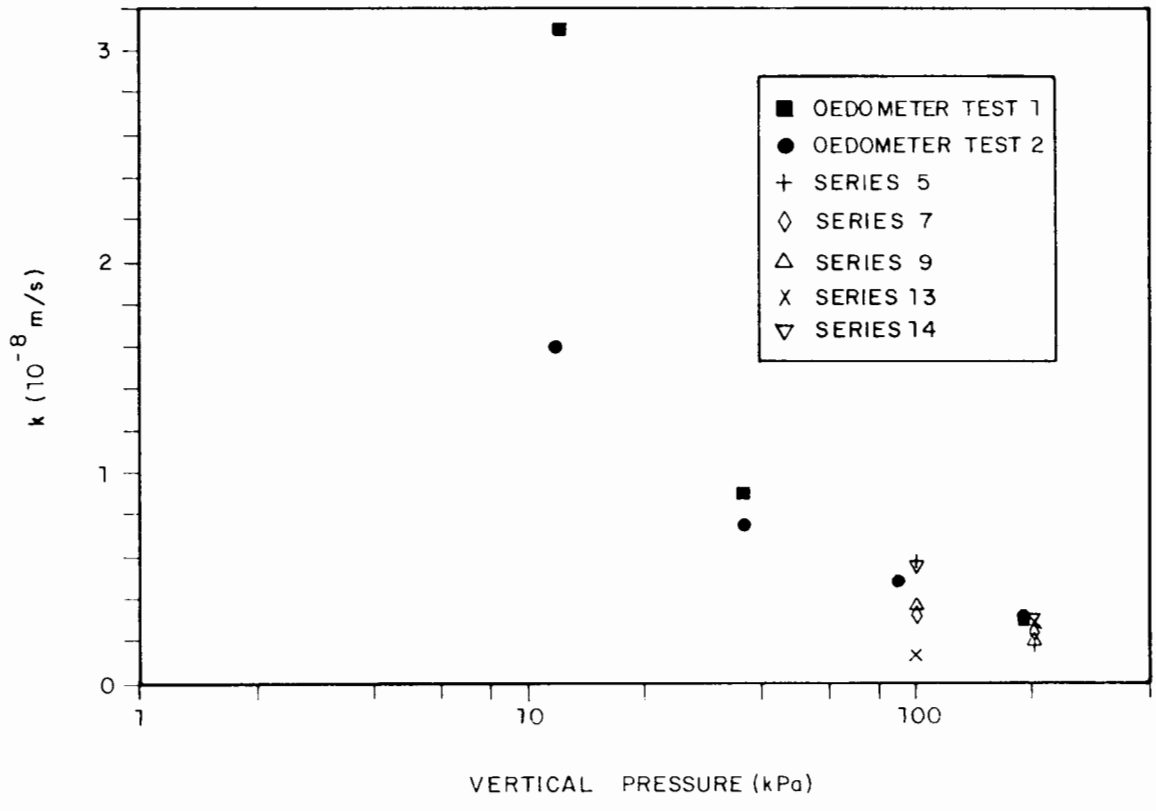

Figure 4.5 Variation of coefficient of permeability with consolidation pressure

depths: four at 60 mm and four at 140 mm. The average value of the undrained shear strength s_u for each level is plotted in Figure 4.6 against the time elapsed from the beginning of the last stage of swelling (σ_v = 0 kPa) up to the moment of the test. Different symbols are used for first and second halves of the clay sample.

The scatter observed can be explained by the fact that the friction between the top platen and the surface of the cylinder may vary between consolidometers and even between batches in the same consolidometer, the internal friction of each ram is also a contributory factor. Although the former may not be significant in affecting consolidation, it certainly has some restraining influence on the swelling of the clay. The reduction of s_u with time is due to a continued gradual swelling process.

Another feature observed is the increasing strength with depth for both halves. Figure 4.7 shows a frequency analysis of the ratio between the average values of s_u at 140 mm and at 60 mm , represented by r_s, and Table 4.1 presents the values of some statistical parameters from the analysis. It is noticeable that the ratio of strengths is smaller for second-half blocks than for first-half ones.

In batch 14 five half samples were allocated to miniature site investigation and to collect samples for triaxial tests (see Figure 4.2). The results are presented in Tables 4.2 (a), 4.2 (b) and 4.2 (c). The sixth sample, the first half of tank 1, was used for a repeated model test.

The diagram of Figure 4.8 shows, for each tank, the time elapsed since the piston pressure was released to 0 kPa until the moment the investigation was initiated.

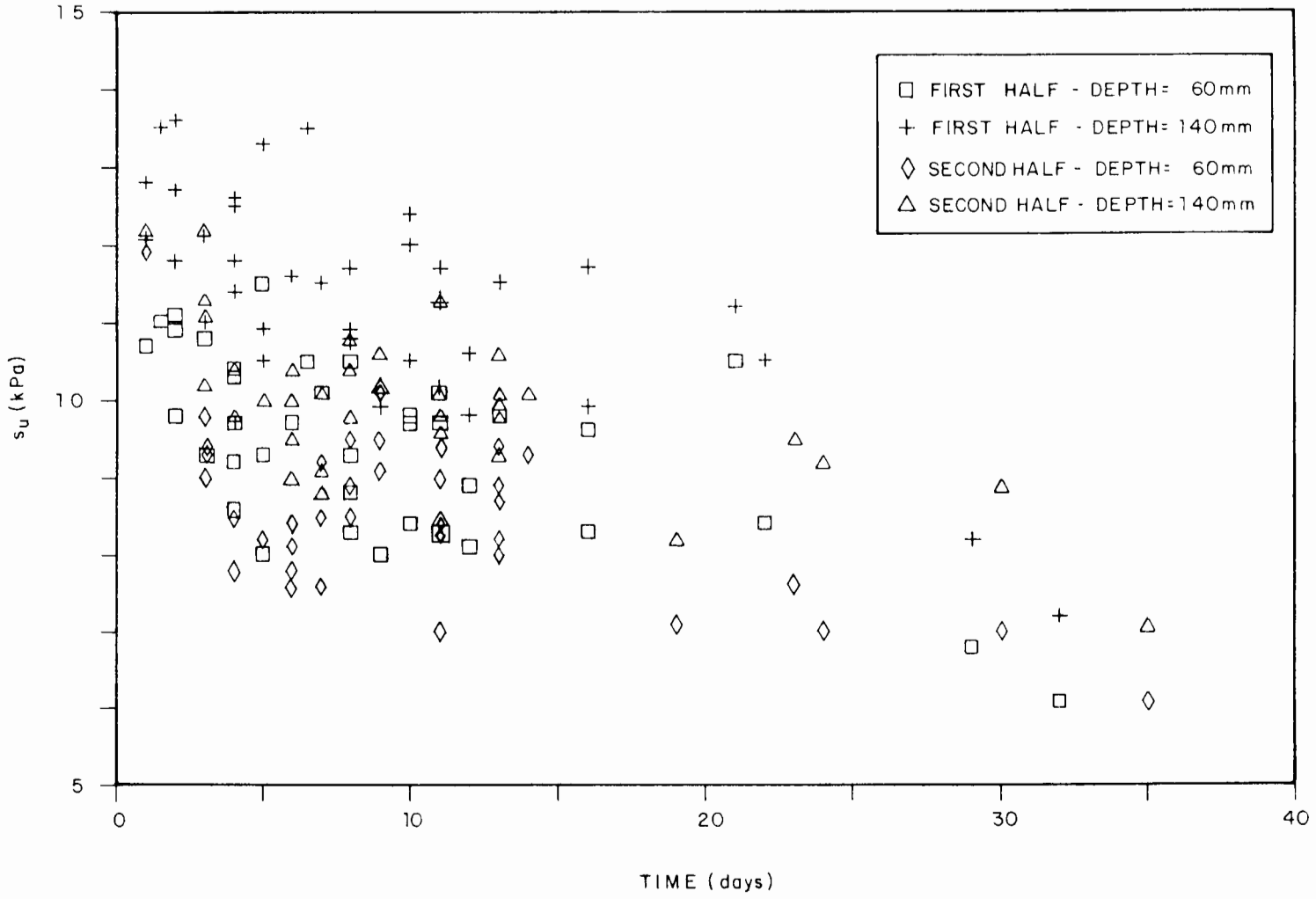

Figure 4.6 Data of average value of undrained shear strength of samples for each depth at various intervals of time from the beginning of the last stage of swelling

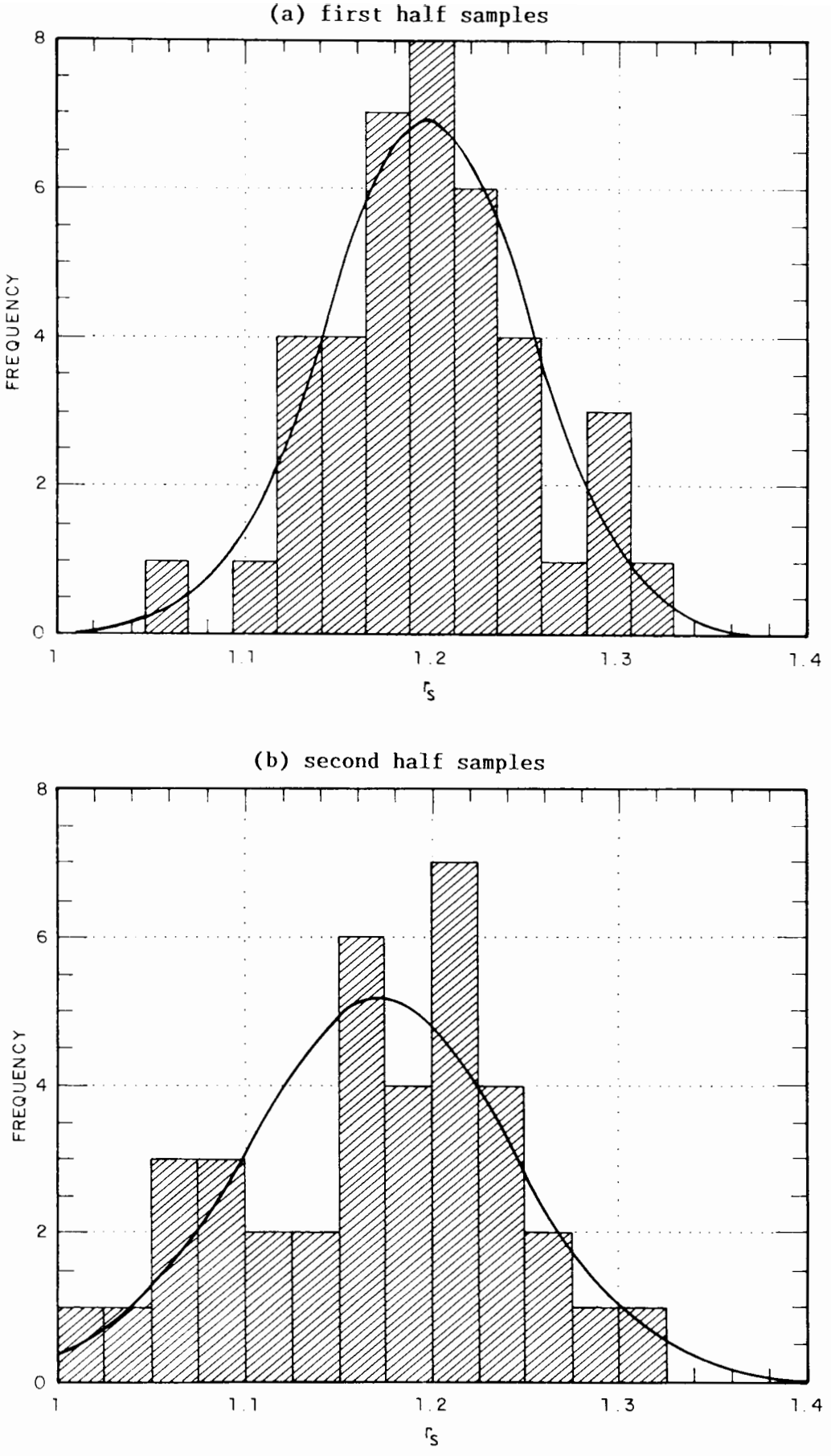

Figure 4.7 Frequency distribution of the ratio between the average values of undrained shear strength of samples at 140 mm and 60 mm

Table 4.1 Statistical parameters from the analysis of r_s

set of samples	r_s			
	minimum	maximum	mean	standard deviation
first halves	1.067	1.313	1.198	0.054
second halves	1.017	1.314	1.171	0.072

The vertical profiles of strength are shown in Figure 4.9, where the mean values are indicated for each level. Tank 3, having been tested after tank 2, reveals a weaker profile both for first and second halves. Tank 1, however, is the strongest second half sample in spite of being the last one to be investigated. Bearing in mind that this sample was tested immediately after the upper block had been removed, this apparent inconsistency may suggest that the friction between the upper block of clay and the cylinder is enough to restrain partially the swelling of the lower block, acting as a "plug" that, once removed, frees the clay to resume swelling.

The water content (w) profiles, illustrated in Figure 4.10, are consistent with the strength profiles, showing a pattern of higher water content at lower strength.

Looking at the horizontal strength profiles in Figure 4.11 from results of vane tests carried out along a diameter of the clay sample, it is evident for first half samples that r_s is smaller at the centre than at 70 mm from the wall.

The second half profiles show clearly for tanks 2 and 3 that at the depth of

Table 4.2 (a) Batch 14 - values of the undrained shear strength s_u (kPa)

sample	test	depth (mm)				d (mm)
		60	100	140	180	
tank 2 1st half	vane	12.2 12.4 11.9 11.7 11.7		14.5 12.4 12.4 12.8 13.2		70.0 147.5 225.0 147.5 70.0
			11.9 12.3 12.6 12.5		14.9 13.7 13.7 14.2	70.0 70.0 70.0 70.0
	triaxial					
	T3B-1			25.7		70.0
	T4A-1	19.0				70.0
	T4B-1			22.3		70.0
tank 3 1st half	vane	11.6 10.9 11.5 11.1 11.7		12.2 11.2 11.4 11.5 12.3		70.0 147.5 225.0 147.5 70.0
			12.3 12.3 12.1 12.0		11.9 12.8 12.2 12.0	70.0 70.0 70.0 70.0
	triaxial					
	T2A-2	10.4				70.0
	T2B-2			13.5		70.0
	T3A-2	17.3				70.0
	T3B-2			18.5		70.0
	T4A-2	16.3				70.0
	T4B-2			19.9		70.0

Note

(1) d = distance from tank wall

Table 4.2 (b) Batch 14 - values of the undrained shear strength s_u (kPa)

sample	test	depth (mm)				d (mm)
		60	100	140	180	
tank 2 2nd half	vane	9.5		9.9		70.0
		8.6		10.3		147.5
		9.0		10.8		225.0
		8.7		10.5		147.5
		9.3		10.0		70.0
			9.5		10.9	70.0
			9.6		10.6	70.0
			9.2		11.1	70.0
			9.3		10.9	70.0
tank 3 2nd half	vane	8.4		8.7		70.0
		7.6		9.3		147.5
		7.3		10.2		225.0
		7.8		9.6		147.5
		7.9		8.6		70.0
			8.4		10.3	70.0
			8.8		9.3	70.0
			8.5		9.9	70.0
			8.3		9.6	70.0
tank 1 2nd half	vane	9.5		11.8		70.0
		10.6		12.4		147.5
		10.5		12.3		225.0
		10.2		11.9		147.5
		9.6		10.3		70.0
			10.8		10.9	70.0
			10.7		10.2	70.0
			10.9		11.3	70.0
			10.3		10.8	70.0

Note

(1) d = distance from tank wall

60 mm s_u is smaller at the centre than near the edges, the ratio between these values being approximately 0.96 for tank 2 and 0.90 for tank 3. At the depth of 140 mm, however, an entirely different pattern can be observed, with s_u larger at the centre, leading to ratios of 1.09 and 1.18 for tanks 2 and 3 respectively. For both tanks the curves are similar and if the one corresponding to tank 3 is shifted about 1 kPa upwards they become

Table 4.2 (c) Batch 14 - values of the water content w (%)

sample	depth (mm)				d (mm)
	60	100	140	180	
tank 2 1st half	52.6 52.6	52.5 52.3	52.2 52.9	52.0 52.9	70.0 70.0
tank 2 2nd half	54.9 54.7	54.4 54.2	54.2 54.5	53.9 54.2	70.0 70.0
tank 3 1st half	54.5 53.6	53.9 53.7	54.2 54.0	53.6 53.4	70.0 70.0
tank 3 2nd half	* 55.8	55.8 55.5	55.4 55.2	54.8 54.5	70.0 70.0
tank 1 2nd half	54.5 54.5	53.8 53.9	54.4 54.0	54.1 54.5	70.0 70.0

Notes

(1) d = distance from tank wall
(2) * = specimen contaminated

practically coincident. Tank 1, however, exhibits a rather different pattern: the clay is stronger at the centre than near the edges at both depths. It is also stronger than any other second half sample.

The small inhomogeneity in strength observed along a diameter in the three second half clay blocks suggests that the lower part of the samples is affected by lateral friction on the upper part, despite the layer of grease between clay and inner face of the tanks. The friction would reduce the vertical effective pressure in zones near the tank wall, producing then a sample stiffer in the centre and becoming slightly weaker at larger radii. After the first half is trimmed off, the clay restarts swelling freely in the centre and with some frictional restraint near the edges. From observation of Figures 4.8 and 4.11 (b), it can be concluded that a few hours of free swelling were not long enough to reverse the initial

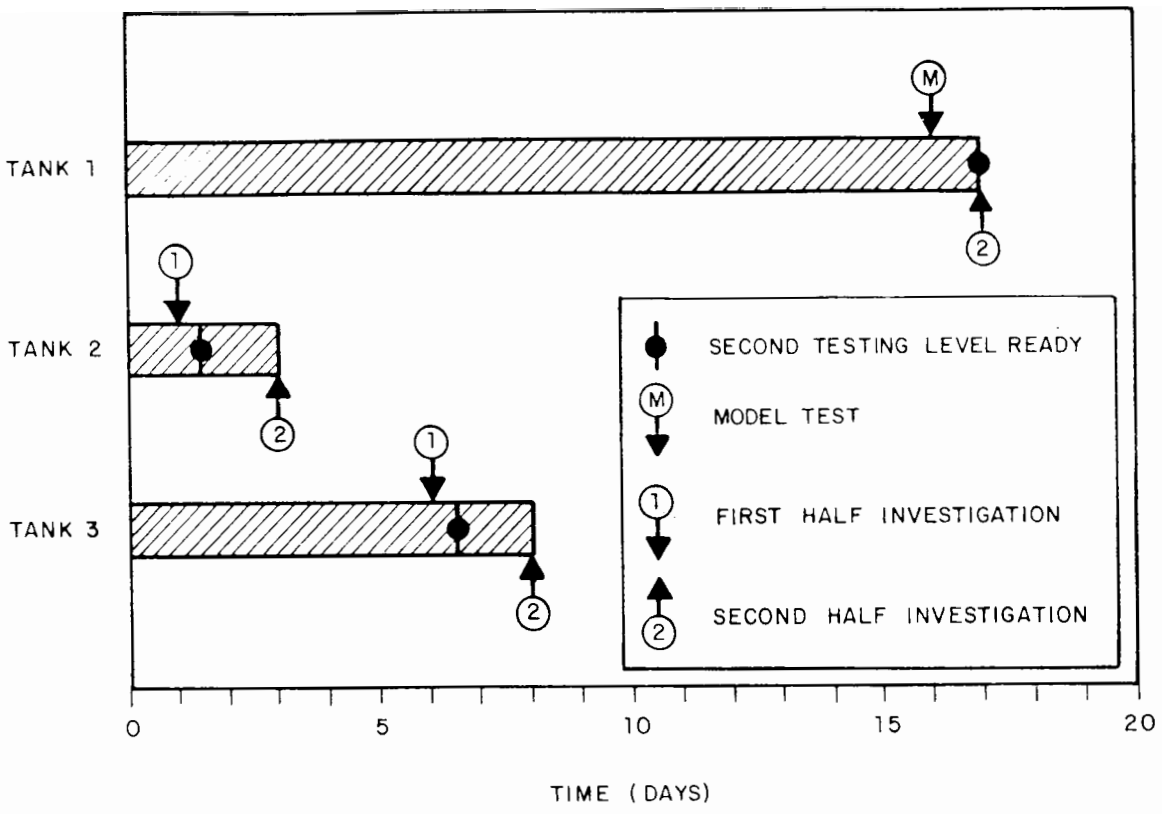

Figure 4.8 Batch 14 - diagram showing the time elapsed since the beginning of the last stage of swelling until the moment of the miniature site investigation

configuration (centre stiffer) at both depths, and approximately 1.5 days could only reverse the situation at a depth of 60 mm.

The range of variation of the ratio between peak and remoulded strength obtained from results of vane tests in five half samples of batch 14 is represented in Figure 4.12. It clearly decreases with depth and, consequently, increases with the OCR.

4.6.2 Triaxial Tests

Preparing and setting up samples of soft clay in a triaxial apparatus is always a difficult task. Any minor disturbance that might occur during the preparation of the sample can damage soft clay samples. In this work, any

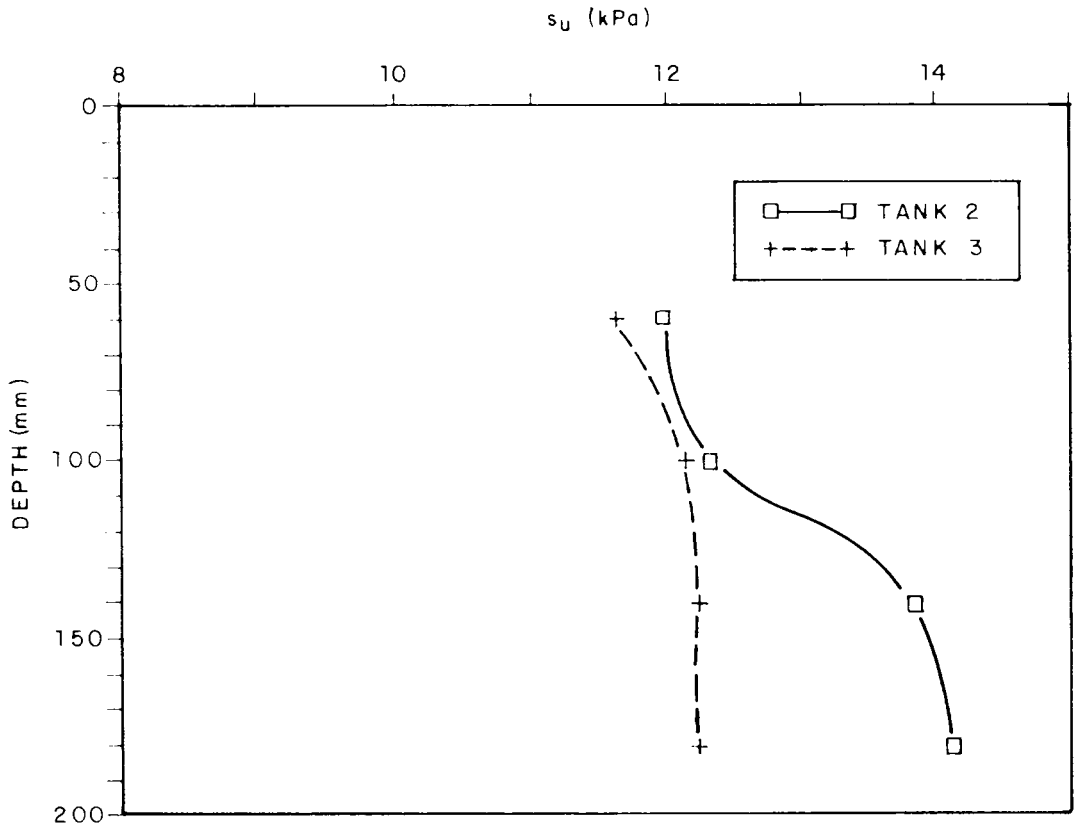

(a) first half samples

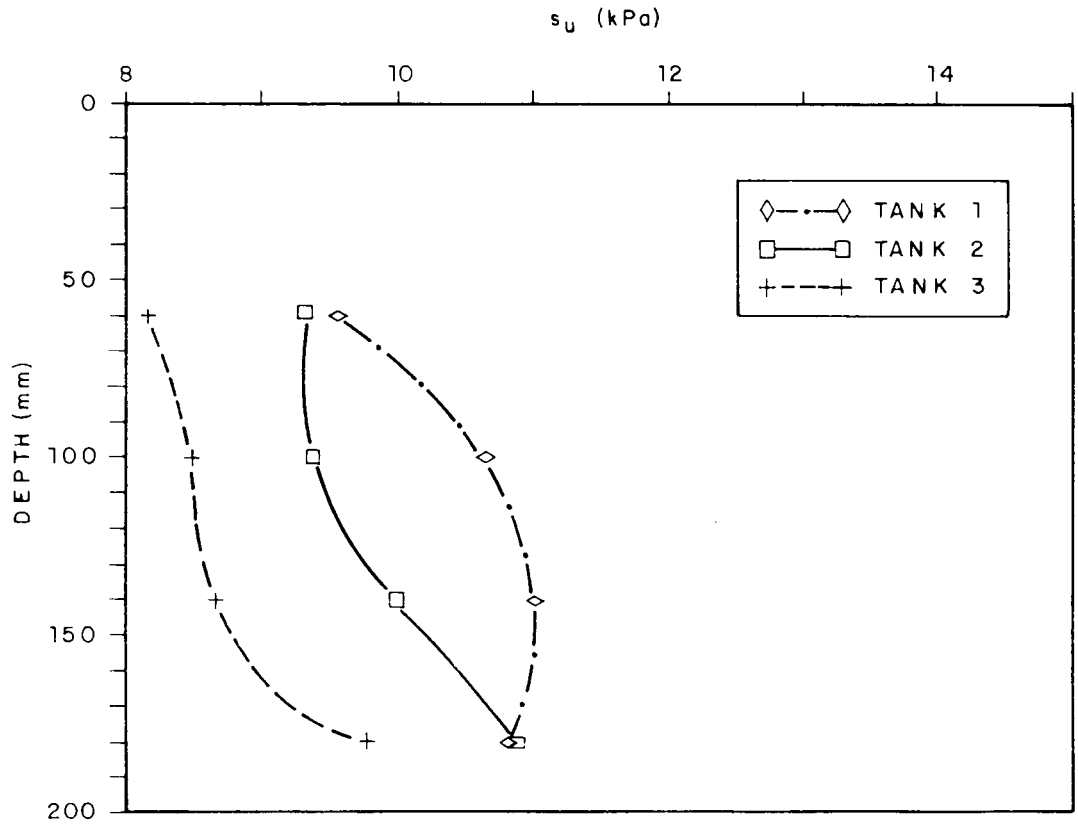

(b) second half samples

Figure 4.9 Batch 14 - vertical profile of undrained shear strength

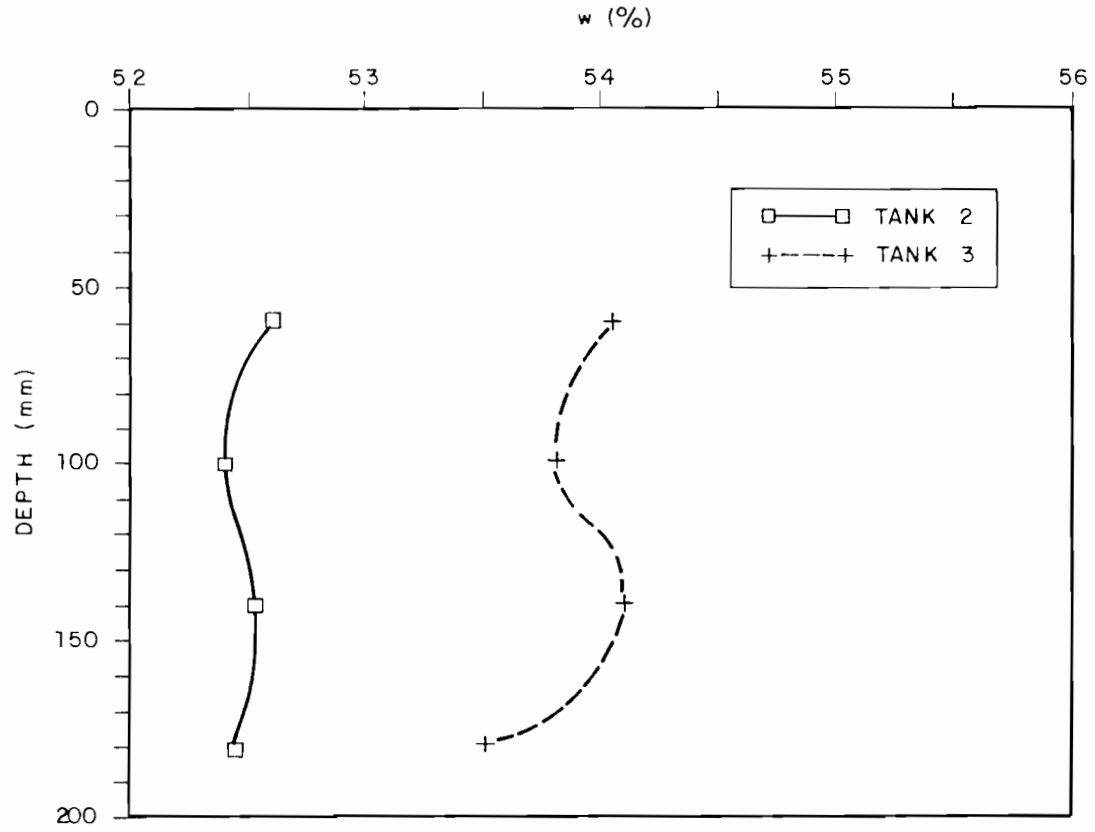

(a) first half samples

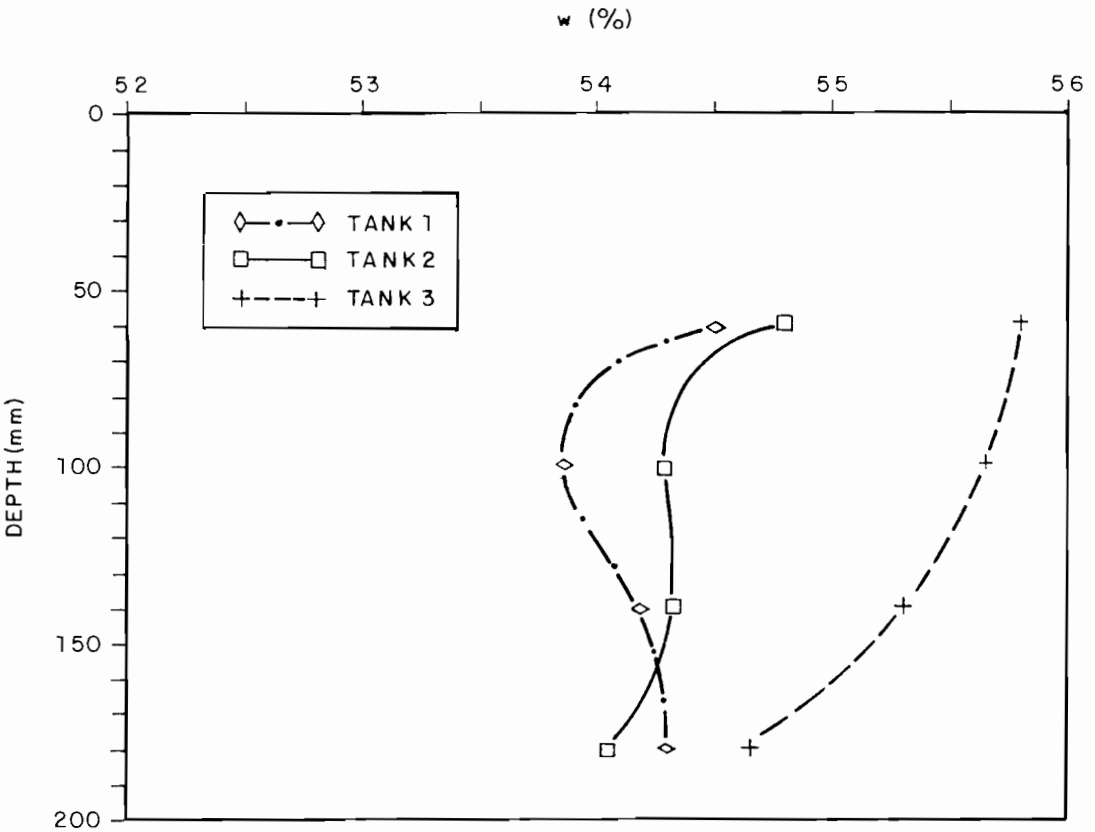

(b) second half samples

Figure 4.10 Batch 14 - vertical profile of water content

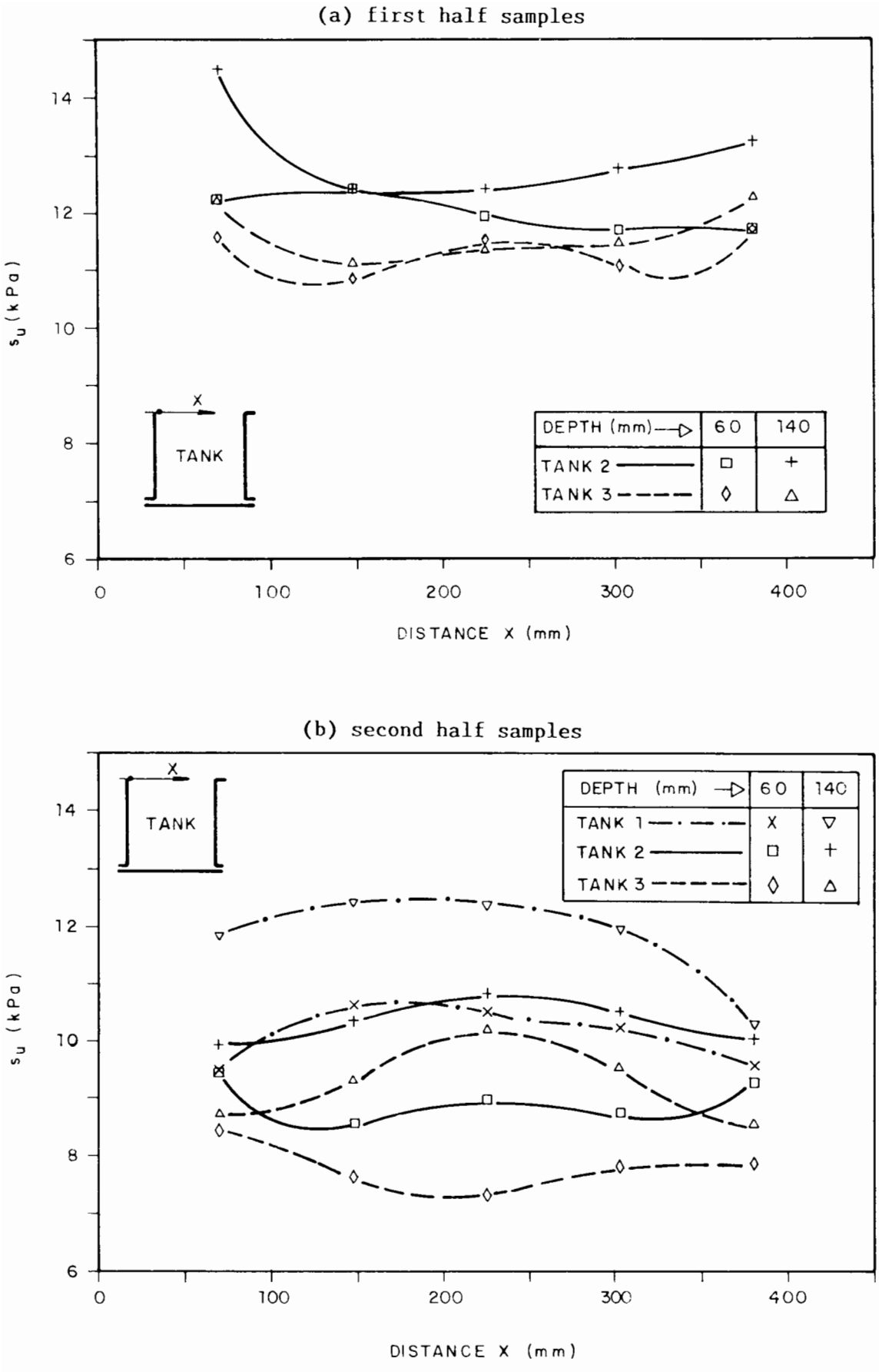

Figure 4.11 Batch 14 - horizontal profile of undrained shear strength

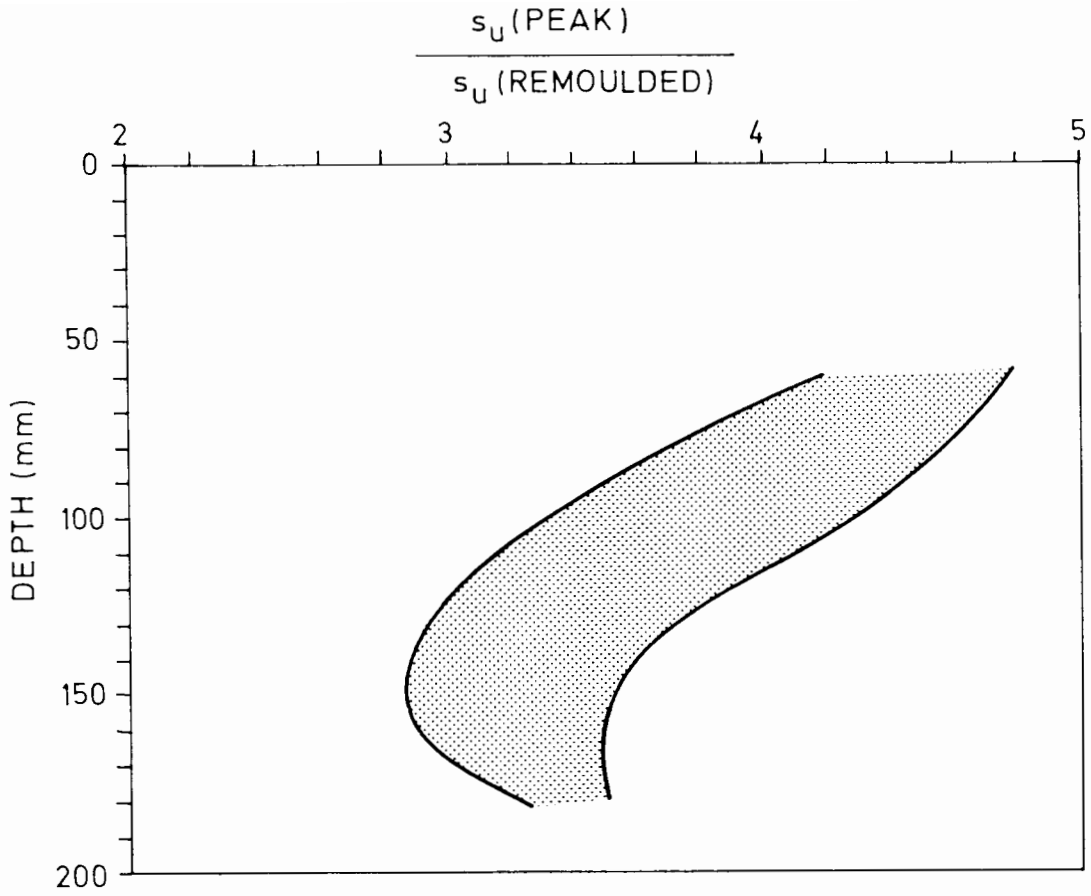

Figure 4.12 Batch 14 - variation of the ratio between peak and remoulded shear strength with depth

sample that for one reason or another was thought not to be of good quality was therefore abandoned.

Nine unconsolidated undrained triaxial tests with measurement of pore pressure were performed altogether and the results plotted in p′ (mean normal principal effective stress) :q (deviator stress) space, shown in Figure 4.13. Seven out of nine tests led to undrained shear strength considerably higher than those obtained by vane tests. The ratio between

triaxial and vane results ranges from 0.89 to 1.95. The reasons for this are not clear but some observations can be made:

(i) The tests are completely different and thus may be differently affected by local disturbance inflicted by the measurement hardware. For instance, the driving of the vane into the clay introduces an increase in the pore pressure near the region to be sheared, decreasing the mean effective pressure and therefore affecting somehow the strength, while the triaxial tests carried out with fixed ends samples suffer end restraint leading to non-uniformities in stresses and strains inside the sample.

(ii) In some tests the stress path in p':q space has an initial slope of about 1:3. This observation might indicate incomplete saturation in spite of all the precautions taken to prevent it. It must be pointed out, however, that test T4B-2, leading to a very high shear strength shows a stress path starting vertically and then slightly curving to the left, while test T2B-2, indicating a much lower strength, shows the initial 1:3 slope. Both tests were carried out on specimens from the same tank and taken from the same depth of 140 mm.

(iii) The same apparent inconsistency was observed by Love (1984) and May (1987), although to a lesser extent.

(iv) There is no fundamental reason why different tests should give the same s_u value (Wroth, 1984).

Figure 4.14 shows the curves corresponding to vertical strain ε versus q and ε versus excess pore pressure Δu for all the tests. Comparing these curves with the stress paths presented in Figure 4.13 it is clear that the tests are consistent among themselves. Table 4.3 shows the critical state parameters derived from the test results. The values of the spacing ratio r and the undrained strength ratio for 1-D normally consolidated clay $(s_u/\sigma'_{vo})_{nc}$ were calculated using the following expressions, respectively:

$$\frac{s_u}{p'_o} = \frac{M}{2}\left(\frac{R}{r}\right)^{\Lambda} \quad \text{and} \qquad [4.1]$$

$$\frac{\left(\frac{s_u}{\sigma'_{vo}}\right)}{\left(\frac{s_u}{\sigma'_{vo}}\right)_{nc}} = R^{\Lambda}\ , \qquad [4.2]$$

where:

s_u = undrained shear strength of the clay;

p'_o = mean effective stress at the beginning of the test;

M = slope of the critical state line in p':q space;

$R = p'_{max}/p'_o$ (overconsolidation ratio);

r = spacing ratio;

Λ = plastic volumetric strain ratio;

σ'_{vo} = vertical effective stress at the beginning of the test (equal to p'_o).

and assuming:

M = 0.9, from revised literature (Steenfelt, Randolph and Wroth, 1981 and Martins, 1983);

Λ = 0.85, from oedometer tests.

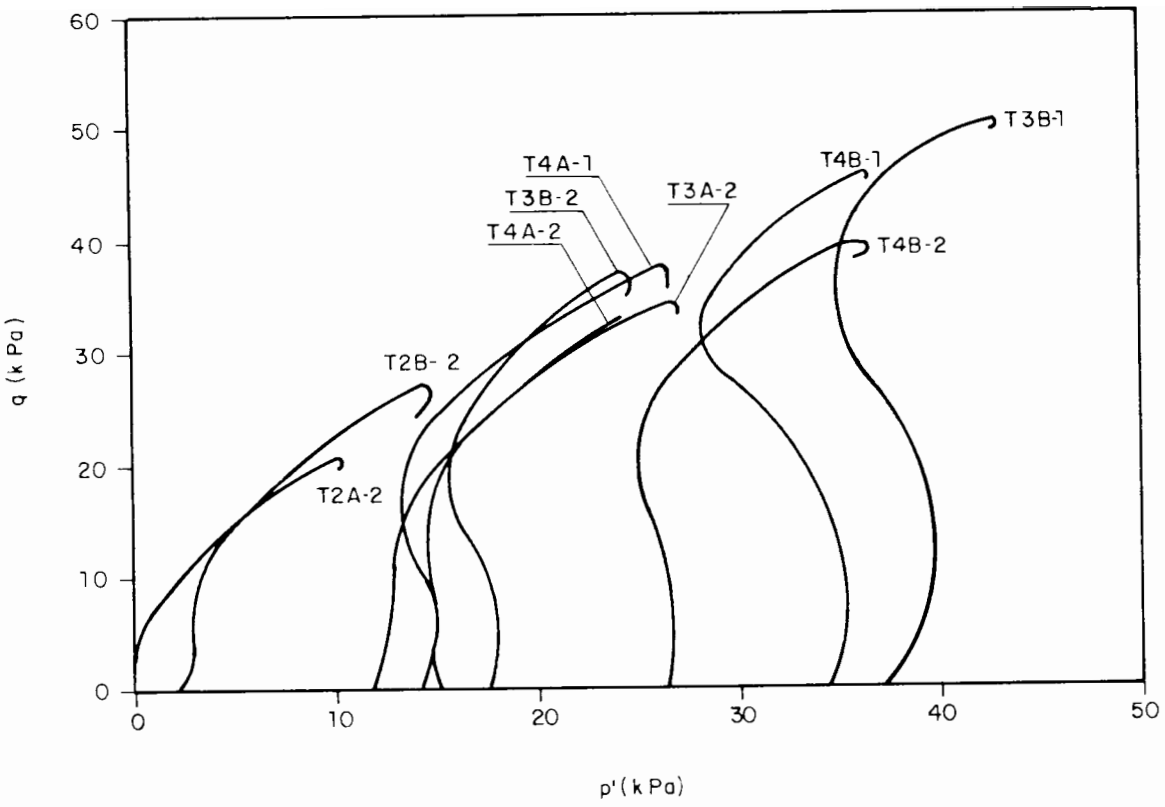

Figure 4.13 Effective stress paths for undrained triaxial compression tests

Table 4.3 Critical state parameters obtained from triaxial tests

test	$p'_o (= \sigma'_{vo})$ (kPa)	s_u (kPa)	R	r	$(s_u/\sigma'_{vo})_{nc}$
T3B-1	37.73	25.67	4.03	2.5	0.21
T4A-1	15.28	18.97	9.95	3.0	0.18
T4B-1	34.38	22.27	4.42	2.9	0.18
T2A-2	0.00	10.40	∞	-	-
T2B-2	1.52	13.53	100.00	3.0	0.18
T3B-2	17.50	18.55	8.69	3.2	0.17
T3A-2	14.03	17.31	10.83	3.3	0.16
T4A-2	11.78	16.27	12.90	3.4	0.16
T4B-2	26.55	19.91	5.73	3.1	0.17

Notes

(1) A corresponds to depth of 60 mm
(2) B corresponds to depth of 140 mm
(3) 1 corresponds to first group of triaxial tests (tank 2 - 1st half)
(4) 2 corresponds to second group of triaxial tests (tank 3 - 1st half)

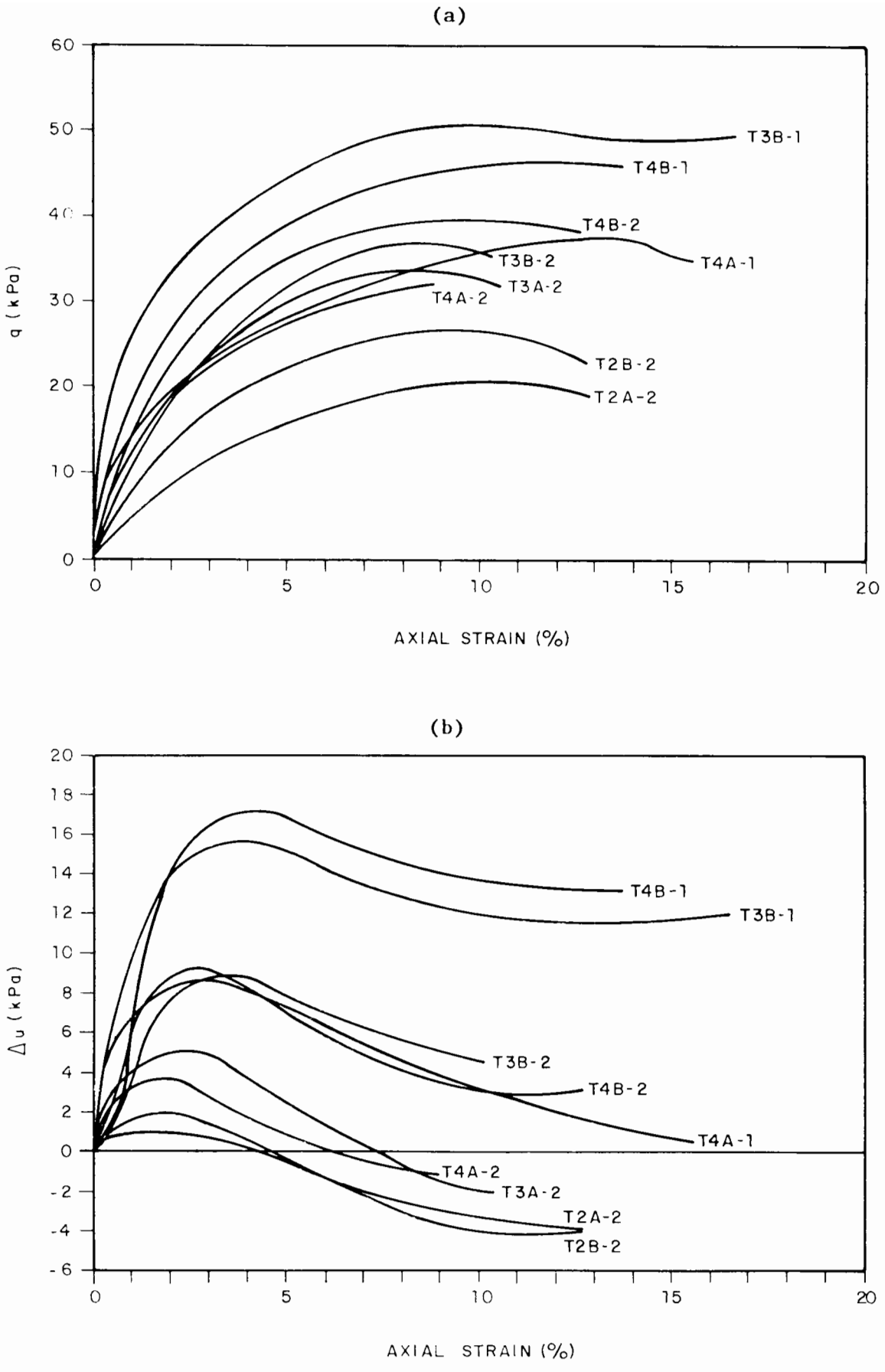

Figure 4.14 Results of undrained triaxial compression tests

Although R varies within a significant range, the values of r and $(s_u/\sigma'_{vo})_{nc}$ only slightly change from test to test. The latter quantity agrees fairly well with the value 0.21 ± 0.01 obtained by Steenfelt, Randolph and Wroth (1981).

The initial rigidity index, defined as the ratio between the secant modulus G_{33} at the point on the stress-strain curve corresponding to a third of the failure stress and the undrained shear strength, G_{33}/s_u, was calculated for each test. The values of G_{33}/s_u are plotted in Figure 4.15, together with the values previously obtained by Davidson (1980) and Fannin (1986) in a similar way. The results of this study seem to agree very well with the trend of decreasing G_{33}/s_u with increasing overconsolidation ratio, in

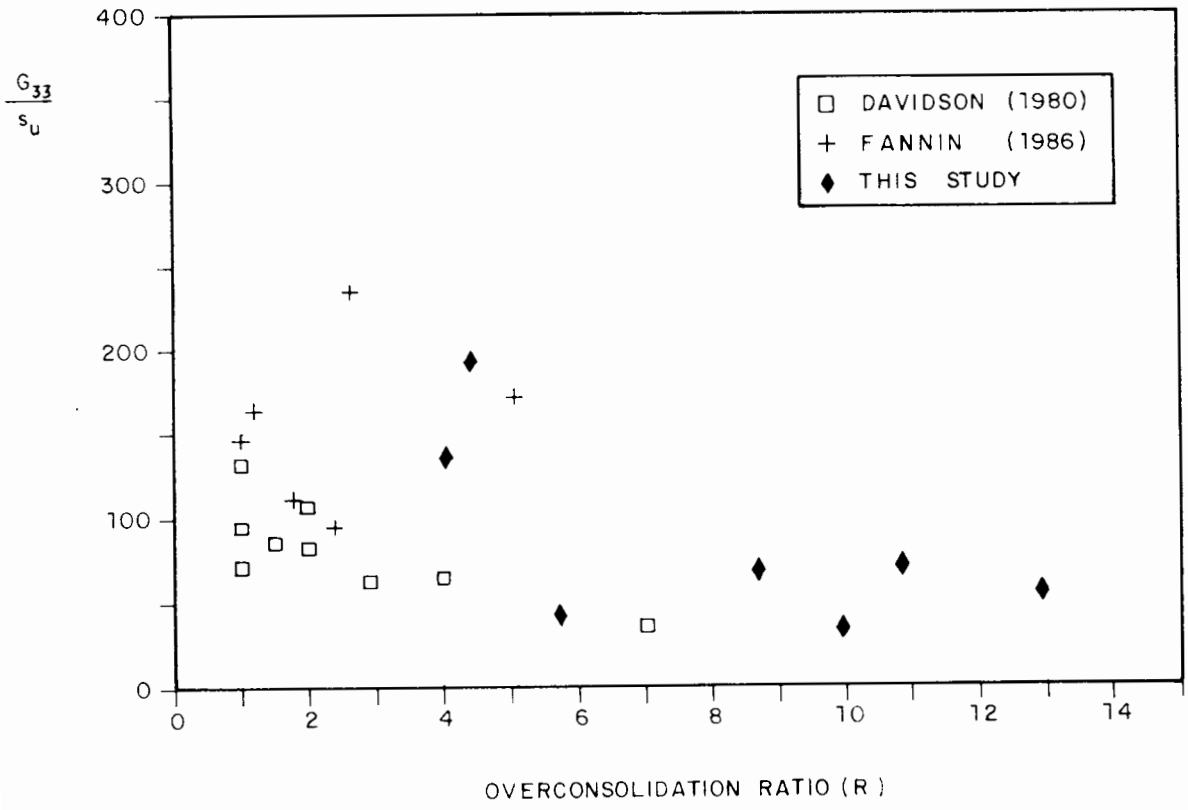

Figure 4.15 Variation of initial rigidity index (corresponding to G_{33}) with overconsolidation ratio

accordance with Wroth, Randolph, Houlsby and Fahey (1979) and Houlsby and Wroth (1985).

4.6.3 Index Strength

Because of the very good repeatability observed in each group of four tests corresponding to a particular depth in a half sample, the shear vane tests were considered reliable enough to define the undrained strength of the clay. Figure 4.16 shows the frequency distribution of the ratio between the maximum and the minimum strength observed in each group of four vane tests performed at the same depth.

The index strength for 100 mm diameter model footing tests was therefore defined as the average of the results of the vane tests carried out:

(a) at the depth of 60 mm for model tests performed at the clay surface;

(b) at the depths of 60 mm and 140 mm for deep model tests performed at the depth of 0.35 D (D = diameter of the footing);

(c) at the depth of 140 mm for deep model tests performed at the depth of 0.70 D.

For 50 mm diameter model footing tests, the index strength was assumed to be the value corresponding to 30 mm depth, derived from linear extrapolation of the average of the vane results at the depths of 60 mm and 140 mm respectively.

From the strength profiles on horizontal planes presented in Section 4.6.1 it is observed that, in 90 % of the results, the strength at the centre of the sample was within ± 12 % of the average strength at 70 mm from the tank boundary.

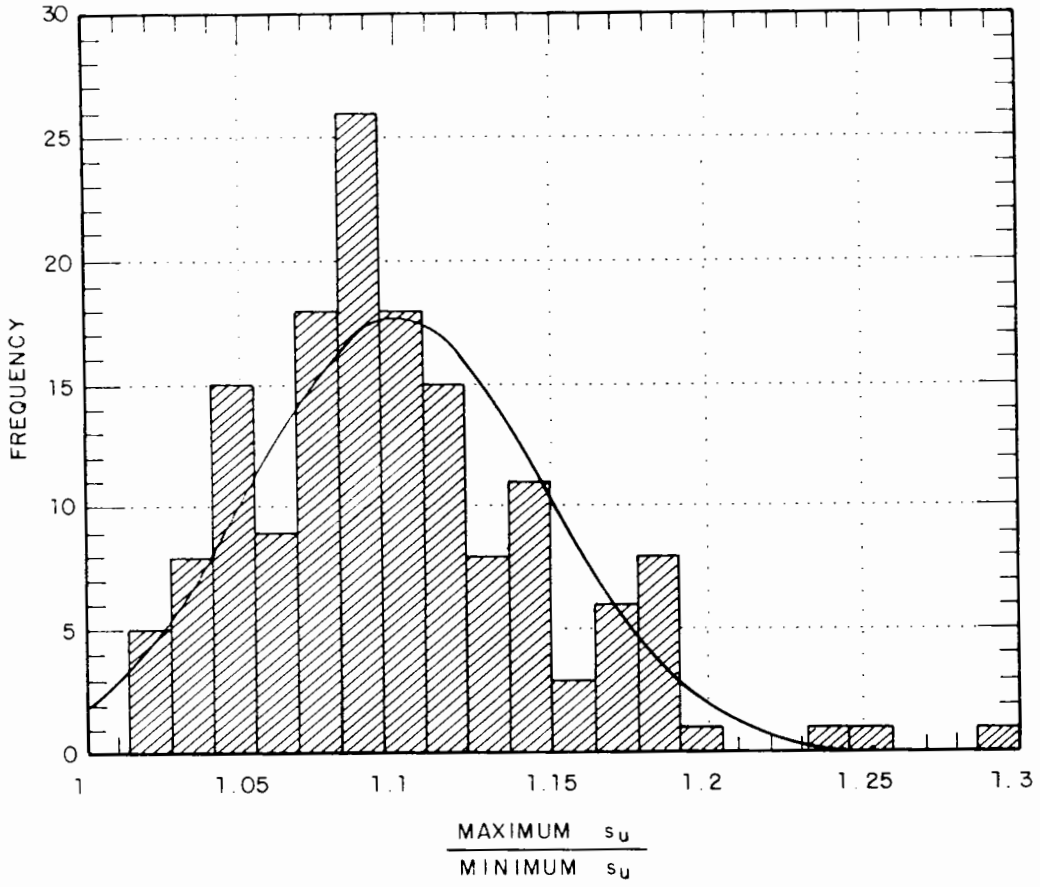

Figure 4.16 Frequency distribution of the ratio between the maximum and the minimum shear strength observed at the same depth

CHAPTER 5

MODEL TESTING PROCEDURES

5.1 Introduction

This chapter describes in detail all the procedures employed during the testing phase of this research. The most relevant aspects of both monotonic loading and cyclic loading tests are highlighted.

5.2 Monotonic Loading Tests

The analysis of the behaviour of footings on clay under combined loads is believed to be realistically achieved by means of physical modelling as long as boundary effects are insignificant and loading can be treated as undrained.

When the clay sample was ready for testing, the bottom tank together with the square base were taken out of the consolidation apparatus and the reaction frame was set up around the former. An approximately 15 mm deep water layer was maintained on the clay surface to guarantee complete saturation of the clay.

After the test on the first level had been carried out, the reaction frame was taken away and the tank lifted about 800 mm so that the plugs on the circular base plate could be removed and the rods attached to the piston plate and to their pedestal plate. The assembly was then lowered to rest on the square base and a vertical load of about 800 N to 1000 N was applied on

the tank to displace it downwards the length of 220 mm. Using a thin wire the extruded clay block was cut in four pieces, to allow the collection of water content specimens, and then trimmed off. The tank was then lifted about 15 mm to allow a water layer on the new clay surface and the triangular plates set between it and the square base. No more than three minutes elapsed from the time the new surface was exposed until the moment water was poured on it. Figure 5.1 represents schematically the procedure described above while Figure 5.2 shows two steps of the operation.

5.2.1 Vertical Central Loading Tests

These tests involved purely vertical central loading and were intended simply as calibration tests to check that the behaviour of the models was as would be predicted by conventional soil mechanics theories.

For this kind of tests the loading device was vertically attached to the horizontal beam of the reaction frame and the loading arm, fitted with load cell TCLZ-100KA, was screwed to the model footing. Two D5/1000A LVDTs were vertically fixed to two holders, having their armatures supported on the upper face of the model footing and symmetrically located in respect to its centre. The footing was then placed at an initial position, which was gently touching the clay surface in each case.

In order to assess the significance of boundary effects it was decided to perform tests on footings of two different sizes, 50 mm and 100 mm in diameter, and also to monitor the ground heave during one 100 mm flat circular footing test. In this test three D5/100H LVDTs were used at 98 mm, 122 mm and 146 mm away from the edge of the footing, in the radial direction and having the armatures resting on the clay surface. Small plastic discs were stuck on the tips of the armatures to prevent any relative displacement

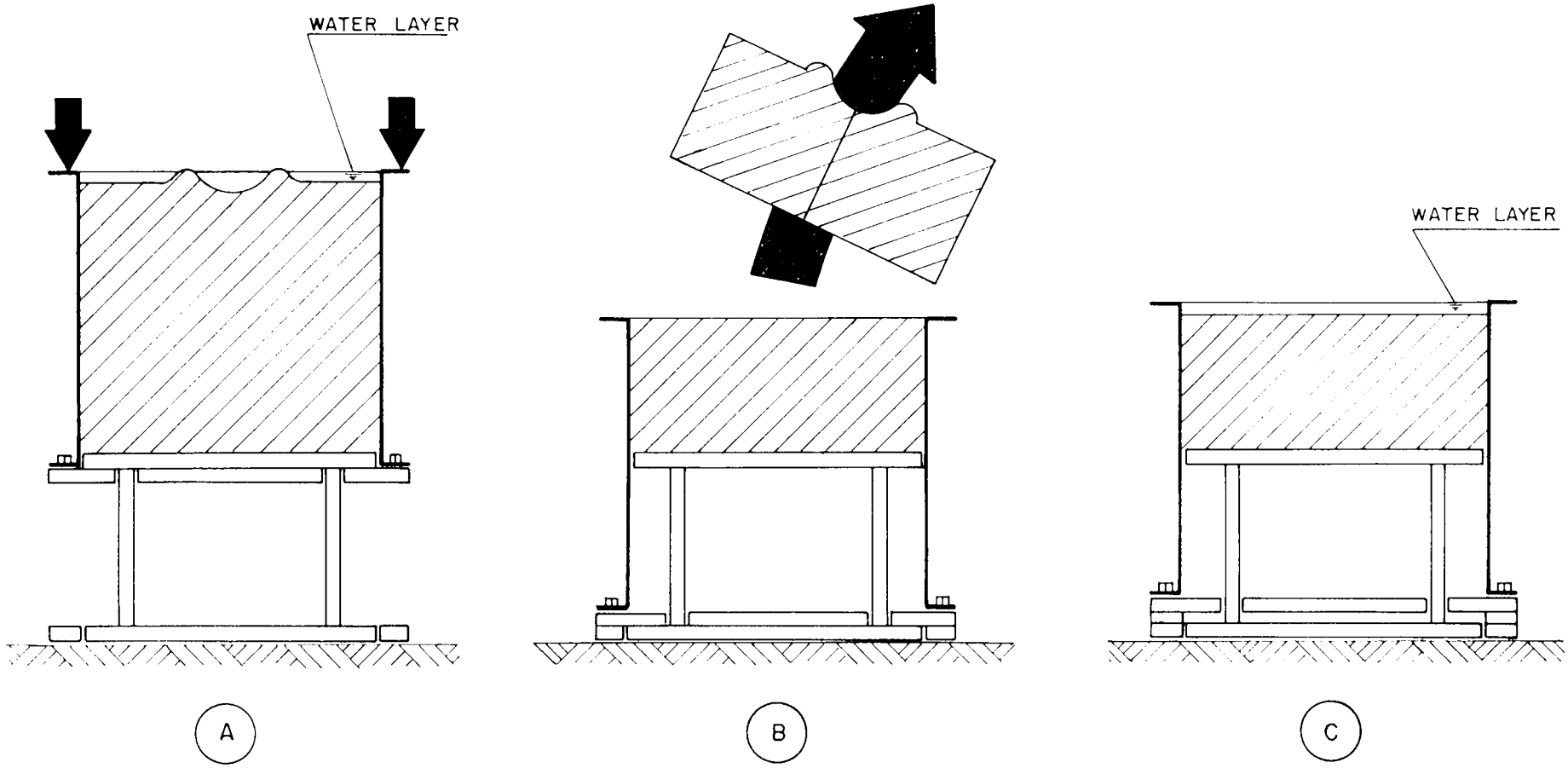

Figure 5.1 Preparation of the second testing level on the same clay sample

Figure 5.2 Two steps of the preparation of the second testing level on the clay sample (left: rods attached to the piston plate; right: tank displaced downwards)

between them and the clay surface.

Tests were carried out on flat circular plate, 150^{o} cone, 120^{o} cone, 90^{o} cone, 60^{o} cone, 120^{o} spud-can and 130^{o} spud-can 50 mm in diameter and flat circular plate, 120^{o} spud-can and 130^{o} spud-can 100 mm in diameter, as shown in Figure 5.3. The vertical displacement rate was 20 mm/min, which was understood to lead to undrained behaviour and the tests went on until any instrument (LVDT or load cell) reached its range limit.

5.2.2 Combined Loading Tests

(a) Standard Tests

These combined loading tests were carried out by applying an initially horizontal constant displacement rate load to a point at a particular height (the loading point) on a bar provided with holes (the loading bar) firmly attached to the model footing. A fixed vertical load was also applied by using a hanger and weights. This configuration of loading was a compromise between a realistic representation of the prototype, a jack-up rig leg subjected to combined vertical and horizontal loading at the contraflexure point, and a modelling allowing a parametric study involving the most relevant variables believed to control the problem: geometry of footing, height of application of horizontal load and vertical load (Figure 5.4).

The set of footings used comprised a flat circular plate, a 120^{o} cone, a 60^{o} cone and a model of a real spud-can (130^{o} spud-can), all 100 mm in diameter. The choice of the larger footing size resulted from the realization of no significant boundary effect detected in the preliminary

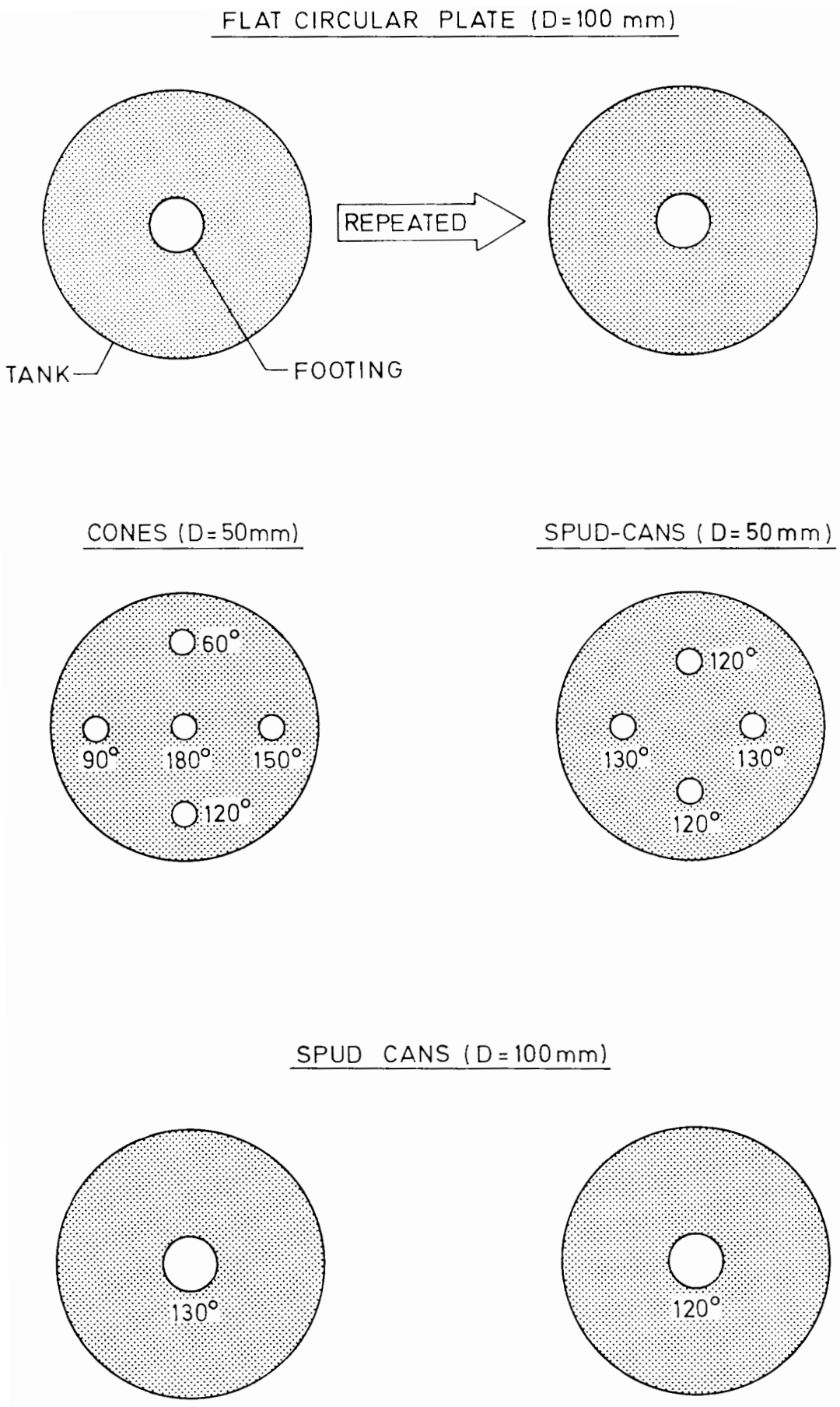

Figure 5.3 Programme of vertical central loading tests

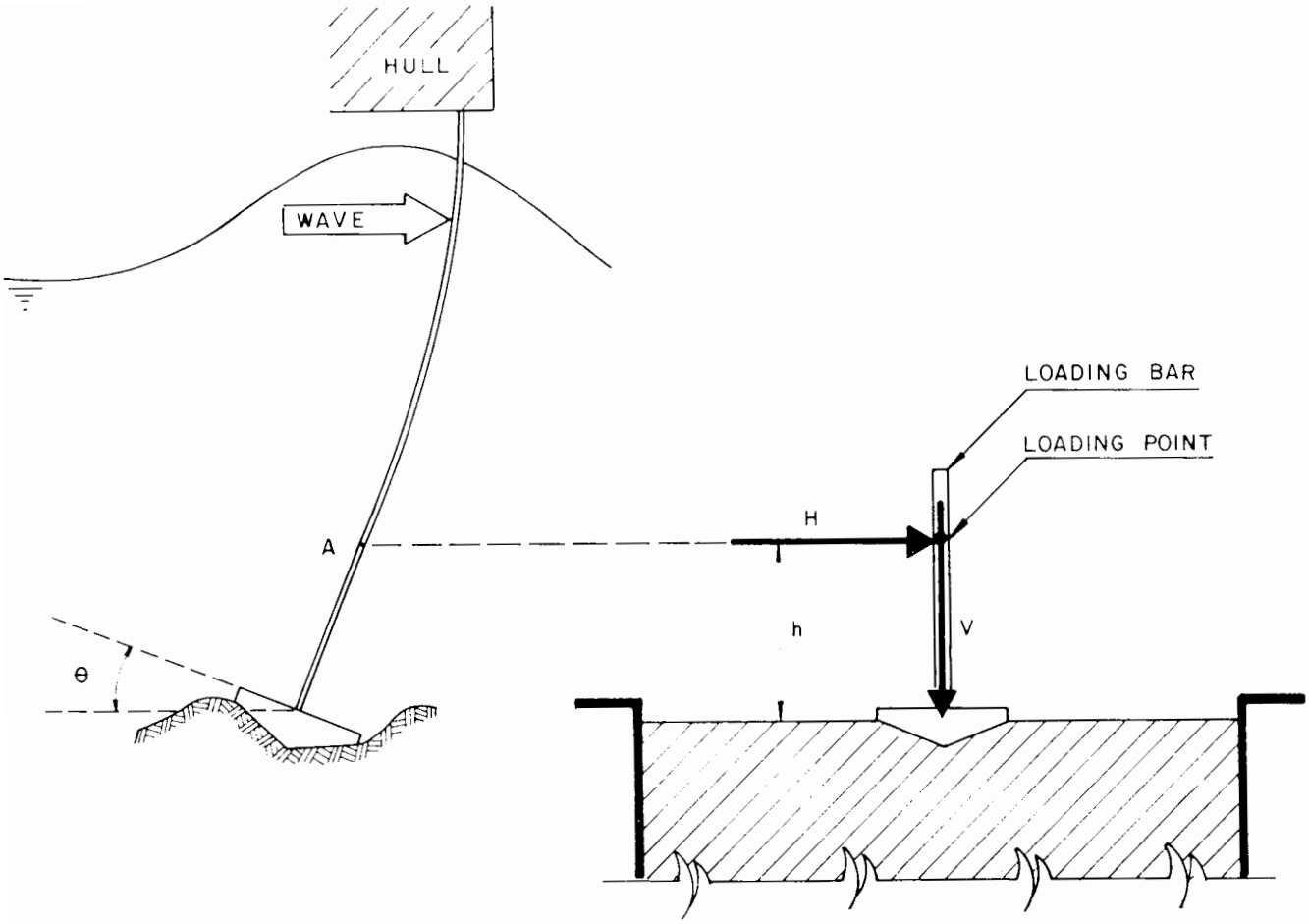

Figure 5.4 Combined loading tests - loading configuration

tests for this case combined with the fact that it provides a more accurate response of the instrumentation.

In a jack-up rig the ratio between the height of the contraflexure point and the footing diameter, h/D, varies typically between 0 and 2.5, the former value representing pin joint behaviour of the footing and the latter full fixity for a typical leg length of 5 diameters. These extreme cases certainly do not occur and must be seen as lower and upper bounds. In this study two values of the height of application of horizontal loads were assumed, approximately 50 mm and 150 mm, leading to ratios h/D of 0.5 and 1.5.

Two values of the fixed vertical load were chosen in this research: the high one corresponding to 75 % of the theoretical collapse load of the flat circular model footing under vertical central loading, i.e. about 330 N, and the low one about 30 % of that value.

The first step in combined loading tests was to screw the loading bar to the model footing and accurately measure the height of the loading point. The next step was the installation of the model footing on the clay sample. In the case of flat circular footings, this was attained simply by placing the model footing on the clay surface. For cones and spud-cans it was achieved by driving the model into the clay until the footing was just penetrated up to its maximum diameter. In the latter case, a load cell TCLZ-100KA and a D5/2000 LVDT were used to register the load and displacement data. In this case, unlike vertical central loading tests set-up, the footing already had the loading bar screwed to its centre and the loading device had to be pinned to the highest hole in the bar (Figure 5.5). The upper face of the model footings remained, at this stage, about 10 mm above the mud line. The loading device was then attached to the reaction frame so that the loading arm was horizontal, as shown in Figure 5.6. The loading arm included a load cell to measure horizontal load.

Four LVDTs D5/1000A were set vertically on the footing at the edges of a 56.6 mm side square. A fifth LVDT D5/1000A was installed horizontally, aligned with the loading arm axis and opposite to it.

The instrumentation lay-out described allowed an absolute knowledge of the model footing load and displacement components on the loading plane at any time during the test.

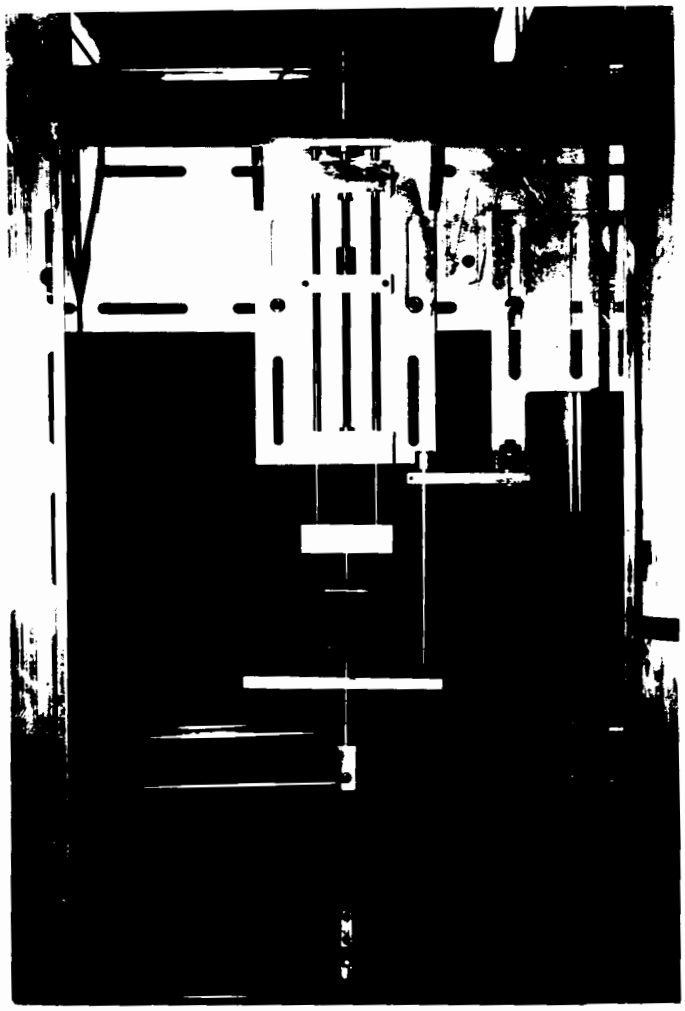

Figure 5.5 Installation of the model footing in the clay sample

At this stage the microcomputer was switched on and the data logging/monitoring software initialized. The vertical dead load was then applied by carefully lowering the hanger with weights until the ball bearings at the tips of its vertical double support were resting on the spherical depressions on the footing (Figure 5.7). As a precaution to reduce friction, some grease was spread on the footing depressions before application of vertical load.

The motor was then switched on and the test continued with the loading arm going forth and back, in a few manually controlled cycles and at a

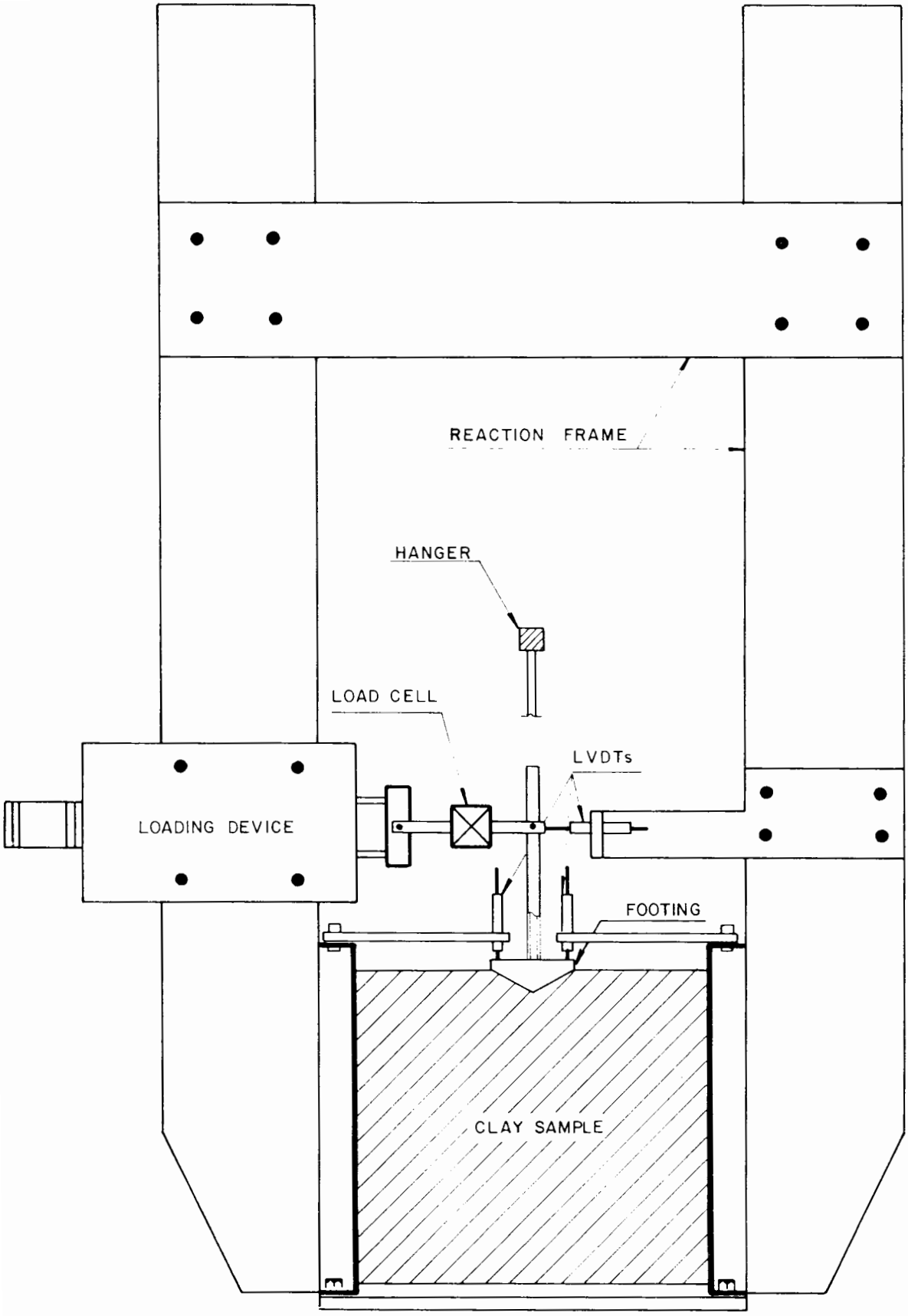

Figure 5.6 Combined loading tests - testing assembly

Figure 5.7 Detail of the hanger supports resting on the model footing

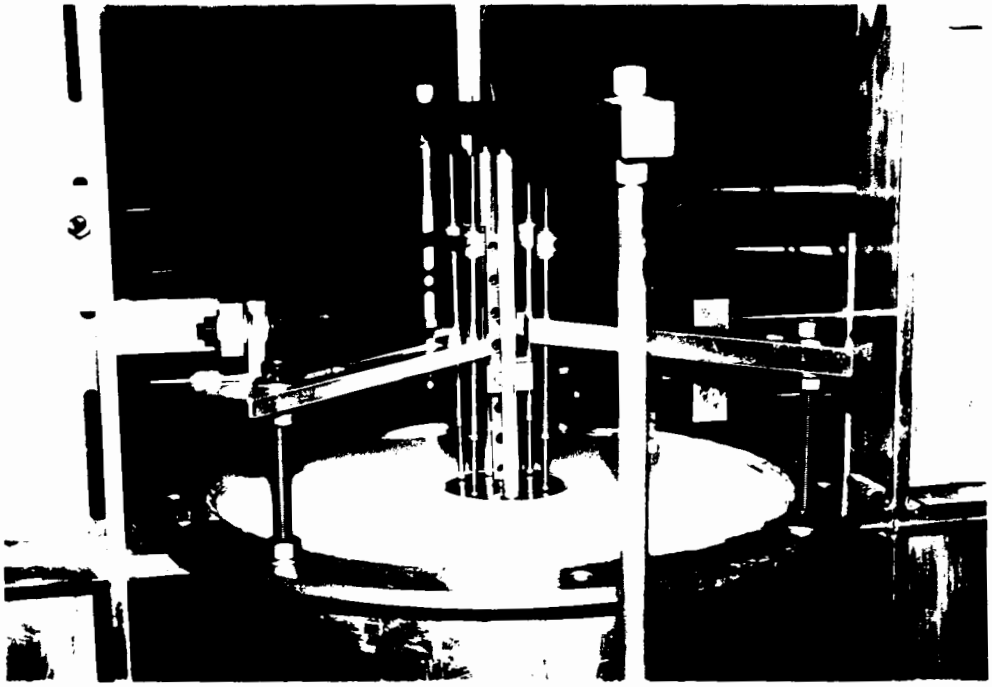

Figure 5.8 View of a typical combined loading standard test set-up

displacement rate of about 4^{o}/min, which was a compromise between undrained behaviour and the speed through which the system was able to acquire data to define relevant parts of the moment versus rotation curve. The test proceeded until it was not possible to work any more within the linear range of the LVDTs. Figure 5.8 displays a typical combined loading standard test set-up.

(b) Deep Tests

Combined loading deep tests were conceived to study the influence of the embedment depth on the behaviour of circular footings. They were similar to standard tests except for the position at which the model footing was placed into the clay sample before the test started: approximately 35 mm and 70 mm deeper than standard tests.

The tests were carried out on 130^{o} spud-can and the four vertical LVDTs were in this case set up on an auxiliary duralumin disc attached between the loading bar and an extension rod screwed to the footing. The height of application of the horizontal load had to be increased to approximately 200 mm because of physical limitations in the assembly and the vertical dead load was applied onto the auxiliary disc. Figure 5.9 illustrates a deep test set-up.

5.2.3 Leg Tests

Leg tests were designed to provide information about the interacting behaviour of a jack-up leg and its foundation through a physically similar model. The purpose is to apply a horizontal deflection to the top of a model jack-up leg, whilst preventing rotation of the top of the leg.

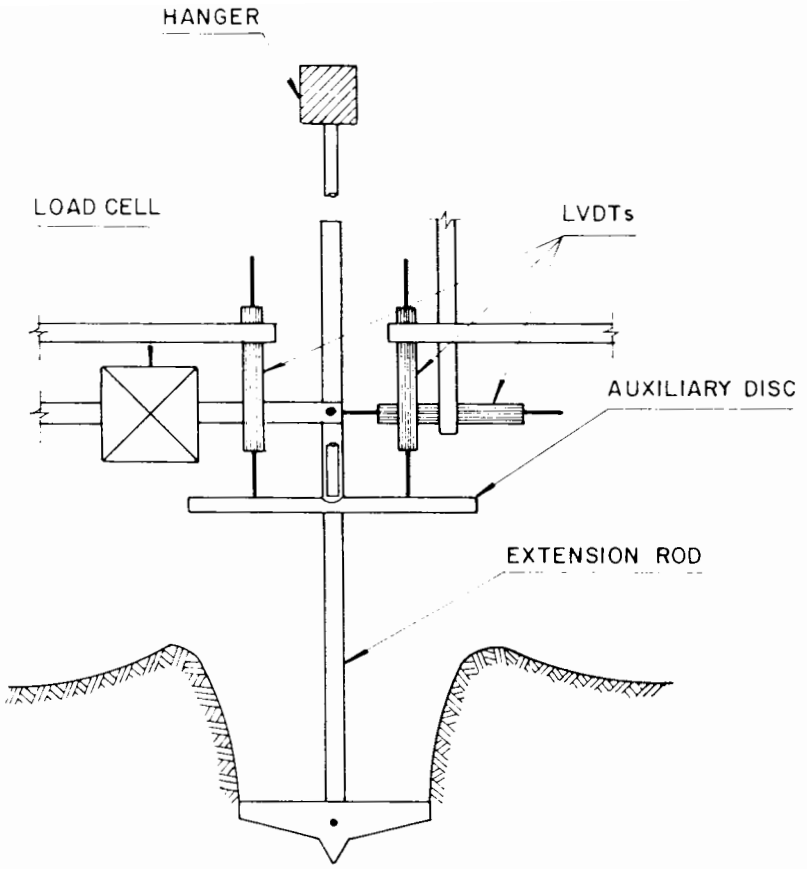

Figure 5.9 Combined loading deep test set-up

The leg model consists of a slender bar fixed to a bipartite stiff plate along its upper part and having a 130^{o} spud-can model footing attached to its lower end (Figure 5.10).

The first step was to bolt the lateral guide to the reaction frame and to spread some light oil on the surface of the perspex strips to reduce friction. The next step was to place the model leg in the starting position by penetrating the footing into the clay by pushing the plate-leg-footing assembly down through the lateral guide. As in the combined loading tests, load and displacement data were collected during this phase. In order to avoid any disturbance during the subsequent set-up operation, the model leg was temporarily fastened to the guide by a "G"-clamp, after its verticality had been checked. The loading device was then bolted horizontally to the

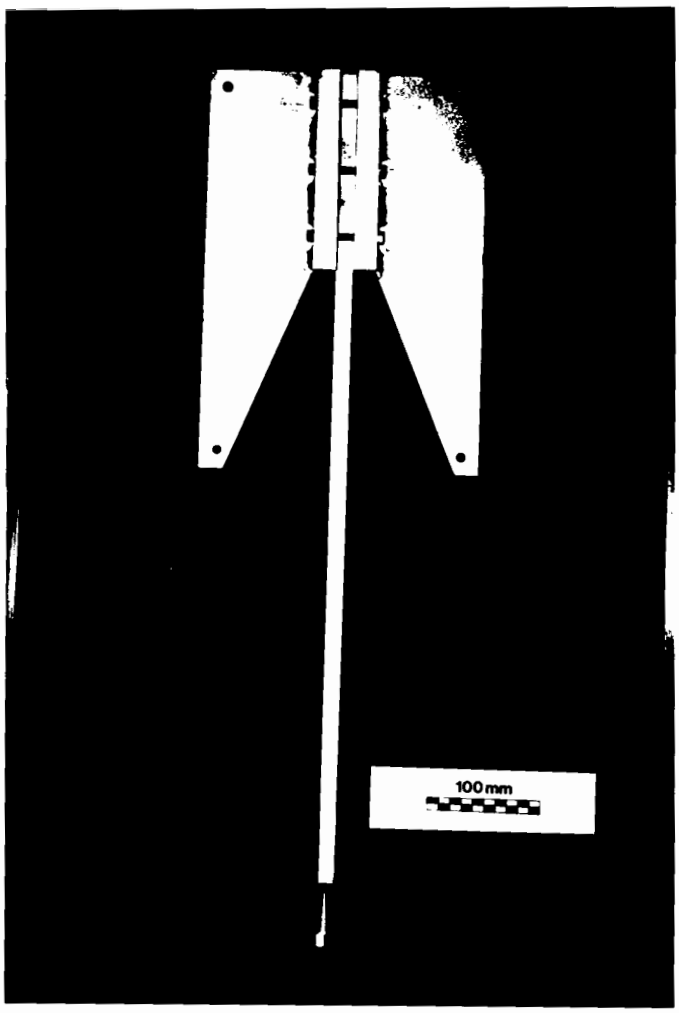

Figure 5.10 Model leg attached to the model footing and to the bipartite stiff plate

reaction frame and two loading arms, fitted with load cells TCLZ-10KA and TCLZ-20KA, were pinned horizontally between it and the plate holding the model leg.

The vertical D5/1000A LVDTs were placed on the model footing in the same way as in standard combined loading tests, and the horizontal one was set a few millimetres above the leg tip. A sixth LVDT (D5/2000) was also placed horizontally near the loading device to measure the horizontal displacement of the loading arms, as shown in Figure 5.11.

Before the test started, a vertical dead load was applied to the top of the leg. This load produces an additional moment on the model footing when the leg deflected, besides the moment induced by the horizontal loading.

The leg test set-up (Figure 5.11) allowed vertical and horizontal displacements of the top of the leg, but restrained any rotation at this point, as is approximately true for real jack-up rigs. The instrumentation provided complete information about load and displacement components on the loading plane at both leg extremities. The displacement ratio was the same as in combined loading tests.

The pertinent data logging/monitoring program displayed, among other numerical information, the moment at the top of the leg throughout the test. This data was important to avoid overloading the leg, causing plastic deformation and therefore permanent bend. The Young modulus and the maximum bending moment in the fully elastic range were derived from a cantilever test performed on a beam cut from the same bar used to make the model legs.

Two legs were used in the tests, 9.0 mm and 14.3 mm in thickness, both 20 mm wide and having a free length of 500 mm. Two vertical dead loads, about 130 N and 330 N, were studied. Only one kind of model footing (the 130^{o} spud-can) was employed.

5.2.4 Data Logging and Control

Programs in BASIC were written to log the data and monitor monotonic loading tests using a microcomputer. A number of programs were developed to meet the particular requirements of different types of tests.

All the programs started with the input of necessary data concerning the

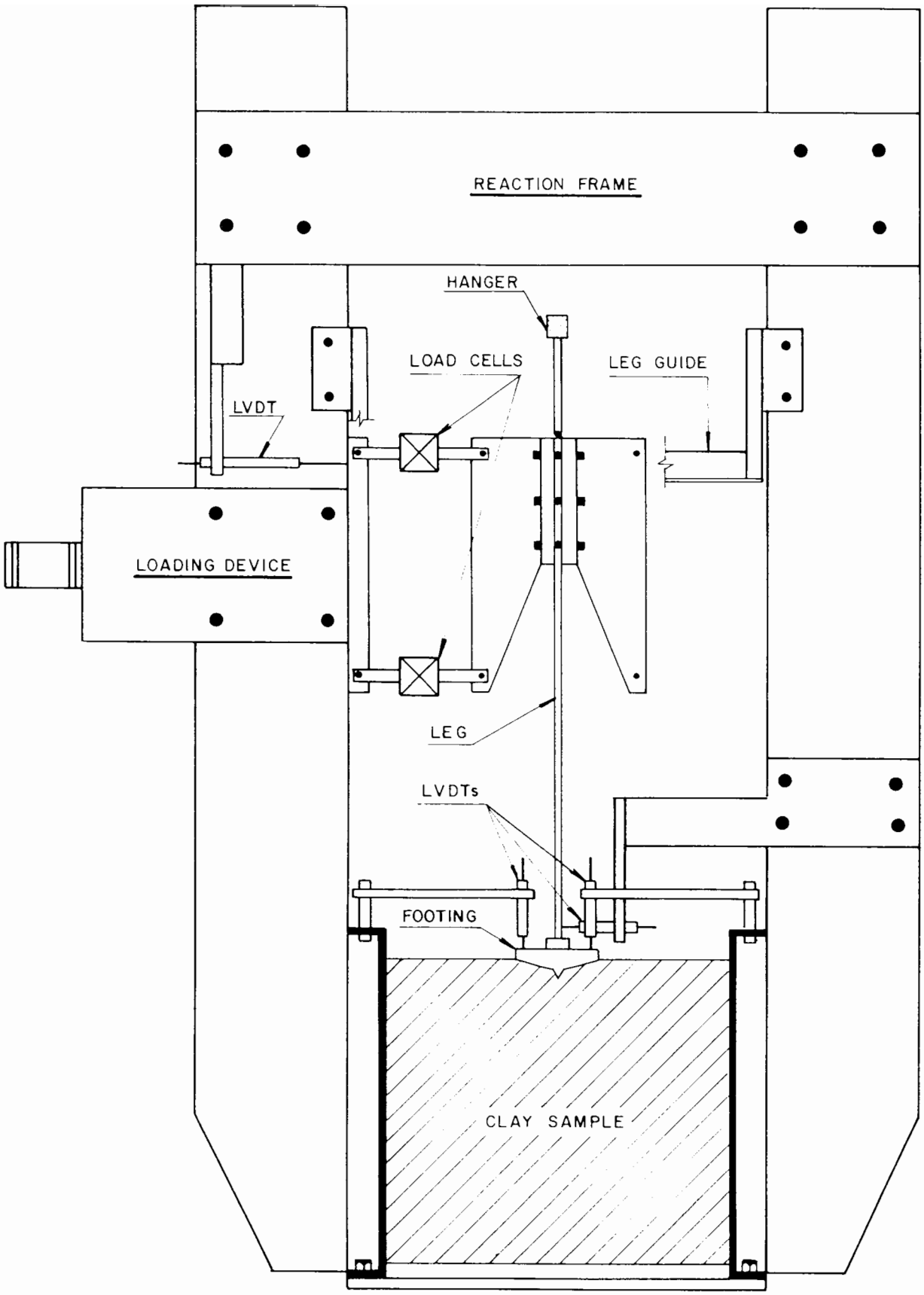

Figure 5.11 Leg tests - testing assembly

test, followed by continuous scanning of all channels. At this stage the voltages read on each channel were displayed on the screen so that a general check could be performed on the instrumentation output, allowing also any positional adjustment of the LVDTs. If everything was in order, a keyboard command triggered an initial read-out of all channels and the test was started. As the testing went on the channels were repeatedly scanned and the increment of a particular component of displacement (vertical or rotation, depending on the type of test) was computed and compared with a pre-defined limit. If this limit was reached, the readings were stored in array variables and, using the calibration coefficients of the instruments, the software displayed on the computer screen essential numerical information about the test. For combined loading and leg tests, the moment versus rotation curve was plotted to allow a better appreciation of the test progress. As a precaution, all the programs triggered an alarm on the microcomputer whenever any transducer was about to reach the limit of its linear range.

The tests were all displacement controlled and operated by means of a control box provided with an on-off switch (Figure 3.6 (a), A) and a potentiometer (Figure 3.6 (a), B) to set the rate and direction of displacement in the loading device. An approximately fixed rate was achieved by manually tuning the potentiometer as the computer displayed the calculated rate within each increment of displacement.

5.3 Cyclic Loading Tests

The problems of modelling cyclic loading are considerably more difficult than those of monotonic loading because of the importance of time. Time can be modelled in many different ways, depending on which time-dependent effect is the most relevant for the phenomenon modelled. If N is the geometric

scale of the model, the interval of time Δt between two events in the prototype would correspond in the model to:

* $\Delta t/\sqrt{N}$ for gravity/inertia controlled movements;
* $\Delta t/N$ when body forces are to be considered;
* $\Delta t/N^2$ when consolidation of a clayey soil is involved.

In this research, consolidation was obviously the only time-dependent effect that should be accounted for when modelling time. However, bearing in mind that the geometric scale is about 200, the period of a horizontal cyclic load to be applied to the model footing simulating the action of oceanic waves of 30 seconds period would be of the magnitude of 7.5×10^{-4} seconds. As analysis of foundations under cyclic loading requires a clear definition of loading and unloading branches in each loading versus displacement loop, meaning the acquisition of a number of data points during a cycle of loading, the correct modelling of time was therefore not possible in this study. Instead, it was decided to adopt the smallest period compatible with the acquisition of a minimum number of data points to have the loops reasonably well defined. To study how the frequency affects the results, another period about four times as large as the first was also used. This procedure led to periods of 8 seconds and 30 seconds.

5.3.1 Standard Tests

Standard cyclic loading tests were performed using the same set-up as in monotonic loading tests, but replacing the displacement controlled loading system with a more sophisticated load controlled system, which applied a sinusoidal load simulating wave action. Effects of oceanic currents were

investigated by introducing an offset to the loading cycle.

Having understood from the first stage of the research that the height of application of horizontal loads affects only slightly the rotational behaviour of footings, and bearing in mind that the real shape of jack-up footings are like the model spud-cans, it was decided to vary only the period, amplitude and offset of moment loading (Figure 5.12) and the vertical load, as below:

period: 8 seconds and 30 seconds;

offset: no offset was the first studying case and the other value, 0.5 Nm, was derived so that the ratio between the maximum and the minimum moment for high amplitude loading was consistent with those obtained for real rigs under storm loads and subjected to dragging forces resulting from high velocity ocean currents;

amplitude: two values were chosen for peak-to-peak amplitude, the higher one corresponding to about twice the value of the average failure moment obtained from monotonic tests minus the offset, leading to 4.0 Nm, and the lower one half of this value, 2.0 Nm;

vertical load: 134 N and 330 N approximately as in monotonic loading tests.

As the rotational behaviour of footings is very little affected by the height of application of the horizontal loads, and therefore this parameter was not included in the parametric study, a value of 100 mm (midway between the values used in the monotonic tests) was adopted.

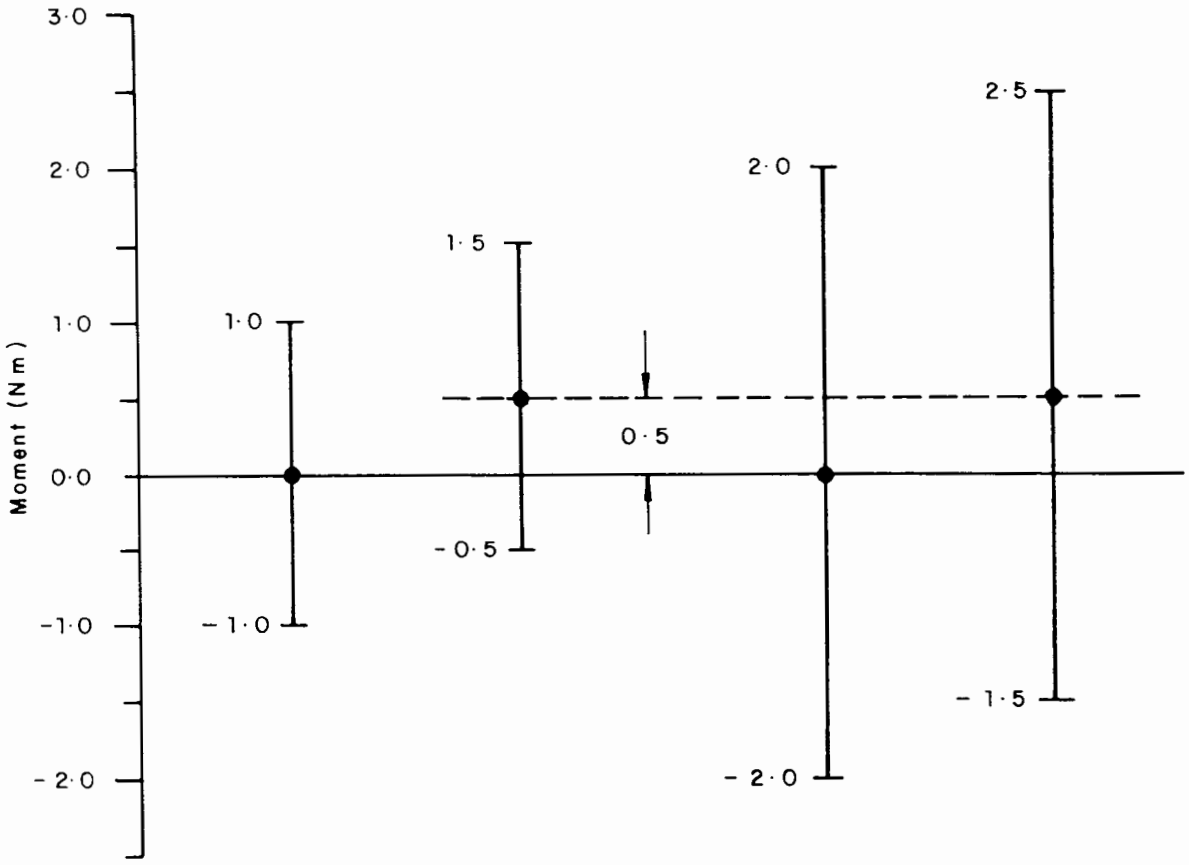

Figure 5.12 Amplitudes and offsets for cyclic moment loading

5.3.2 Special Tests

Special tests were designed to cover some peculiarities of real loading conditions:

(i) double amplitude tests, intended to study the effects of high amplitude cyclic loading after a sequence of low amplitude cycles of load had been applied. This procedure approximately simulates the action of a storm increasing in intensity;

(ii) tests with bursts of cycling, intended to evaluate how the repeated application of a number of cycles of load followed by a resting time affects the rotational behaviour of the footing. These simulate a sequence of storms followed by calm weather.

These tests were conducted under vertical load of about 330 N, 8 seconds period and either with or without offset of moment loading. Double amplitude tests were carried out with a moment amplitude of 2.0 Nm for 300/400 cycles followed then by a second amplitude of 4.0 Nm. Bursts of cycling tests were performed by applying series of 50 cycles of 4.0 Nm amplitude moment loading followed by a resting time.

The definition of the resting time in the context of special tests (ii) was a compromise between an interval long enough to guarantee dissipation of most of the pore pressures built up during cyclic loading and the minimum duration of the whole test. In order to provide an approximate assessment of the most appropriate interval, two footing settlement tests were carried out on clay samples on the day after standard cyclic tests had been performed. The procedure consisted simply of applying and removing a fixed vertical load on a spud-can model footing placed in the clay sample and monitoring the settlements using four vertical LVDTs. A program written for this purpose datalogged the tests and displayed the settlement versus time curve on the microcomputer screen.

A fixed vertical load of 330 N was applied in the two tests and the results suggest that after about 60 minutes more than 90 % of the pore pressure built up has been dissipated, as illustrated in Figure 5.13.

5.3.3 Data Logging and Control

The data logging/monitoring software for cyclic loading tests was similar to the programs employed in monotonic loading tests. The scans of the data were, however, triggered by pre-set intervals of time instead of intervals of displacement.

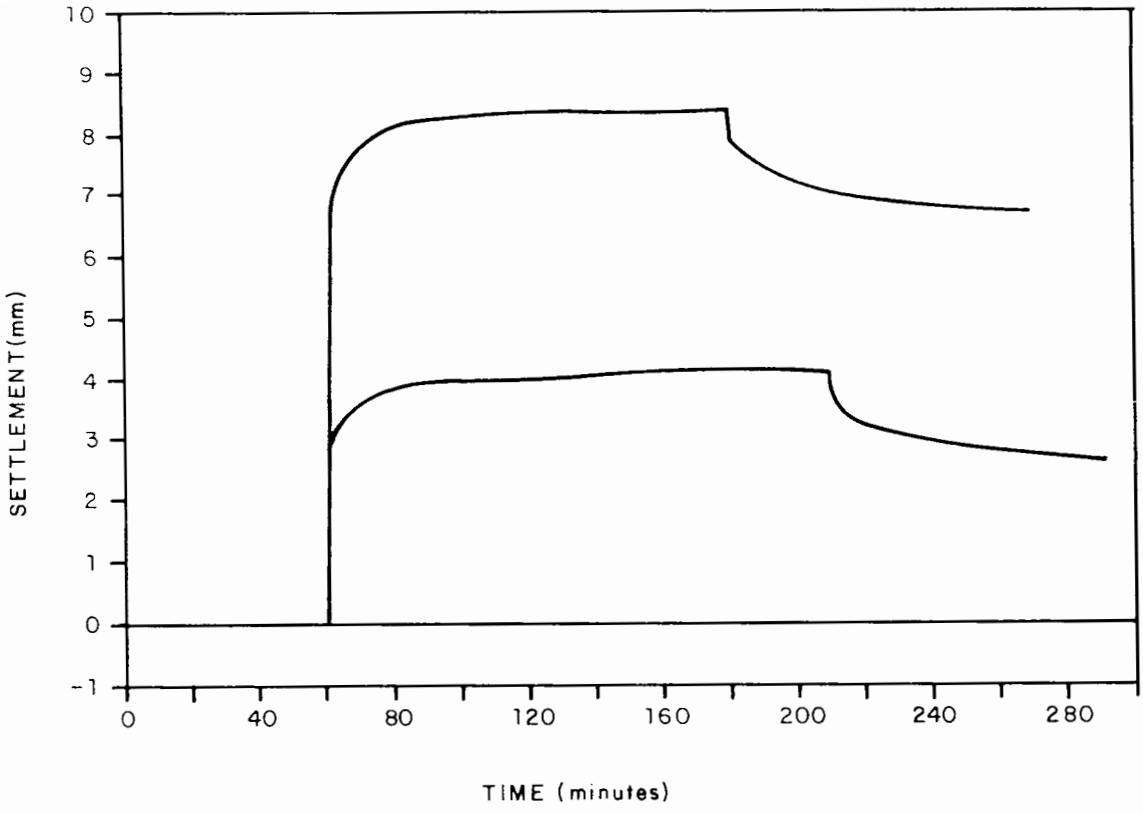

Figure 5.13 Results of two settlement tests on a 130° spud-can model footing

A program was written to allow manual control of the loading device through the keyboard of the microcomputer, an indispensable facility for the set-up operation. Switch B in Figure 3.6 (b) changes the operational mode of the system from automatic to manual and vice versa.

The flow chart of the loading control and data logging system is represented in Figure 5.14. The heart of the system is a servo amplifier, which is basically a feedback system that drives the d.c. tacho-motor of the loading device. It compares the "command" voltage, a sinusoidal wave function generated by microcomputer A, with the "slave" voltage, an amplified signal coming from the load cell.

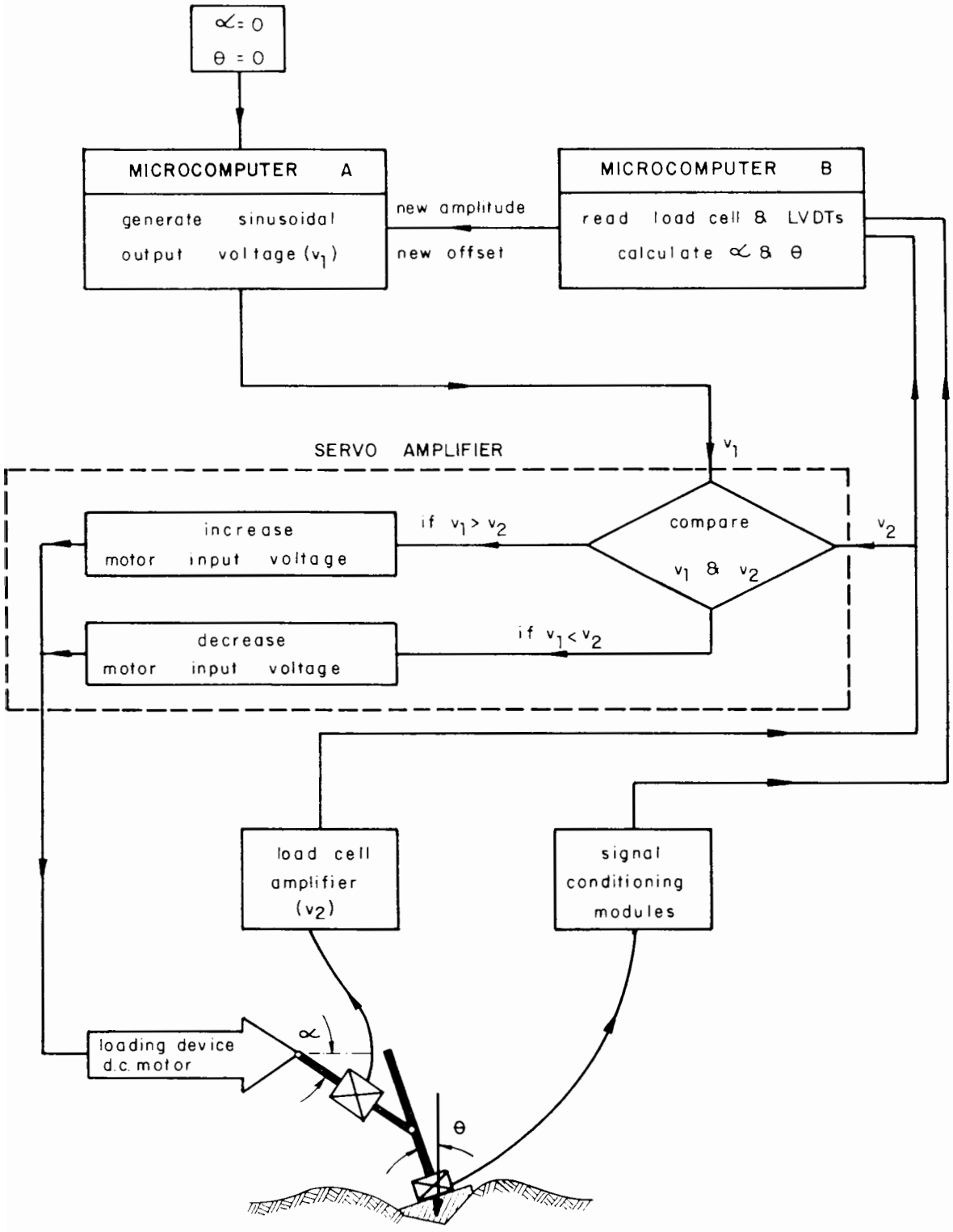

Figure 5.14 Flow chart of the cyclic loading control and data logging system

As the command voltage rises, the servo amplifier detects a difference between this and the slave voltage. It therefore drives the motor in the right direction to cause compression of the load cell so that the slave voltage coming from this rises to the same level as the command voltage. As this continues to rise and eventually fall, the motor follows the varying input, turning then the command voltage into a sinusoidal compression and tension profile. Figure 5.15 shows typical data points obtained from the load cell (corresponding to the slave voltage) compared with the sinusoidal loading function generated (corresponding to the command voltage).

The loading arm, set horizontally before any load is applied to the footing, becomes inclined as the footing settles during the test. To keep a constant amplitude of horizontal loading and therefore a constant moment amplitude,

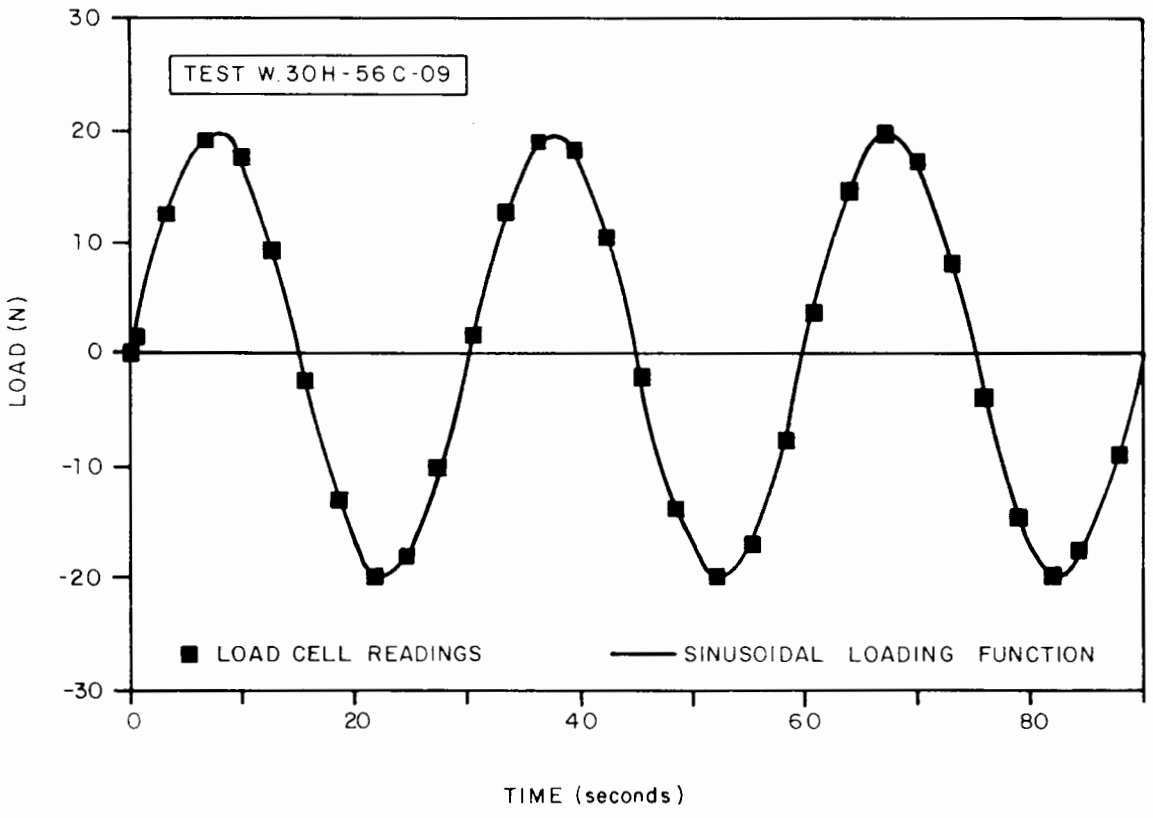

Figure 5.15 Data points obtained from the load cell compared with the sinusoidal loading function generated

the command voltage must be adjusted (Figure 5.16 (a)). The rotation of the footing also introduces a small eccentricity in the fixed vertical load which, for large angles and loads, represents a significant variation in the offset of loading and must be accounted for if a constant offset is required (Figure 5.16 (b)).

The above mentioned corrections are achieved through microcomputer B which, data logging the test, performs necessary calculations for monitoring purposes and also updates the sinusoidal function parameters, sending this information to microcomputer A through a communication channel linking both machines.

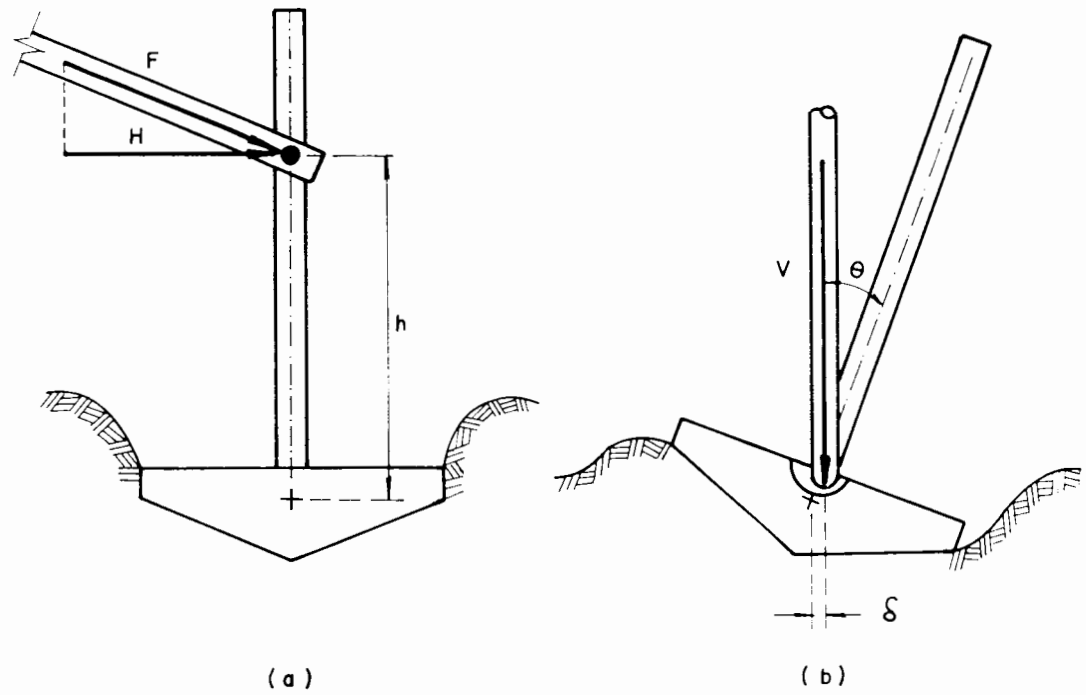

Figure 5.16 Deviations from initial set-up considered by the control system to keep a constant amplitude (a) and offset (b) of cyclic moment loading

CHAPTER 6

EXPERIMENTAL RESULTS - MONOTONIC LOADING

6.1 Introduction

After the end of each test, the files containing the raw data (i.e. the voltages corresponding for every channel in every scan), stored on 5 1/4" floppy disks, were sent to the departmental mainframe computer, a VAX 11/780. These data were then processed through FORTRAN programs written for this purpose for each kind of test. Using the voltages corresponding to each transducer, their respective calibration coefficients and the particular parameters concerning the test, the software calculated the loads and displacements throughout the test, introducing all the necessary corrections such as eccentricity of vertical load, inclination of the loading arm and the force induced by the spring of the horizontal LVDT.

There is an arbitrary choice of the point on the footing to which the loading system (vertical load, horizontal load and moment) is reduced, although the definition must be geometrically consistent among the various shapes used in the study. Other definitions could have been adopted but, for the sake of simplicity, the loading system was reduced to the point corresponding to the centre of the lowest maximum circumference of the footing (Figure 6.1). In the following sections this point is always referred to as the "centre" of the model footing.

Figure 6.2 shows the numbering system used to identify the main features of each test.

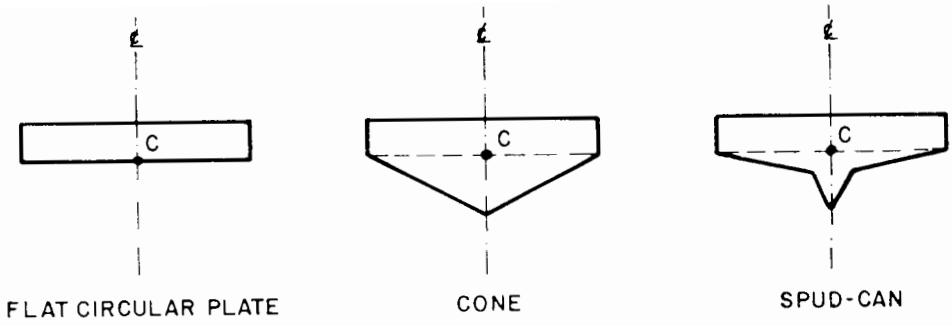

Figure 6.1 Definition of footing centre (point C)

A few cycles of loading and unloading were used for combined loading tests and special tests. This procedure was not intended to simulate cyclic loading but to acquire as much data as possible for analysis, bearing in mind that it takes from three to four weeks to prepare a batch of samples.

Three tests were lost for reasons involving malfunction of the electronics, excessive disturbance during set-up or anomalous results observed during analysis. This total represented only about 6 % of the tests. Among the curves presented in this chapter, a few have one or more small missing segments, corresponding to points out of the linear range of the LVDTs, while the irregularities in some of them are due to datalogging inaccuracies.

The test results are presented by using a combination of tables and curves. The former are intended to indicate the values of fixed parameters related to each test and the latter to show the test progress in terms of non-dimensional variables. The following symbols define the properties of the clay sample as well as the geometry, loads and displacements on the model footing:

s_u = index strength of the clay;

w = ground heave;

D = diameter of the model footing;

$A = \pi D^2/4$;

β = cone apex angle or enveloping angle for spud-cans;

V = vertical load;

M = moment applied;

θ = rotation angle;

y = horizontal displacement;

z = vertical displacement;

h = height of application of horizontal loading;

d = initial depth of the model footing.

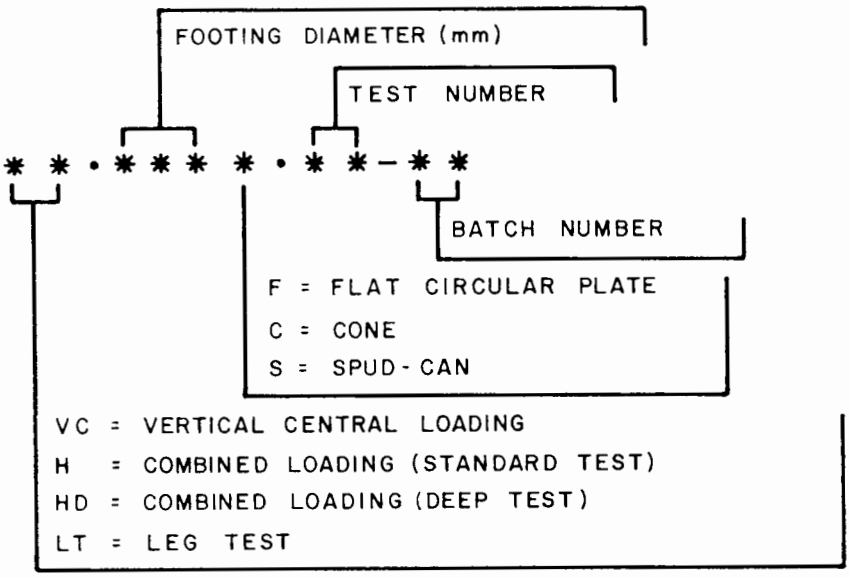

Figure 6.2 Numbering system used to identify the main features of each test

6.2 Vertical Central Loading Tests

Table 6.1 shows the characteristics of each of the 12 tests performed, excluding test VC.100F.02-01 which was lost. Figure 5.3, in Chapter 5, illustrates the lay-out of this programme.

Figure 6.3 shows the results of two tests on flat circular footings 50 mm and 100 mm in diameter. The curves are very close to each other, suggesting no significant scale effect, and exhibit the same pattern of behaviour. No definite bearing capacity can be inferred from these tests since the upper branches of the curves indicate a plastic stiffness, reflecting the increasing strength of the clay with depth and possibly, to some extent, the influence of the embedment of the footing on the failure load.

Table 6.1 Vertical central loading tests

test	footing	D (mm)	s_u (kPa)
VC.100F.01-01	circular plate	100	10.7
VC.50F.03-01	circular plate	50	10.8
VC.50C.04-01	150^o cone	50	10.8
VC.50C.05-01	120^o cone	50	10.8
VC.50C.06-01	90^o cone	50	10.8
VC.50C.07-01	60^o cone	50	10.8
VC.100S.08-01	130^o spud-can	100	8.5
VC.100S.09-01	120^o spud-can	100	8.8
VC.50S.10-01	130^o spud-can	50	9.7
VC.50S.11-01	130^o spud-can	50	9.7
VC.50S.12-01	120^o spud-can	50	9.7
VC.50S.13-01	120^o spud-can	50	9.7

Notes

(1) test VC.100F.02-01 was lost
(2) D = diameter of the model footing
(3) s_u = index strength of the clay sample

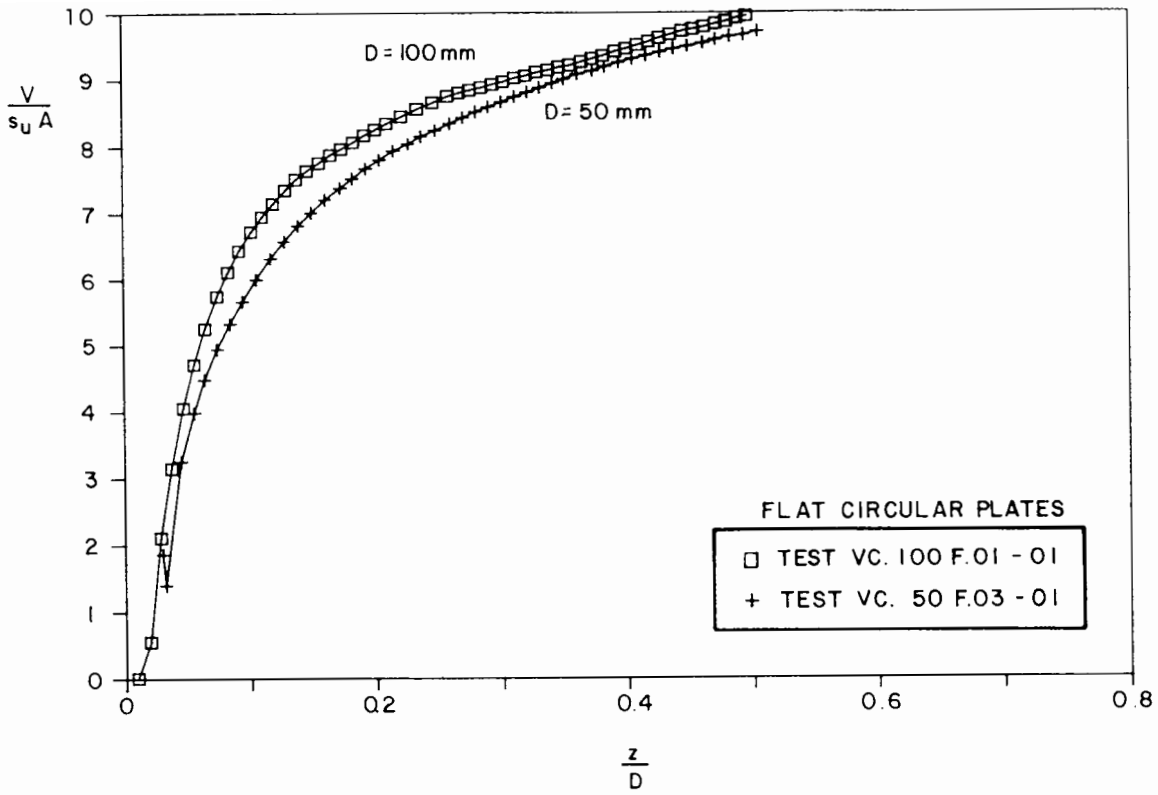

Figure 6.3 Dimensionless load versus displacement curves for flat circular plates

Figure 6.4 shows the variation of the derivative of the load with respect to the displacement, $\Delta(V/s_u A)/\Delta(z/D)$, with the displacement, z/D, for the two tests mentioned above. The curves therefore represent the variation of the tangent stiffness with the displacement. The agreement between the curves is good and they lead to a constant dimensionless plastic stiffness of the order of 3.

During test VC.100F.01-01 the ground heave was measured at three positions: approximately 1.0D, 1.2D and 1.5D distance from the edge of the model footing, in the radial direction, and the results are presented in Figure 6.5. It can be noticed that the ground heave is almost negligible at a distance of more than 1.0D and is less than 1 % of the footing displacement at a distance of 1.5D. This result confirms that tests on 100 mm diameter

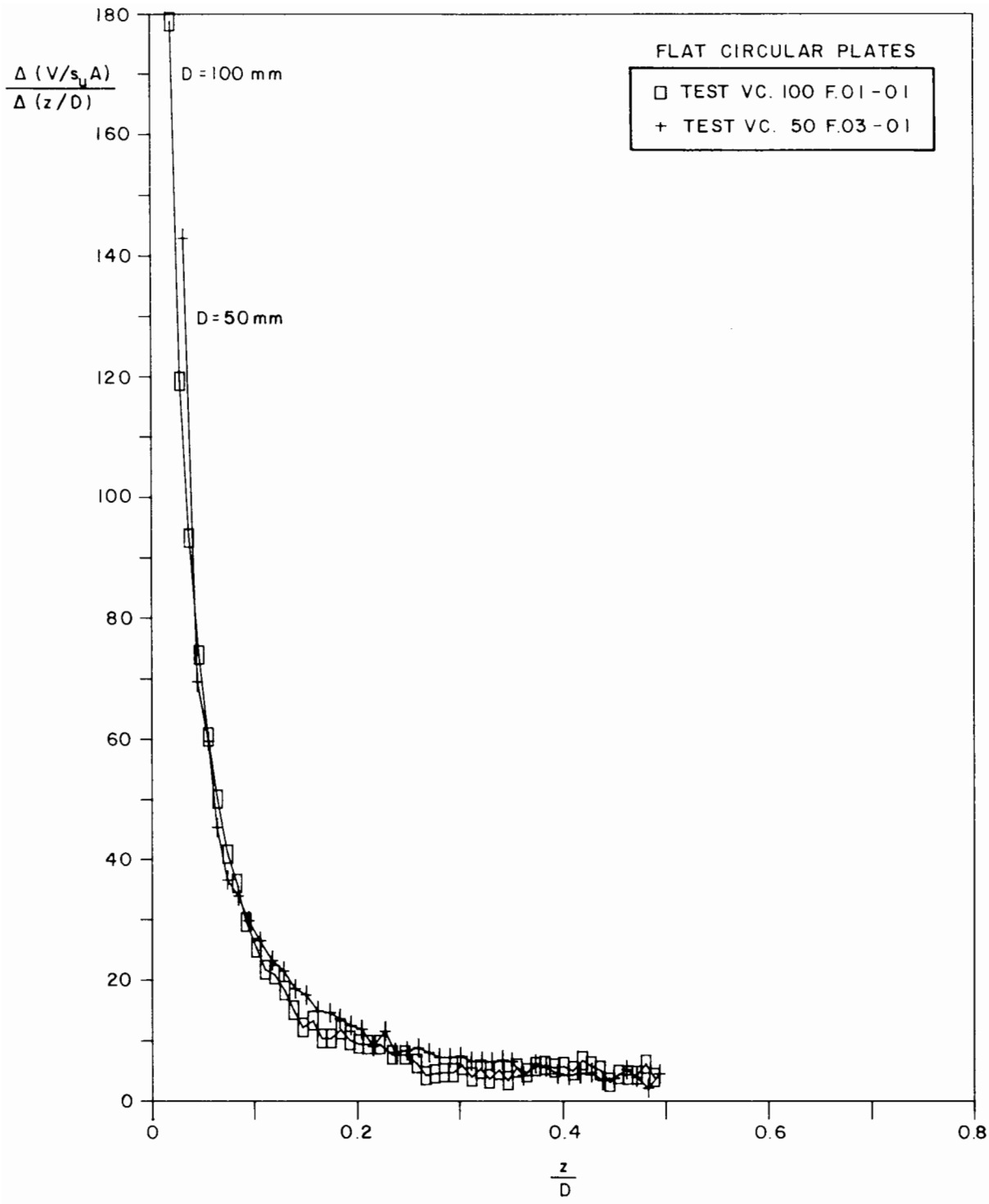

Figure 6.4 Dimensionless derivative of the load versus displacement curves for flat circular plates

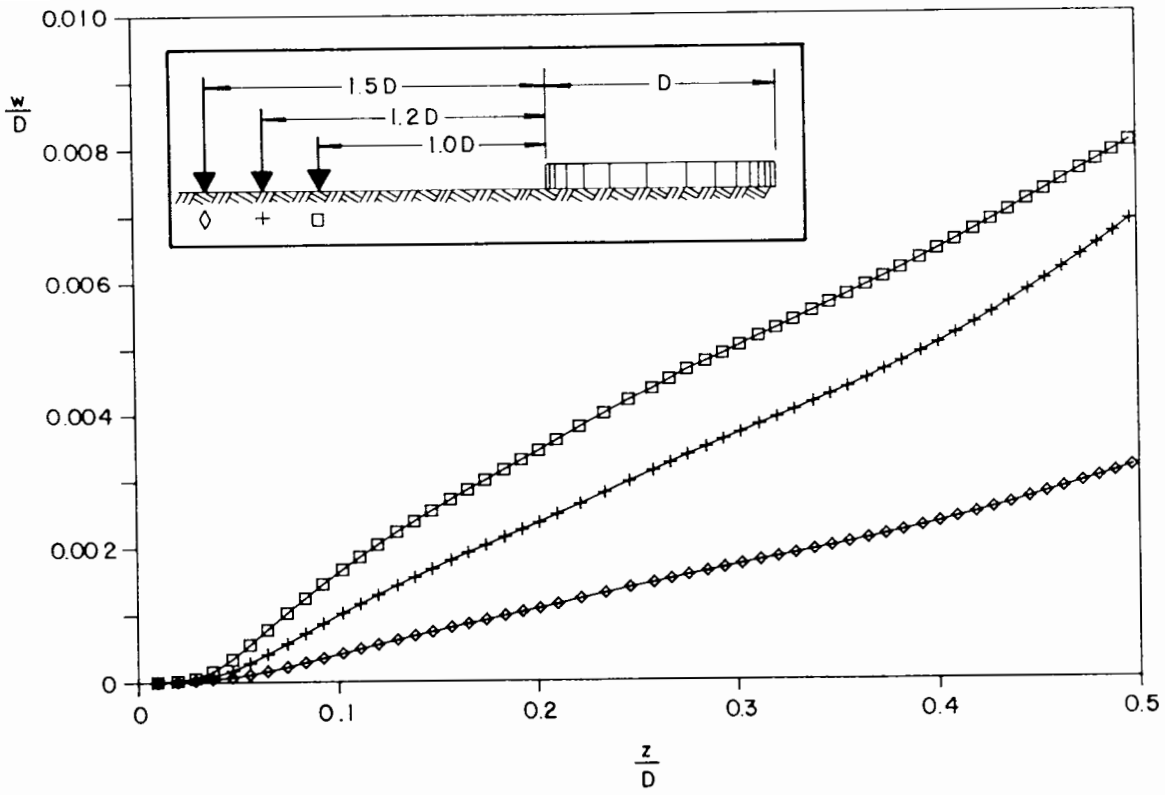

Figure 6.5 Dimensionless ground heave versus footing displacement curves for test VC.100F.01-01

models can be carried out satisfactorily in the 450 mm diameter tank.

Figure 6.6 shows the results of five tests carried out on 50 mm diameter model footings: a flat circular plate, 150^{o} cone, 120^{o} cone, 90^{o} cone and 60^{o} cone. The vertical displacements were measured from the moment the tip of the cones touched the clay surface. The "S" shape of the curves for the cones reflects the increase in the bearing area until the maximum value was reached, at which stage the cone shoulder just touched the clay surface. This pattern can be predicted purely from dimensional analysis and must be accordingly a branch of a parabola. The corresponding derivative curves presented in Figure 6.7 confirm this pattern as the initial part of each curve is approximately a straight line. Although theoretically all the lines for the cones should pass through the origin, it can be observed that some

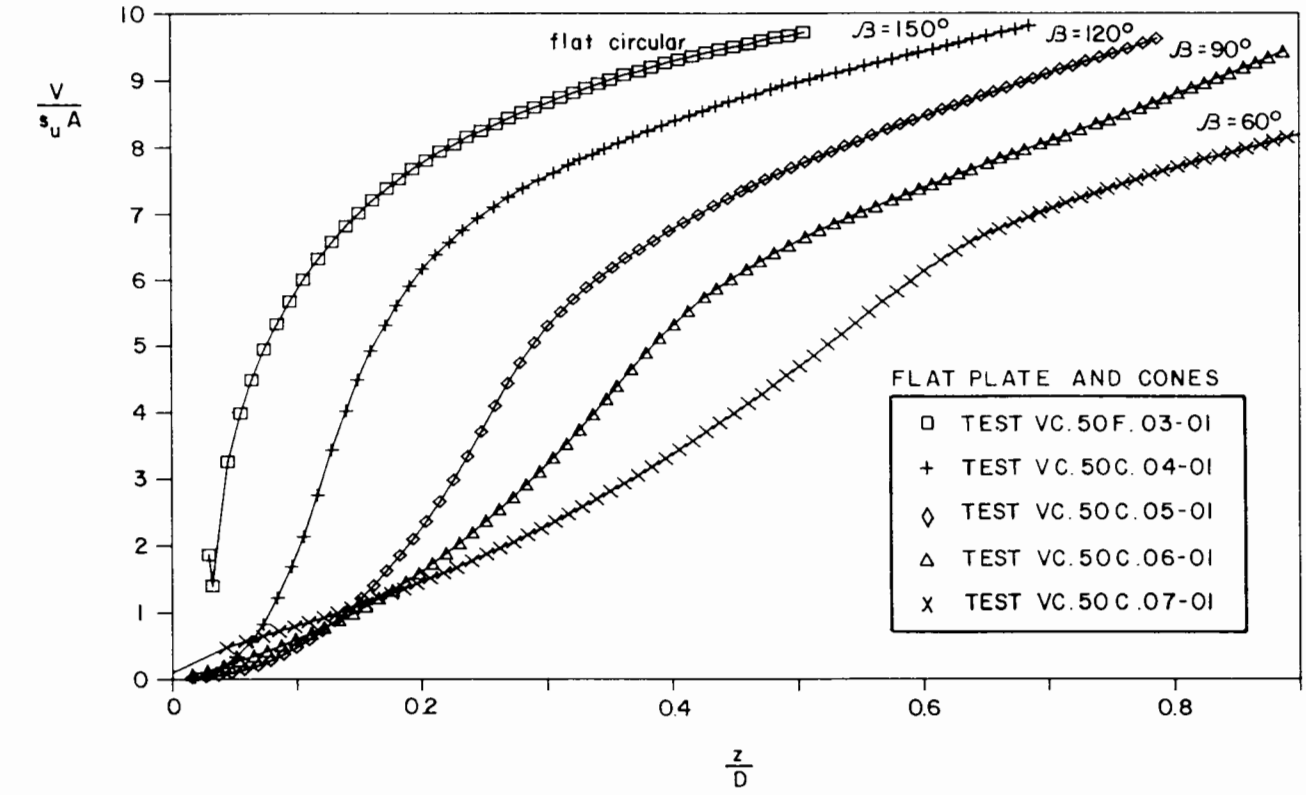

Figure 6.6 Dimensionless load versus displacement curves for a flat circular plate and various cones

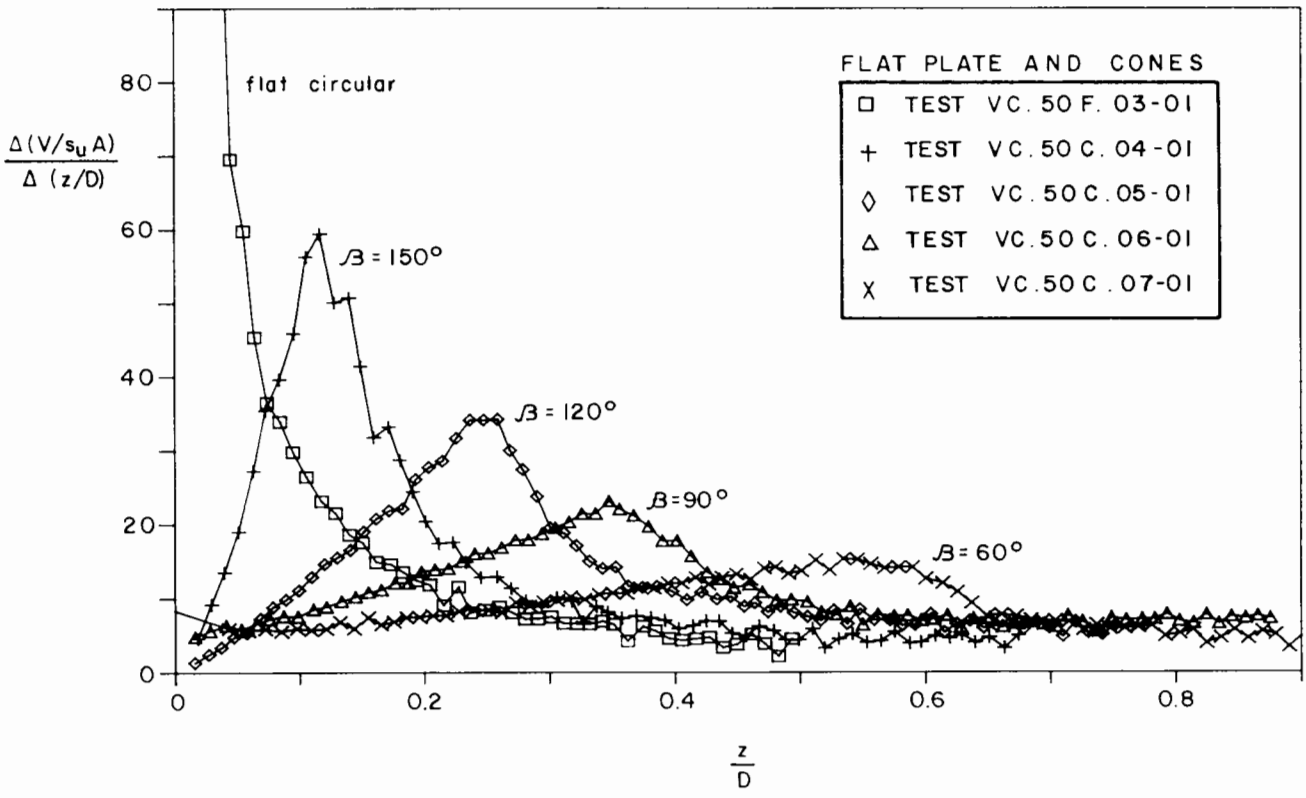

Figure 6.7 Dimensionless derivative of the load versus displacement curves for a flat circular plate and various cones

of them exhibit an intercept. This indicates an inaccuracy in the initial position of the footing owing to the physical difficulty in setting up small size footings. The displacements corresponding to the points where the cone shoulders touch the clay can be easily derived from the curves and are obviously represented by their maxima. From the geometry of the cones these displacements would be 0.87D for 60^{o} cone, 0.5D for 90^{o} cone, 0.29D for 120^{o} cone and 0.13D for 150^{o} cone, if no ground heave occurred. The difference between these values and those experimentally observed is therefore accounted for by the average ground heave around the footing, which is 0.34D, 0.15D, 0.03D and 0.01D for 60^{o} cone, 90^{o} cone, 120^{o} cone and 150^{o} cone respectively. This result is very consistent since the larger the volume of clay displaced, the higher the ground heave induced.

The dimensionless plastic stiffness in these cases varies from 3 to 7.

Figures 6.8 and 6.9 show the load versus displacement curves for 120^{o} spud-can and 130^{o} spud-can models respectively. Results of tests on two 50 mm and one 100 mm diameter models are included in each figure. The "S" shape in this case is noticeably much sharper than in the case of cones and this is due to the geometrical design of these footings. For each type of spud-can the curves are satisfactorily consistent among themselves, confirming once again no significant scale effect. The derivative curves, represented in Figures 6.10 and 6.11, show again inaccuracies in initial positioning of the footings. In each curve the double cone of the spud-can is reflected by two straight lines in the section corresponding to the increasing slope. For the 120^{o} spud-can the first straight line is longer than for 130^{o} spud-can, corresponding to a longer tip section. Spud-can models exhibited dimensionless plastic stiffness varying from 4 to 8.

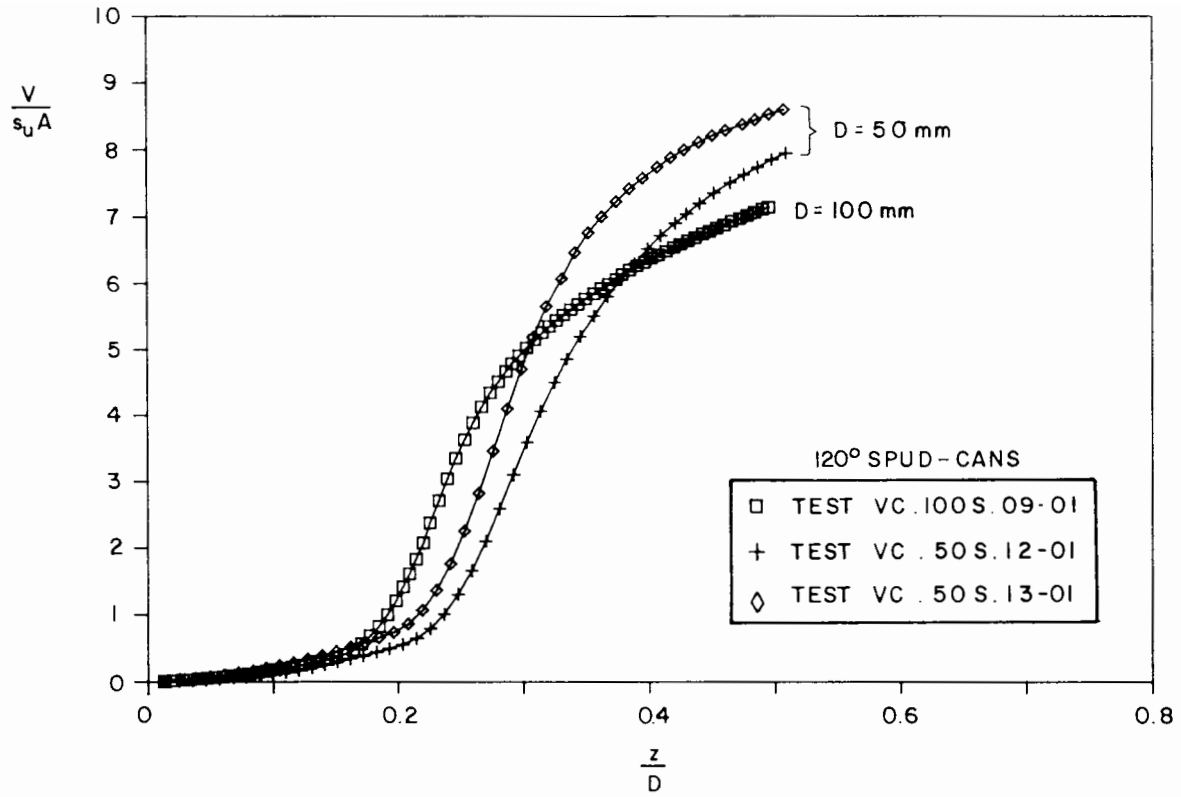

Figure 6.8 Dimensionless load versus displacement curves for 120° spud-cans

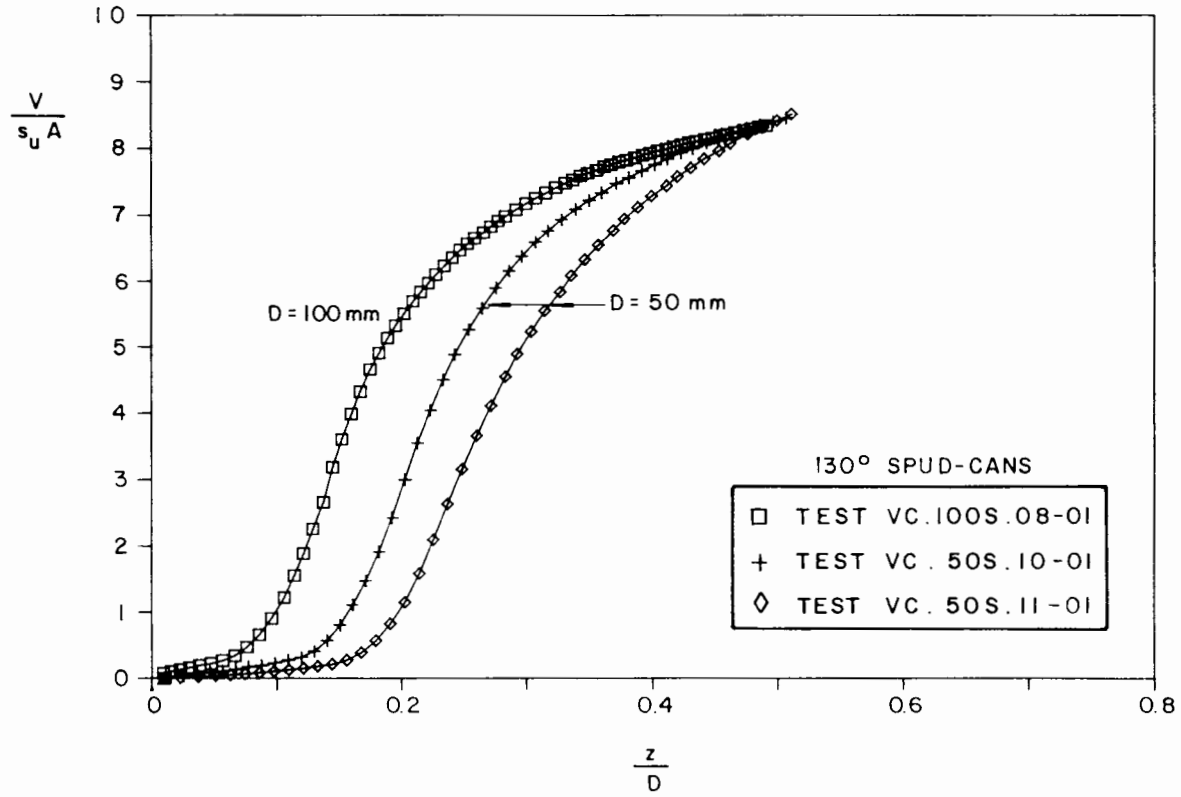

Figure 6.9 Dimensionless load versus displacement curves for 130° spud-cans

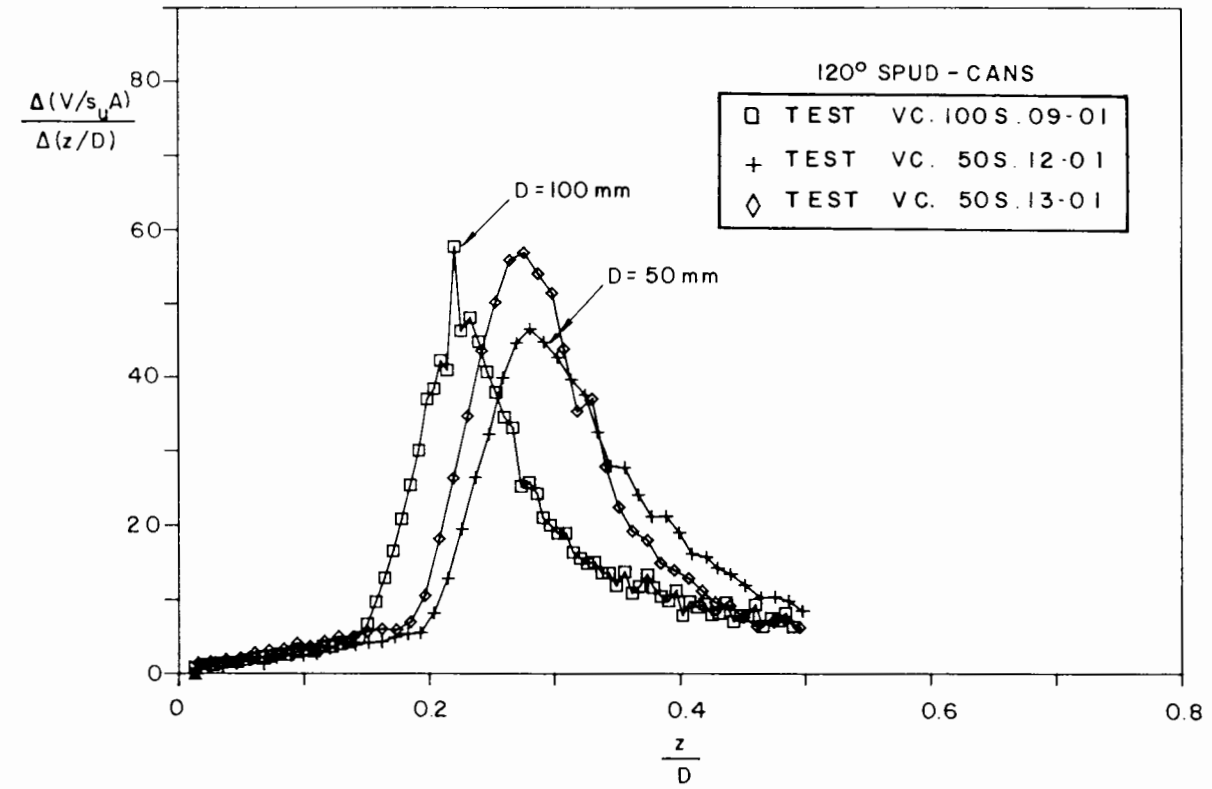

Figure 6.10 Dimensionless derivative of the load versus displacement curves for 120° spud-cans

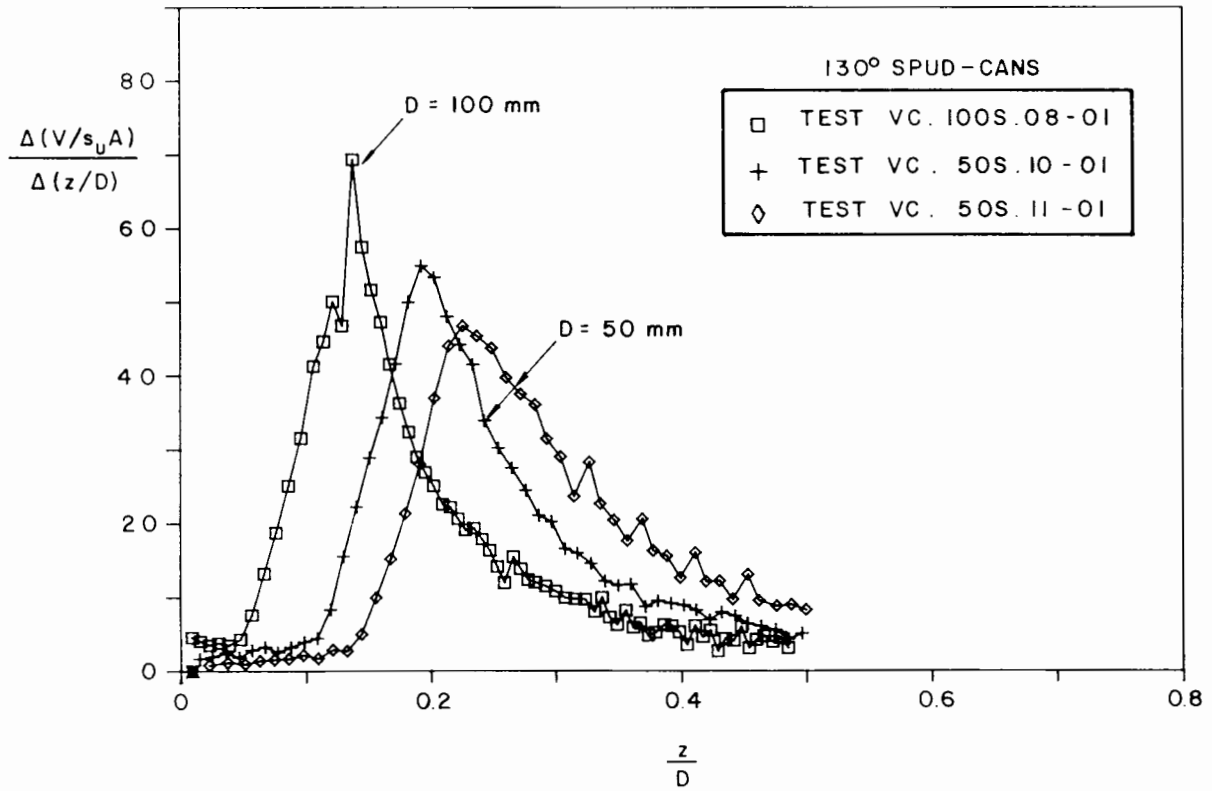

Figure 6.11 Dimensionless derivative of the load versus displacement curves for 130° spud-cans

6.3 Main Series of Combined Loading Tests

The fixed quantities for the main series of combined loading tests are presented in Table 6.2. In this table V_{max} represents the maximum load observed during the driving operation to set the footing at its initial position (see Section 5.2.2 (a)), this load being immediately removed after that. The fixed vertical load V is later applied immediately before the beginning of the test.

The tests are grouped by the type of footing, each group comprises four tests and each test involves a particular combination of a height of application of horizontal loading, either 0.5D or 1.5D, and a fixed vertical load, either a low value ($1.7s_uA$ to $2.3s_uA$) or a high value ($4.0s_uA$ to $5.4s_uA$), as displayed in Tables 6.3 and 6.4.

An exception is the first test in this series (test H.100F.14-02) which was carried out with h/D = 1.0. The results of this test were not included in the analysis.

Some of the tests in the main series were intentionally repeated to check repeatability. Those considered of best quality, whenever such judgment could be unmistakably made, were chosen for further analysis of groups of tests. Repeated tests are further presented in Section 6.3.2.

6.3.1 A Representative Group of Tests

(a) Flat Circular Plate

Figures 6.12 and 6.13 show the moment versus rotation curves for a flat

circular footing with h/D = 0.5 and different vertical loads. As in vertical central loading tests, there is no definite failure value observed, both tests exhibiting an initial stiff behaviour, gradually decreasing up to

Table 6.2 Main series of combined loading tests

test	footing	s_u (kPa)	V (N)	h (mm)	V_{max} (N)
H.100F.14-02	circular plate	9.3	133.3	101.0	0
H.100F.15-02	circular plate	8.5	133.1	51.0	0
H.100F.16-02	circular plate	9.7	133.2	151.0	0
H.100F.18-02	circular plate	10.5	329.1	151.0	0
H.100C.20-03	120° cone	9.2	135.3	151.6	270.1
H.100C.21-03	120° cone	9.3	135.4	51.6	360.4
H.100C.22-03	120° cone	9.3	332.0	151.6	315.4
H.100C.23-03	120° cone	9.1	330.6	51.6	340.3
H.100C.24-03	60° cone	8.3	335.0	151.4	328.5
H.100C.25-03	60° cone	8.7	334.8	51.4	337.8
H.100C.26-04	60° cone	8.6	139.8	151.4	299.9
H.100C.27-04	60° cone	7.6	139.5	51.4	355.5
H.100S.28-04	130° spud-can	8.4	134.2	151.5	247.8
H.100S.29-04	130° spud-can	8.3	134.3	51.5	346.2
H.100S.30-04	130° spud-can	8.9	329.6	151.5	362.4
H.100S.31-04	130° spud-can	7.7	329.5	51.5	279.1
H.100S.32-05	130° spud-can	8.3	134.2	51.5	242.8
H.100F.33-05	circular plate	9.0	329.0	51.5	0
H.100S.49-07	130° spud-can	8.0	329.9	151.0	231.3
H.100C.50-08	60° cone	9.8	139.1	150.7	418.3
H.100C.51-08	60° cone	9.0	138.9	50.7	478.1
H.100C.52-08	120° cone	9.7	135.0	150.8	412.3
H.100C.53-08	120° cone	7.6	134.8	50.8	322.3

Notes

(1) tests H.100F.17-02 and H.100F.19-02 were lost
(2) s_u = index shear strength of the clay sample
(3) V = fixed vertical load
(4) h = height of application of horizontal load
(5) V_{max} = maximum vertical load applied to the model footing before testing

Table 6.3 Representative group of combined loading tests

		low V/s_uA	high V/s_uA
circular plate	h/D = 0.5 h/D = 1.5	H.100F.15-02 H.100F.16-02	H.100F.33-05 H.100F.18-02
120^o cone	h/D = 0.5 h/D = 1.5	H.100C.53-08 H.100C.52-08	H.100C.23-03 H.100C.22-03
60^o cone	h/D = 0.5 h/D = 1.5	H.100C.51-08 H.100C.50-08	H.100C.25-03 H.100C.24-03
130^o spud-can	h/D = 0.5 h/D = 1.5	H.100S.29-04 H.100S.28-04	H.100S.31-04 H.100S.49-07

Table 6.4 Repeated group of combined loading tests

		low V/s_uA	high V/s_uA
circular plate	h/D = 0.5 h/D = 1.5		
120^o cone	h/D = 0.5 h/D = 1.5	H.100C.21-03 H.100C.20-03	
60^o cone	h/D = 0.5 h/D = 1.5	H.100C.27-04 H.100C.26-04	
130^o spud-can	h/D = 0.5 h/D = 1.5	H.100S.32-05	H.100S.30-04

a more or less constant plastic stiffness. Test H.100F.33-05, with higher vertical load, shows a stiffer response on unloading and reloading than test H.100F.15-02 and this may be evidence of partial separation between the footing surface and the clay sample in the more lightly loaded test. The anomalous shape of the end of the first loop in test H.100F.15-02 (point A) is an artefact due to interference with the equipment. Comparing the test results there is no marked difference in stiffness in the initial section of the curves due to different values of V/s_uA. Test H.100F.33-05, however, was able to develop higher values of moment after the first cycle.

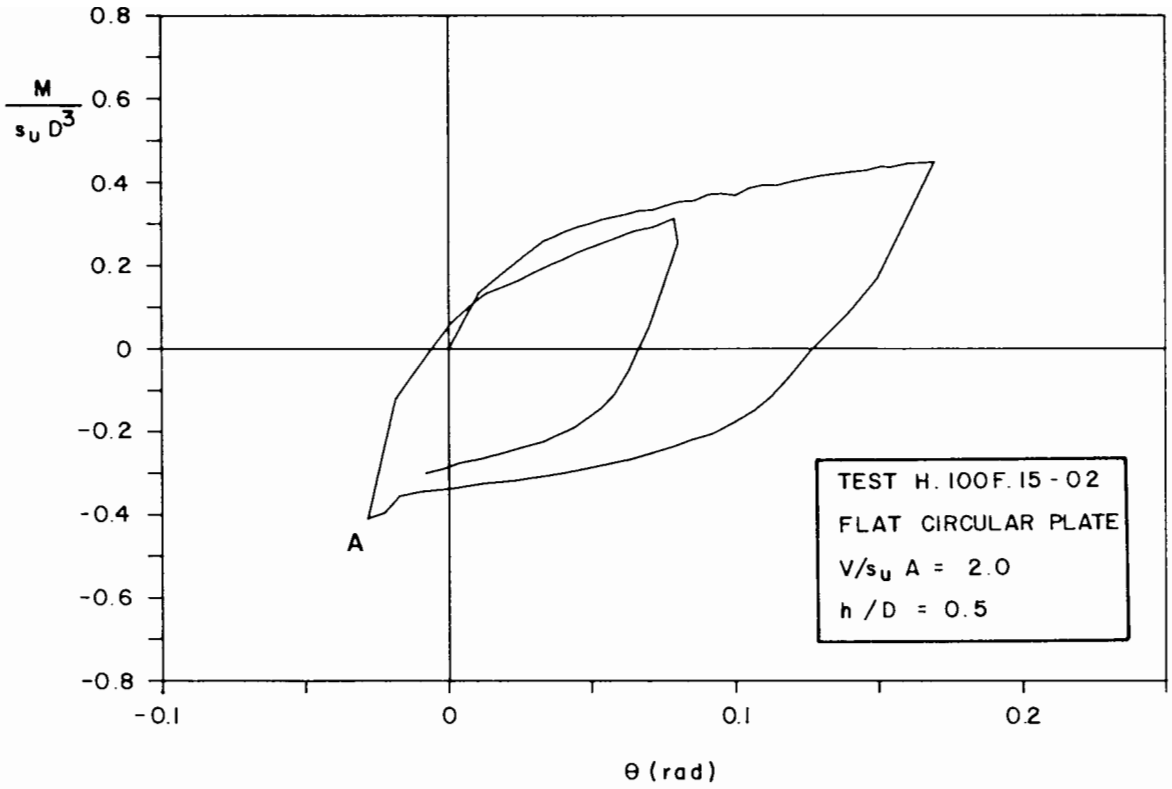

Figure 6.12 Dimensionless moment versus rotation curve for a flat circular footing (h/D = 0.5, low vertical load)

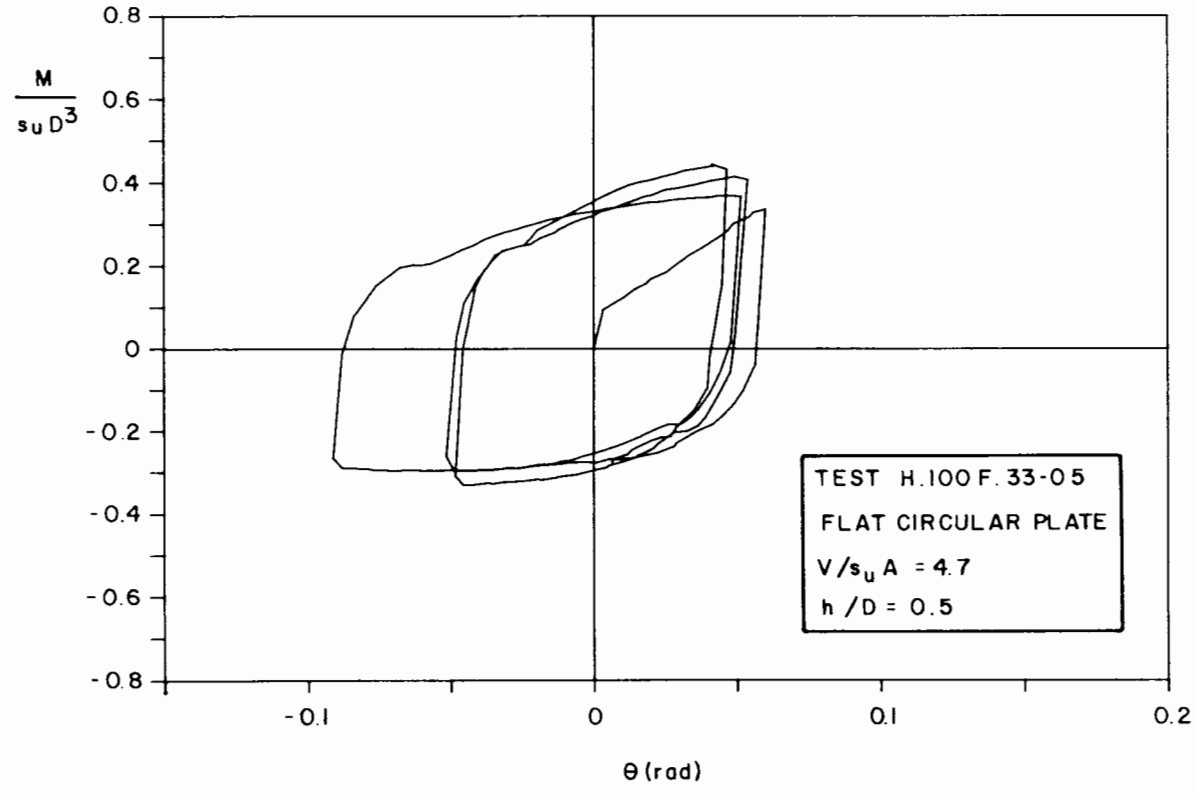

Figure 6.13 Dimensionless moment versus rotation curve for a flat circular footing (h/D = 0.5, high vertical load)

Figures 6.14 and 6.15 present results of equivalent tests performed with h/D = 1.5. In test H.100F.16-02 the horizontal loading was only applied monotonically without being reversed.

In general, the parameters h/d and V/s_uA do not seem to have markedly influenced the rotational behaviour of the flat circular footing as far as small rotations are concerned. The plastic stiffness seems to be more noticeably affected by vertical load.

Figure 6.16 represents the displacement path of the centre of the footing during the tests. It can be noticed that the total horizontal displacement in one cycle is about the same for tests with the same value of h/D either for high or low value of V/s_uA. The smaller amplitude of horizontal displacement is observed in the tests at high h/D value, i.e. a lower horizontal load for a given moment. As it would be expected, high vertical load leads to larger vertical displacements.

(b) 120^o Cone

The rotational behaviour of the 120^o cone is represented in Figures 6.17, 6.18, 6.19 and 6.20. The curves corresponding to low vertical load (tests H.100C.52-08 and H.100C.53-08), are very similar for both h/D of 0.5 and 1.5. The first loading branches in these cases are situated above all the other upper sections, exhibiting a stiffer response. The patterns of the remaining branches are very alike, showing an elongated shape. One cycle was intentionally performed with a reduced amplitude to check how this would affect the shape of the loop and, as can be observed, it featured steeper slopes for the upper and lower branches than those of higher amplitude cycles. Curves for high vertical load (tests H.100C.22-03 and H.100C.23-03),

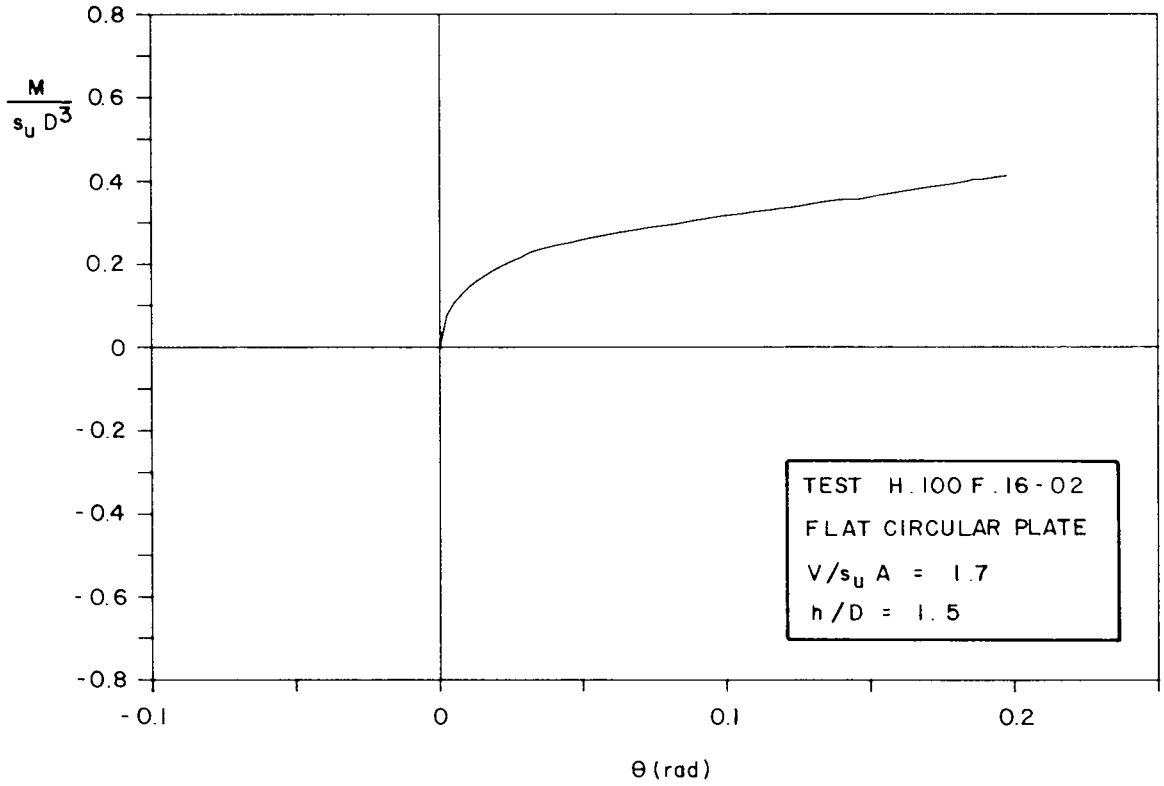

Figure 6.14 Dimensionless moment versus rotation curve for a flat circular plate (h/D = 1.5, low vertical load)

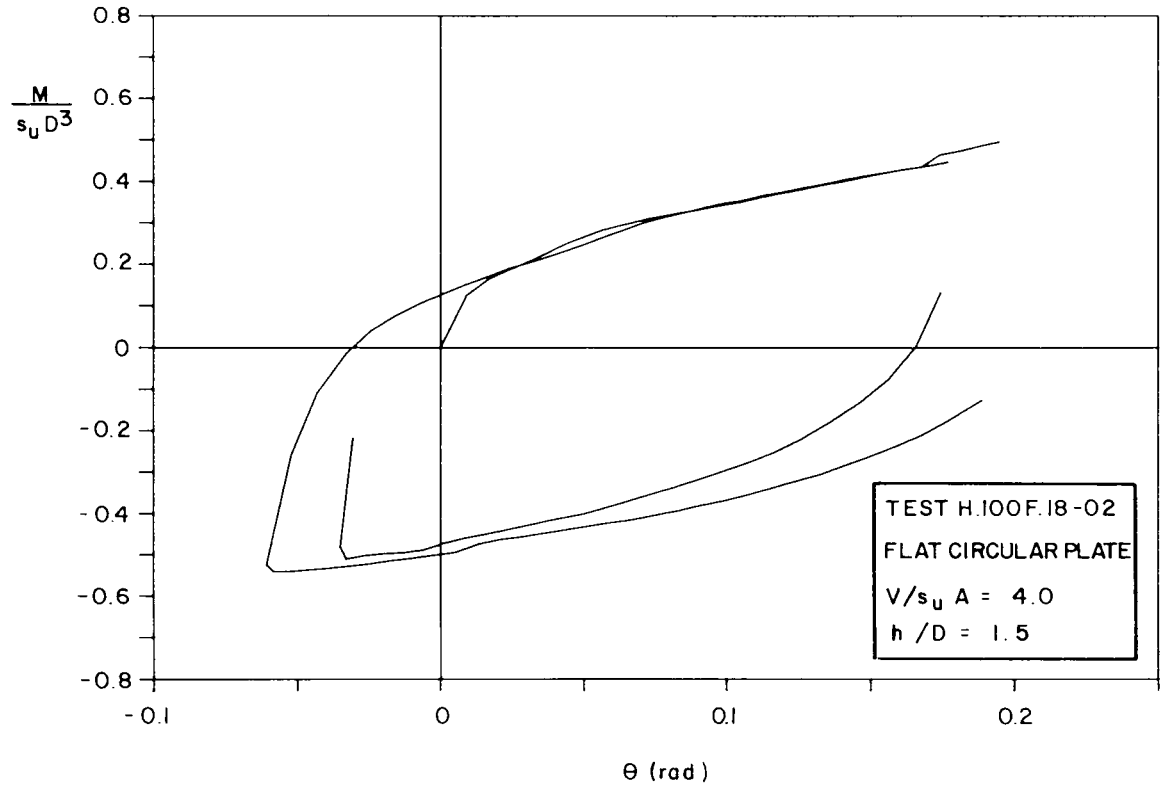

Figure 6.15 Dimensionless moment versus rotation curve for a flat circular plate (h/D = 1.5, high vertical load)

reveal a stiffer plastic behaviour than for low vertical load, although a less significant difference can be noticed in the initial parts of the four curves. The height of application of horizontal load seems to play no important role.

The horizontal displacement versus vertical displacement curves (referred to the centre of the footing) are plotted in Figure 6.21 and the behaviour observed is the one that would be expected in accordance with the corresponding magnitudes of horizontal and vertical loads.

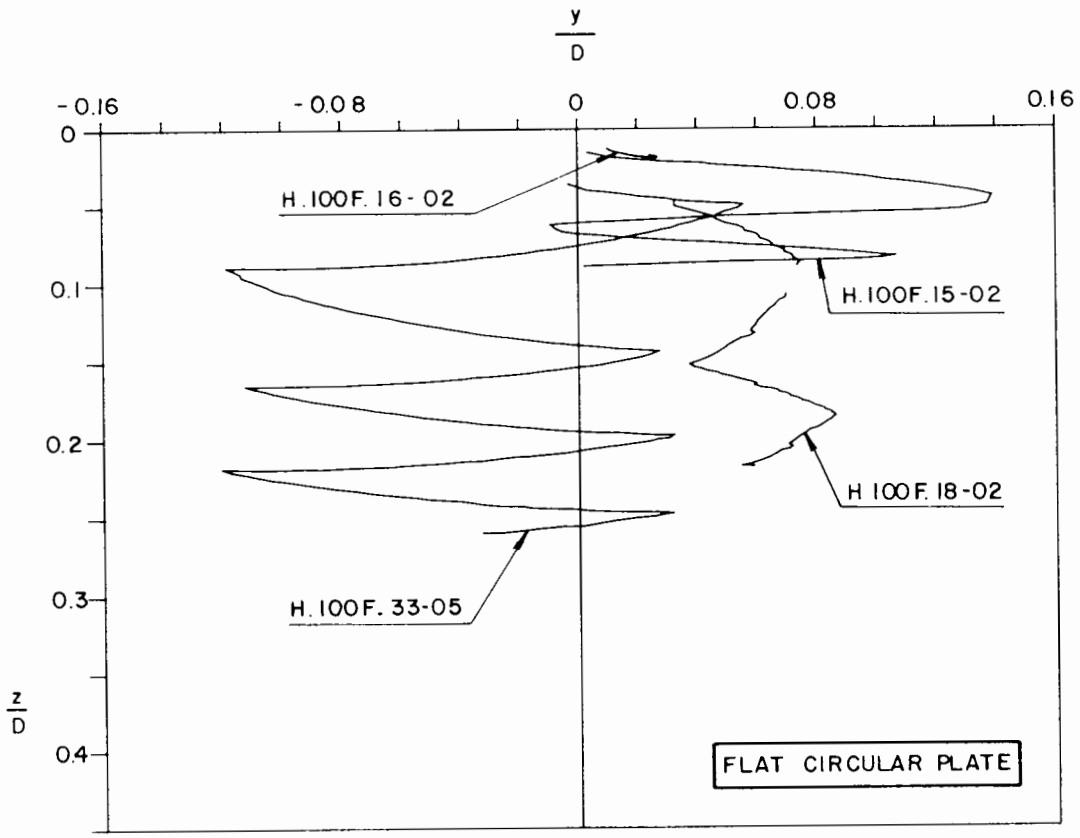

Figure 6.16 Displacement path of the centre of the flat circular plate during the tests

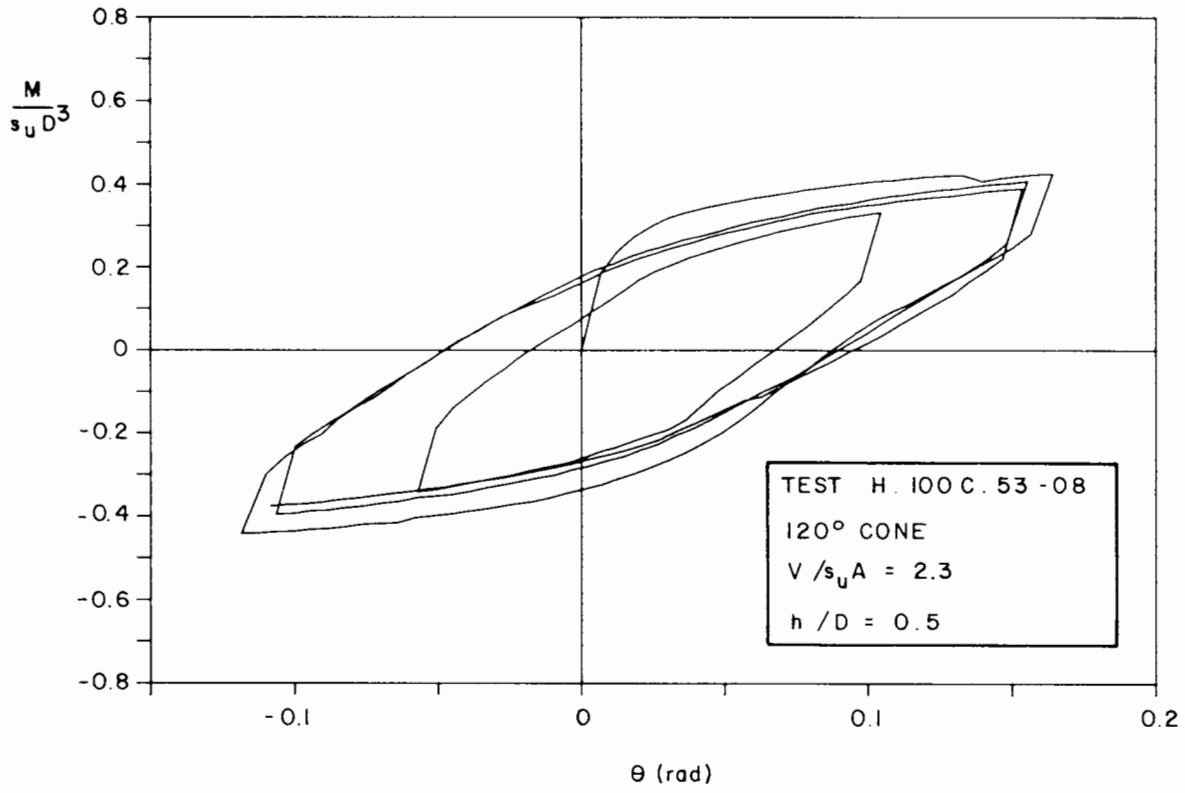

Figure 6.17 Dimensionless moment versus rotation curve for 120^{o} cone (h/D = 0.5, low vertical load)

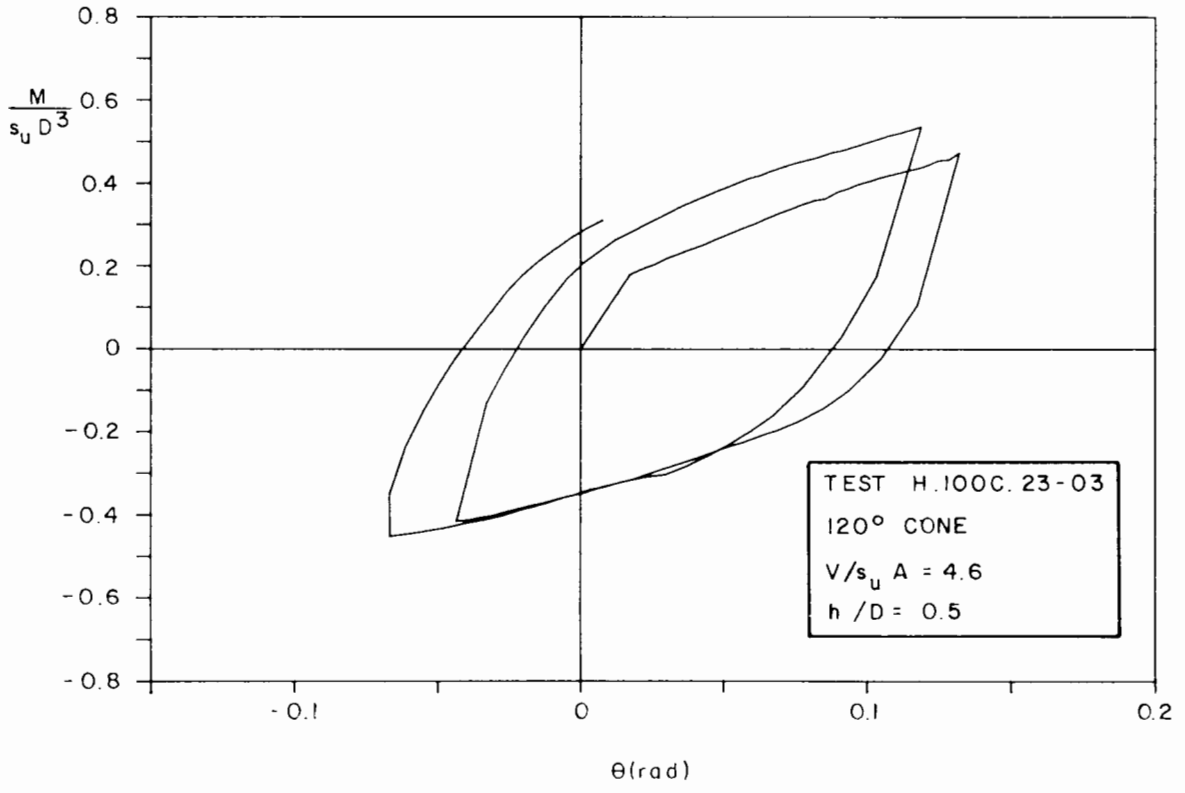

Figure 6.18 Dimensionless moment versus rotation curve for 120^{o} cone (h/D = 0.5, high vertical load)

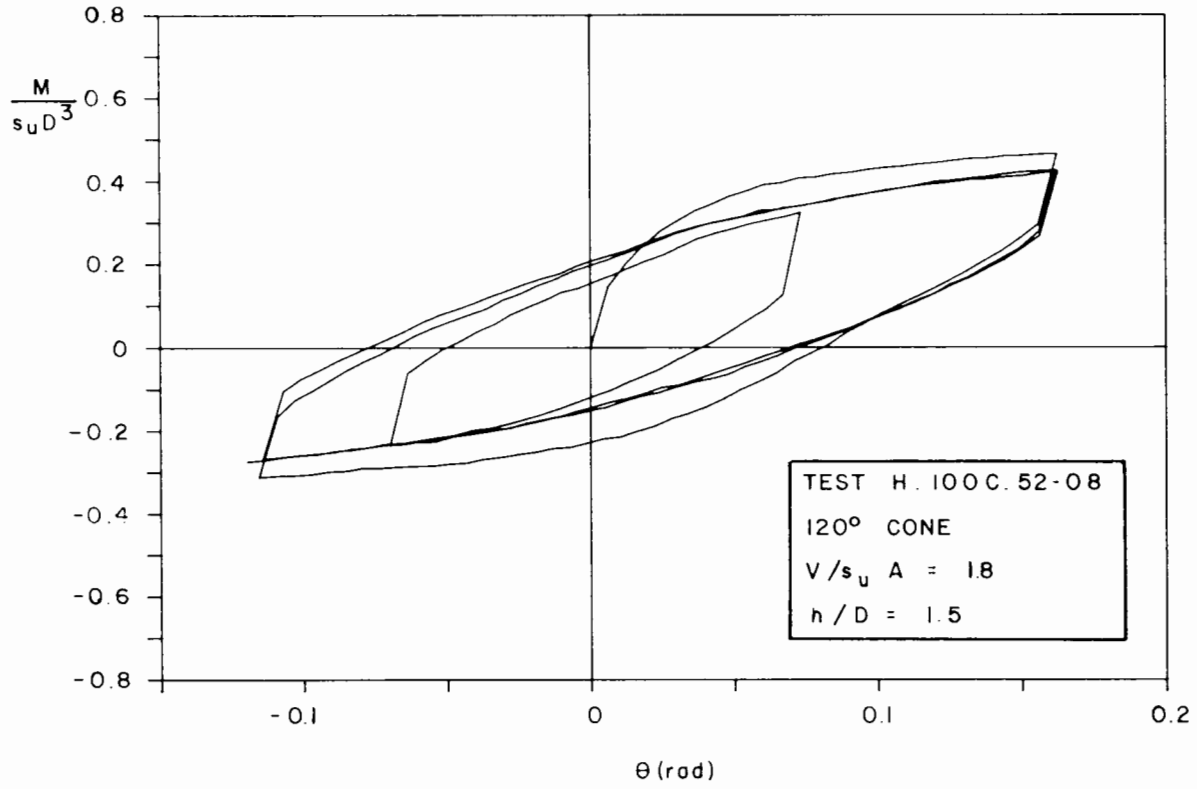

Figure 6.19 Dimensionless moment versus rotation curve for 120° cone (h/D = 1.5, low vertical load)

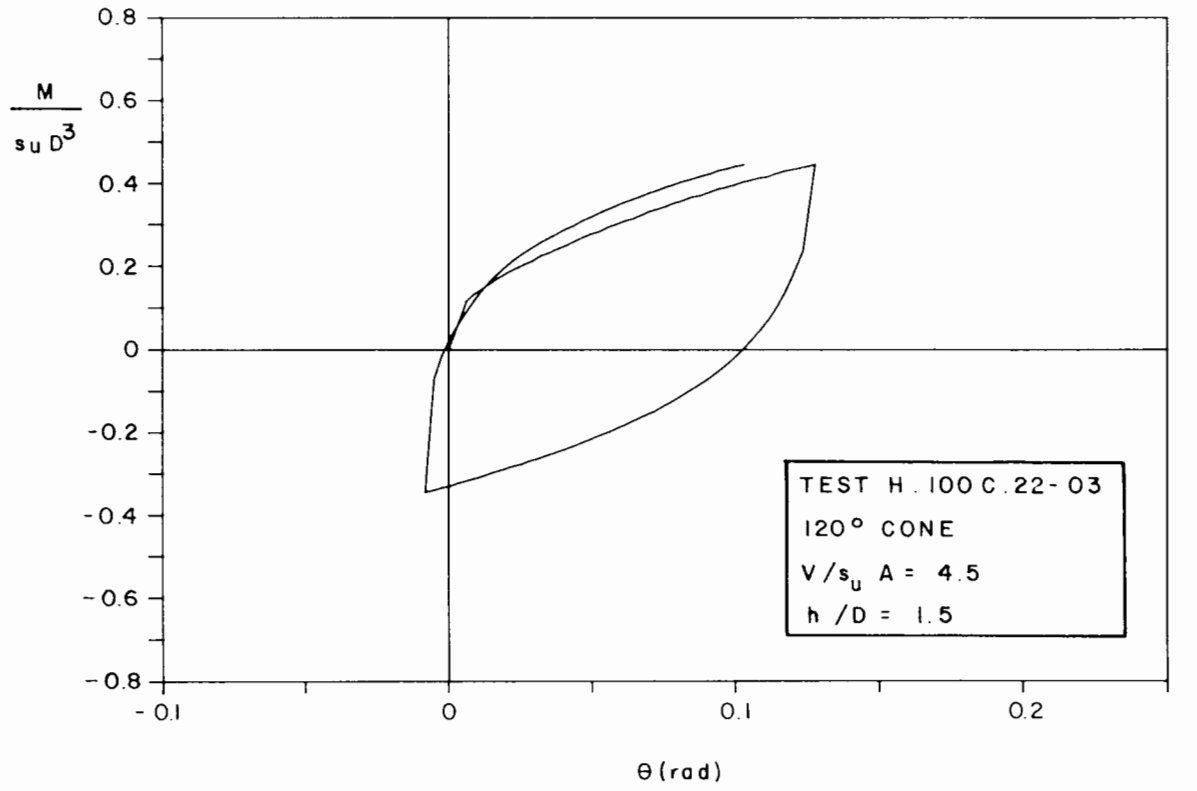

Figure 6.20 Dimensionless moment versus rotation curve for 120° cone (h/D = 1.5, high vertical load)

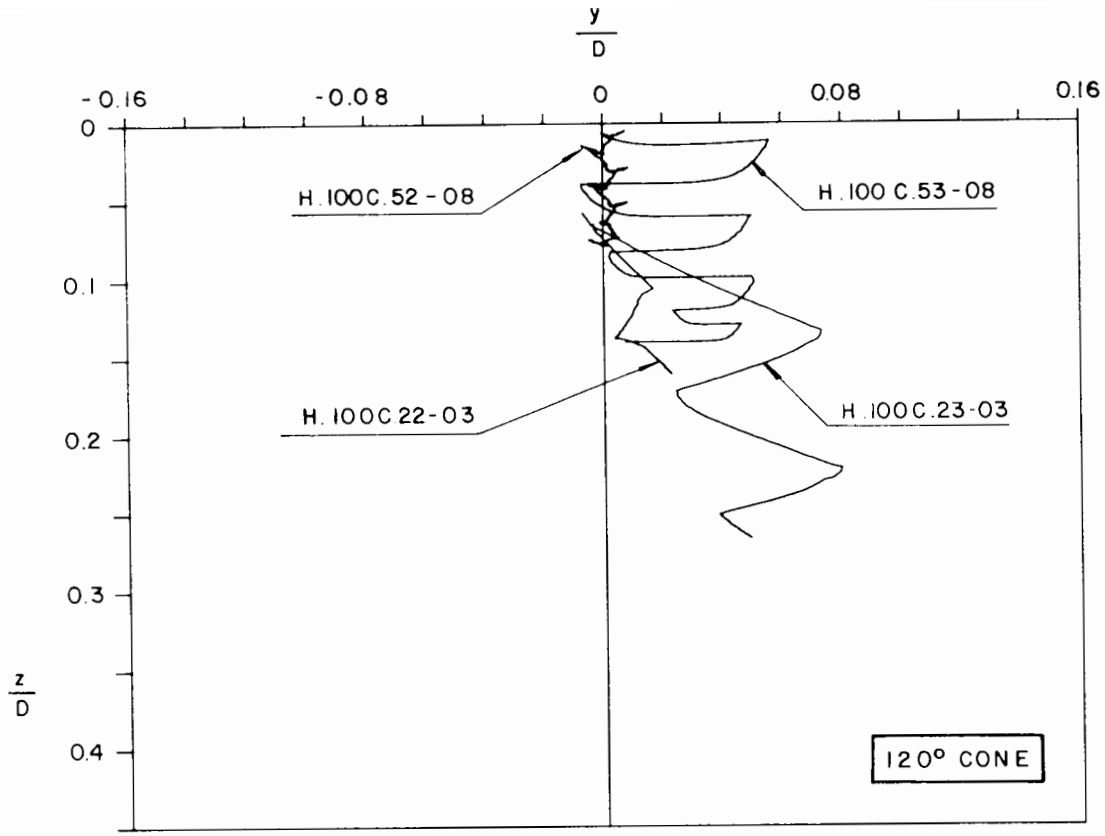

Figure 6.21 Displacement path of the centre of the 120° cone during the tests

(c) 60° Cone

Figures 6.22, 6.23, 6.24 and 6.25 illustrate the moment versus rotation curves for 60° cone. Almost all the features observed for 120° cone are also present in this case. Nevertheless, the shape of the loops corresponding to low vertical load (tests H.100C.50-08 and H.100C.51-08) is a little different, resembling a parallelogram and therefore featuring a more linear elastic behaviour followed also by almost linear plasticity.

The displacement path of the centre of the footing is presented in Figure 6.26. In this case the total horizontal displacement per cycle is about the same in any case, this fact probably being related to the greater embedment

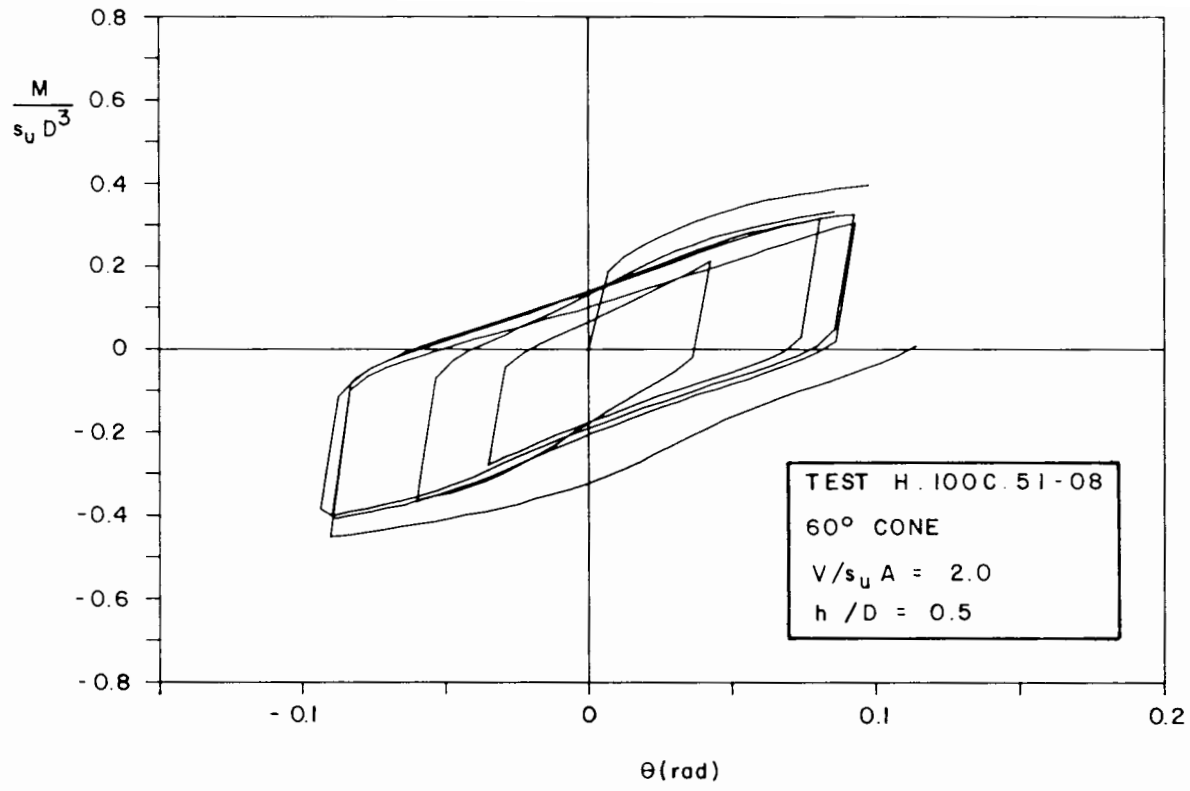

Figure 6.22 Dimensionless moment versus rotation curve for 60° cone (h/D = 0.5, low vertical load)

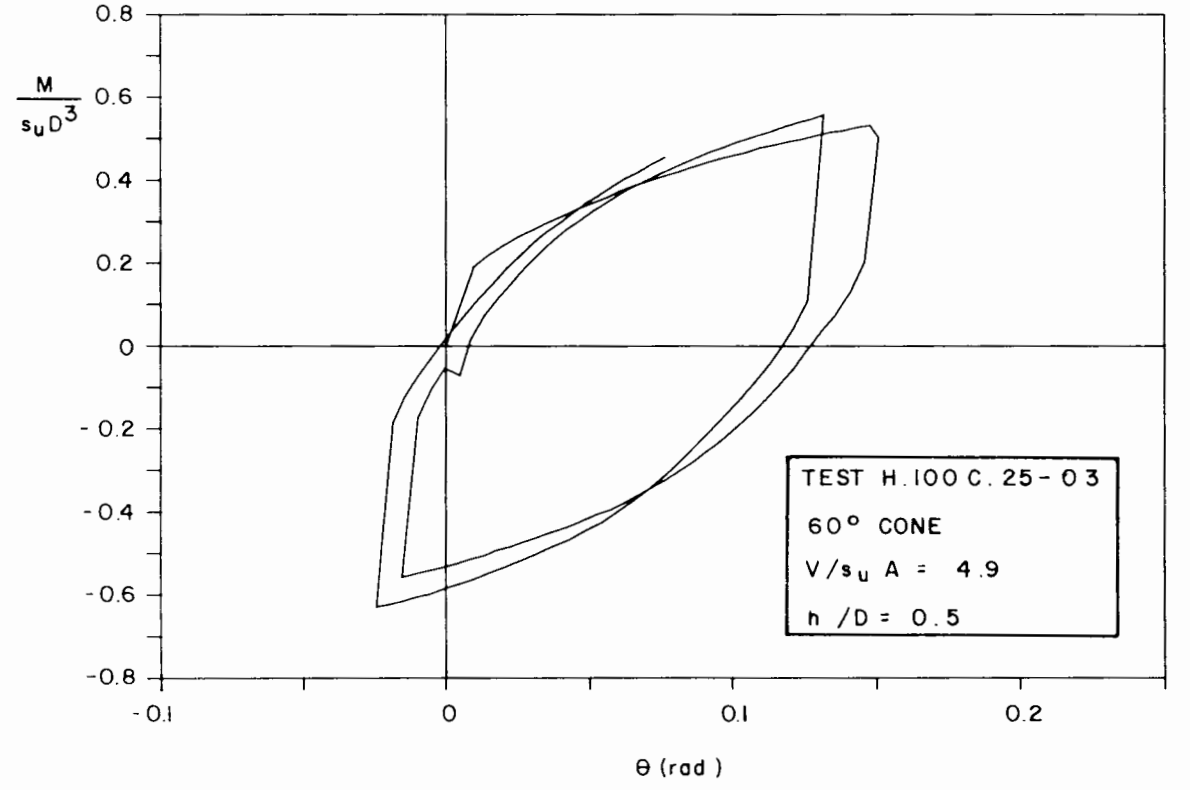

Figure 6.23 Dimensionless moment versus rotation curve for 60° cone (h/D = 0.5, high vertical load)

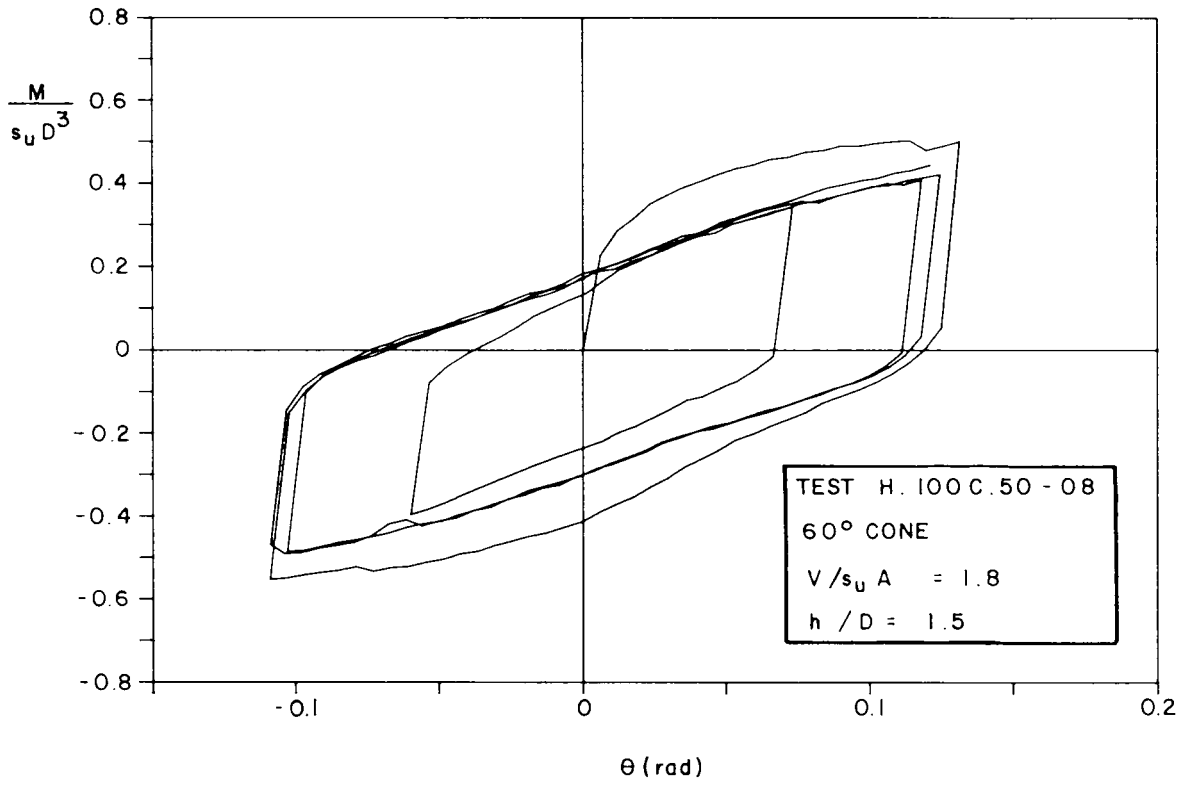

Figure 6.24 Dimensionless moment versus rotation curve for 60^{o} cone (h/D = 1.5, low vertical load)

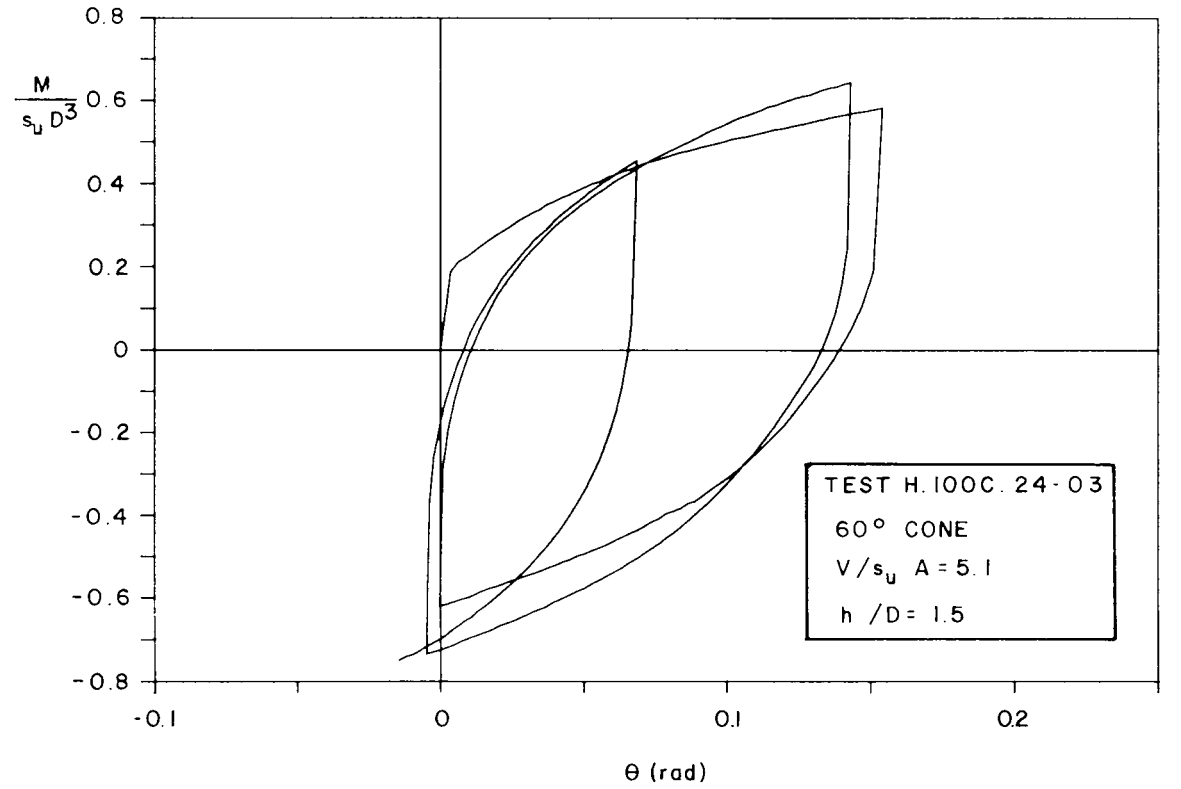

Figure 6.25 Dimensionless moment versus rotation curve for 60^{o} cone (h/D = 1.5, high vertical load)

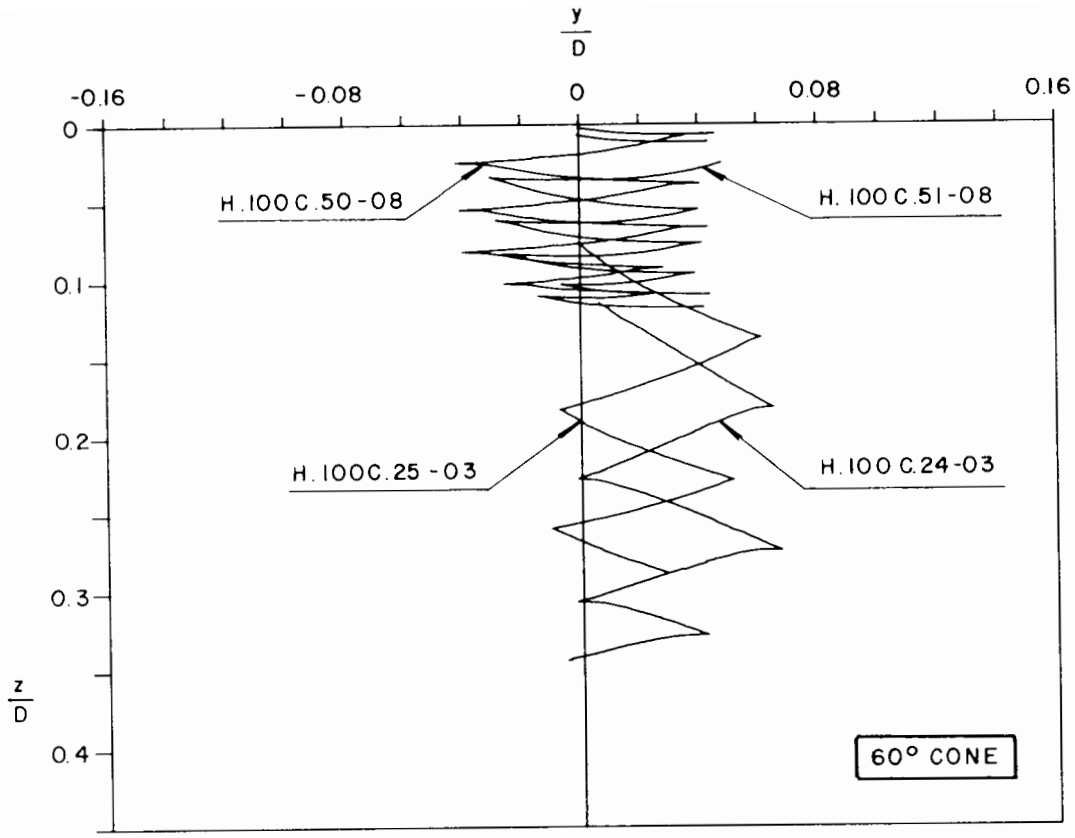

Figure 6.26 Displacement path of the centre of the 60^{o} cone during the tests

inherent in this kind of footing leading to a smaller movement of the position of the centre, irrespective of the horizontal load applied. The vertical displacements are consistent with the vertical loads.

(d) 130^{o} Spud-Can

Figures 6.27, 6.28, 6.29 and 6.30 present the moment versus rotation results for the 130^{o} spud-can model. No remarkable features can be identified from these curves, either for those of same h/D or those of approximately same $V/s_{u}A$. In test H.100S.49-07 a series of elastic unloading and reloading loops were performed intending to generate more data to define better the elastic rotational behaviour of this kind of footing.

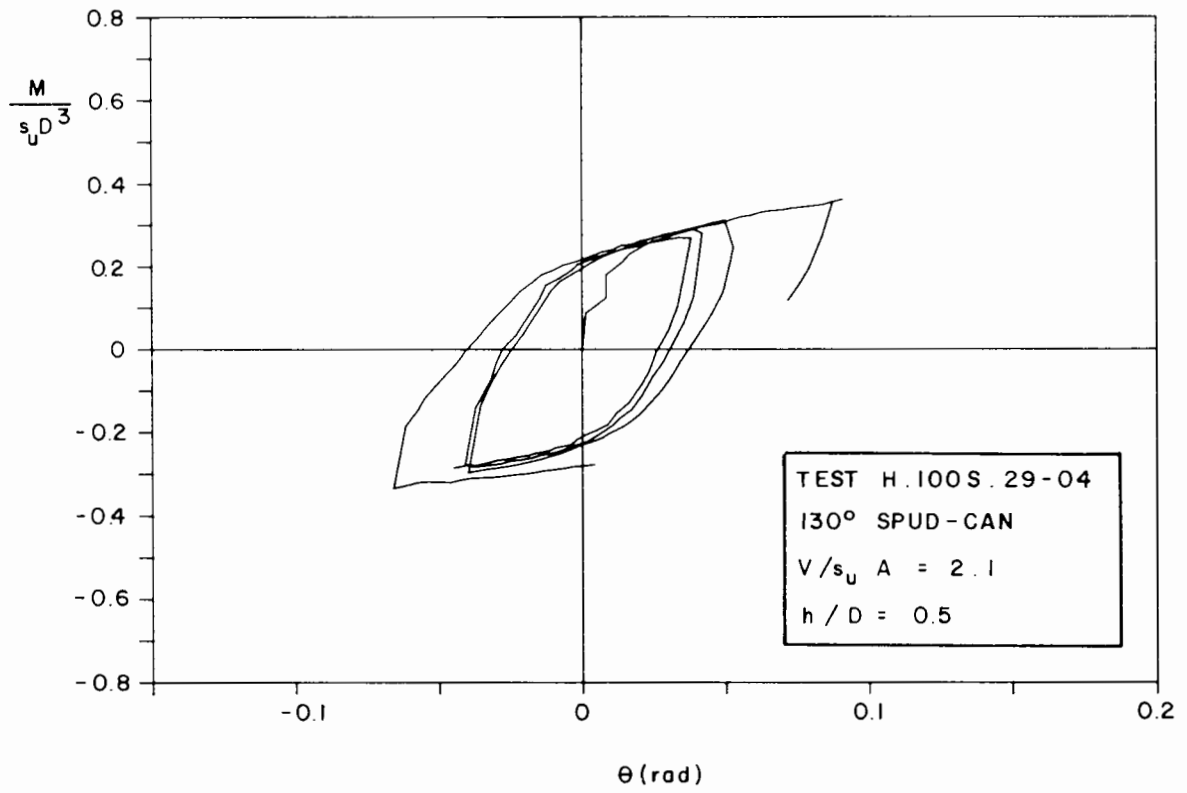

Figure 6.27 Dimensionless moment versus rotation curve for 130° spud-can (h/D = 0.5, low vertical load)

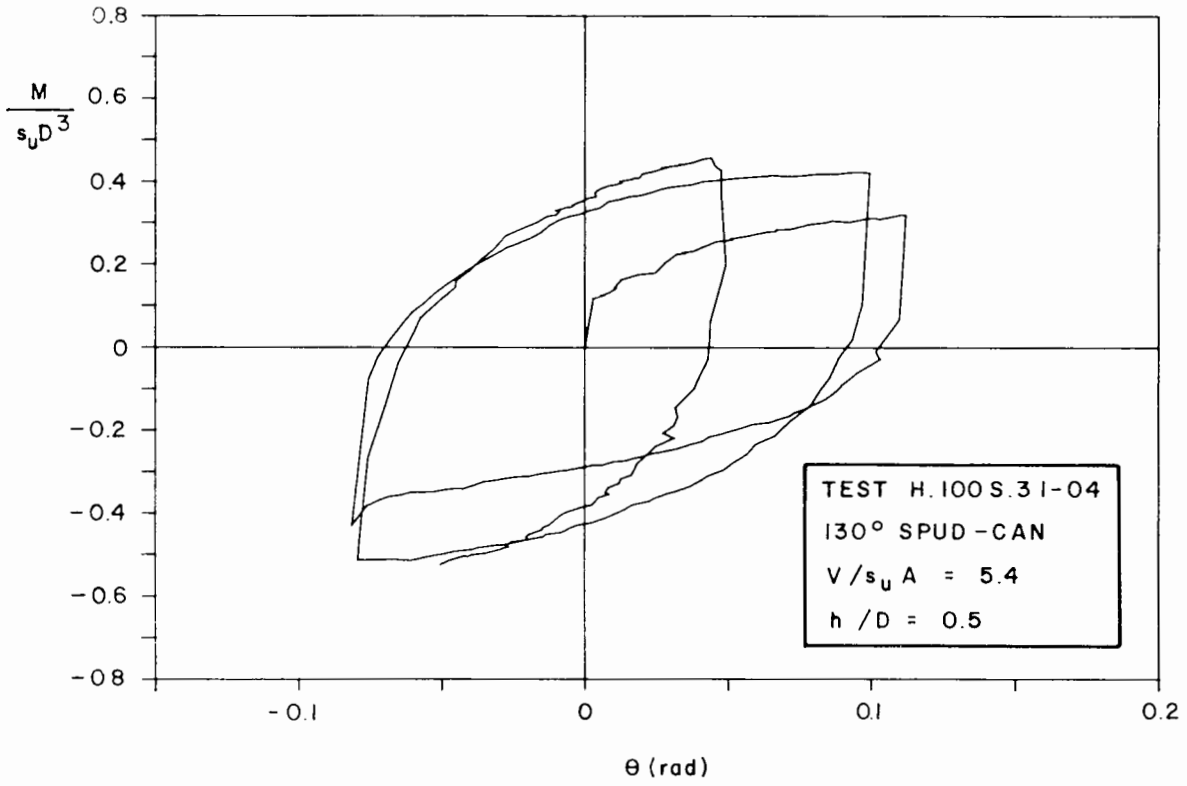

Figure 6.28 Dimensionless moment versus rotation curve for 130° spud-can (h/D = 0.5, high vertical load)

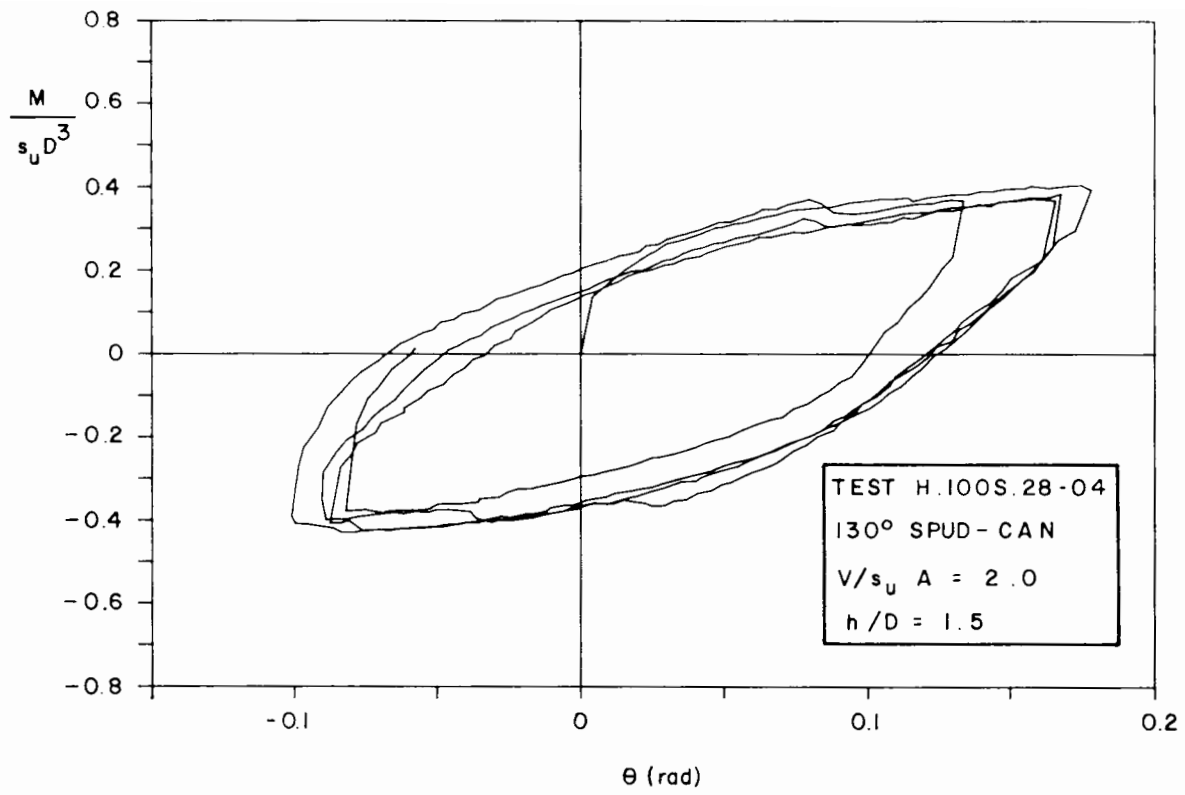

Figure 6.29 Dimensionless moment versus rotation curve for 130° spud-can (h/D = 1.5, low vertical load)

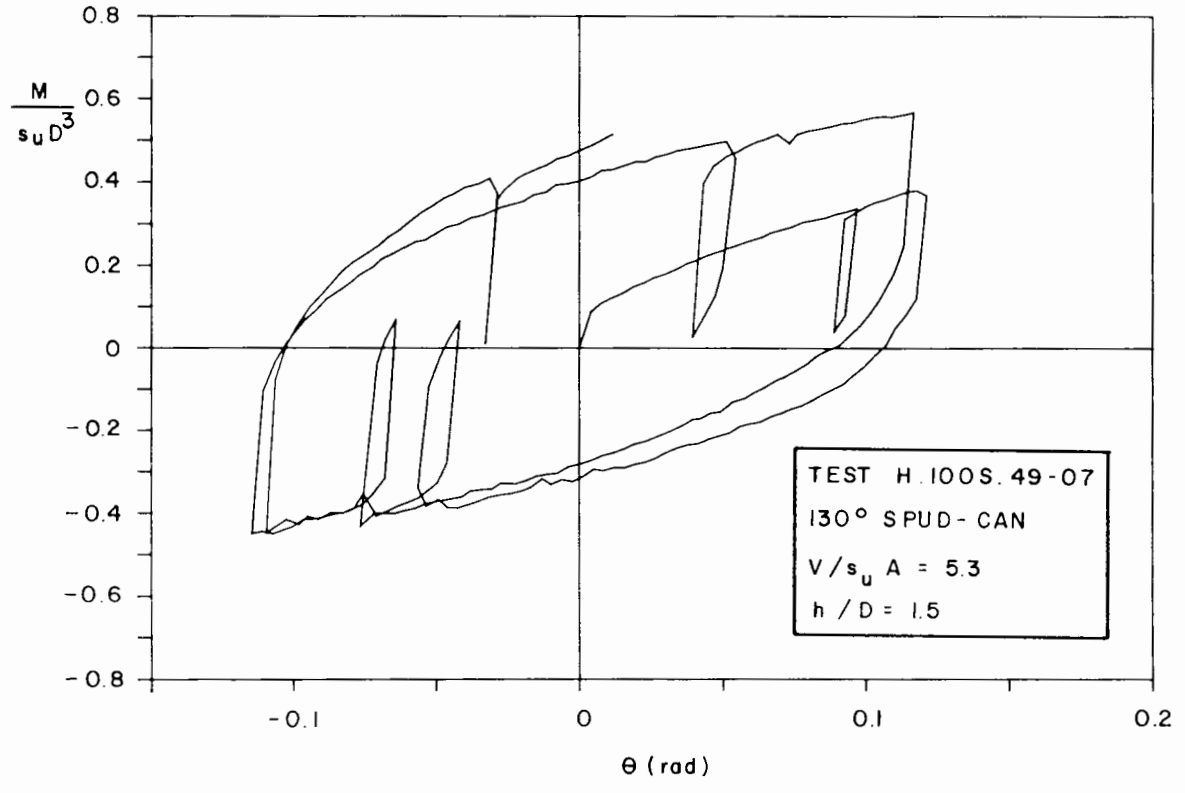

Figure 6.30 Dimensionless moment versus rotation curve for 130° spud-can (h/D = 1.5, high vertical load)

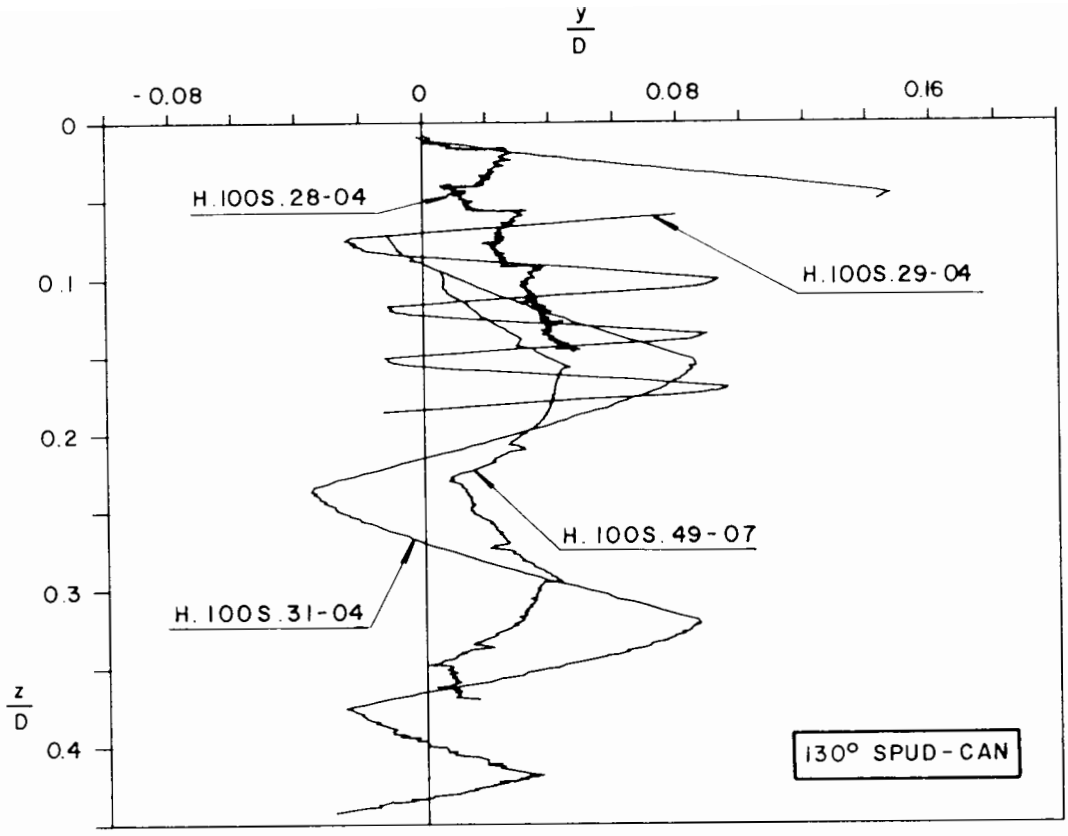

Figure 6.31 Displacement path of the centre of the 130° spud-can during the tests

Figure 6.31 shows that the magnitudes of the horizontal displacements of the centre of the spud-can are as large as those of circular plate, the displacement path being entirely compatible with the loading.

6.3.2 Repeated Tests

Table 6.4 displays the allocation of the repeated tests. The main values of the parameters involved in these tests are presented in Table 6.2.

Figures 6.32, 6.33, and 6.34 show the results of repeat tests (point A in Figure 6.33 is due to interference with the equipment). Comparing these curves with the corresponding ones in the representative group (Figures 6.17, 6.22 and 6.27 respectively) a strong similarity can be noticed between

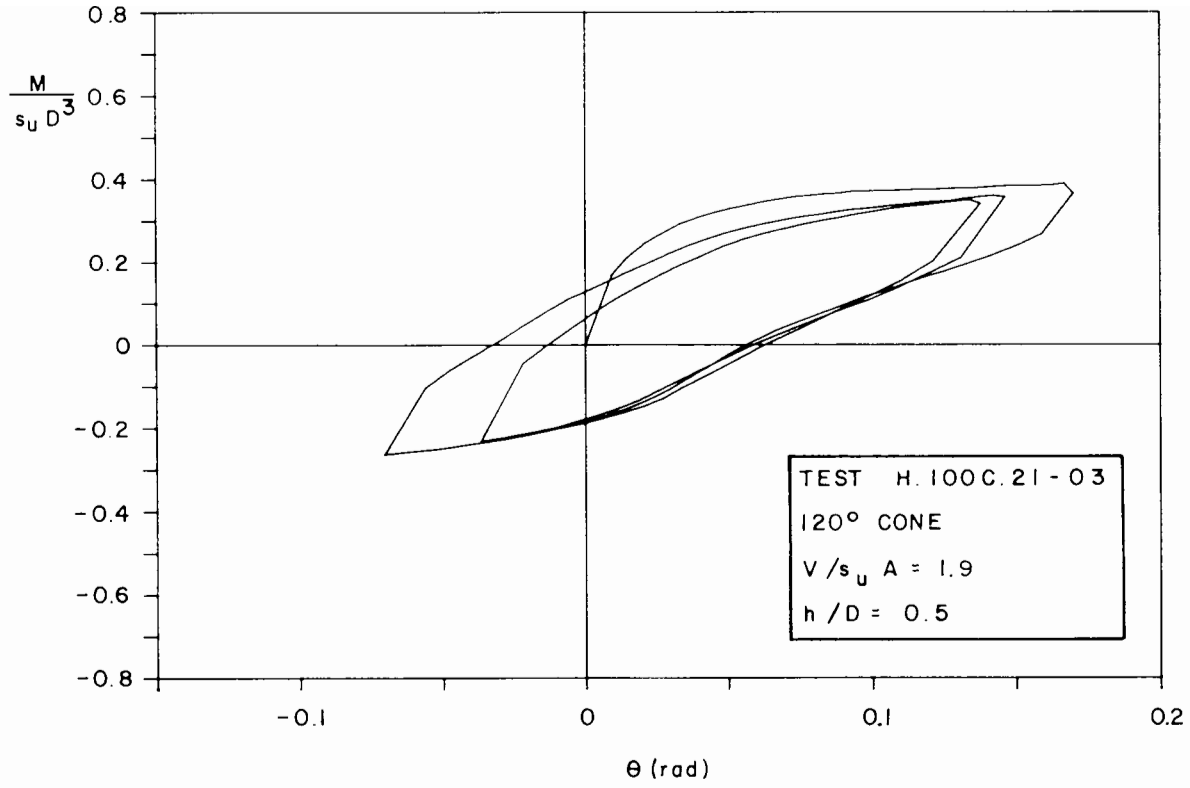

Figure 6.32 Dimensionless moment versus rotation curve for 120° cone (repeated test, h/D = 0.5, low vertical load)

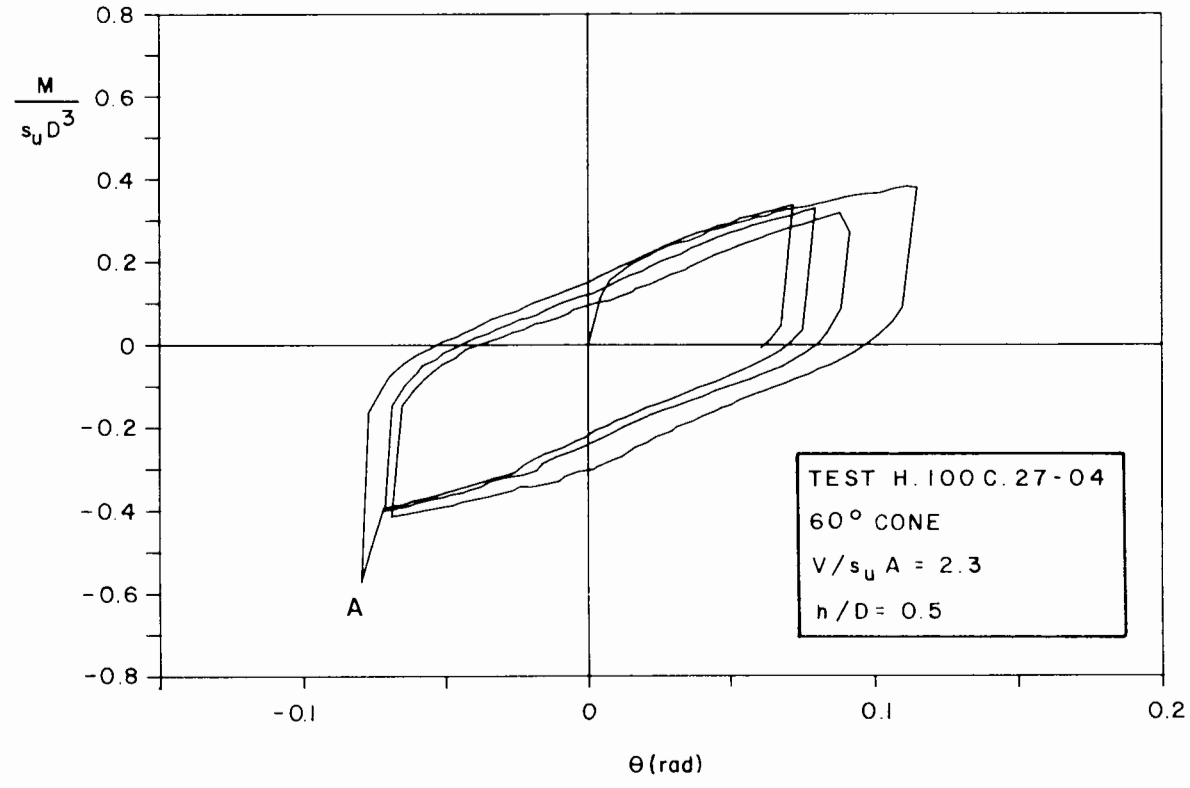

Figure 6.33 Dimensionless moment versus rotation curve for 60° cone (repeated test, h/D = 0.5, low vertical load)

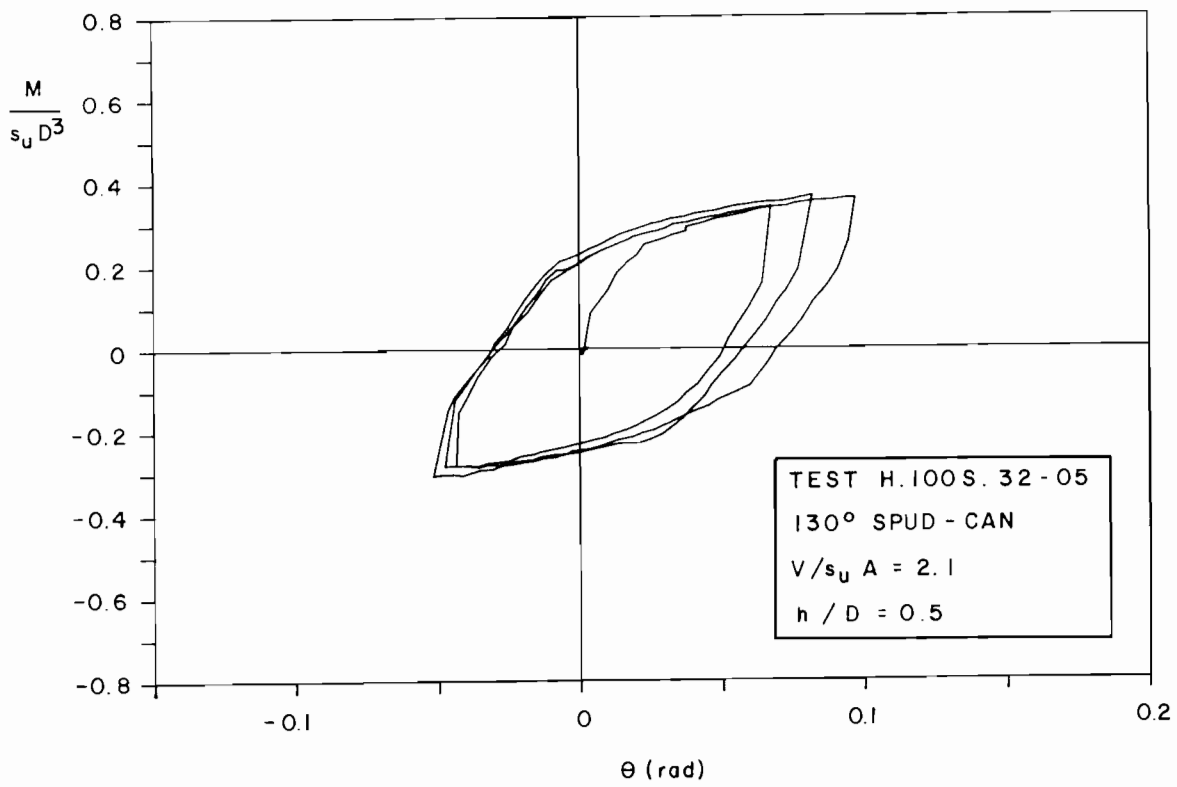

Figure 6.34 Dimensionless moment versus rotation curve for 130° spud-can (repeated test, h/D = 0.5, low vertical load)

them, indicating good repeatability in the tests.

6.4 Special Tests

6.4.1 Deep Tests

Tables 6.5, 6.6 and 6.7 display the parameters for the representative group as well as the repeated tests of this series. The value h/D is always 0.2 and d/D assumes the values 0.35 and 0.70, as reported in Section 5.2.2 (b), d being the initial depth at which the spud-can model was placed by driving before the beginning of the test.

Figures 6.35, 6.36, 6.37 and 6.38 show the moment versus rotation curves for each test performed. Although they clearly indicate a stiffer behaviour when

Table 6.5 Deep tests

test	s_u (kPa)	V (N)	h (mm)	d (mm)	V_{max} (N)
HD.100S.40-06	7.5	138.4	204.3	35	385.6
HD.100S.41-06	8.9	334.2	204.3	70	575.1
HD.100S.42-06	7.2	138.3	204.3	70	396.2
HD.100S.43-06	6.6	334.1	204.3	35	373.5
HD.100S.47-07	7.8	140.2	199.5	35	567.6
HD.100S.48-07	9.0	338.5	199.5	35	540.0

Notes

(1) model footing: 130^o spud-can
(2) s_u = index shear strength of the clay sample
(3) V = fixed vertical load
(4) h = height of application of horizontal load
(5) d = initial depth of the model footing (embedment)
(6) V_{max} = maximum vertical load applied to the model footing before testing

Table 6.6 Representative group of deep tests

	low V/s_uA	high V/s_uA
d/D = 0.35	HD.100S.47-07	HD.100S.48-07
d/D = 0.70	HD.100S.42-06	HD.100S.41-06

Table 6.7 Repeated group of deep tests

	low V/s_uA	high V/s_uA
d/D = 0.35 d/D = 0.70	HD.100S.40-06	HD.100S.43-06

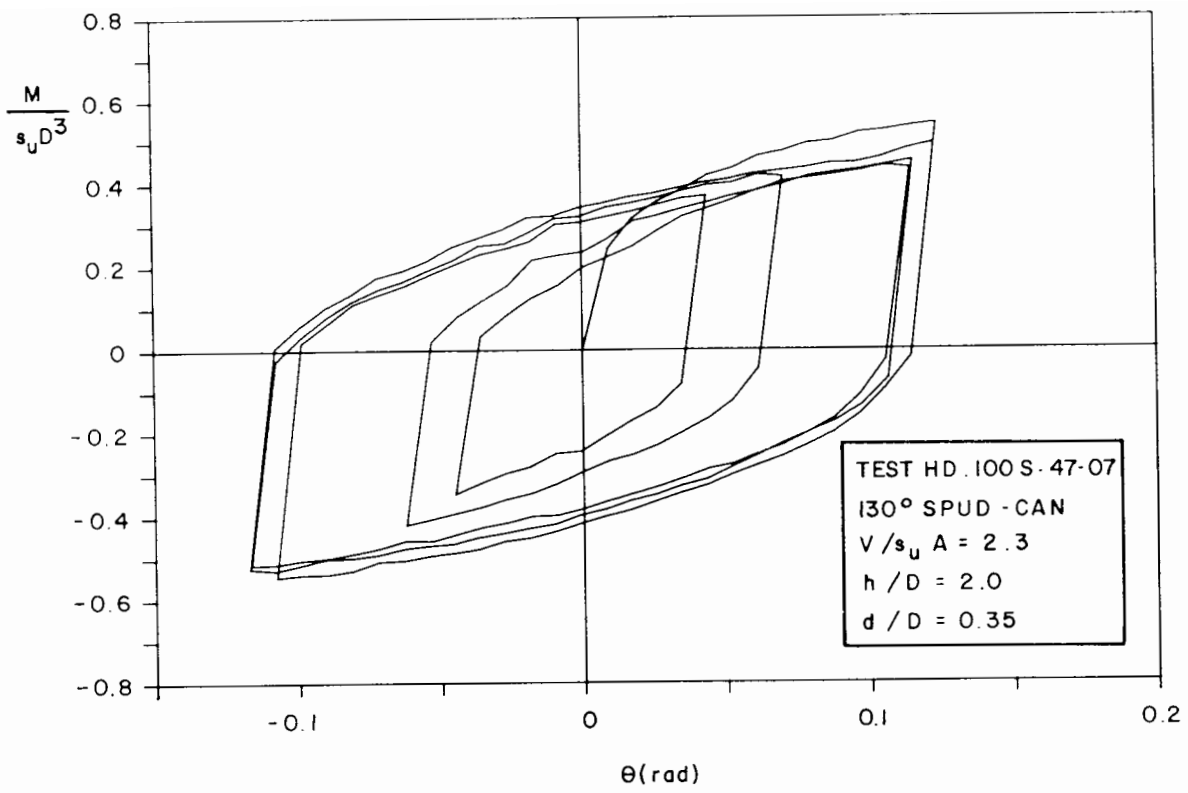

Figure 6.35 Dimensionless moment versus rotation curve for 130° spud-can (deep test, h/D = 2.0, d/D = 0.35, low vertical load)

compared with standard tests on the spud-can (d/D = 0), no considerable difference can be observed between the patterns at d/D = 0.35 and d/D = 0.70. The shape of the loops for low vertical load (tests HD.100S.42-06 and HD.100S.47-07), is much more like a parallelogram than the corresponding standard tests (H.100S.28-04 and H.100S.29-04), which resembled ellipses.

Figure 6.39 represents the results of the repeated test HD.100S.40-06, carried out with $V/s_u A = 2.3$ and d/D = 0.35, that should be compared with test HD.100S.47-07 (Figure 6.35). Ignoring the irregularities manifested in the former test, a good repeatability may be observed.

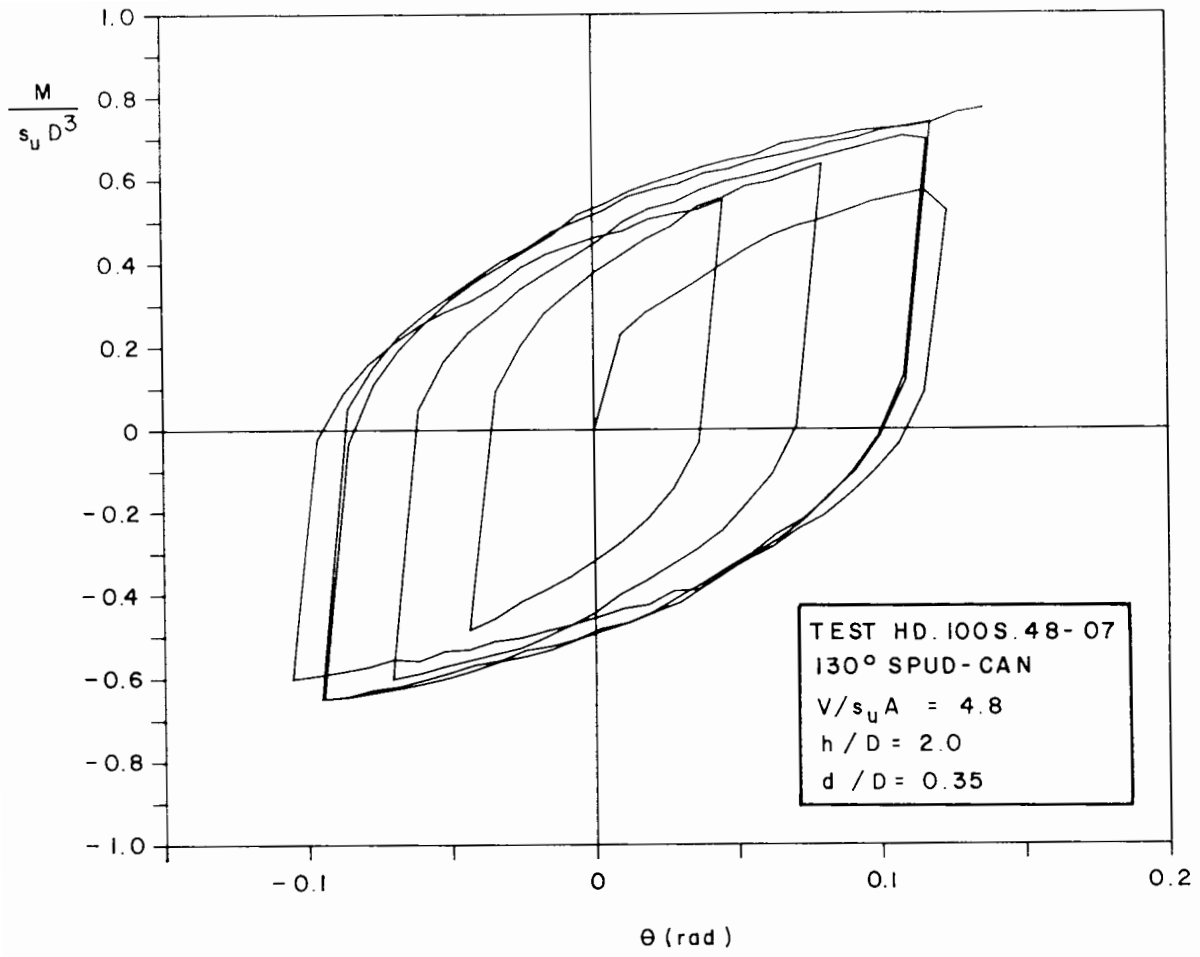

Figure 6.36 Dimensionless moment versus rotation curve for 130° spud-can (deep test, h/D = 2.0, d/D = 0.35, high vertical load)

6.4.2 Leg Tests

Five leg tests were carried out, one of them being a repeated test. Two stiffnesses of leg were employed, corresponding either to t/D = 0.09 or t/D = 0.143, where t is the thickness of the leg, and two fixed vertical loads applied, either a low value (corresponding to $V/s_u A$ = 2.1 to 2.4) or a high value (corresponding to $V/s_u A$ = 4.9 to 5.3). The ratio between the stiffnesses of the legs is approximately 4. Tables 6.8, 6.9 and 6.10 show the parameters for the leg tests.

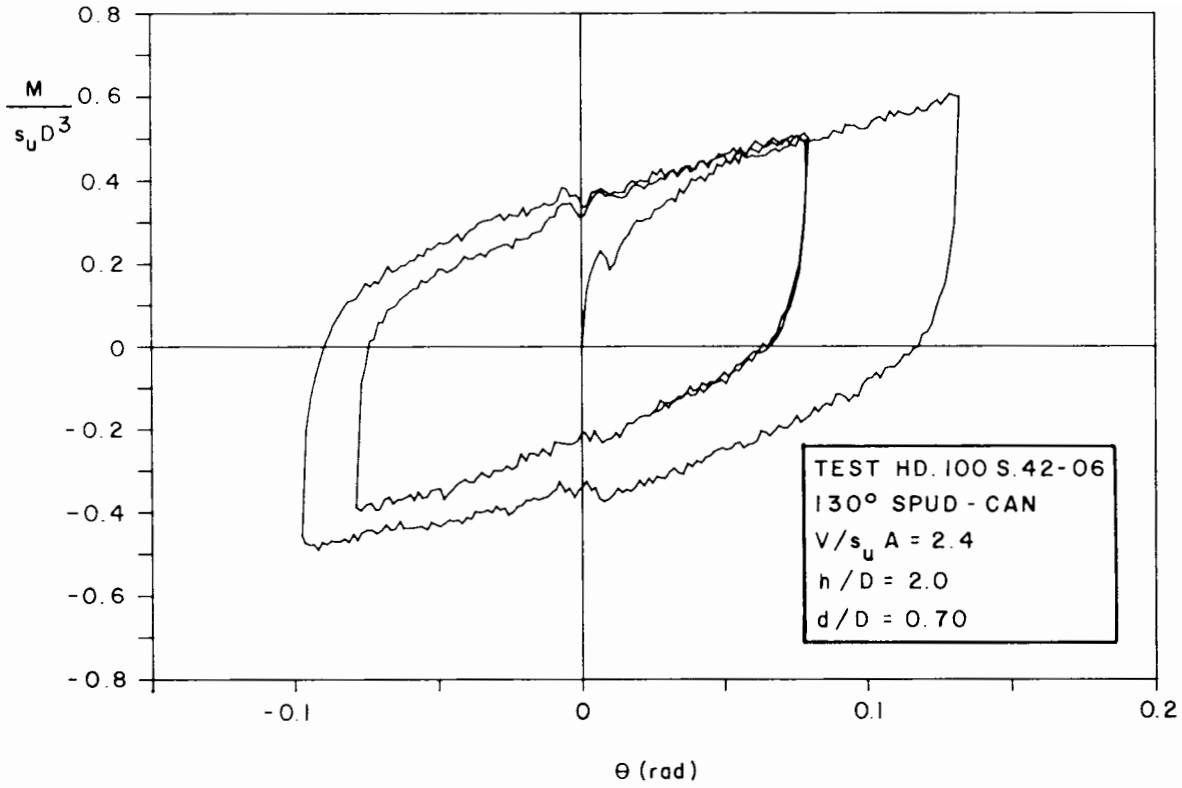

Figure 6.37 Dimensionless moment versus rotation curve for 130° spud-can (deep test, h/D = 2.0, d/D = 0.70, low vertical load)

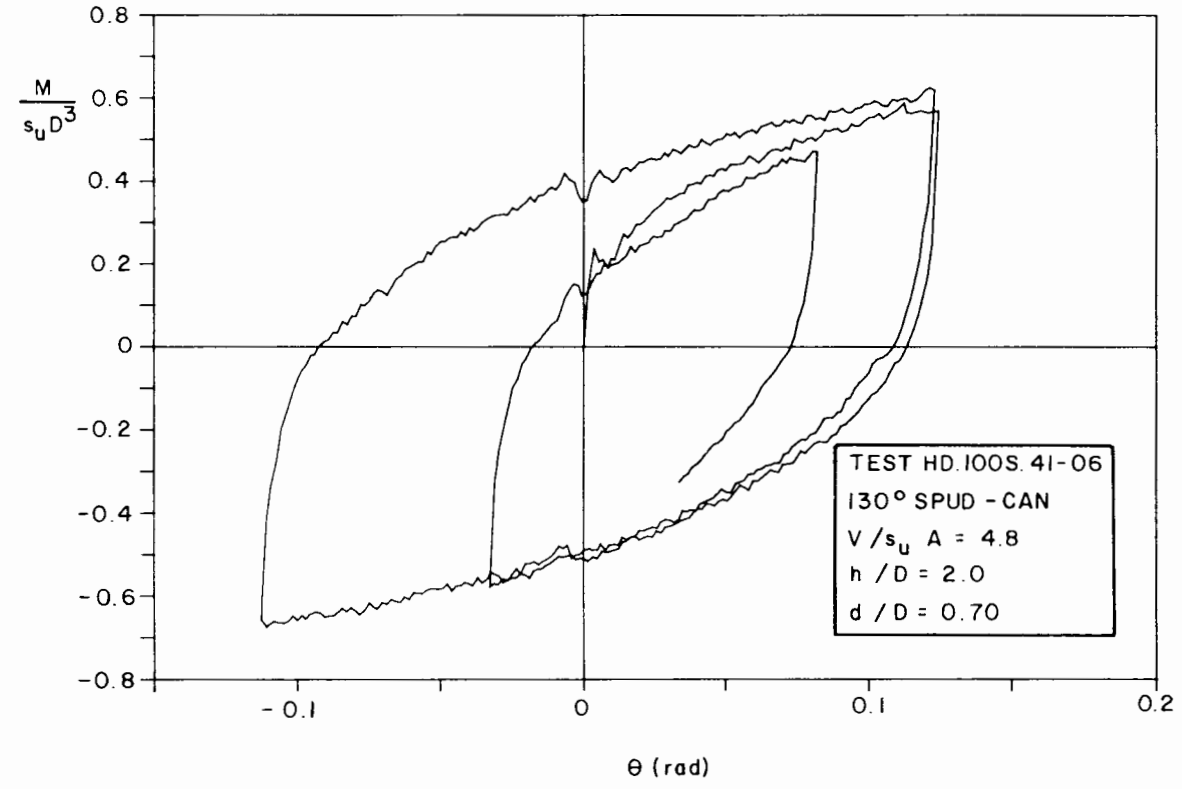

Figure 6.38 Dimensionless moment versus rotation curve for 130° spud-can (deep test, h/D = 2.0, d/D = 0.70, high vertical load)

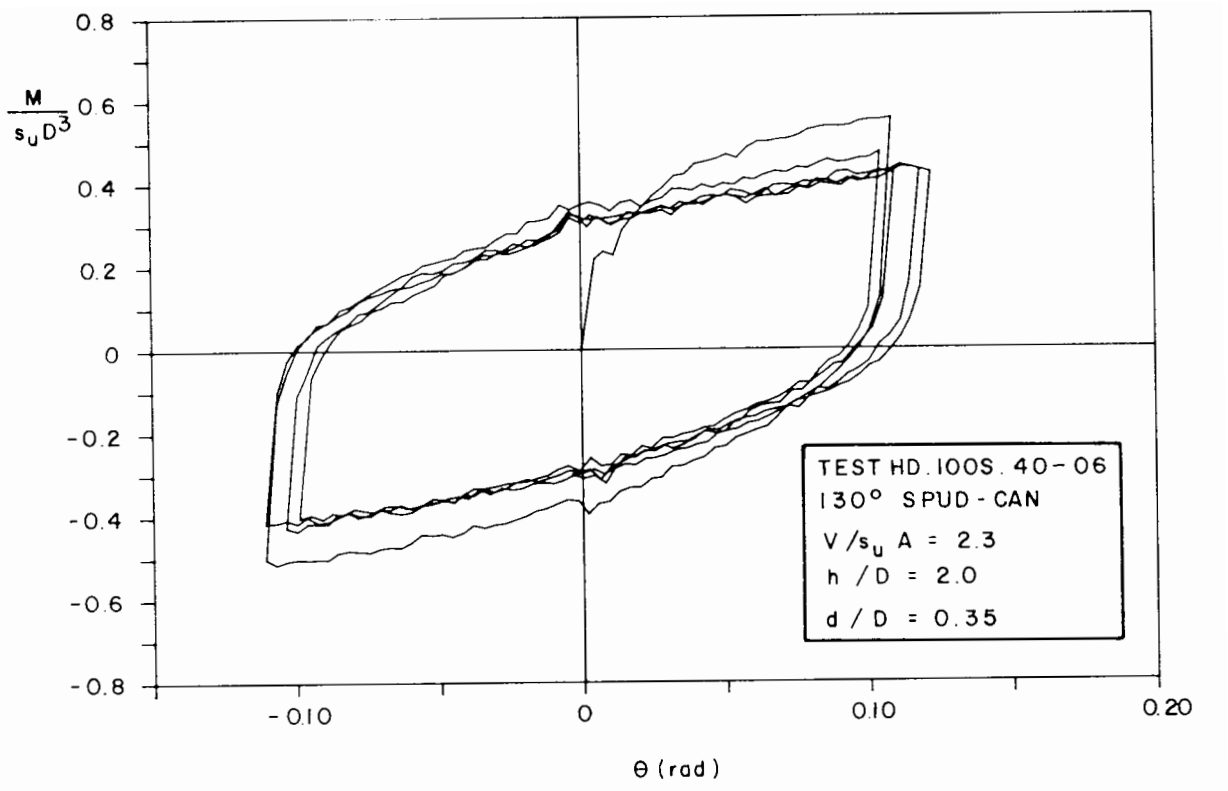

Figure 6.39 Dimensionless moment versus rotation curve for 130° spud-can (repeated deep test, h/D = 2.0, d/D = 0.35, low vertical load)

Figure 6.40 shows all the forces applied to the plate-leg-footing structure which, together with the relevant distances, led to the determination of the moment at the footing centre. The deflection δ was inferred from the horizontal LVDT readings.

The results of this special series of tests are presented in two different ways:

(a) footing moment versus rotation curves, as in the main series of combined loading tests;

(b) the moment at the footing, nondimensionalized as $\lambda M/V$ versus the quantity $(\lambda lH/V + \lambda\delta)$, where:

$\lambda = \sqrt{V/EI}$;

V = fixed vertical load;

E = Young modulus of the material of the leg;

I = 2nd moment of area of the cross section of the leg;

H = horizontal load;

l = length of the leg;

δ = deflection of the leg when subjected to a bending moment.

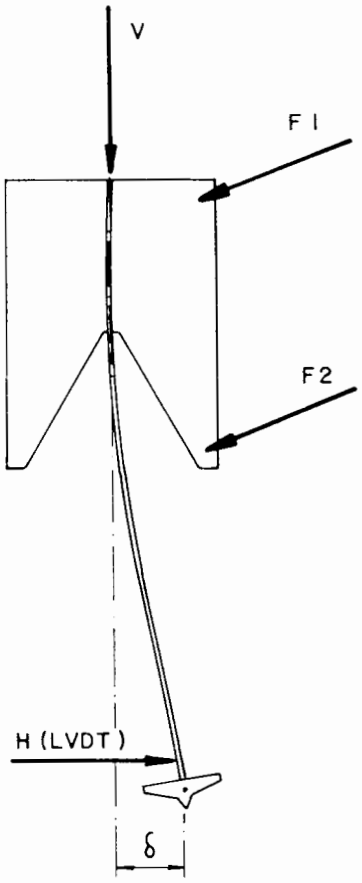

Figure 6.40 Forces applied to the model plate-leg-footing structure

Table 6.8 Leg tests

test	s_u (kPa)	V (N)	t (mm)	V_{max} (N)
LT.100S.38-06	8.4	326.1	9.0	258.9
LT.100S.39-06	7.0	129.5	9.0	214.7
LT.100S.44-07	8.0	326.7	14.3	313.2
LT.100S.45-07	7.8	325.8	9.0	327.8
LT.100S.46-07	8.0	129.3	14.3	282.5

Notes

(1) model footing: 130^{o} spud-can
(2) s_u = index shear strength of the clay sample
(3) V = fixed vertical load
(4) t = thickness of the leg
(5) V_{max} = maximum vertical load applied to the model footing before testing

Table 6.9 Representative group of leg tests

	low V/s_uA	high V/s_uA
t/D = 0.090	LT.100S.39-06	LT.100S.38-06
t/D = 0.143	LT.100S.46-07	LT.100S.44-07

Table 6.10 Repeated group of leg tests

	low V/s_uA	high V/s_uA
t/D = 0.090 t/D = 0.143		LT.100S.45-07

The curves (b) can be represented by the equation:

$$\lambda M/V = a(\lambda lH/V + \lambda\delta) \qquad [6.1]$$

or, in its dimensional form:

$$M = a(Hl + V\delta) \qquad [6.2]$$

where a is a variable coefficient that assumes the value zero if the footing is pinned to the soil, and 1/2 if it is fully fixed.

The results in terms of moment versus rotation curves are presented in Figures 6.41, 6.42, 6.43 and 6.44. The irregularities observed in the curves may be associated with:

* the flexibility of the assembly, releasing part of the energy stored in an irregular way;

* some friction between the top plate and the leg guide showing up, in spite of the precautions taken to reduce it to negligible levels;

* inaccuracies related to instrumentation accuracy and the complexity of the set-up.

Four tests (including a repeated one) exhibited an initial negative moment (after application of the vertical load), while tests performed with high vertical load produced loops clearly asymmetric in shape, developing higher negative values of moment than positive ones. This anomalous behaviour may be explained by the initial loading causing permanent asymmetric

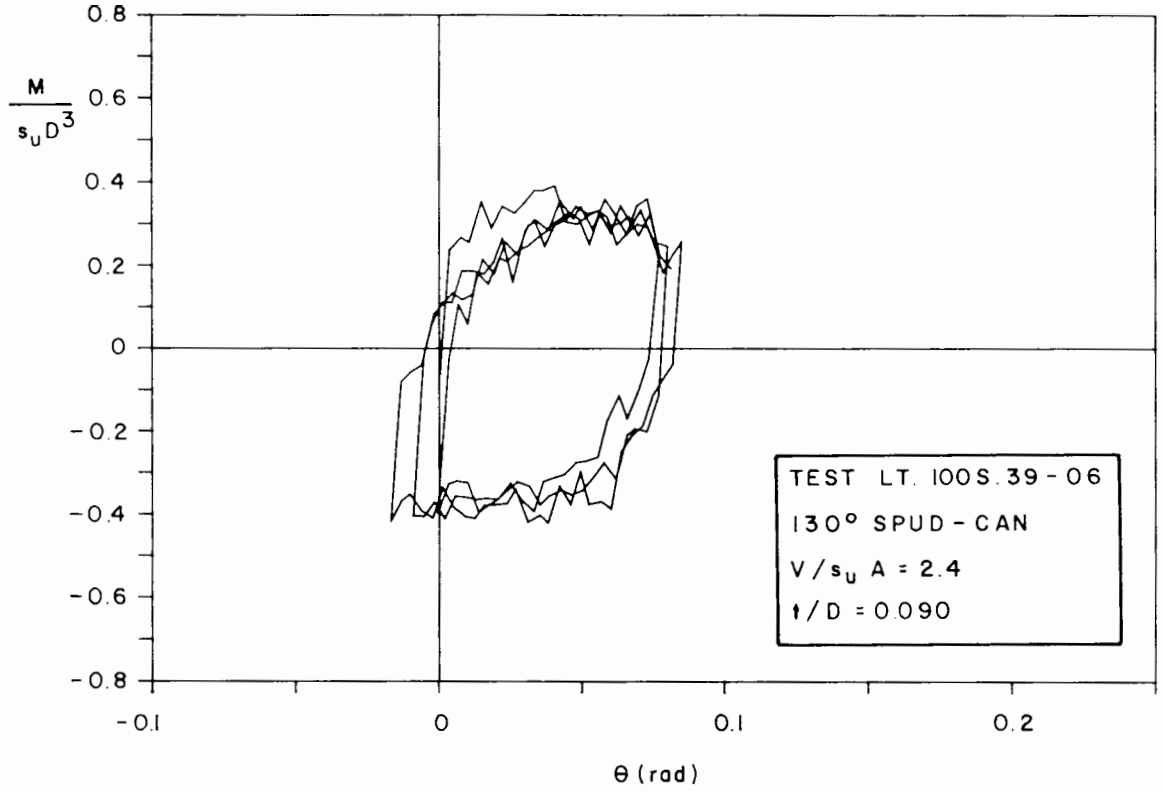

Figure 6.41 Dimensionless moment versus rotation curve for 130° spud-can (leg test, t/D = 0.090, low vertical load)

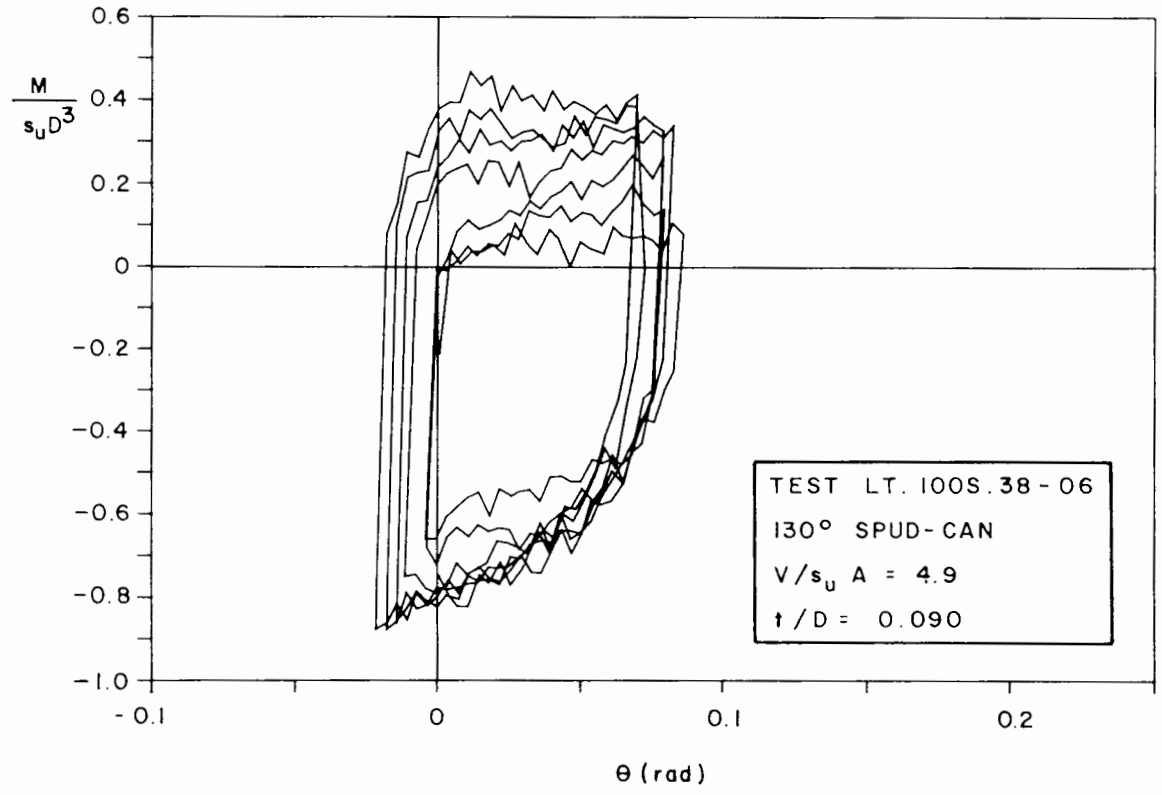

Figure 6.42 Dimensionless moment versus rotation curve for 130° spud-can (leg test, t/D = 0.090, high vertical load)

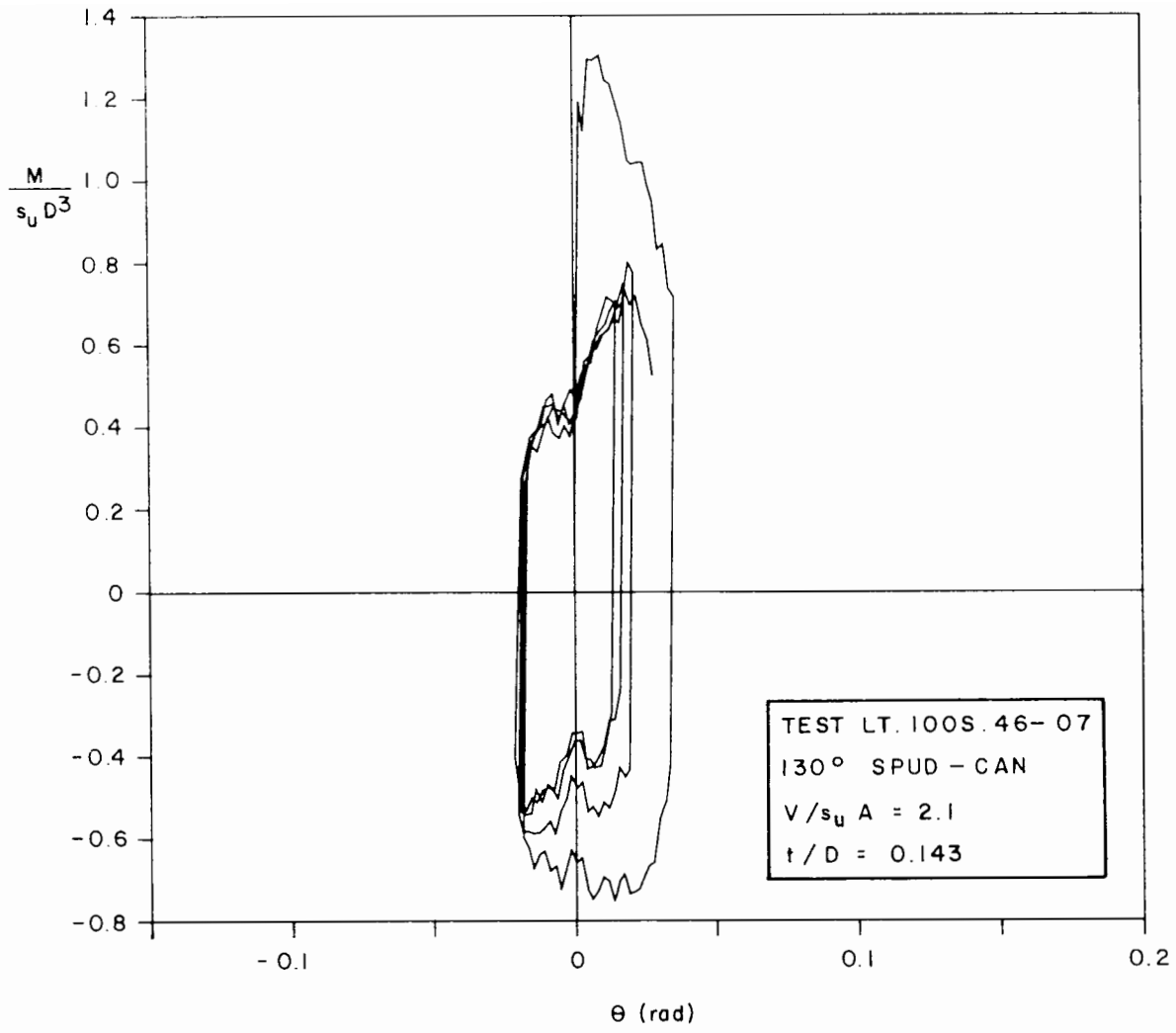

Figure 6.43 Dimensionless moment versus rotation curve for 130° spud-can (leg test, t/D = 0.143, low vertical load)

deformation. Test LT.100S.46-07 (Figure 6.43) shows an atypical extremely high initial stiffness and this certainly may be accounted for by some initial friction in the assembly and therefore this information must not be relied upon.

The results are presented in the other format, $\lambda M/V$ versus $(\lambda lH/V + \lambda\delta)$, in Figures 6.45, 6.46, 6.47 and 6.48. For reference, a straight line with slope 0.5 is drawn in each figure, representing a full fixity behaviour. Generally a high fixity occurs in the beginning of each test, decreasing substantially

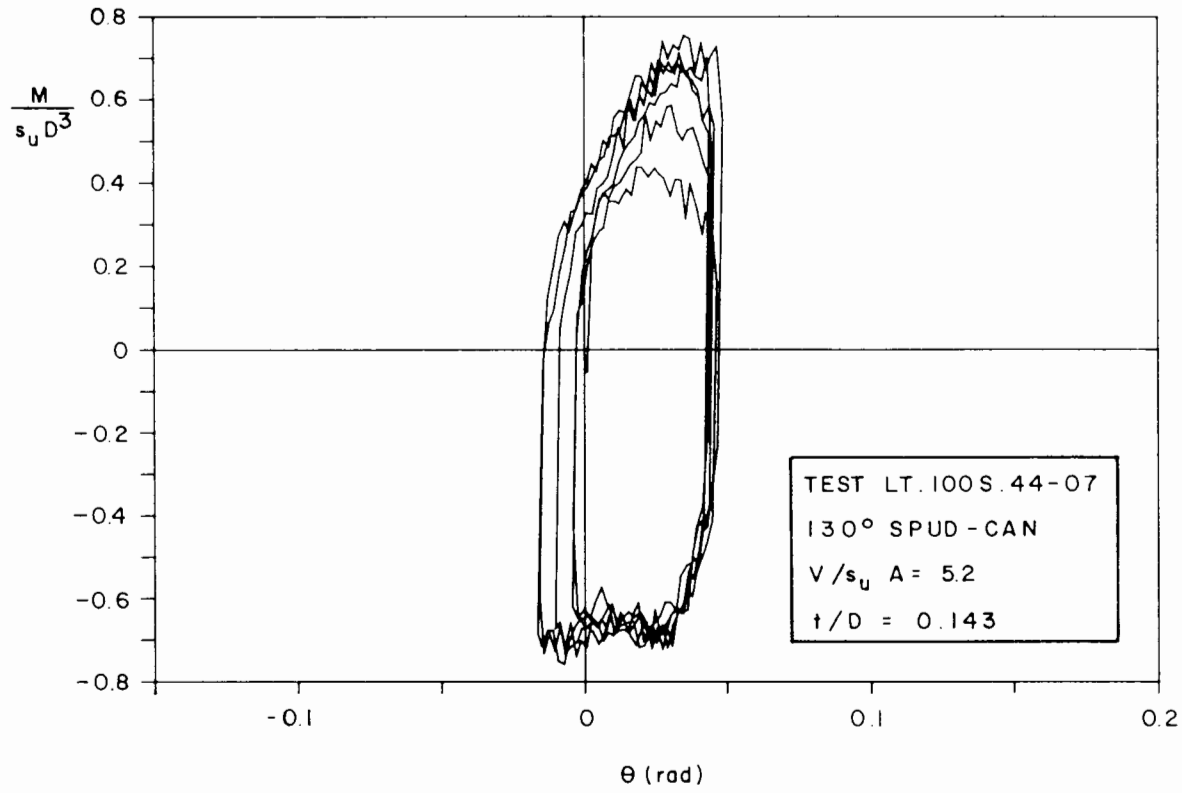

Figure 6.44 Dimensionless moment versus rotation curve for 130° spud-can (leg test, t/D = 0.143, high vertical load)

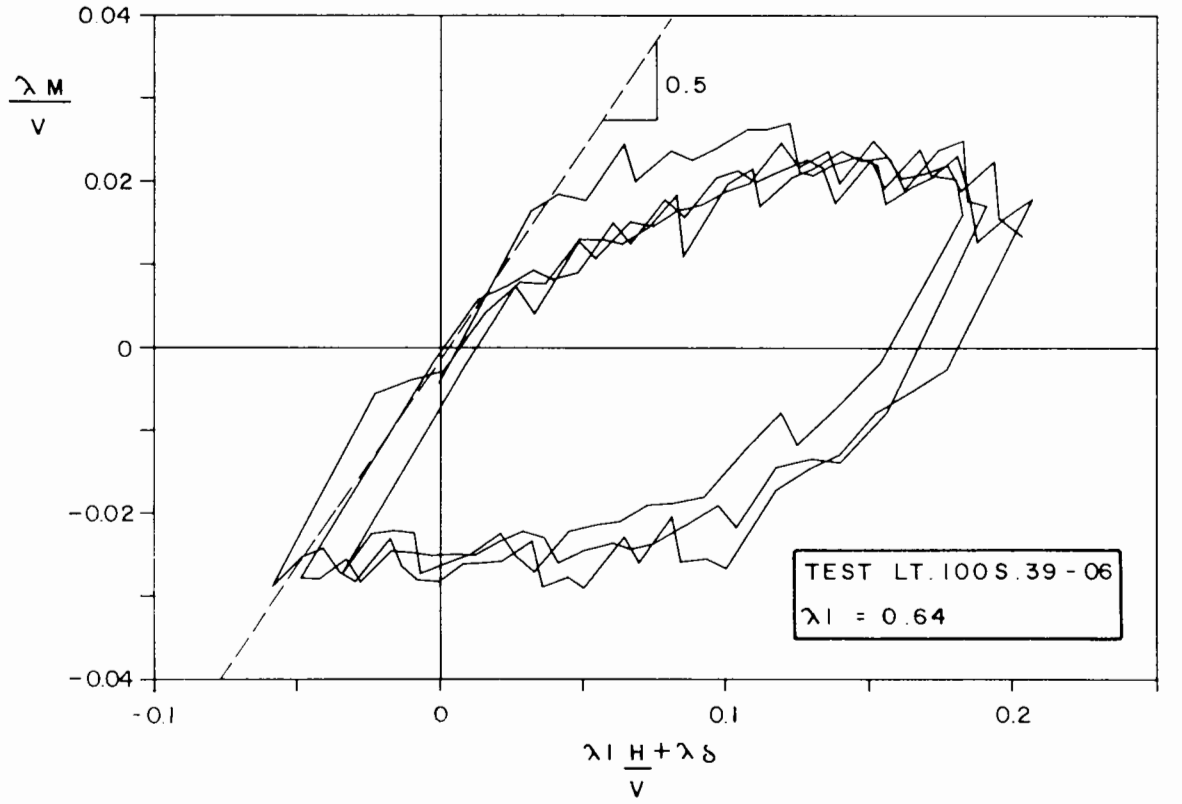

Figure 6.45 Variation of the dimensionless moment at the footing with the quantity ($\lambda l H/V + \lambda\delta$) for $\lambda l = 0.64$ (the dashed line represents full fixity behaviour)

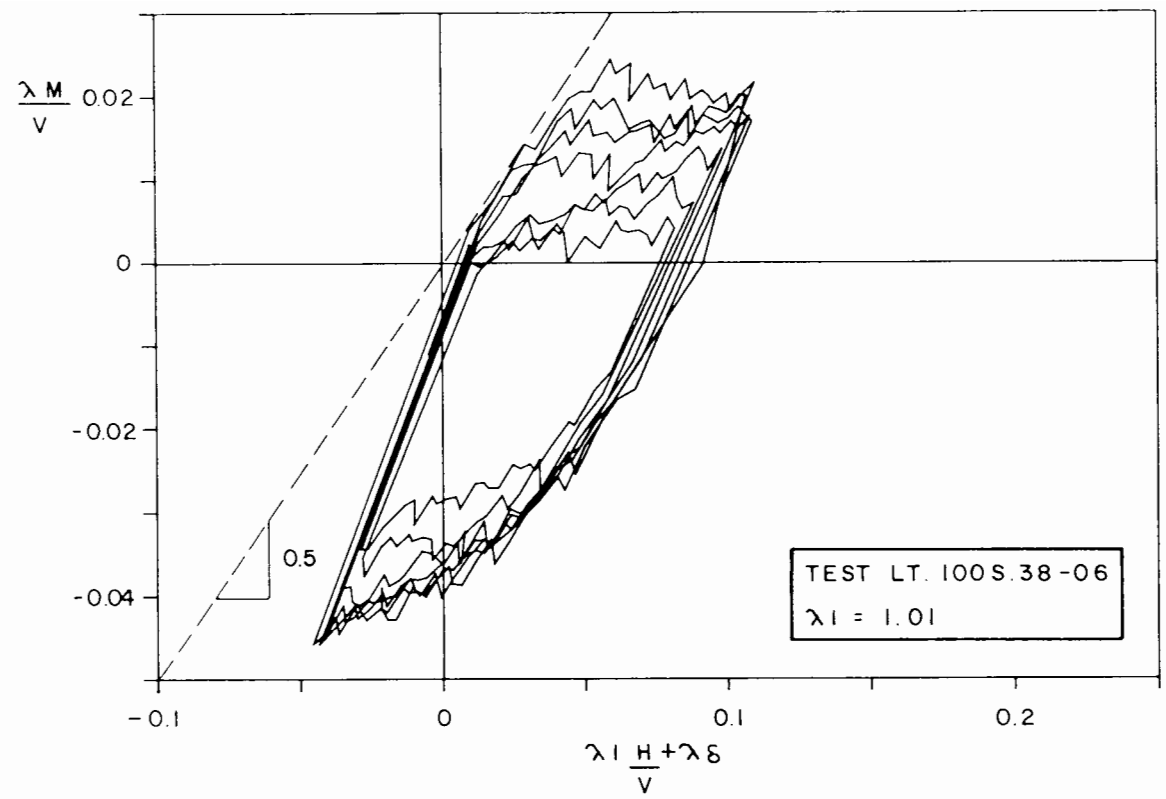

Figure 6.46 Variation of the dimensionless moment at the footing with the quantity ($\lambda lH/V + \lambda\delta$) for $\lambda l = 1.01$ (the dashed line represents full fixity behaviour)

as the test goes on. In some cases the initial slope is slightly larger than 0.5 and this can only be explained by the compliance of the system top plate and loading device, allowing a small rotation at the top of the leg.

Figures 6.49 and 6.50 show the results of one repeated test performed in this series (test LT.100S.45-07). The pattern of behaviour is practically the same as in test LT.100S.38-06 (Figures 6.42 and 6.46), carried out under identical conditions.

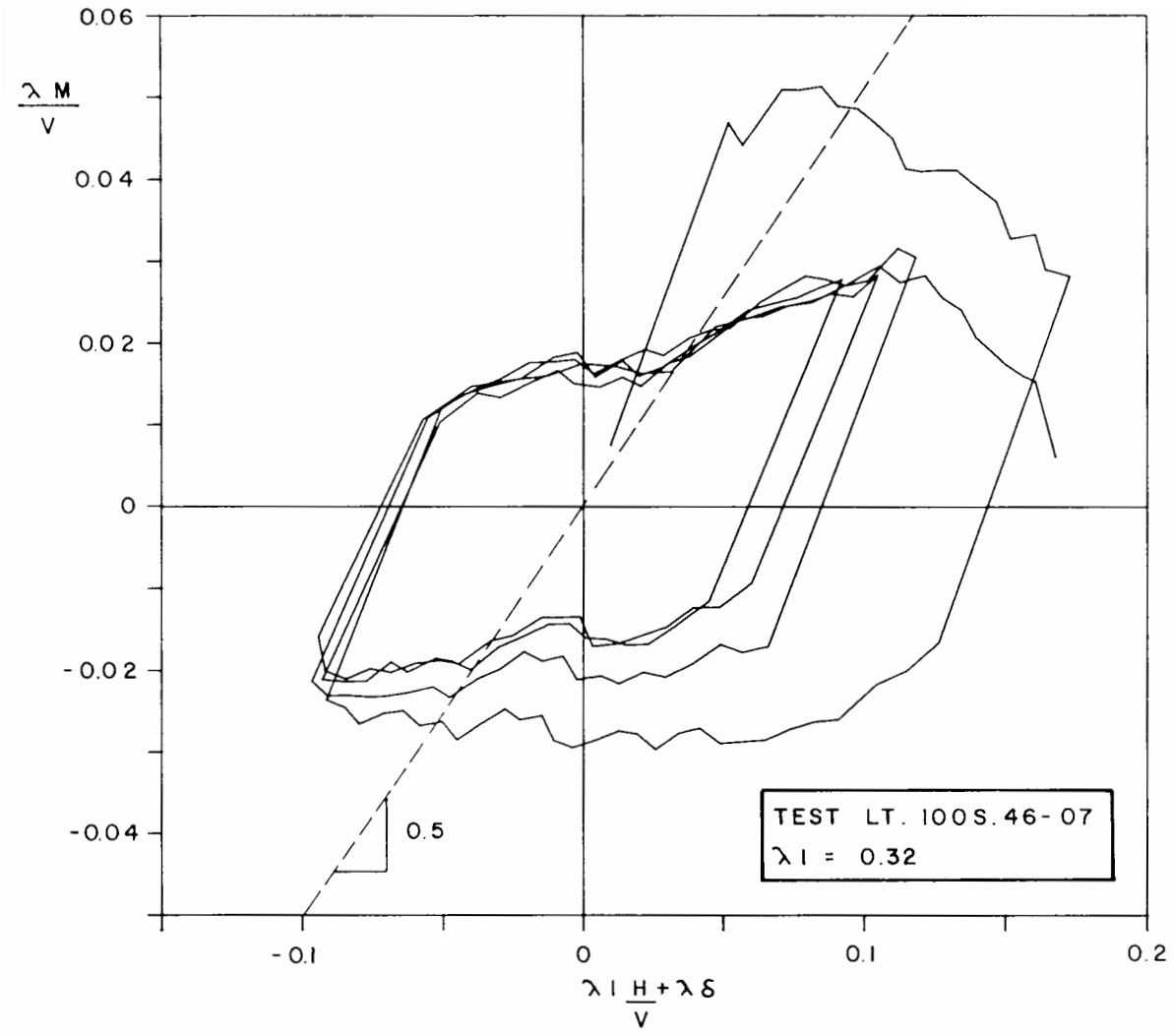

Figure 6.47 Variation of the dimensionless moment at the footing with the quantity ($\lambda l H/V + \lambda\delta$) for $\lambda l = 0.32$ (the dashed line represents full fixity behaviour)

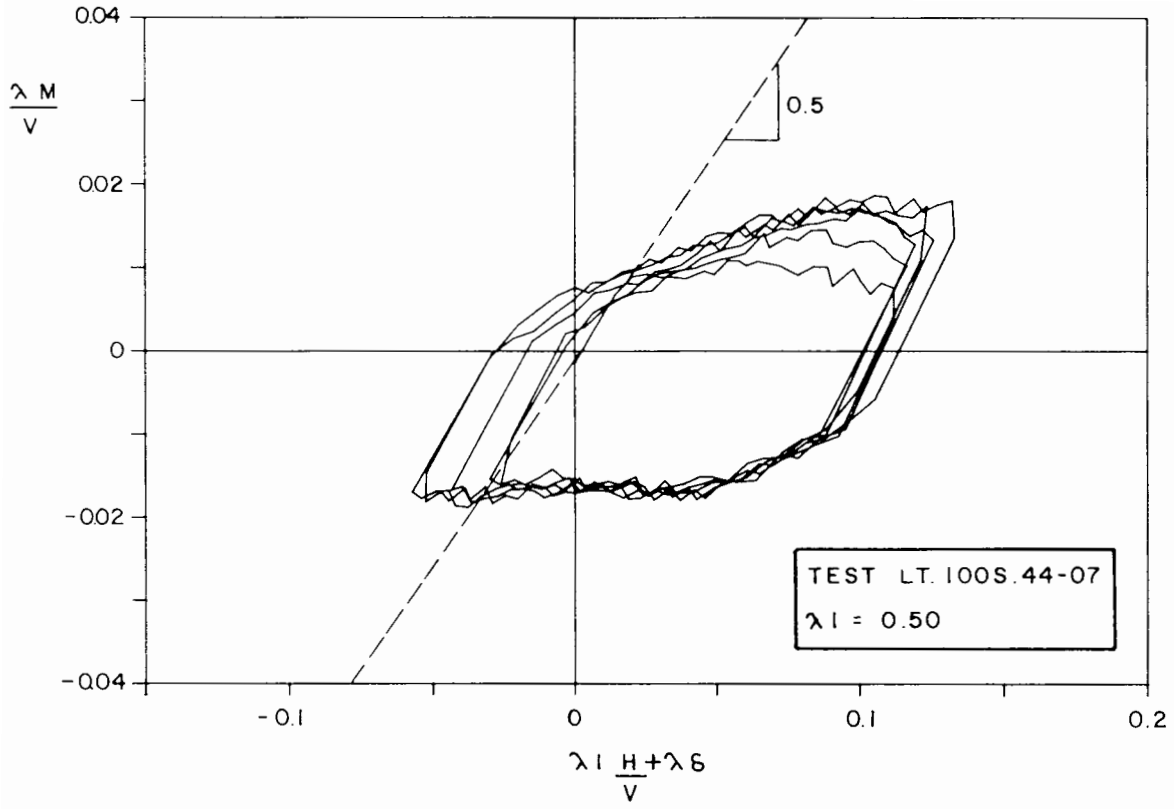

Figure 6.48 Variation of the dimensionless moment at the footing with the quantity ($\lambda lH/V + \lambda\delta$) for $\lambda l = 0.50$ (the dashed line represents full fixity behaviour)

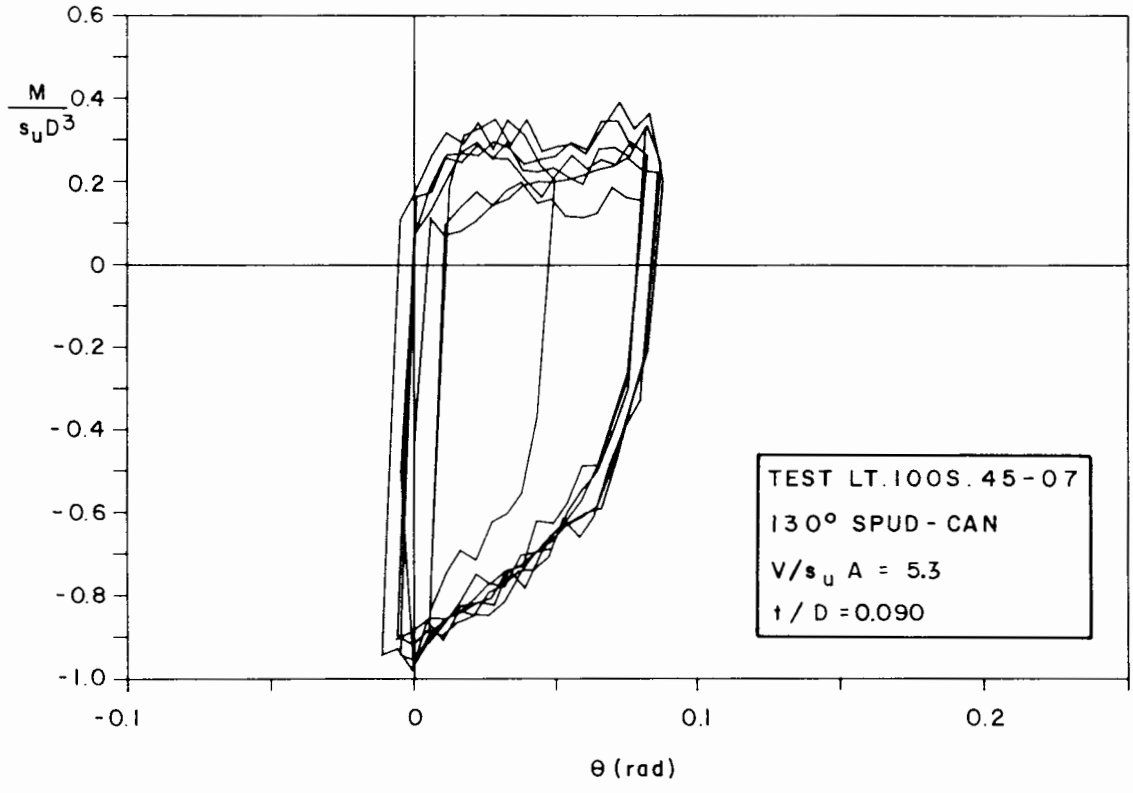

Figure 6.49 Dimensionless moment versus rotation curve for 130^{o} spud-can (repeated leg test, t/D = 0.090, high vertical load)

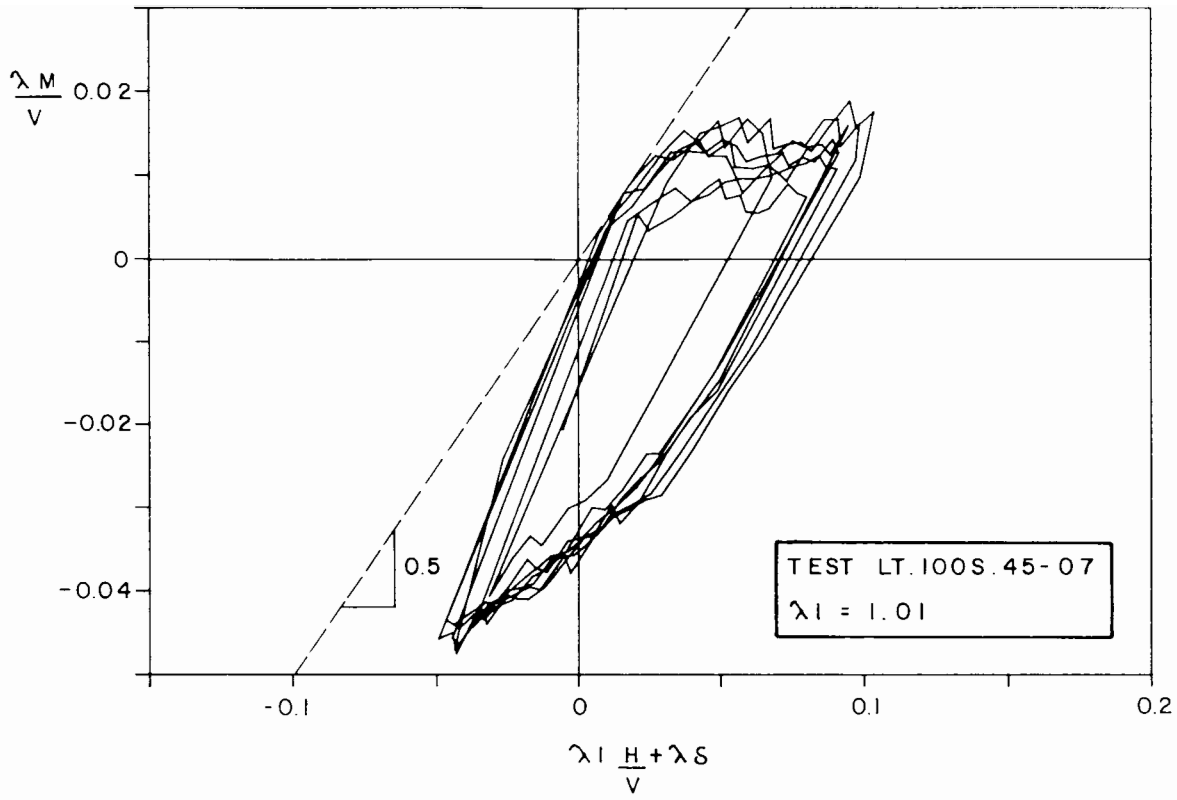

Figure 6.50 Variation of the dimensionless moment at the footing with the quantity ($\lambda l H/V + \lambda\delta$) for $\lambda l = 1.01$ - repeated leg test (the dashed line represents full fixity behaviour)

CHAPTER 7

EXPERIMENTAL RESULTS - CYCLIC LOADING

7.1 Introduction

As in the monotonic loading tests, after the end of each cyclic loading test the fixed parameters and the data corresponding to the voltage reading of every transducer were sent to the mainframe computer for processing. In this case, however, the data were processed in two stages through FORTRAN programs: (i) initially all the relevant loads and displacements were calculated and (ii) using these results the following numerical information for each cycle were obtained:

(a) cumulative displacements;

(b) variation of the rotation angle associated with the peak-to-peak moment amplitude;

(c) rotational energy dissipated.

Cumulative displacements are defined in this work as the displacements corresponding to the maximum value of the moment within each cycle. Variation of the rotation angle associated with the peak-to-peak moment amplitude (for the sake of simplicity hereafter referred to only as variation of rotation) and rotational energy dissipated are represented in Figure 7.1 (a).

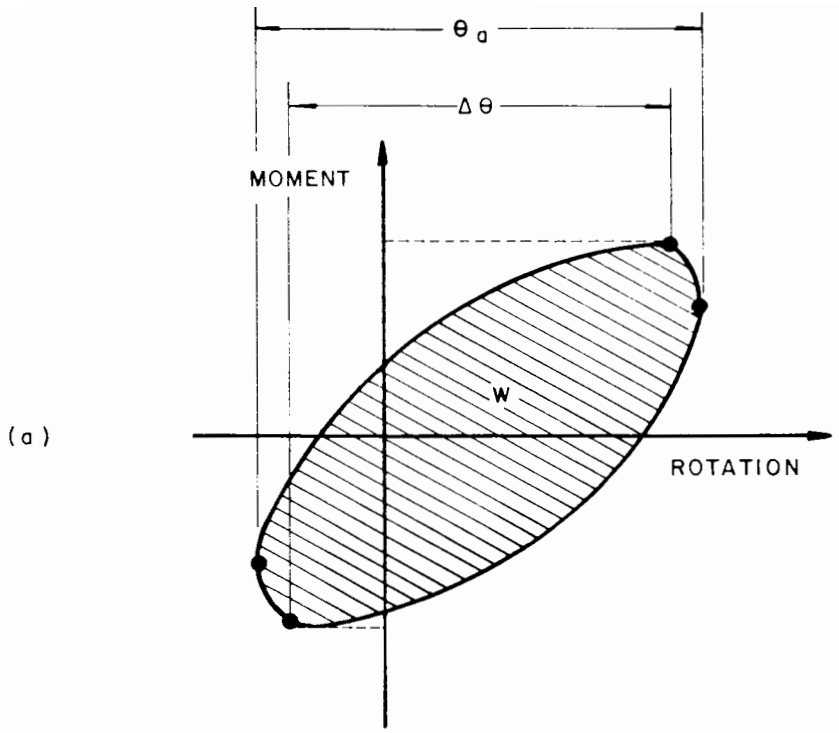

(a)

θ_a = PEAK-TO-PEAK AMPLITUDE OF ROTATION

$\Delta\theta$ = VARIATION OF THE ROTATION ANGLE

AREA W = ROTATIONAL ENERGY DISSIPATED

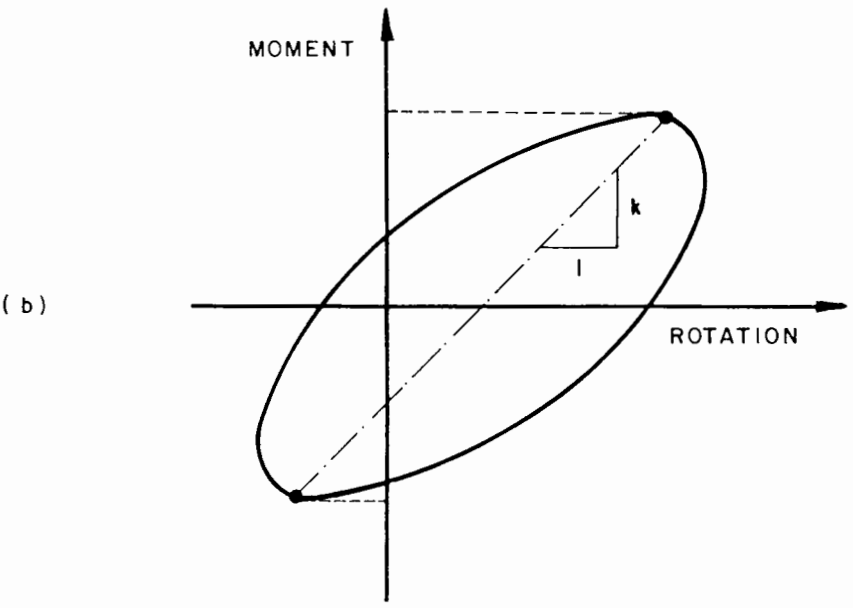

(b)

k = EQUIVALENT ROTATIONAL STIFFNESS

Figure 7.1 Definition of some parameters adopted in cyclic loading tests

Figure 7.2 presents the key for identification of some of the characteristics of each test from the test number.

A total of 31 tests were performed altogether in this phase, and 3 of them were lost for reasons related to malfunction in the driving/control system. Tests W.30L.54C-09, W.6L.60C-10 and W.6H.61C-10, were used to select the fixed parameters of the testing programme, and were performed with parameters different from those eventually established. Their results were therefore abandoned. Five tests were repeated to check repeatability, the better one in each pair being chosen for further analysis.

The results of cyclic loading tests are presented by means of tables and curves, observing the same procedure as in monotonic loading tests, and the following symbols are used in addition to those already defined in Section 6.1:

N = number of cycles performed;

M_a = peak-to-peak amplitude of moment;

$\Delta\theta$ = variation of rotation;

θ_c = cumulative rotation;

W = rotational energy dissipated during a complete cycle of loading.

Most of the curves presented in this chapter provide information about the cumulative non-dimensional displacements, variation of rotation and non-dimensional rotational energy dissipated per cycle with the number of cycles, this last quantity being represented in logarithmic scale.

In some cases a slight undulatory pattern is observed in the values of the variables. This can be explained by the fact that the point of maximum

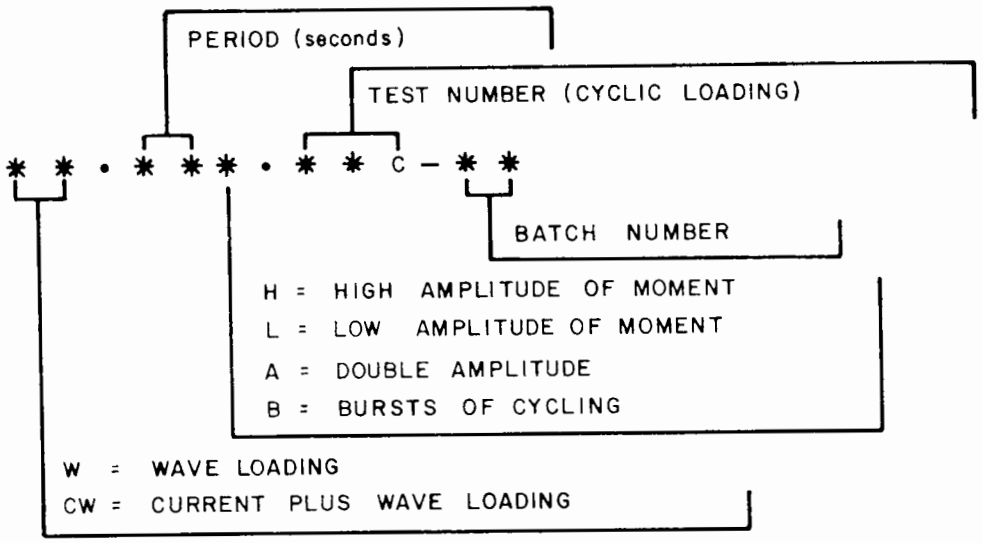

Figure 7.2 Numbering system used to identify the main features of each test

moment observed does not necessarily correspond to the real maximum and, because a complete cycle of data reading is slightly longer than a complete cycle of loading (due to unavoidable delays when the pre-set time interval is reached and triggers the data-logging routine), the observed maximum tends to go up until it reaches the point closest to the real maximum, dropping again afterwards.

The equivalent non-dimensional rotational stiffness in each cycle, defined in Figure 7.1 (b), can be easily obtained through the expression:

$$k = \frac{M_a}{s_u D^3 \Delta\theta} \qquad [7.1]$$

7.2 Main Series of Tests

Table 7.1 shows the values of the fixed parameters for each test of the main series and also additional information about observations of the state of the clay surface disturbed during the test. The following classification

criterion was adopted to define the area affected by the foundation (D is the diameter of the footing), which is contained in a circle of radius R:

EC = 1	when	$0 < R \leq 0.85D$
EC = 2	when	$0.85D < R \leq 1.20D$
EC = 3	when	$1.20D < R \leq 1.55D$
EC = 4	when	$1.55D < R \leq 1.90D$
EC = 5	when	$1.90D < R \leq 2.25D$

Table 7.1 Main series of cyclic loading tests

test	s_u (kPa)	V (N)	M_a (Nm)	M_o (Nm)	T (s)	V_{max} (N)	EC
W.30L.55C-09	8.5	133.8	2.0	0	30	361.0	1
W.30H.56C-09	10.5	133.8	4.0	0	30	367.0	1
CW.30L.57C-09	9.5	133.9	2.0	0.5	30	378.6	1
CW.30H.58C-09	9.8	133.9	4.0	0.5	30	393.7	2
W.30L.59C-09	8.4	133.8	2.0	0	30	269.5	1
W.8L.63C-10	8.4	133.8	2.0	0	8	252.4	2
CW.8L.65C-10	9.5	133.9	2.0	0.5	8	396.7	1
W.30L.66C-11	11.0	330.0	2.0	0	30	348.4	1
CW.30L.67C-11	7.8	330.4	2.0	0.5	30	246.9	5
W.30H.68C-11	10.5	329.9	4.0	0	30	438.9	2
CW.30H.69C-11	8.9	330.5	4.0	0.5	30	241.8	4
W.8H.70C-11	10.1	133.8	4.0	0	8	408.2	2
CW.8H.71C-11	9.4	133.9	4.0	0.5	8	321.3	2
W.8H.72C-12	10.7	329.9	4.0	0	8	462.0	2
W.8L.73C-12	9.4	330.0	2.0	0	8	311.2	2
CW.8H.74C-12	10.4	330.1	4.0	0.5	8	461.0	2
CW.8L.75C-12	8.1	330.3	2.0	0.5	8	244.3	3
CW.30H.76C-12	9.7	330.4	4.0	0.5	30	406.7	3
CW.30L.77C-12	9.4	330.0	2.0	0.5	30	400.2	3
W.30H.83C-13	8.2	330.0	4.0	0	30	344.9	5
CW.8L.84C-14	9.6	330.1	2.0	0.5	8	457.0	1

Notes

(1) tests CW.8H.62C-10 and W.8H.64C-10 were lost
(2) tests W.30L.54C-09, W.6L.60C-10 and W.6H.61C-10 were abandoned
(3) s_u = index shear strength of the clay sample
(4) V = fixed vertical load
(5) M_a = peak-to-peak amplitude of the moment loading
(6) M_o = offset of the moment loading
(7) T = period of the moment loading
(8) V_{max} = maximum vertical load applied to the model footing before testing
(9) EC = index related to the area of the clay surface affected by the foundation at the end of the test

Figure 7.3 illustrates the clay surface after the end of test W.30H.83C-13, classified as EC = 5.

The tests are grouped by fixed vertical load, either a low value ($1.6s_uA$ to $2.0s_uA$) or a high value ($3.8s_uA$ to $5.4s_uA$), and by peak-to-peak amplitude of the moment loading, either assuming a low value ($0.18s_uD^3$ to $0.26s_uD^3$) or a high value ($0.37s_uD^3$ to $0.49s_uD^3$), as illustrated in Tables 7.2 and 7.4. Each group involves four tests, each test representing the combination of a period of sinusoidal loading (either 8 seconds or 30 seconds), and an offset of the moment loading, either zero (simulating only wave action and denoted by W in test codes and tables) or a value between $0.05s_uD^3$ and $0.06s_uD^3$ (simulating the associated action of current and wave and denoted by CW).

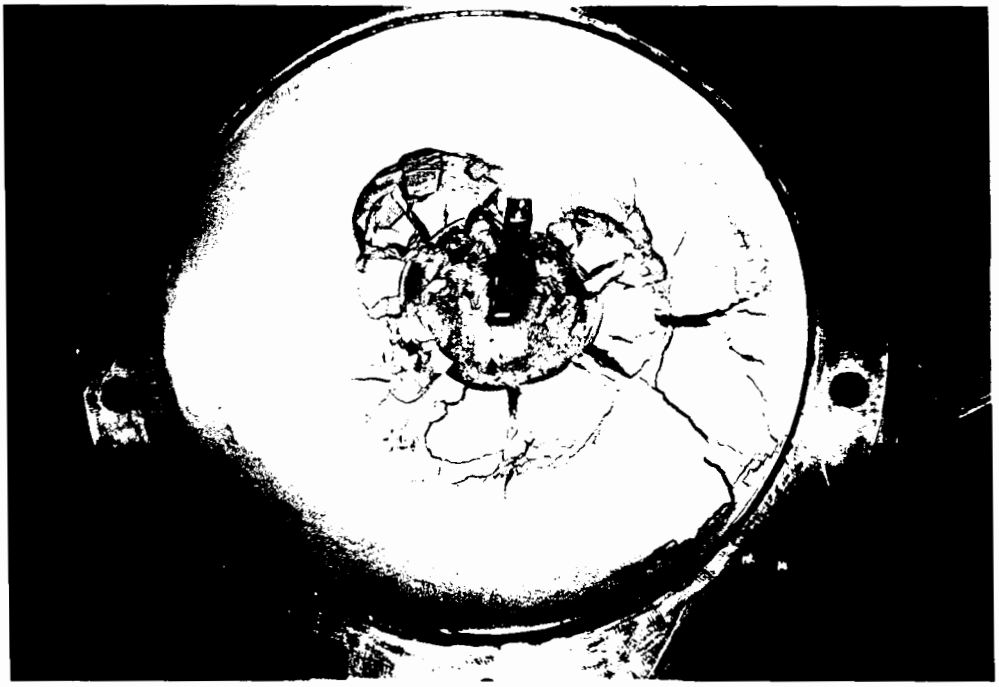

Figure 7.3 Aspect of the clay surface after the end of test W.30H.83C-13

7.2.1 A Representative Group of Tests

Table 7.2 shows how the representative tests were allocated within the groups described in the previous section while Table 7.3 shows the values of the non-dimensional vertical load, amplitude and offset of moment applied.

Figure 7.4 shows the shape of the dimensionless moment versus rotation hysteresis loops for tests W.30H.56C-09 and W.30H.83C-13, both corresponding to 30 seconds period and high amplitude of moment loading with no offset. The former test was carried out with low vertical load, $V/s_uA = 1.6$, and the latter one with high vertical load, $V/s_uA = 5.1$. The hysteresis loops for the ten first cycles are in both cases very similar to ellipses, which would be the result obtained for a pure linear viscoelastic behaviour. Test W.30H.56C-09 features an overall stiffer response in the first cycle than test W.30H.83C-13, this dissimilar behaviour being accounted for by the

Table 7.2 Representative group of cyclic loading tests

		low V/s_uA		**high** V/s_uA	
		8s period	30s period	8s period	30s period
low M_a/s_uD^3	**W**	W.8L.63C-10	W.30L.59C-09	W.8L.73C-12	W.30L.66C-11
	CW	CW.8L.65C-10	CW.30L.57C-09	CW.8L.84C-14	CW.30L.77C-12
high M_a/s_uD^3	**W**	W.8H.70C-11	W.30H.56C-09	W.8H.72C-12	W.30H.83C-13
	CW	CW.8H.71C-11	CW.30H.58C-09	CW.8H.74C-12	CW.30H.76C-12

Table 7.3 Loading parameters of the main series of cyclic loading tests

		low V/s_uA		high V/s_uA	
		8s period	30s period	8s period	30s period
low M_a/s_uD^3	W	V/s_uA=2.0 M_a/s_uD^3=0.24 M_o/s_uD^3=0	V/s_uA=2.0 M_a/s_uD^3=0.24 M_o/s_uD^3=0	V/s_uA=4.5 M_a/s_uD^3=0.21 M_o/s_uD^3=0	V/s_uA=3.8 M_a/s_uD^3=0.18 M_o/s_uD^3=0
	CW	V/s_uA=1.8 M_a/s_uD^3=0.21 M_o/s_uD^3=0.05	V/s_uA=1.8 M_a/s_uD^3=0.21 M_o/s_uD^3=0.05	V/s_uA=4.4 M_a/s_uD^3=0.21 M_o/s_uD^3=0.05	V/s_uA=4.5 M_a/s_uD^3=0.21 M_o/s_uD^3=0.05
high M_a/s_uD^3	W	V/s_uA=1.7 M_a/s_uD^3=0.40 M_o/s_uD^3=0	V/s_uA=1.6 M_a/s_uD^3=0.38 M_o/s_uD^3=0	V/s_uA=3.9 M_a/s_uD^3=0.37 M_o/s_uD^3=0	V/s_uA=5.1 M_a/s_uD^3=0.49 M_o/s_uD^3=0
	CW	V/s_uA=1.8 M_a/s_uD^3=0.43 M_o/s_uD^3=0.05	V/s_uA=1.7 M_a/s_uD^3=0.41 M_o/s_uD^3=0.05	V/s_uA=4.0 M_a/s_uD^3=0.38 M_o/s_uD^3=0.05	V/s_uA=4.3 M_a/s_uD^3=0.41 M_o/s_uD^3=0.05

maximum non-dimensional moment, M/s_uD^3, in the former test reaching a value about 28 % higher than in the latter one, introducing thus a large permanent rotation in the direction of the loading. It is noticeable, however, that the initial stiffnesses are practically the same in both tests.

Considering the loops corresponding to the 1st, 5th, 10th and 100th (96th for test W.30H.56C-09) cycle, shown in Figure 7.5, it is clear that test W.30H.56C-09 exhibits work softening while test W.30H.83C-13 reveals work hardening. The large cumulative rotation angle of the latter test is discussed later.

(a)

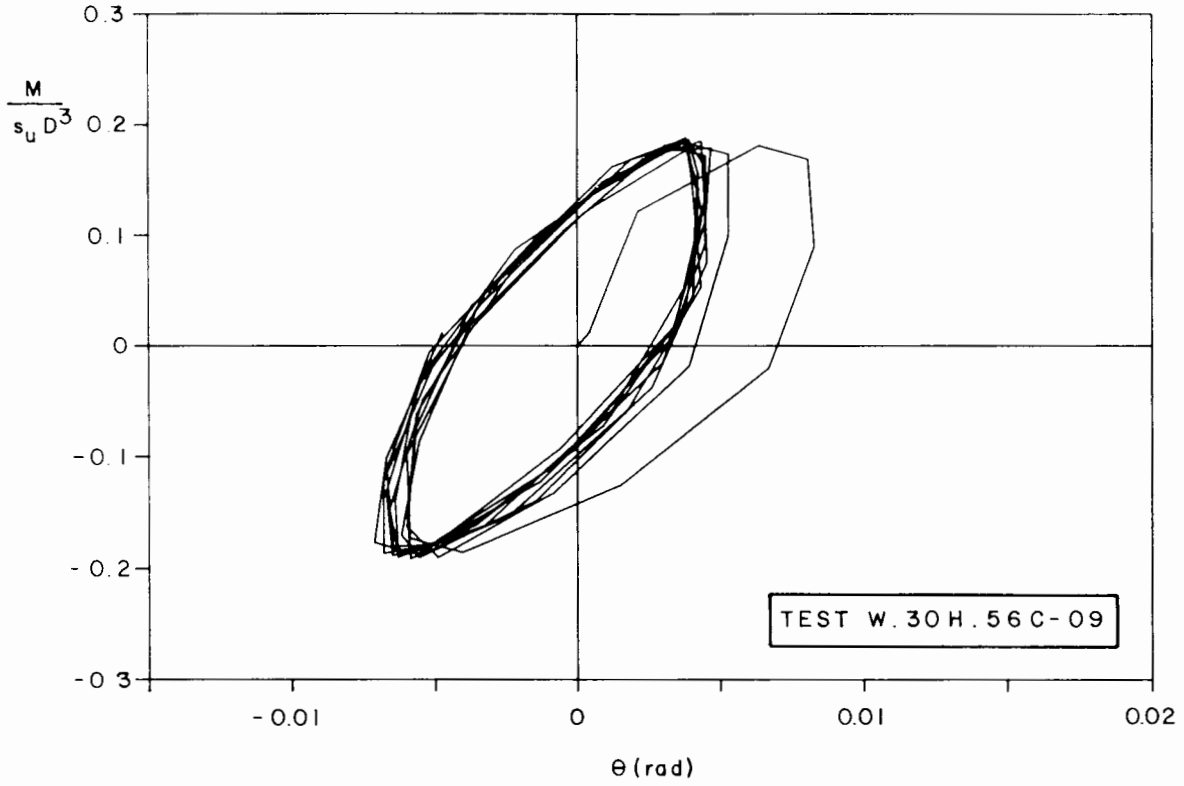

(b)

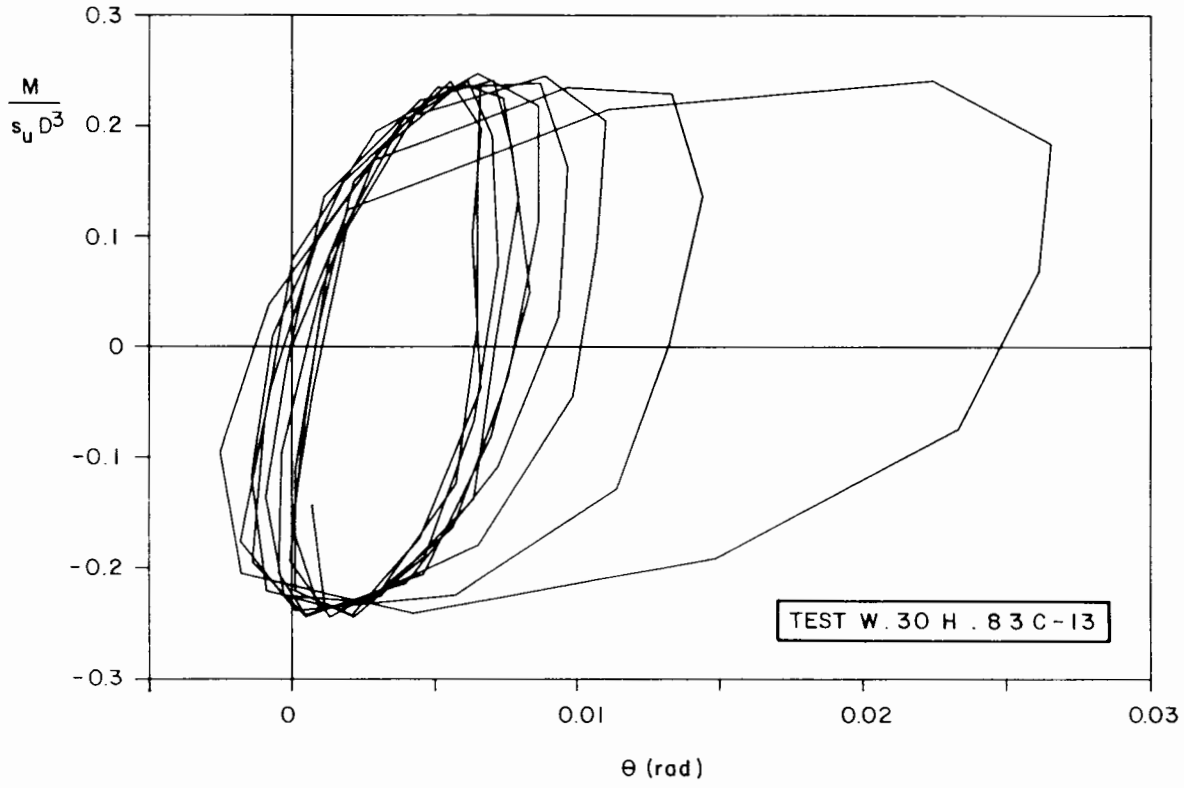

Figure 7.4 Dimensionless moment versus rotation hysteresis loops for the ten first cycles of tests W.30H.56C-09 and W.30H.83C-13

(a)

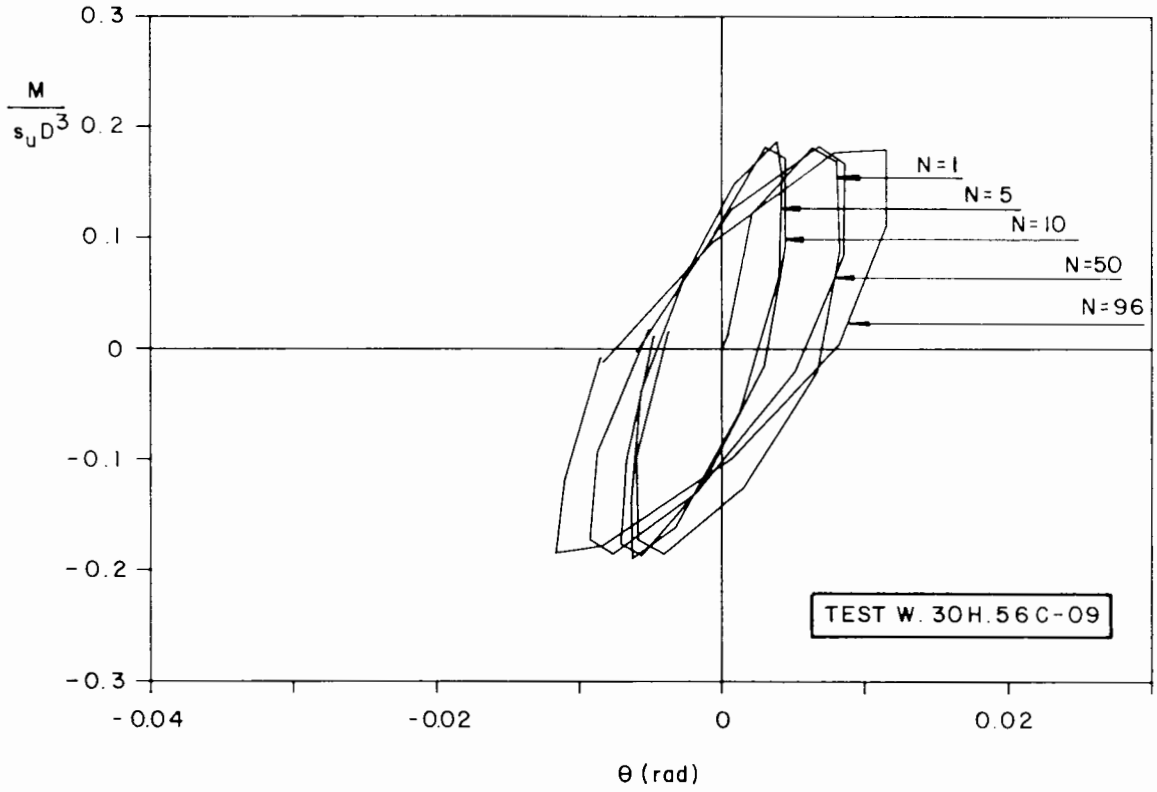

(b)

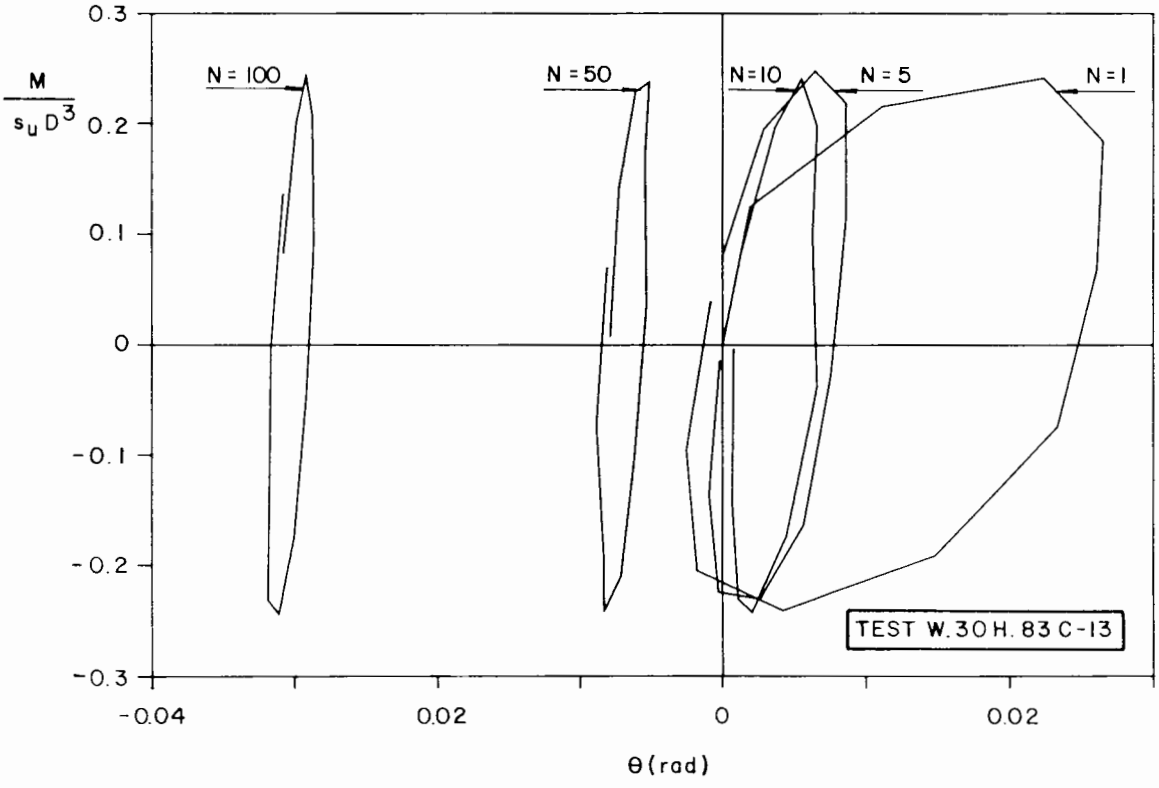

Figure 7.5 Dimensionless moment versus rotation hysteresis loops at various stages during tests W.30H.56C-09 and W.30H.83C-13

Figures 7.6, 7.7, 7.8 and 7.9 show how the cumulative rotation angle varied with the number of cycles. Tests with no offset of moment generally exhibit a more stable behaviour for 30 seconds period, the exception being test W.30H.83C-13 (represented by diamonds in Figure 7.9), performed with high vertical load and high amplitude of moment, which shows a much higher cumulative rotation angle than a similar test performed with 8 seconds period (test W.8H.72C-12, represented by squares in the same figure). It is worth noting that test W.30H.83C-13 produced an extensive failure pattern (EC = 5) as displayed in Figure 7.3.

Tests with an offset of moment show a general trend of rotation angle being accumulated in the same direction as the offset, as would be expected. However, tests carried out with high vertical load and high amplitude of moment show some degree of fluctuation in cumulative rotation which even shows a large negative value in test CW.30H.76C-12 (represented by triangles in Figure 7.9). This anomalous behaviour may be explained by the fact that the mechanism of failure was due mainly to the high vertical load (EC = 3) and shows no preferential direction of movement. Rotation against the direction of the offset of moment may occur in such cases.

The cumulative dimensionless horizontal displacement versus number of cycles curves are presented in Figures 7.10, 7.11, 7.12, and 7.13. It can be observed that the trend of behaviour is similar to the cumulative rotation angle. Test CW.30H.76C-12 (represented by triangles in Figure 7.13), performed with an offset in the moment loading and therefore also of the horizontal loading, exhibits a backwards displacement of approximately 0.007D between the 30th (point A) and the 320th (point B) cycles, after which the direction of the movement is reversed. This anomaly is also accounted for by a general failure being developed while the test was progressing.

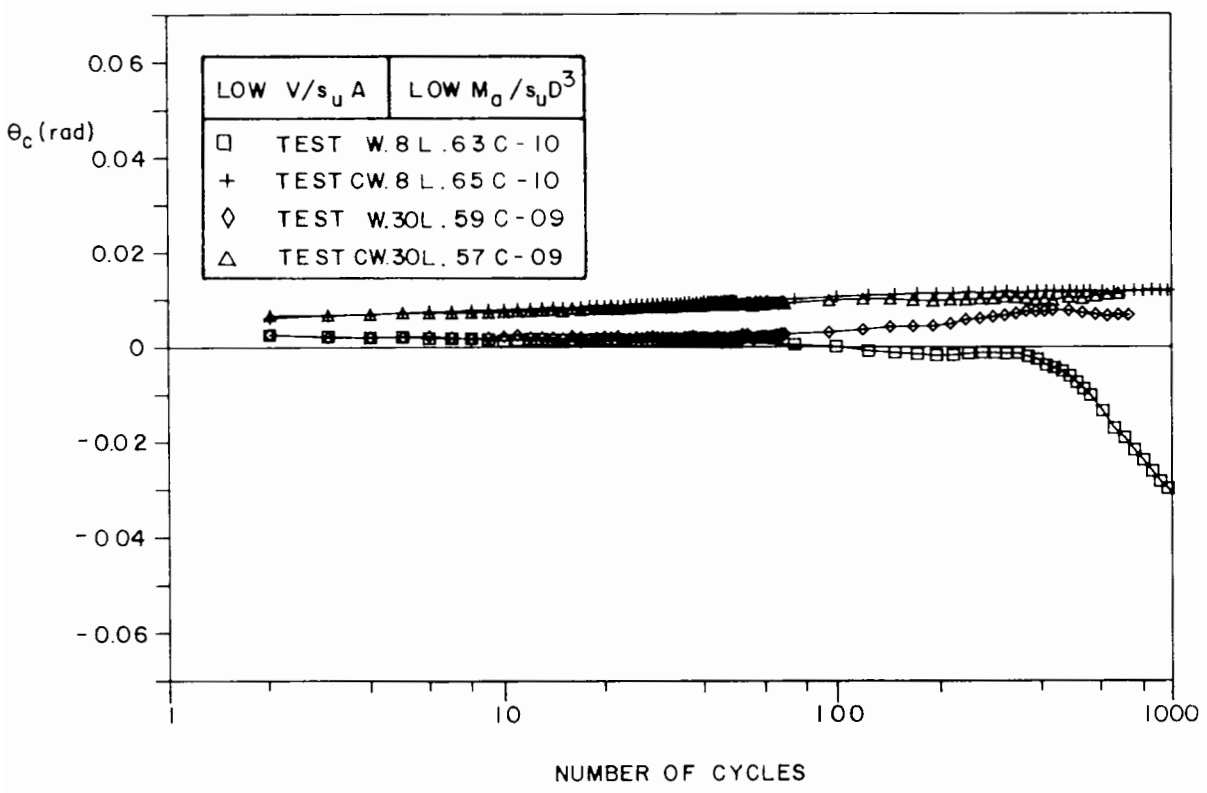

Figure 7.6 Cumulative rotation angle versus number of cycles curves (low vertical load, low amplitude of moment)

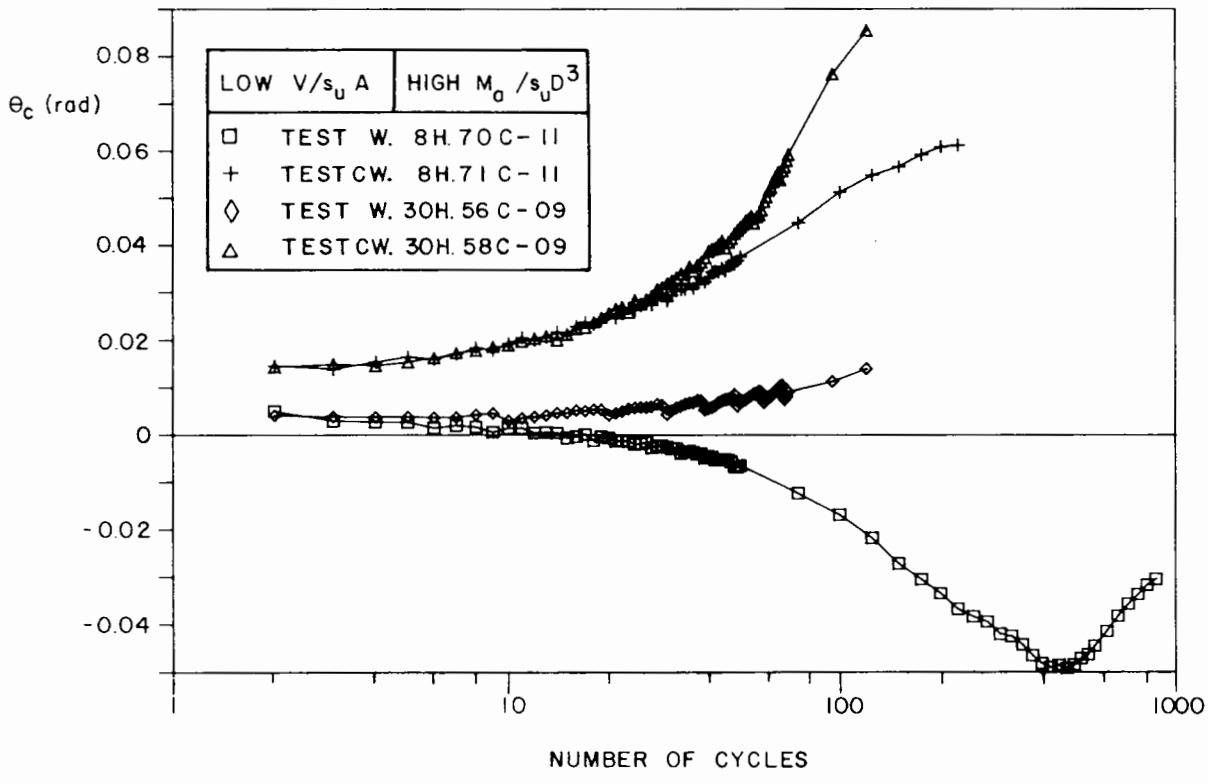

Figure 7.7 Cumulative rotation angle versus number of cycles curves (low vertical load, high amplitude of moment)

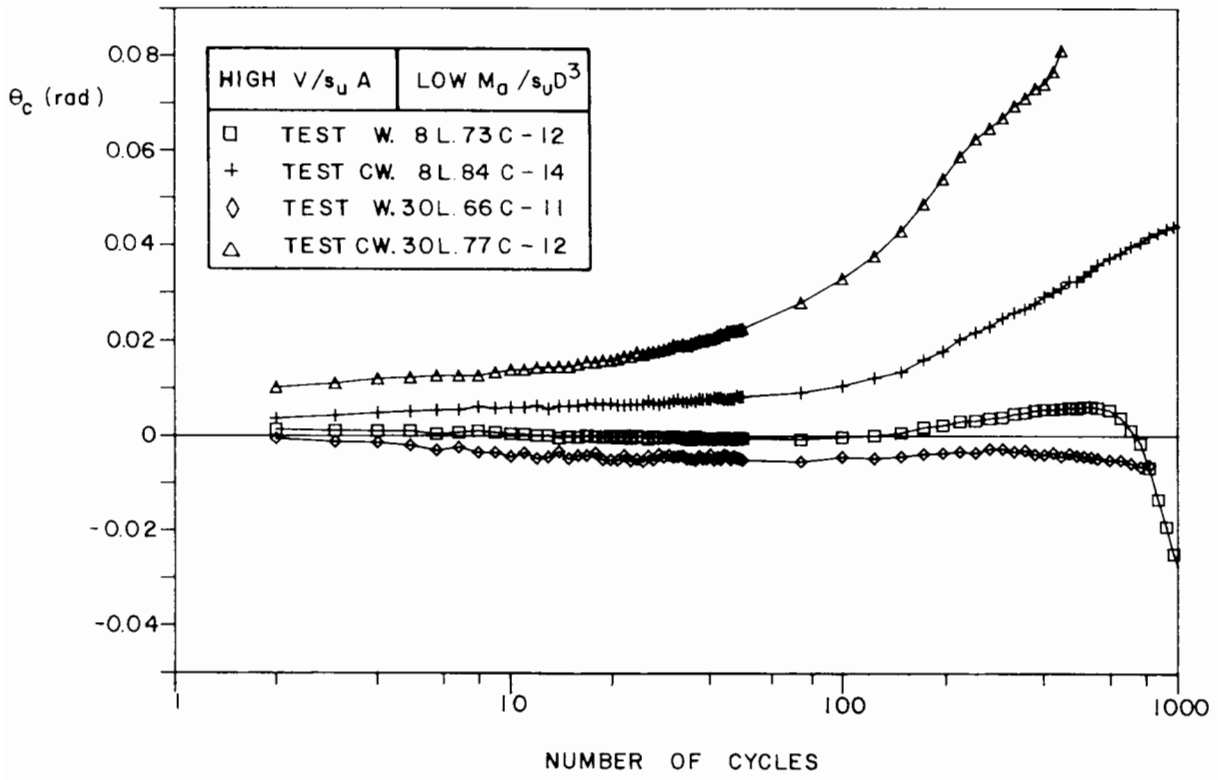

Figure 7.8 Cumulative rotation angle versus number of cycles curves (high vertical load, low amplitude of moment)

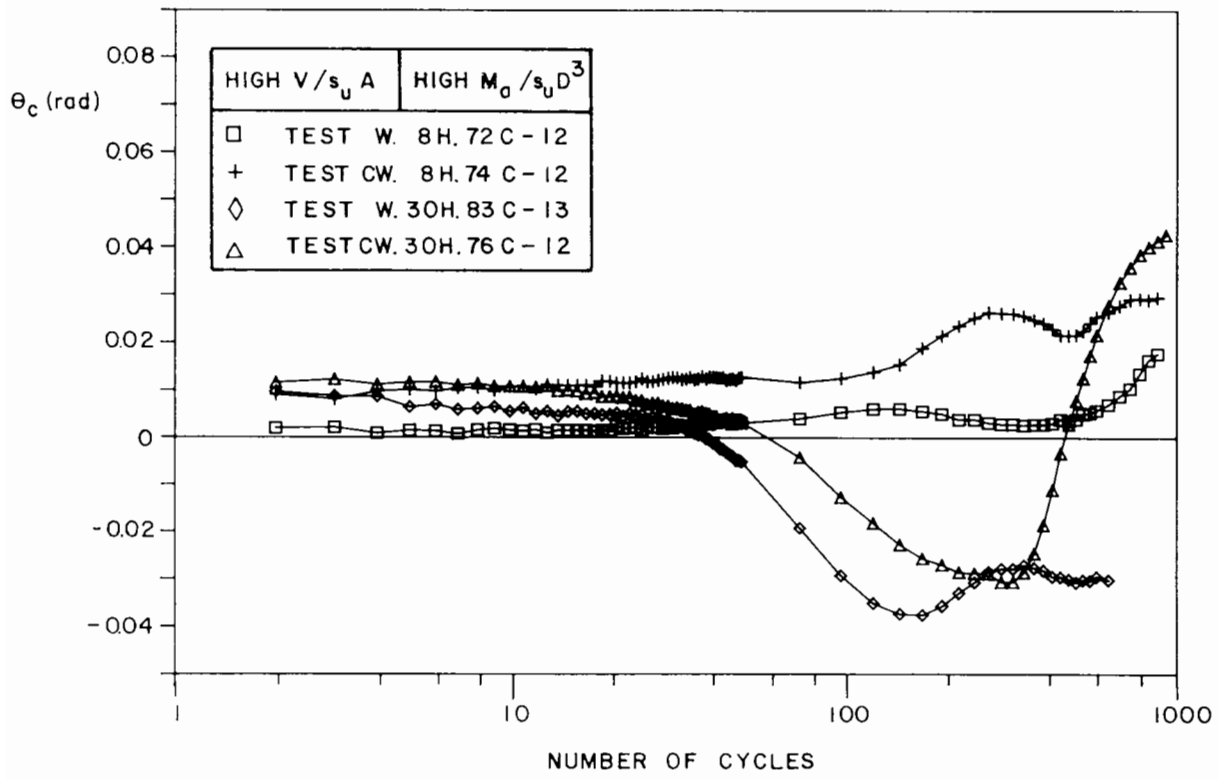

Figure 7.9 Cumulative rotation angle versus number of cycles curves (high vertical load, high amplitude of moment)

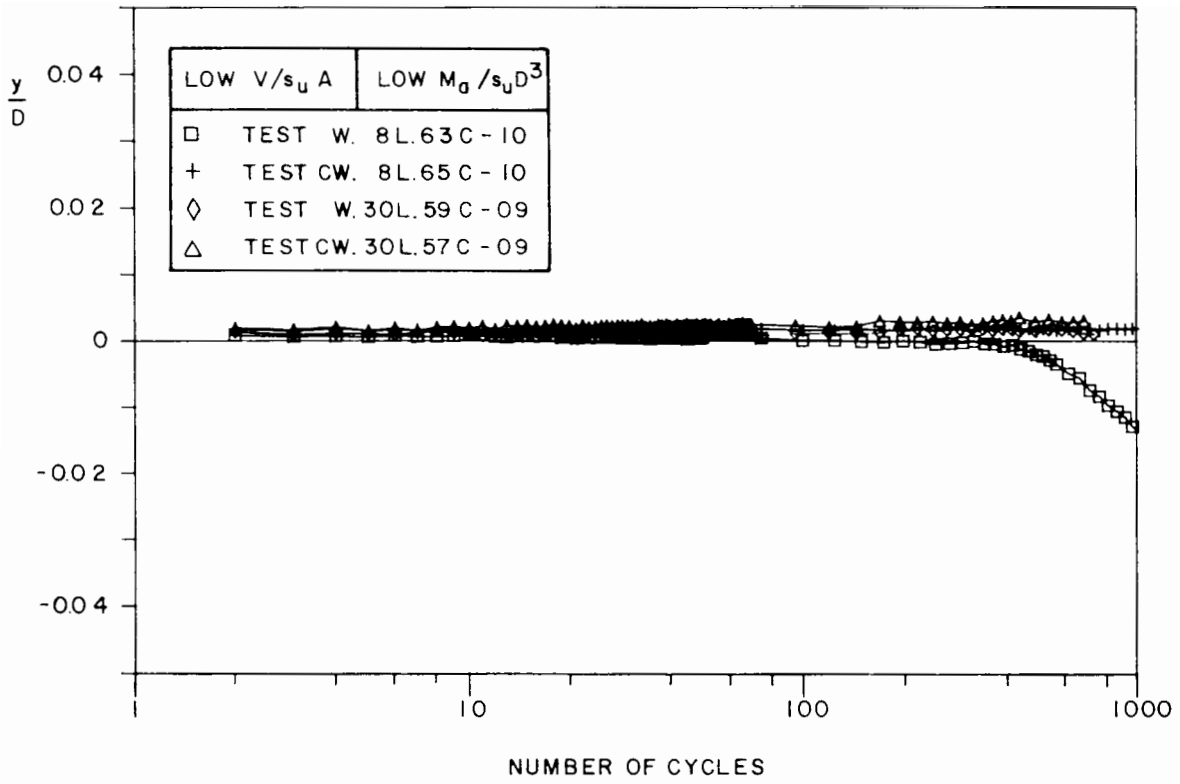

Figure 7.10 Cumulative dimensionless horizontal displacement versus number of cycles curves (low vertical load, low amplitude of moment)

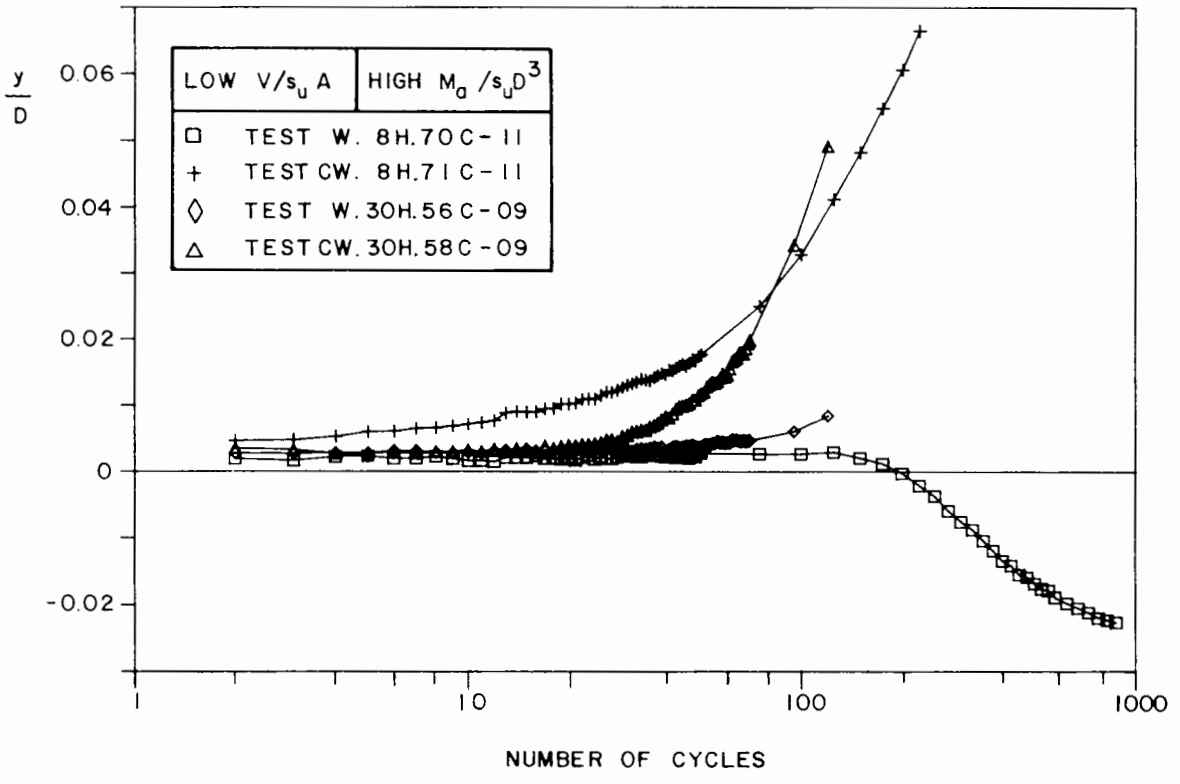

Figure 7.11 Cumulative dimensionless horizontal displacement versus number of cycles curves (low vertical load, high amplitude of moment)

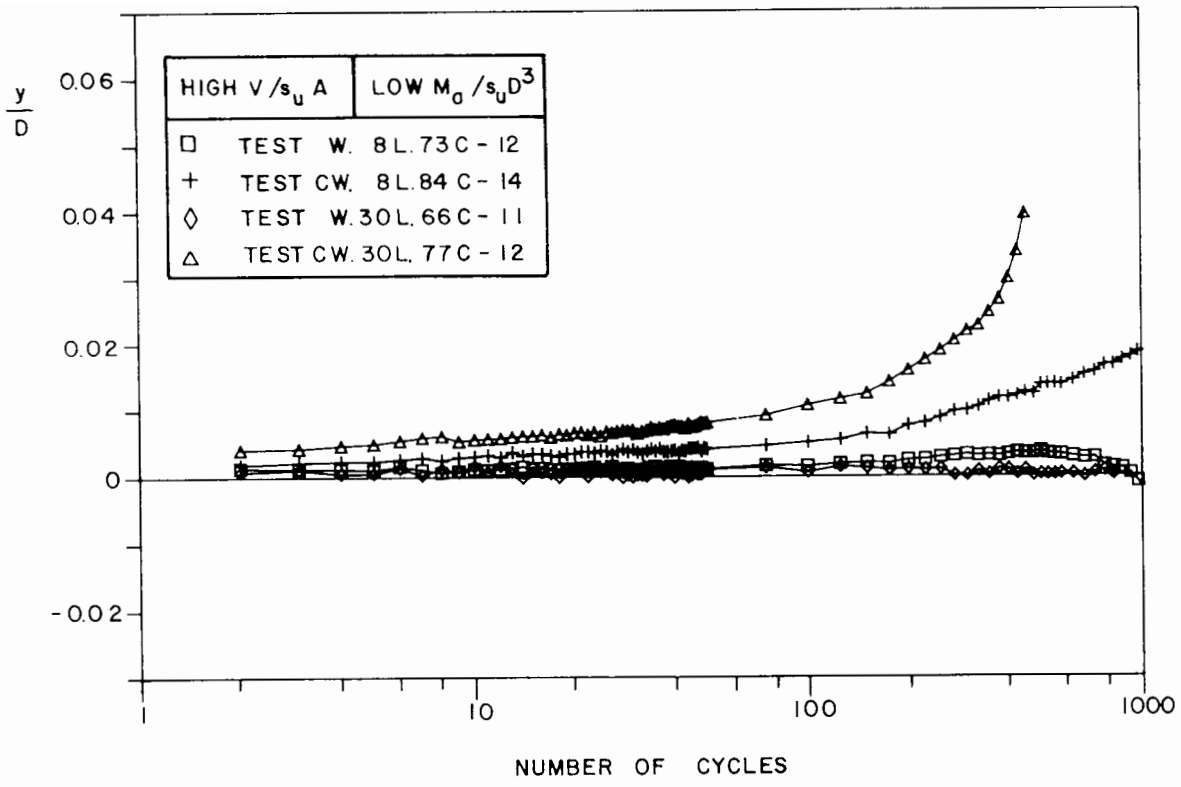

Figure 7.12 Cumulative dimensionless horizontal displacement versus number of cycles curves (high vertical load, low amplitude of moment)

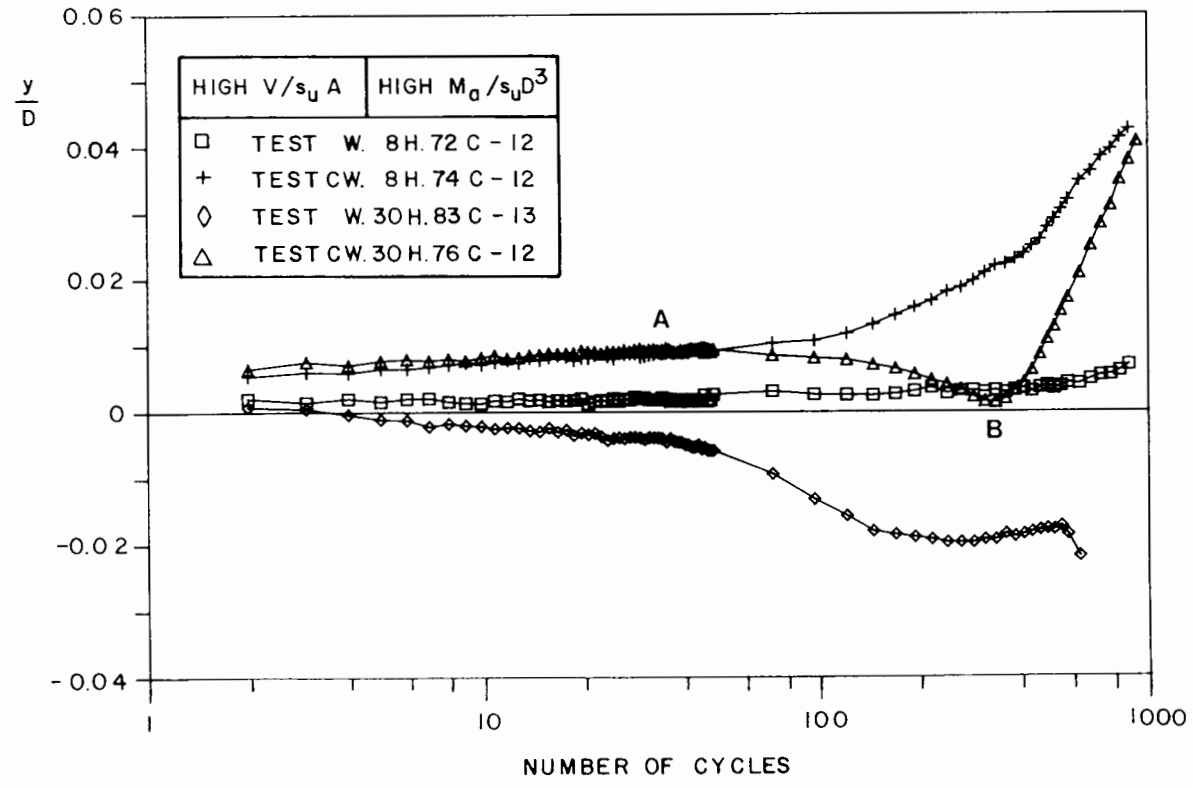

Figure 7.13 Cumulative dimensionless horizontal displacement versus number of cycles curves (high vertical load, high amplitude of moment)

For low vertical load (Figures 7.10 and 7.11), the cumulative horizontal displacement is noticeably larger for high amplitude of moment (and horizontal load) than for low amplitude, as would be expected. For high vertical load (Figures 7.12 and 7.13) and except for slow W tests (30 seconds period, no offset of moment loading), however, the magnitudes of the horizontal displacement are not markedly different for low and high amplitude of moment.

Test CW.30L.77C-12 (represented by triangles in Figure 7.12) exhibits cumulative horizontal displacements increasing steeply from approximately the 380th cycle on, showing a progressive failure process (EC = 3).

Figures 7.14, 7.15, 7.16 and 7.17 show the evolution of the cumulative dimensionless vertical displacement with the number of cycles. Allowing for differential initial settlements, which vary with the values of V/s_uA, the results suggest that the subsequent cumulative vertical displacements are more strongly related to the amplitude of moment than to the value of the vertical load.

Tests performed with low vertical load and low amplitude of moment (Figure 7.14) show increment of vertical displacement (after the application of the vertical load) less than 0.01D for about 700 cycles, test W.8L.63C-10 (data points represented by squares) being an exception and exhibiting an increment of settlement of about 0.05D for 1000 cycles.

For high vertical load and low amplitude of moment (Figure 7.16) the increment of vertical displacement for 800 cycles varies from about 0.03D to 0.06D in three tests of the group. Test CW.30L.77C-12 (data points represented by triangles), limited to 475 cycles of loading, exhibited a final increment of settlement of about 0.08D.

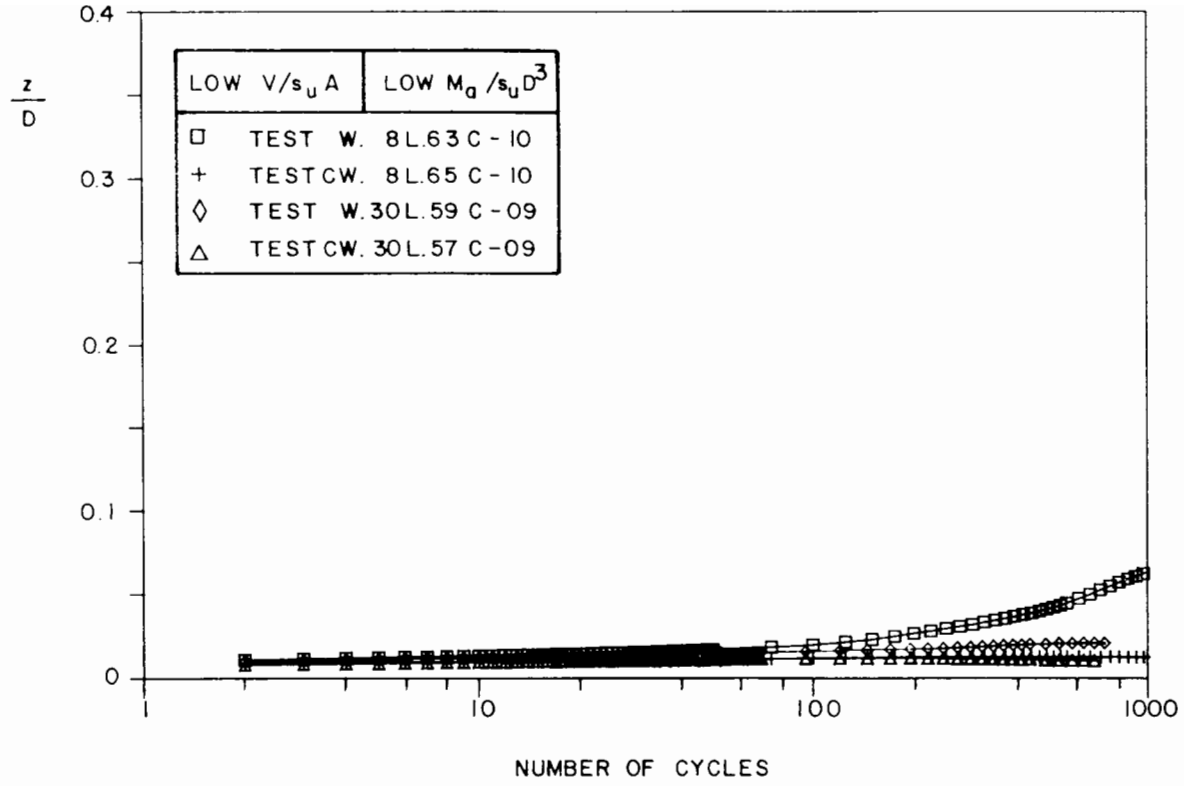

Figure 7.14 Cumulative dimensionless vertical displacement versus number of cycles curves (low vertical load, low amplitude of moment)

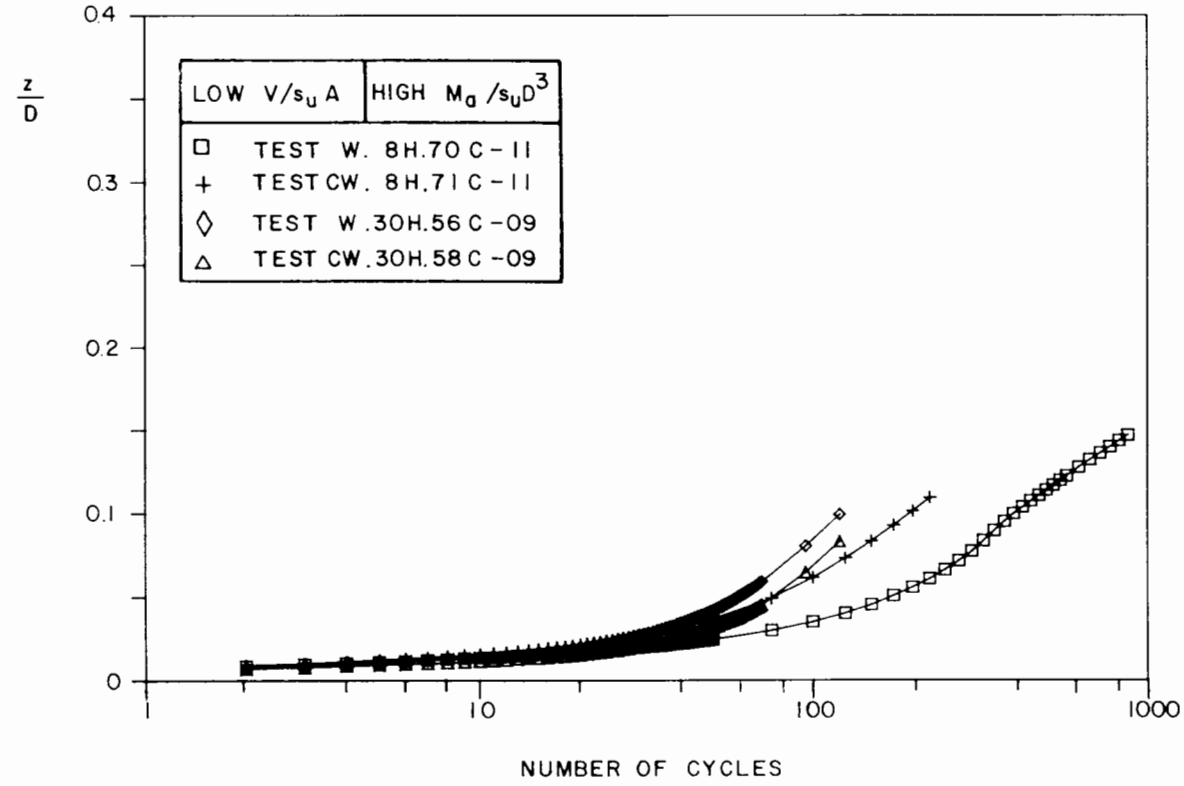

Figure 7.15 Cumulative dimensionless vertical displacement versus number of cycles curves (low vertical load, high amplitude of moment)

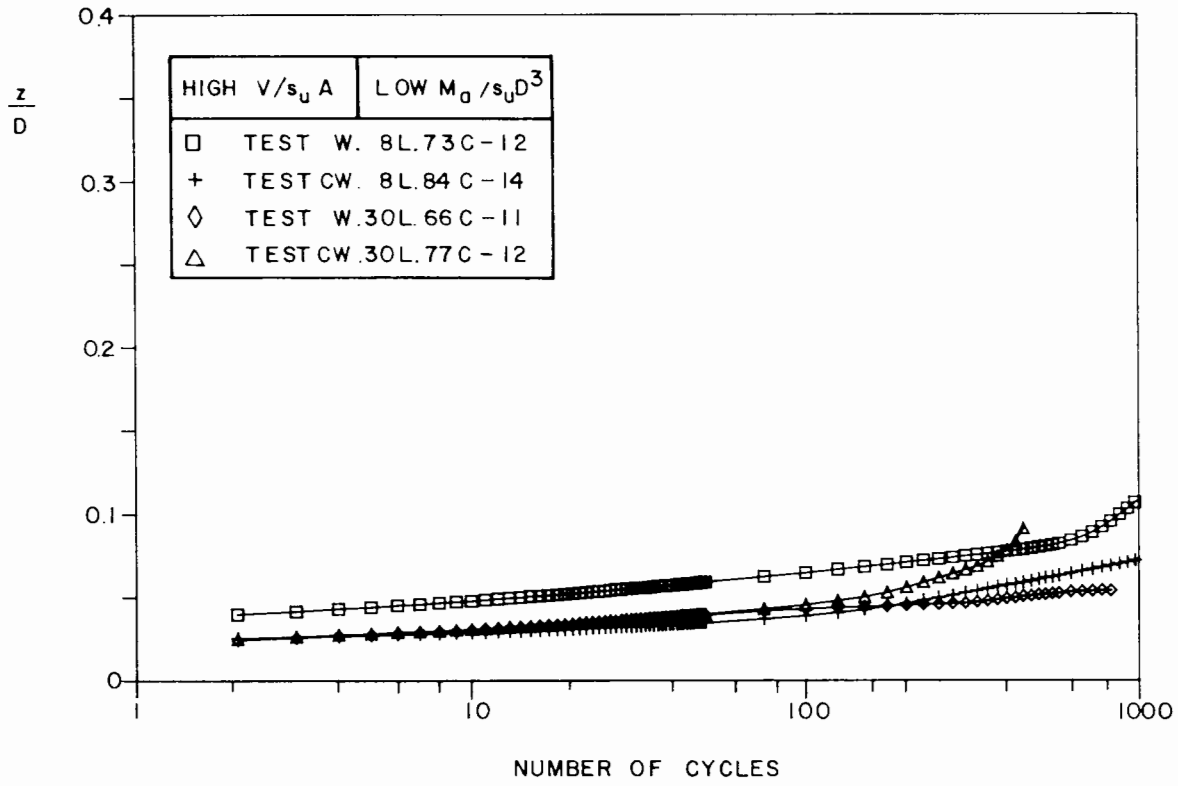

Figure 7.16 Cumulative dimensionless vertical displacement versus number of cycles curves (high vertical load, low amplitude of moment)

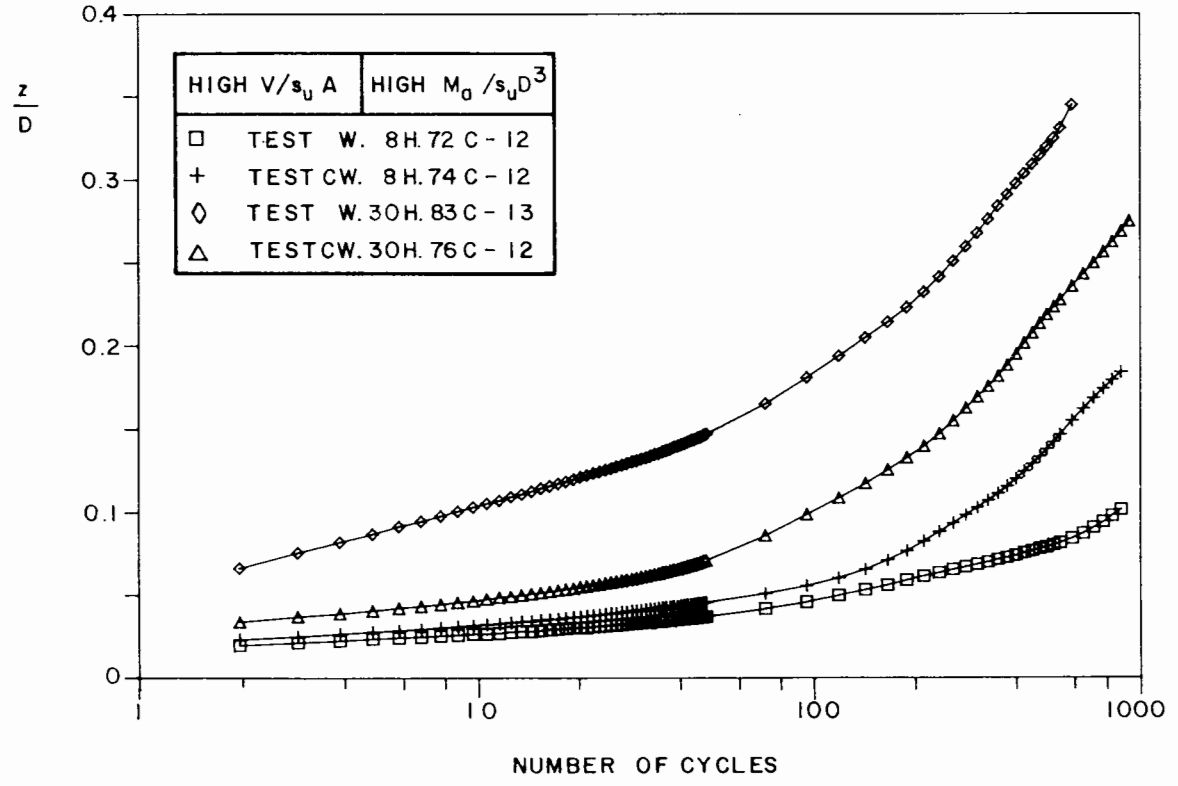

Figure 7.17 Cumulative dimensionless vertical displacement versus number of cycles curves (high vertical load, high amplitude of moment)

Slow tests (30 seconds period) with high amplitude of moment (represented by diamonds and triangles in Figures 7.15 and 7.17) seem to produce larger cumulative vertical displacements than fast tests (8 seconds period, represented by squares and crosses in the same figures).

In many cases the cumulative vertical displacement is approximately linear with the number of cycles after about 600 cycles. This feature, however, is clearer on linear rather than logarithmic plots (not shown).

Figures 7.18, 7.19, 7.20 and 7.21 show the variation of rotation $\Delta\theta$ (Figure 7.1) versus number of cycles. Despite the irregularities owing to inaccuracies in the data logging system (the process involves the measurement of very small rotations) the patterns of behaviour are clearly identifiable.

Tests with low vertical load and low amplitude of moment become steadily stiffer with the number of cycles when an offset of moment is applied (tests CW.30L.57C-09 and CW.8L.65C-10, represented by triangles and crosses respectively in Figure 7.18), while tests with no offset (W.30L.59C-09 and W.8L.63C-10, represented by diamonds and squares respectively in the same figure) stiffen up to about 30 to 40 cycles, slightly softening then up to 1000 cycles.

In the group of tests corresponding to low vertical load and high amplitude of moment (Figure 7.19), slow tests (represented by diamonds and triangles) are more flexible at 100 cycles than fast tests (represented by squares and crosses). Test W.30H.56C-09 (diamonds) becomes increasingly more flexible with the number of cycles, the variation of rotation at 100 cycles being approximately 180 % higher than its initial value. Test CW.30H.58C-09 (triangles) features an initial slight stiffening behaviour, becoming more

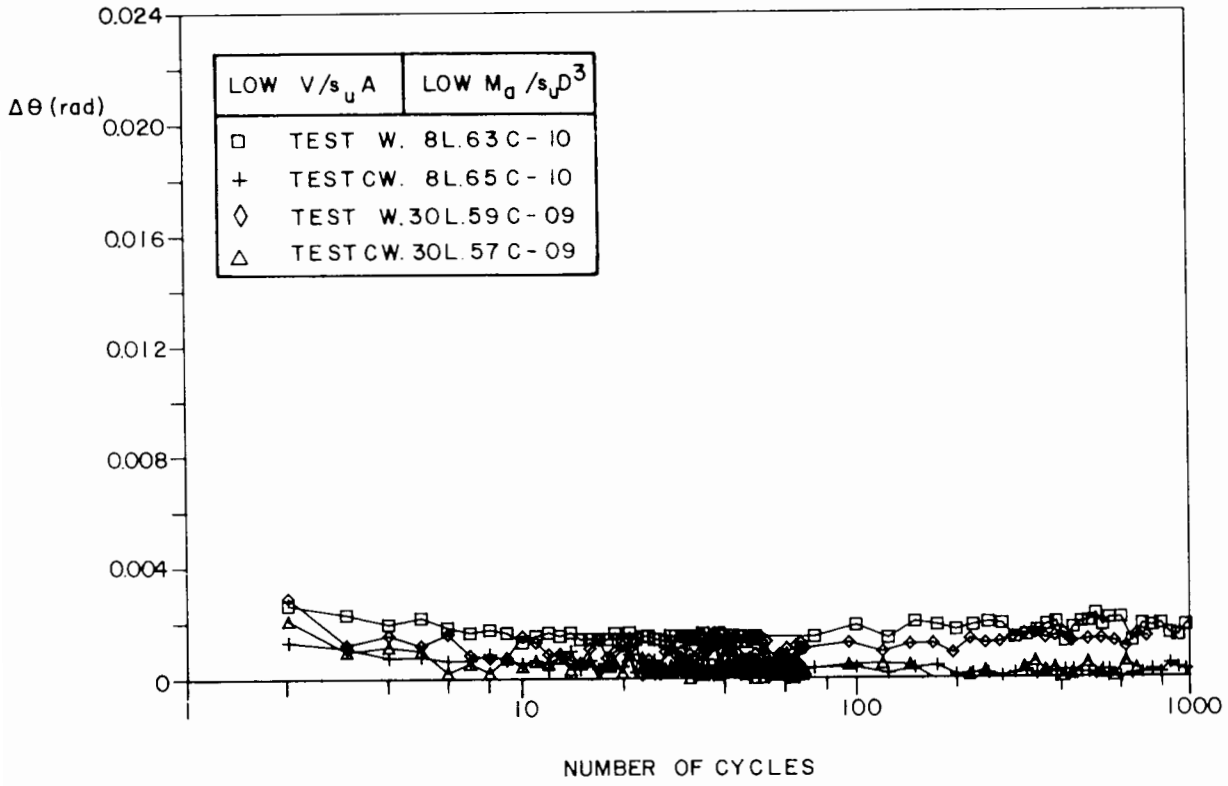

Figure 7.18 Variation of rotation versus number of cycles curves (low vertical load, low amplitude of moment)

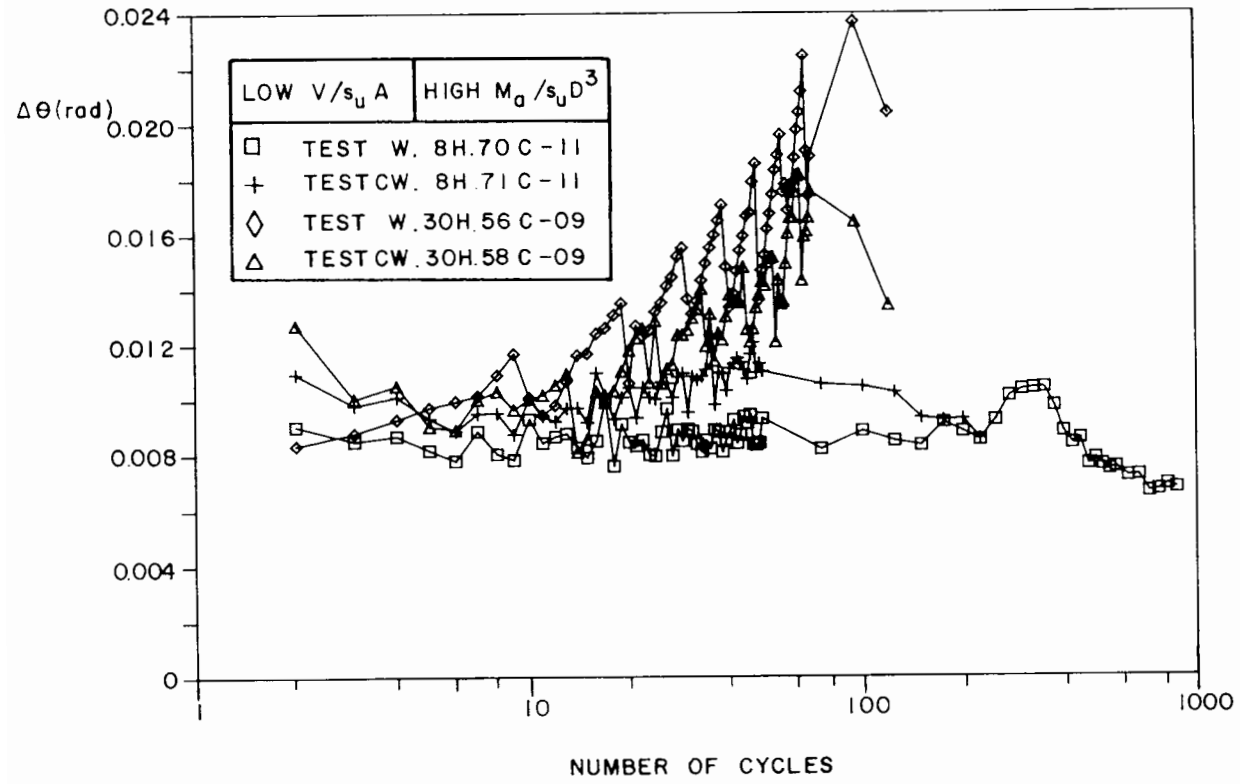

Figure 7.19 Variation of rotation versus number of cycles curves (low vertical load, high amplitude of moment)

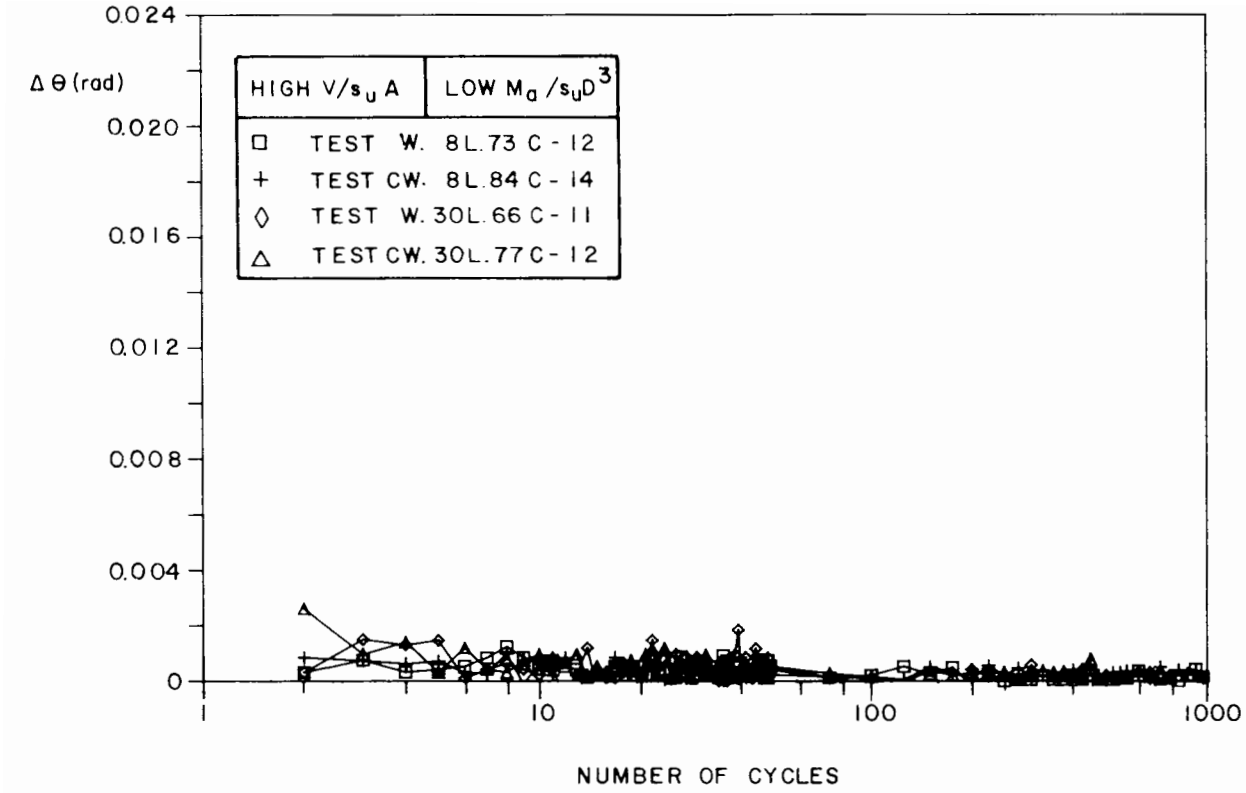

Figure 7.20 Variation of rotation versus number of cycles curves (high vertical load, low amplitude of moment)

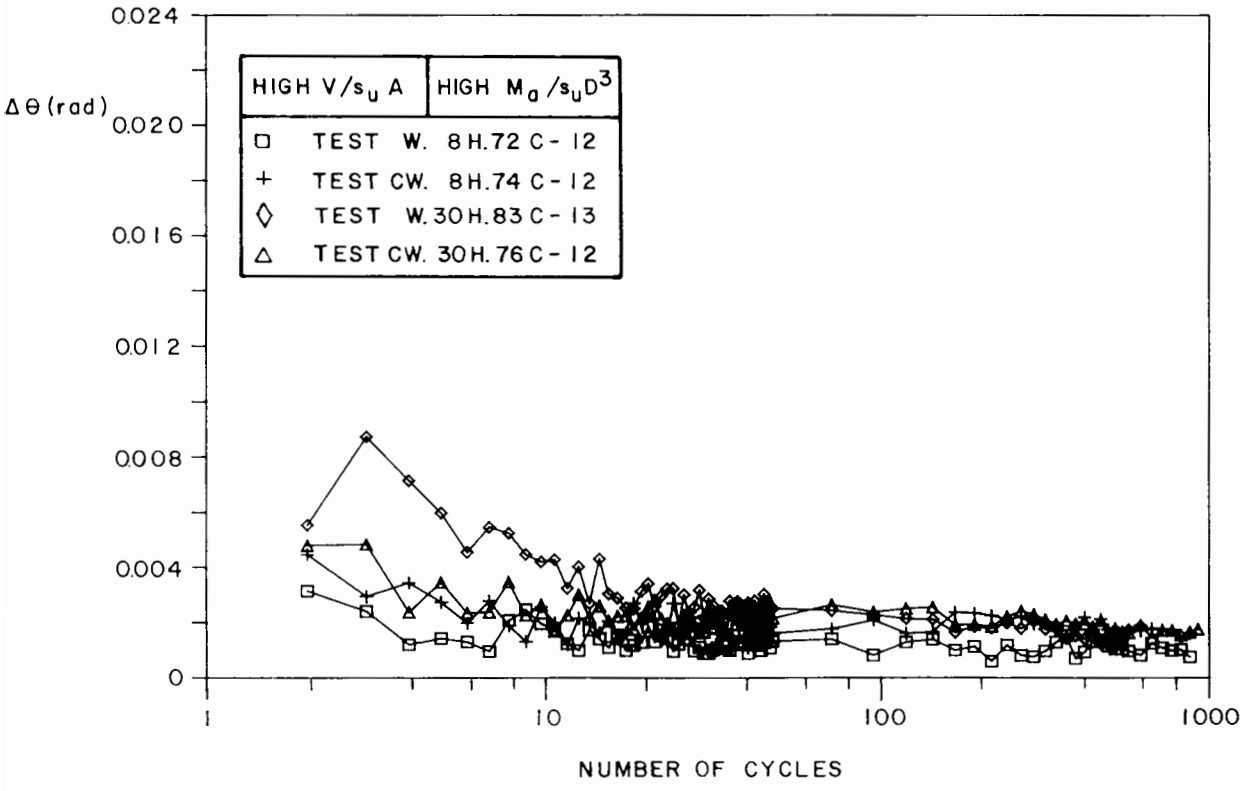

Figure 7.21 Variation of rotation versus number of cycles curves (high vertical load, high amplitude of moment)

flexible from the 6th cycle on and following approximately the same pattern as test W.30H.56C-09. Fast tests tend to show a constant value of $\Delta\theta$, allowing for some fluctuation observed.

The results of tests carried out with high vertical load (Figures 7.20 and 7.21) indicate a steady reduction in the variation of rotation $\Delta\theta$ with the number of cycles for each amplitude and offset of moment and for both periods, the magnitude of $\Delta\theta$ being in accordance with the magnitude of the amplitude of moment, as would be expected. Test W.30H.83C-13 (represented by diamonds in Figure 7.21) shows the most flexible response of the group of high vertical load and high amplitude of moment tests up to about 50 cycles.

The curves showing the dimensionless rotational energy dissipated per cycle $W/s_u D^3$ versus number of cycles are shown in Figures 7.22, 7.23, 7.24 and 7.25. The shape of these curves is remarkably similar to that of the curves for the variation of rotation. In slow tests with low vertical load and high amplitude of moment (represented by diamonds and triangles in Figure 7.23) the energy dissipated per cycle at 100 cycles is about 30 % and 80 % higher than their initial values for tests CW.30H.58C-09 (triangles) and W.30H.56C-09 (diamonds) respectively, while for fast tests (represented by squares and crosses in the same figure) this parameter tends slightly to decrease with the number of cycles.

Tests performed with high vertical load and high amplitude of moment (Figure 7.25) exhibit a marked fall in the energy dissipated per cycle with the progress of the test. The initial values of this parameter are rather different among the tests (varying from $0.0009 s_u D^3$ to $0.0054 s_u D^3$ per cycle), being higher for slow tests (represented by diamonds and triangles),

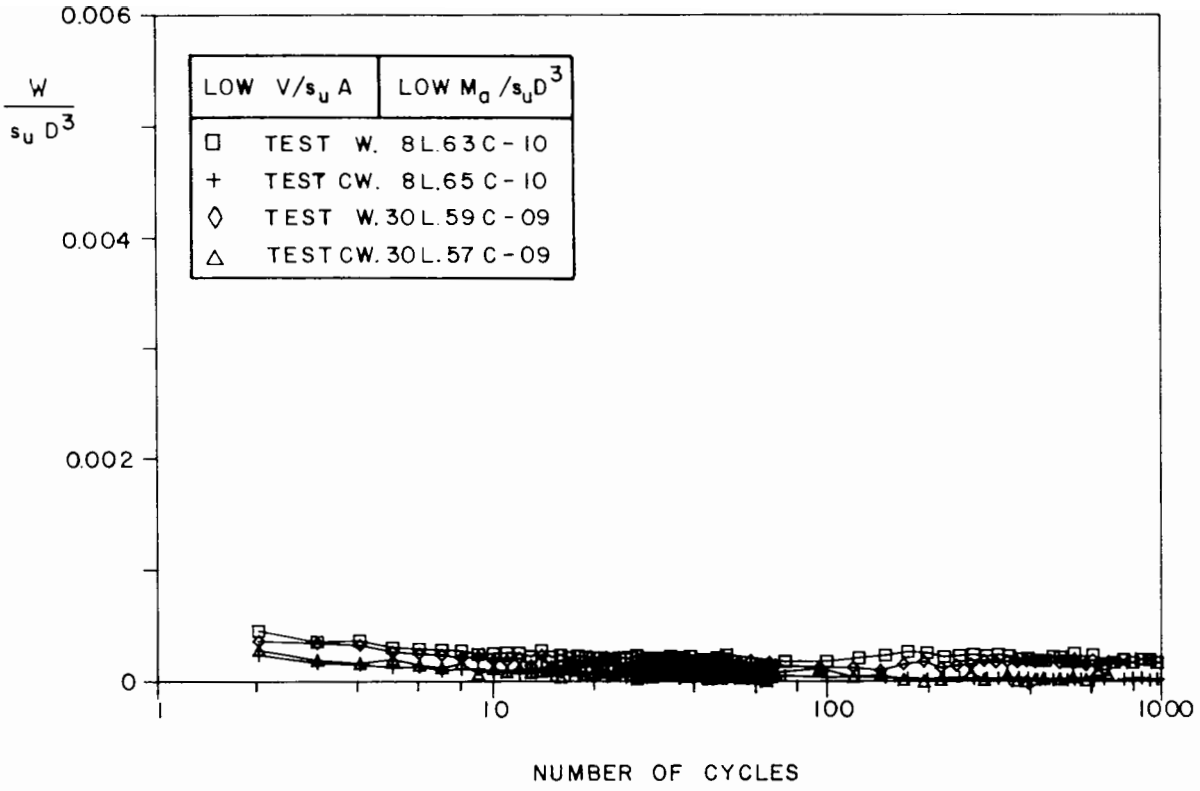

Figure 7.22 Dimensionless energy dissipated per cycle versus number of cycles curves (low vertical load, low amplitude of moment)

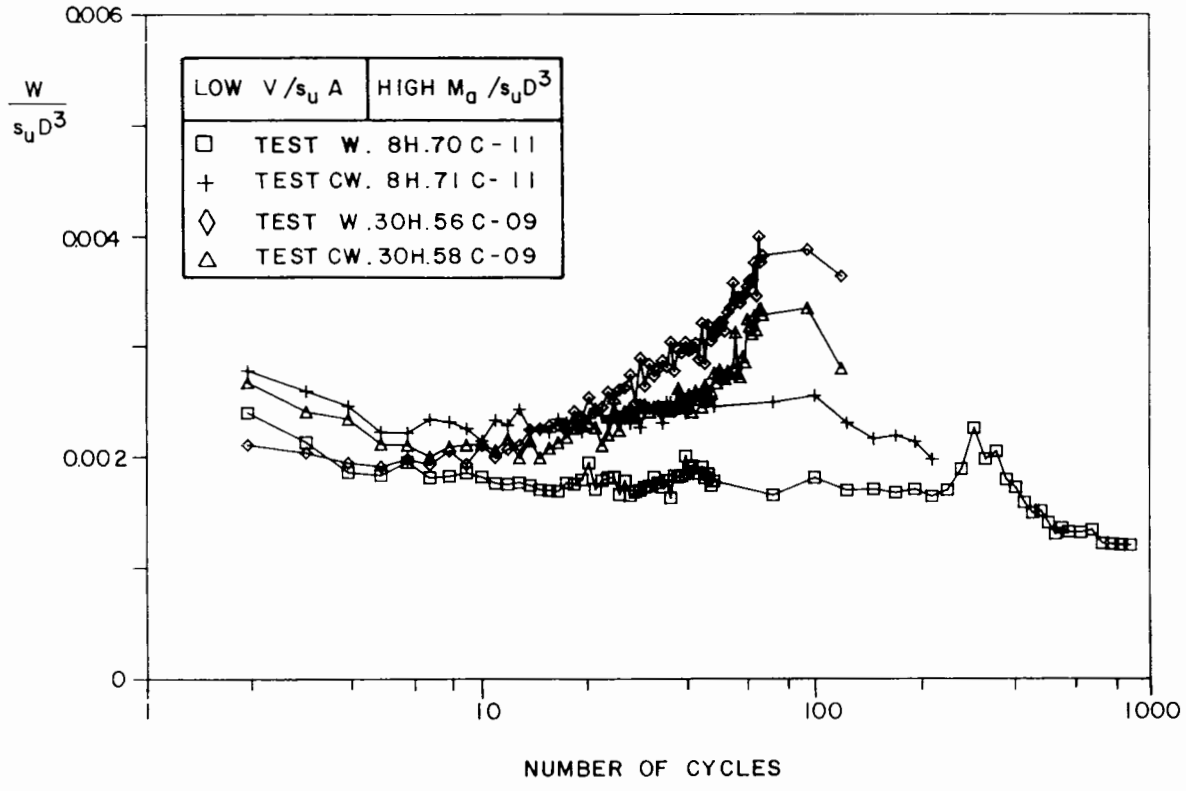

Figure 7.23 Dimensionless energy dissipated per cycle versus number of cycles curves (low vertical load, high amplitude of moment)

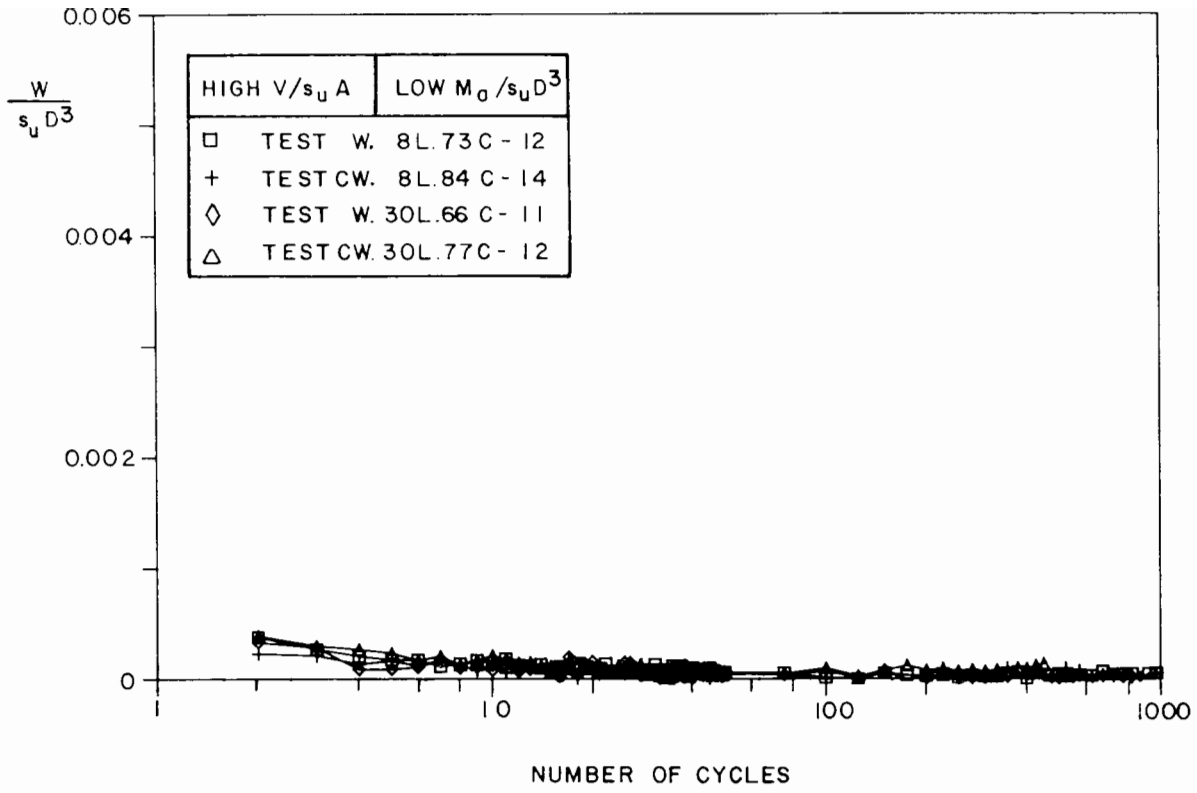

Figure 7.24 Dimensionless energy dissipated per cycle versus number of cycles curves (high vertical load, low amplitude of moment)

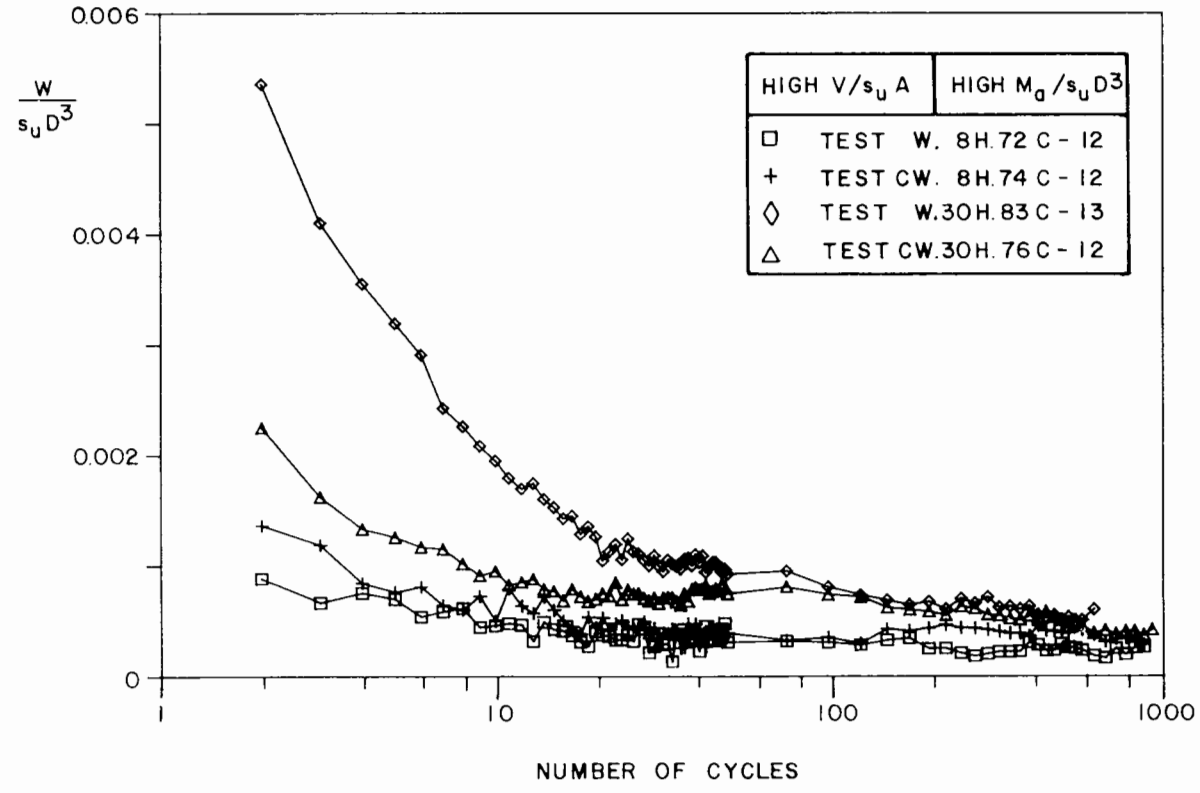

Figure 7.25 Dimensionless energy dissipated per cycle versus number of cycles curves (high vertical load, high amplitude of moment)

converging to a much narrower band after about 400 cycles (from $0.0002 s_u D^3$ to $0.0006 s_u D^3$ per cycle).

Tests with low amplitude of moment (Figures 7.22 and 7.24) dissipated very little energy, the initial values being less than $0.0005 s_u D^3$ per cycle. The energy dissipated per cycle for low vertical load is higher for tests with symmetric moment loading (represented by squares and diamonds in Figure 7.22) than for tests with an offset in the moment (represented by crosses and triangles in the same figure), although the difference is not significant when compared with typical magnitudes of $W/s_u D^3$ observed in tests with high amplitude of moment loading. At high vertical load (Figure 7.24) for any combination of offset of moment and of period, the energy dissipated per cycle is less than for the case of low vertical load.

7.2.2 Repeated Tests

The details of the repeated tests are given in Table 7.4, while Table 7.5 presents the values of the non-dimensional loading parameters for each test.

Fairly good repeatability has been observed in cyclic loading tests. It must be pointed out, however, that repeated tests were performed with the same loading and geometric parameters but, for reasons already discussed in Chapter 4, with some differences in the clay strength. This led to slight differences between dimensionless loading parameters in each pair of tests, initially supposed to be entirely identical, with inevitable consequences for the results.

Figures 7.26, 7.27, 7.28, 7.29 and 7.30 present a complete set of results involving tests CW.8L.84C-14 (represented by squares) and CW.8L.75C-12 (represented by crosses). It is worth mentioning that the results of test CW.8L.84C-14 (included in the representative group of tests), having already been presented, are in this section repeated for comparison purposes. Both tests were carried out under the same loading conditions but on clay samples of different strengths. The value of s_u in the former test is 19 % higher and this is apparent in the results: test CW.8L.84C-14 exhibits a lower total vertical displacement (about 35 % of the values for test CW.8L.75C-12, as indicated in Figure 7.28), a stiffer pattern of rotational behaviour (Figure 7.29) and a lower energy dissipated per cycle (Figure 7.30). Although the horizontal displacements are almost the same for both tests (Figure 7.27), the curves for the cumulative rotation angle (Figure 7.26) are rather different.

Figure 7.31 shows the clay surface at various stages during the progress of

Table 7.4 Repeated cyclic loading tests

		low V/s_uA		**high** V/s_uA	
		8s period	30s period	8s period	30s period
low M_a/s_uD^3	**W**		W.30L.55C-09		
	CW			CW.8L.75C-12	CW.30L.67C-11
high M_a/s_uD^3	**W**				W.30H.68C-11
	CW				CW.30H.69C-11

Table 7.5 Loading parameters of the repeated cyclic loading tests

		low V/s_uA		high V/s_uA	
		8s period	30s period	8s period	30s period
low M_a/s_uD^3	W		$V/s_uA=2.0$ $M_a/s_uD^3=0.24$ $M_o/s_uD^3=0$		
	CW			$V/s_uA=5.2$ $M_a/s_uD^3=0.25$ $M_o/s_uD^3=0.06$	$V/s_uA=5.4$ $M_a/s_uD^3=0.26$ $M_o/s_uD^3=0.06$
high M_a/s_uD^3	W				$V/s_uA=4.0$ $M_a/s_uD^3=0.38$ $M_o/s_uD^3=0$
	CW				$V/s_uA=4.7$ $M_a/s_uD^3=0.45$ $M_o/s_uD^3=0.06$

test CW.8L.75C-12. Figure 7.31 (a) illustrates the surface immediately after the application of the vertical load (V = 330.3 N). Some ground heave with radial cracks can be observed in Figure 7.31 (b), corresponding to 105 cycles of loading. Figure 7.31 (c) shows a volume of clay displaced on one side of the loading plane, at the 516th cycle. Finally, by the end of the test (1002 cycles), a large volume of clay displaced by the foundation can be noticed on both sides of the loading plane (Figure 7.31 (d)).

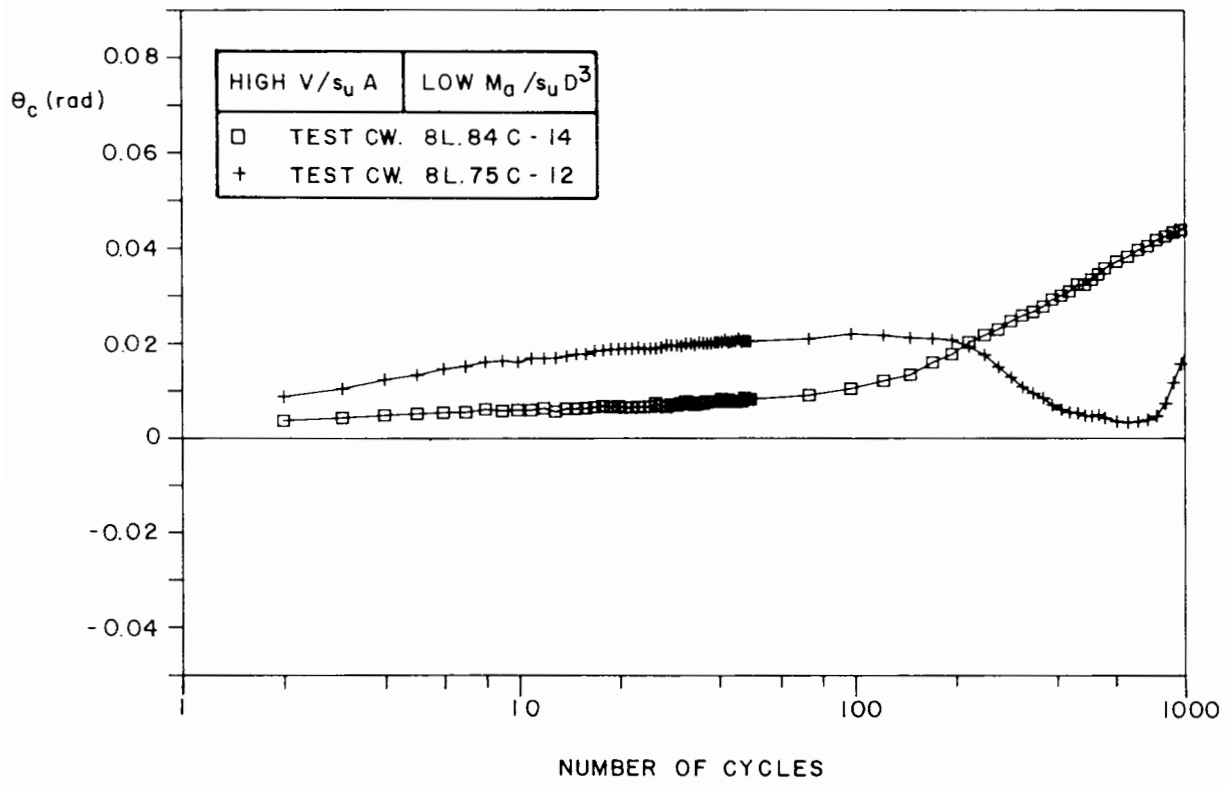

Figure 7.26 Cumulative rotation angle versus number of cycles curves for two tests carried out under the same loading conditions

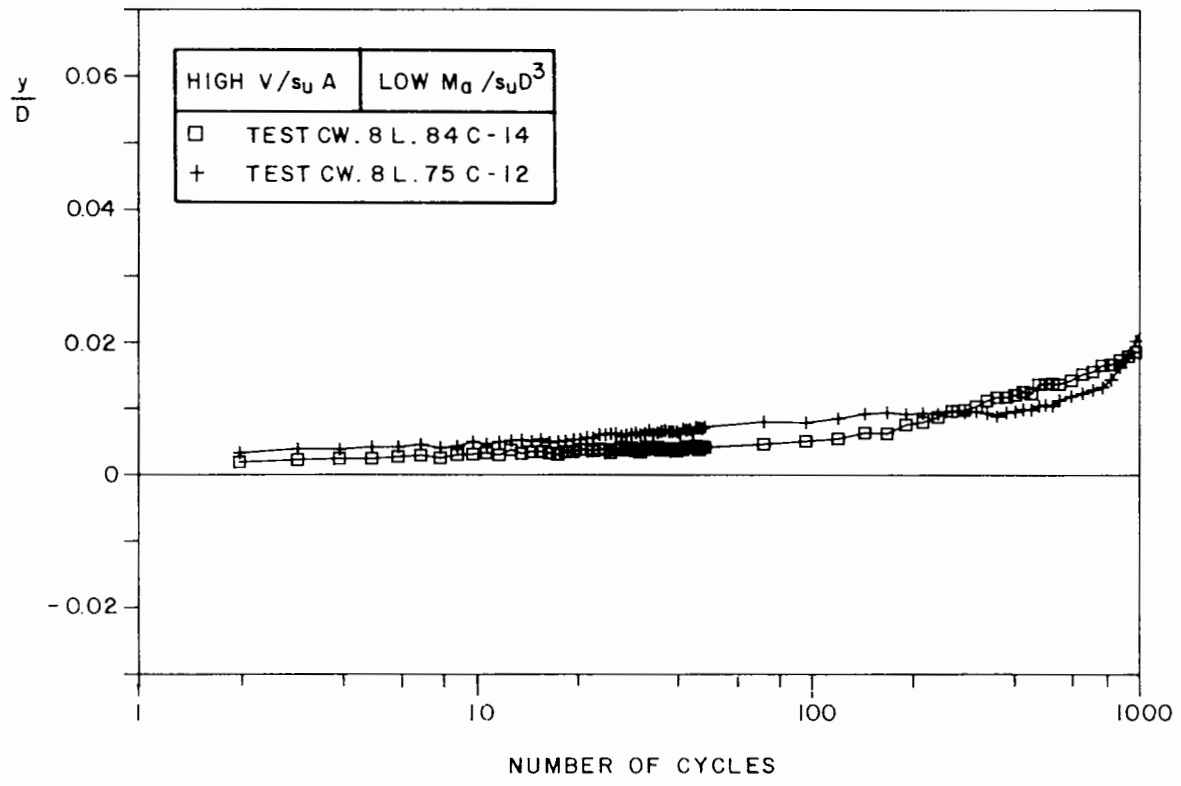

Figure 7.27 Cumulative dimensionless horizontal displacement versus number of cycles curves for two tests carried out under the same loading conditions

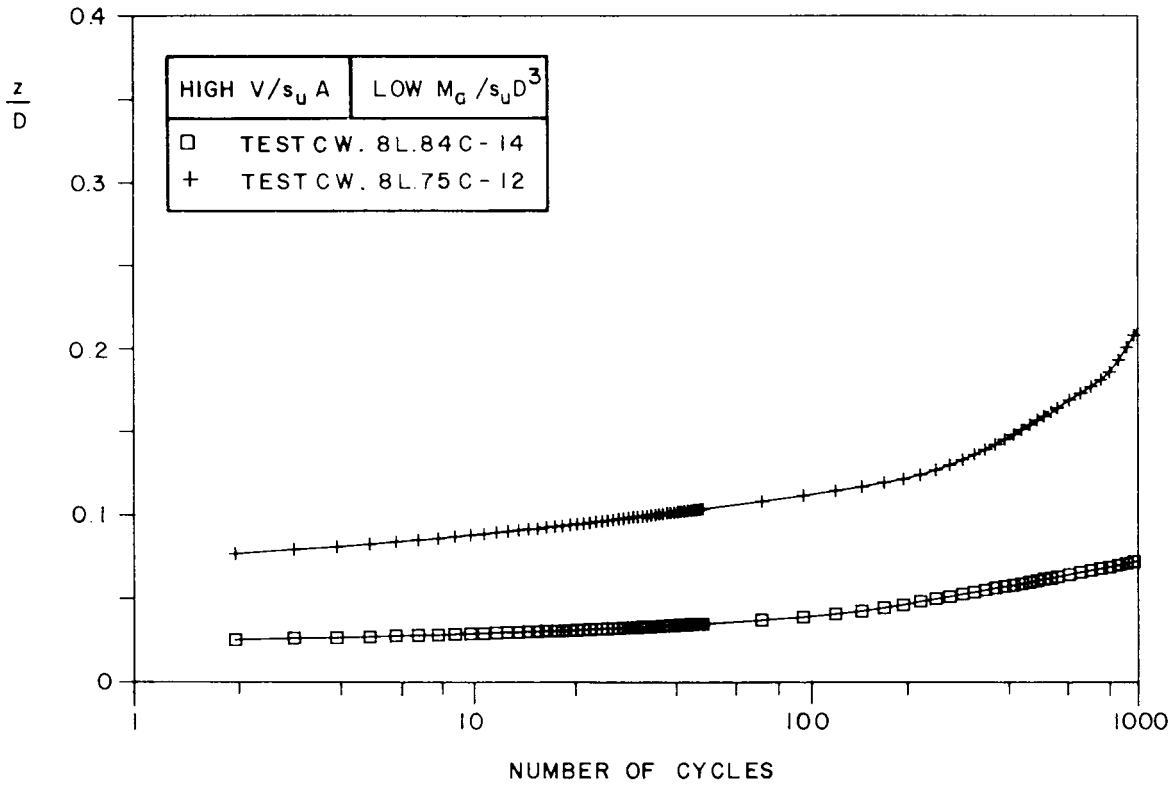

Figure 7.28 Cumulative dimensionless vertical displacement versus number of cycles curves for two tests carried out under the same loading conditions

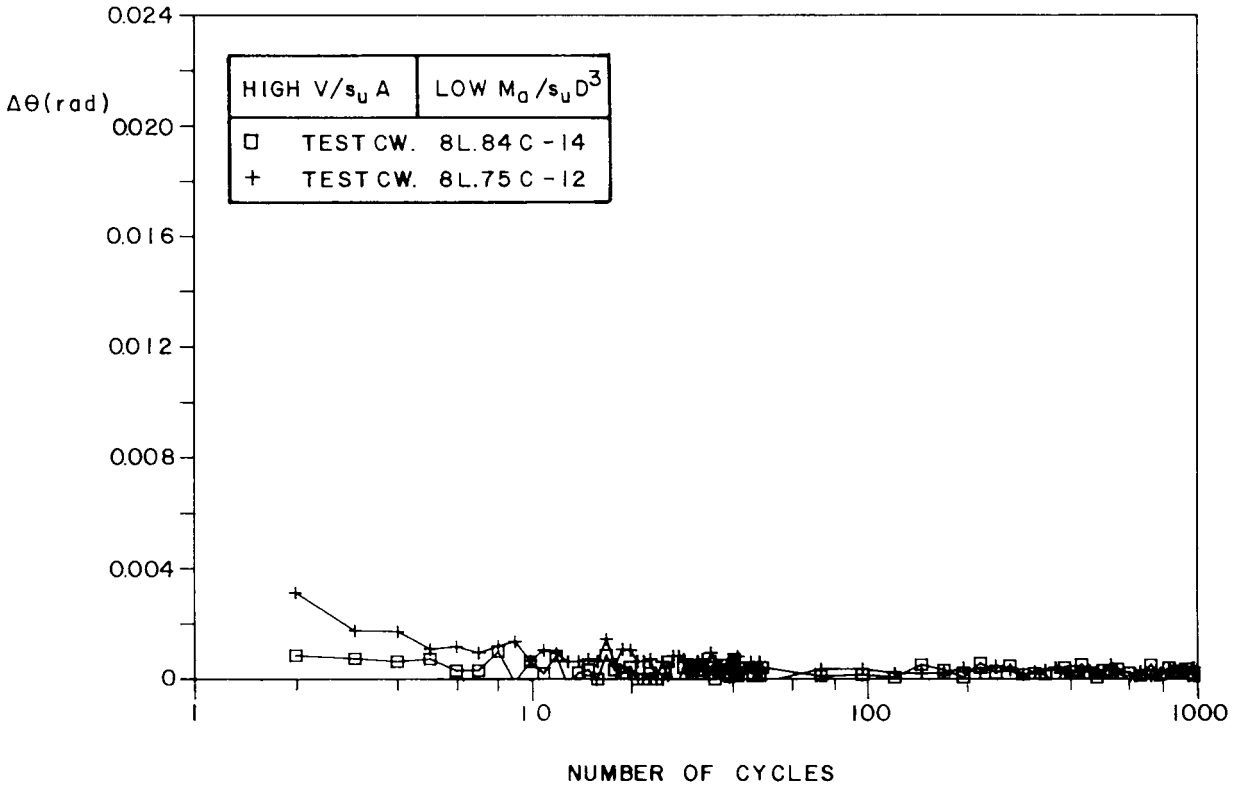

Figure 7.29 Variation of rotation versus number of cycles curves for two tests carried out under the same loading conditions

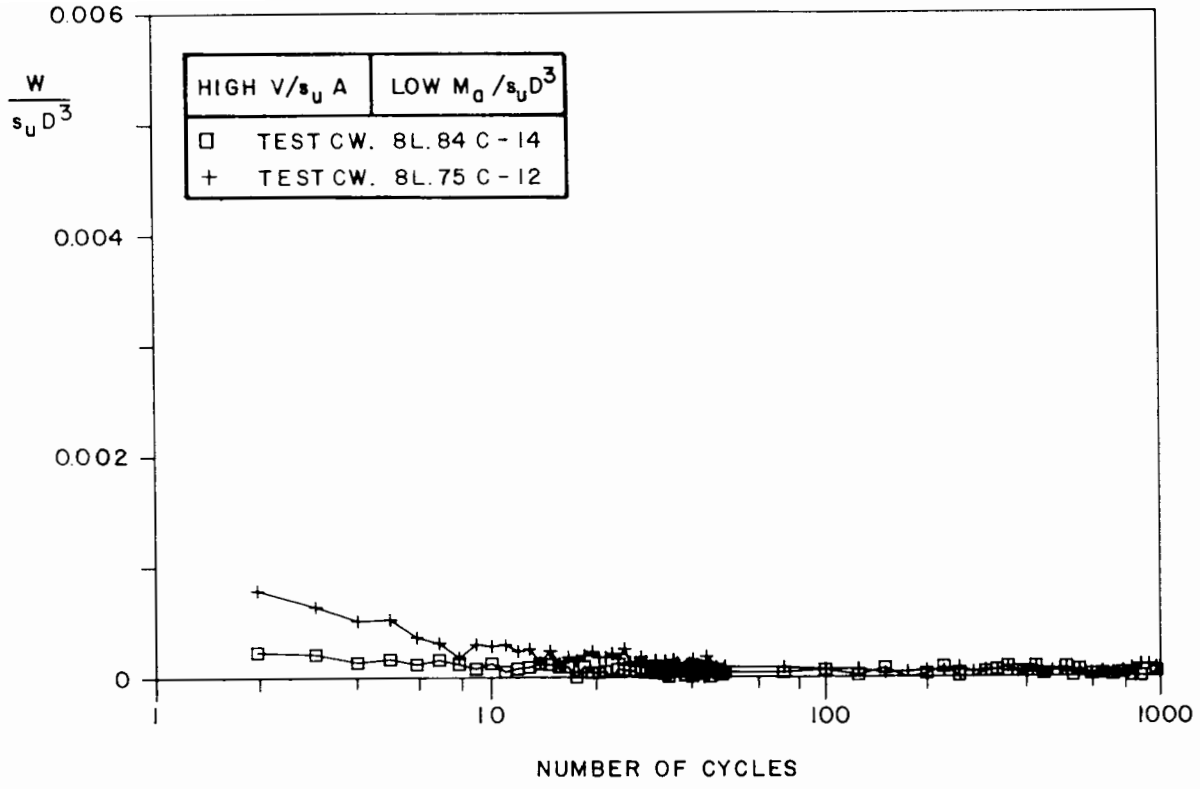

Figure 7.30 Dimensionless energy dissipated per cycle versus number of cycles curves for two tests carried out under the same loading conditions

7.3 Special Tests

Table 7.6 shows all the relevant data concerning special tests, while Tables 7.7 and 7.8 show the details and values of the non-dimensional loading parameters involved.

7.3.1 Double Amplitude Tests

Figures 7.32, 7.33, 7.34, 7.35 and 7.36 show the results of tests W.8A.78C-13 (represented by squares) and CW.8A.79C-13 (represented by crosses), performed with high vertical load and 8 seconds period. In test W.8A.78C-13 the spud-can model was subjected to 400 cycles of low amplitude moment followed by 374 cycles of high amplitude moment, no offset being

(a) N = 0

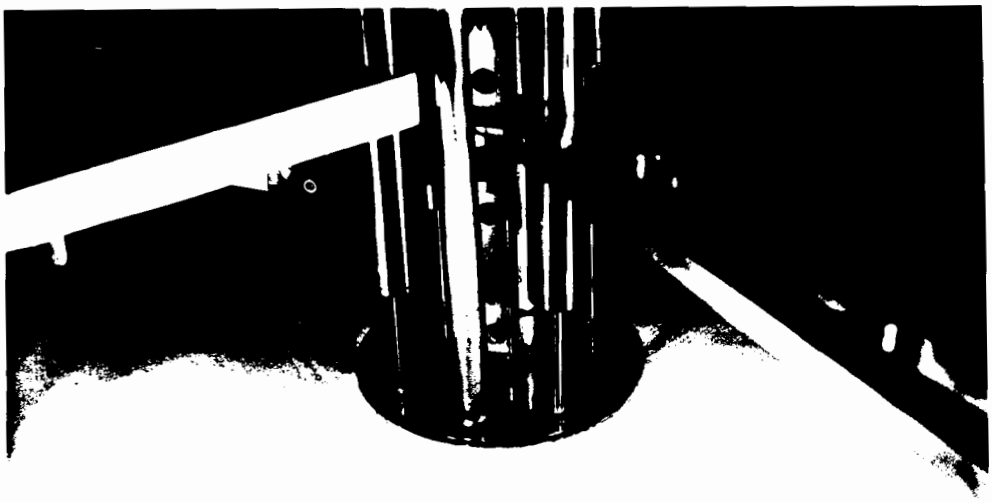

(b) N = 105

Figure 7.31 Aspect of the clay surface at various stages during test CW.8L.75C-12 (N = number of cycles) (continued next page)

(c) N = 516

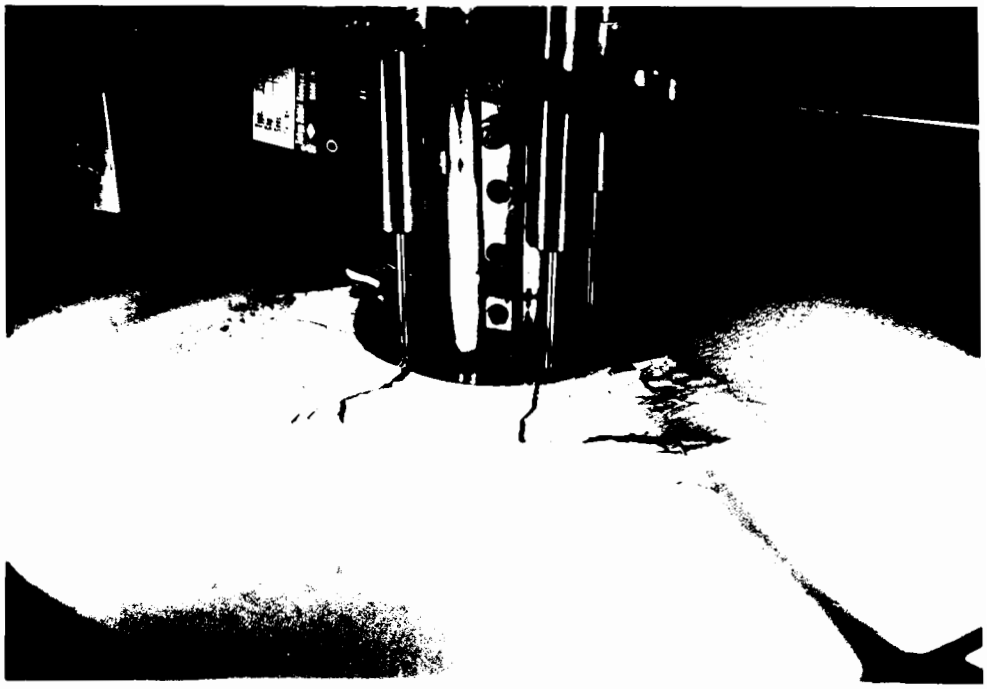

(d) N = 1002

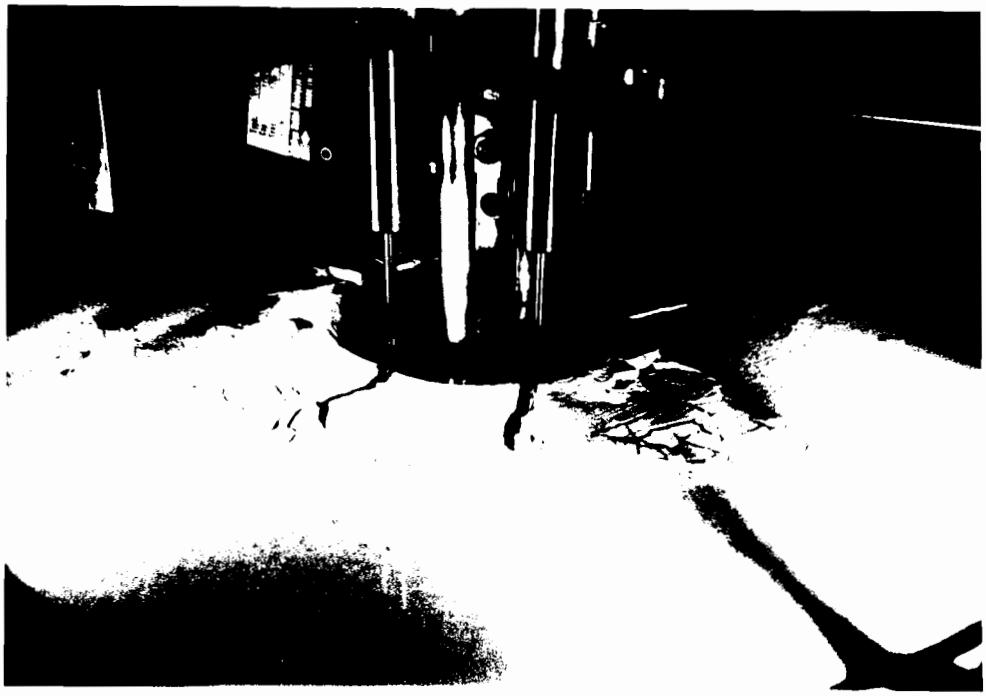

Figure 7.31 (continued)

Table 7.6 Special cyclic loading tests

test	s_u (kPa)	V (N)	M_a (Nm)	M_o (Nm)	T (s)	V_{max} (N)	EC
W.8A.78C-13	10.9	329.9	2.0/4.0	0	8	431.9	2
CW.8A.79C-13	9.8	330.0	2.0/4.0	0.5	8	402.7	2
W.8B.80C-13	9.3	330.0	4.0	0	8	313.2	3
CW.8B.82C-13	9.7	330.1	4.0	0.5	8	406.2	1

Notes

(1) test CW.8B.81C-13 was lost
(2) s_u = index shear strength of the clay sample
(3) V = fixed vertical load
(4) M_a = peak-to-peak amplitude of the moment loading
(5) M_o = offset of the moment loading
(6) T = period of the moment loading
(7) V_{max} = maximum vertical load applied to the model footing before testing
(8) EC = index related to the area of the clay surface affected by the foundation at the end of the test (see Section 7.2)

Table 7.7 Special cyclic loading tests

		high V/s_uA
		8s period
double amplitude (low & high M_a/s_uD^3)	W	W.8A.78C-13
	CW	CW.8A.79C-13
bursts of cycling (high M_a/s_uD^3)	W	W.8B.80C-13
	CW	CW.8B.82C-13

Table 7.8 Loading parameters of the special cyclic loading tests

		high V/s_uA
		8s period
double amplitude (low & high M_a/s_uD^3)	W	$V/s_uA=3.9$ $M_a/s_uD^3=0.18/0.37$ $M_o/s_uD^3=0$
	CW	$V/s_uA=4.3$ $M_a/s_uD^3=0.20/0.41$ $M_o/s_uD^3=0.05$
bursts of cycling (high M_a/s_uD^3)	W	$V/s_uA=4.5$ $M_a/s_uD^3=0.43$ $M_o/s_uD^3=0$
	CW	$V/s_uA=4.3$ $M_a/s_uD^3=0.41$ $M_o/s_uD^3=0.05$

introduced in this case. Test CW.8A.79C-13 was carried out under a constant offset of moment of $0.05s_uD^3$ and a low amplitude of moment for the first 300 cycles and high amplitude for the following 149 cycles.

The results suggest that the amplitude of moment loading plays an important role in the pattern of the cumulative displacements. As would be expected, the values of the variation of rotation and energy dissipated per cycle are

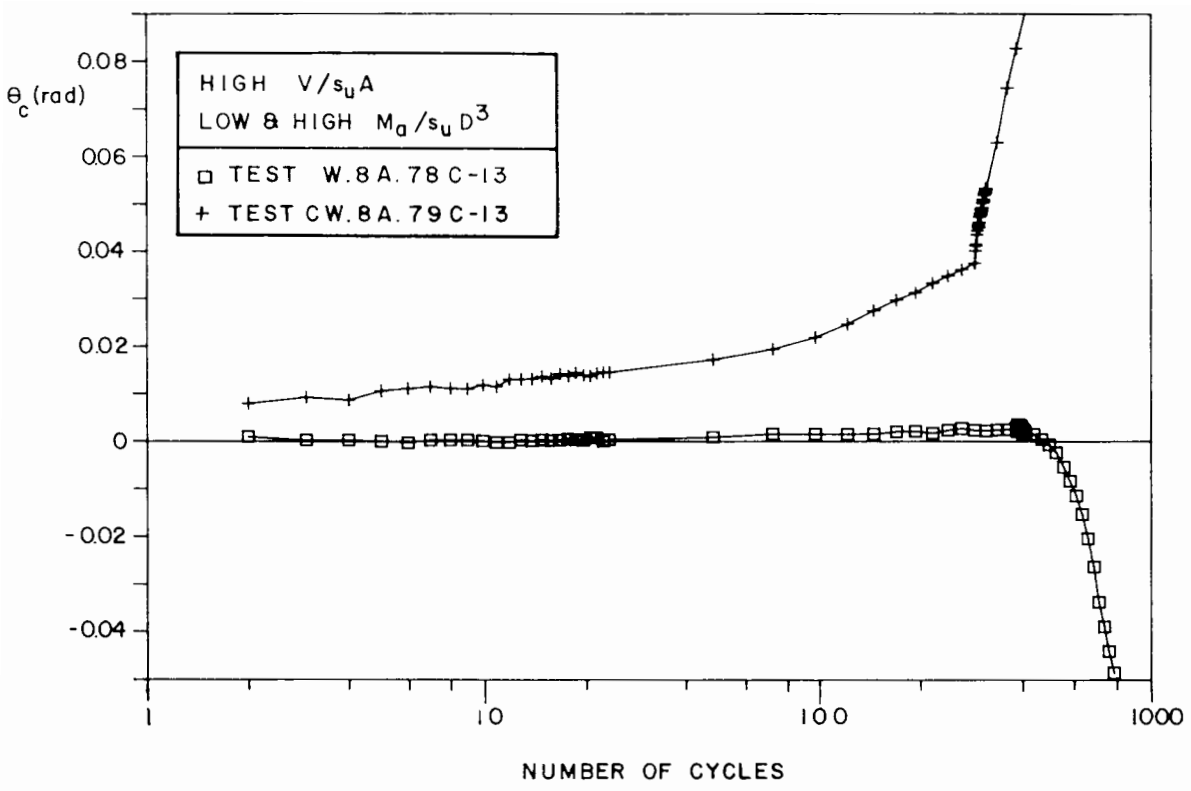

Figure 7.32 Cumulative rotation angle versus number of cycles curves for double amplitude tests

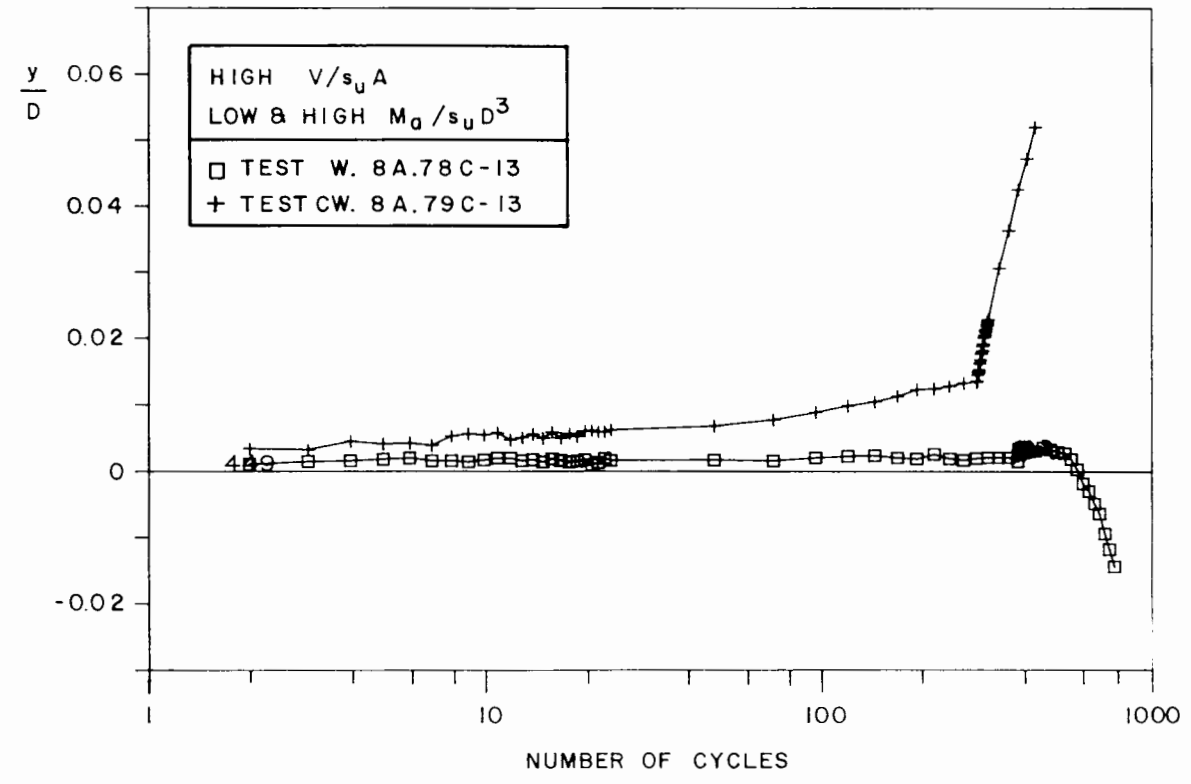

Figure 7.33 Cumulative dimensionless horizontal displacement versus number of cycles curves for double amplitude tests

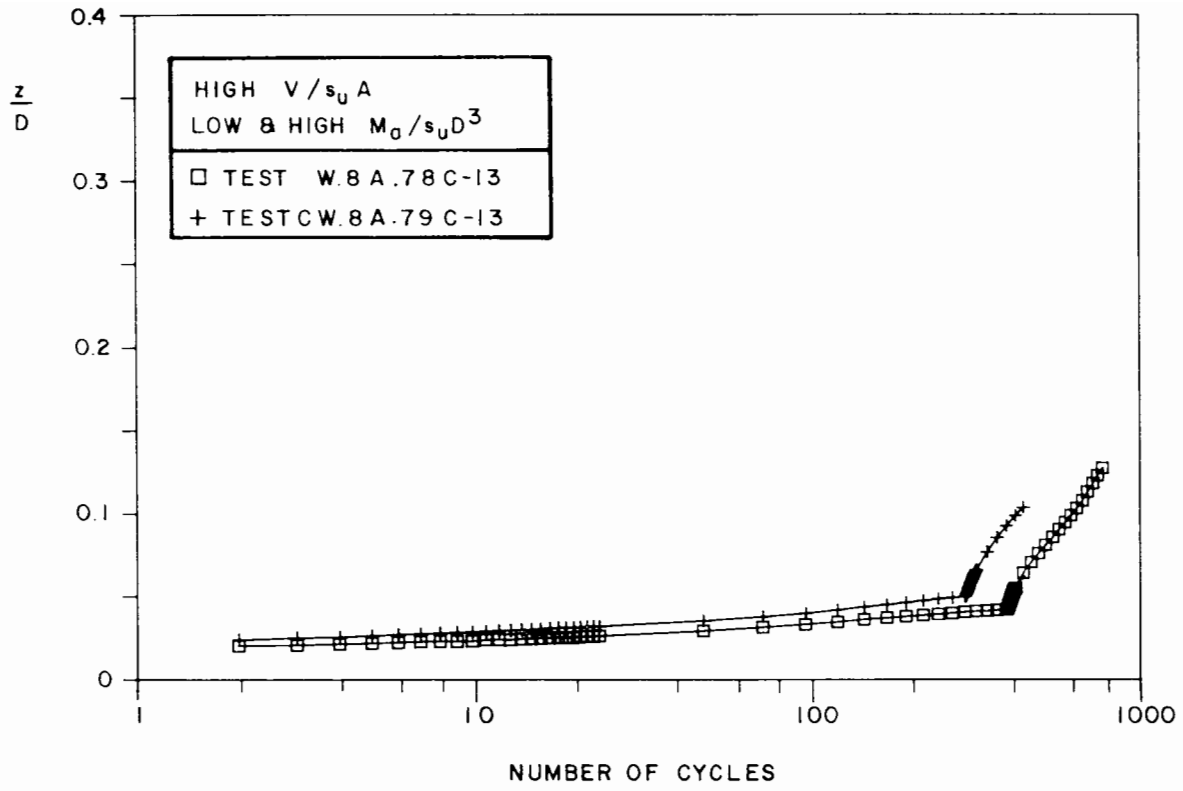

Figure 7.34 Cumulative dimensionless vertical displacement versus number of cycles curves for double amplitude tests

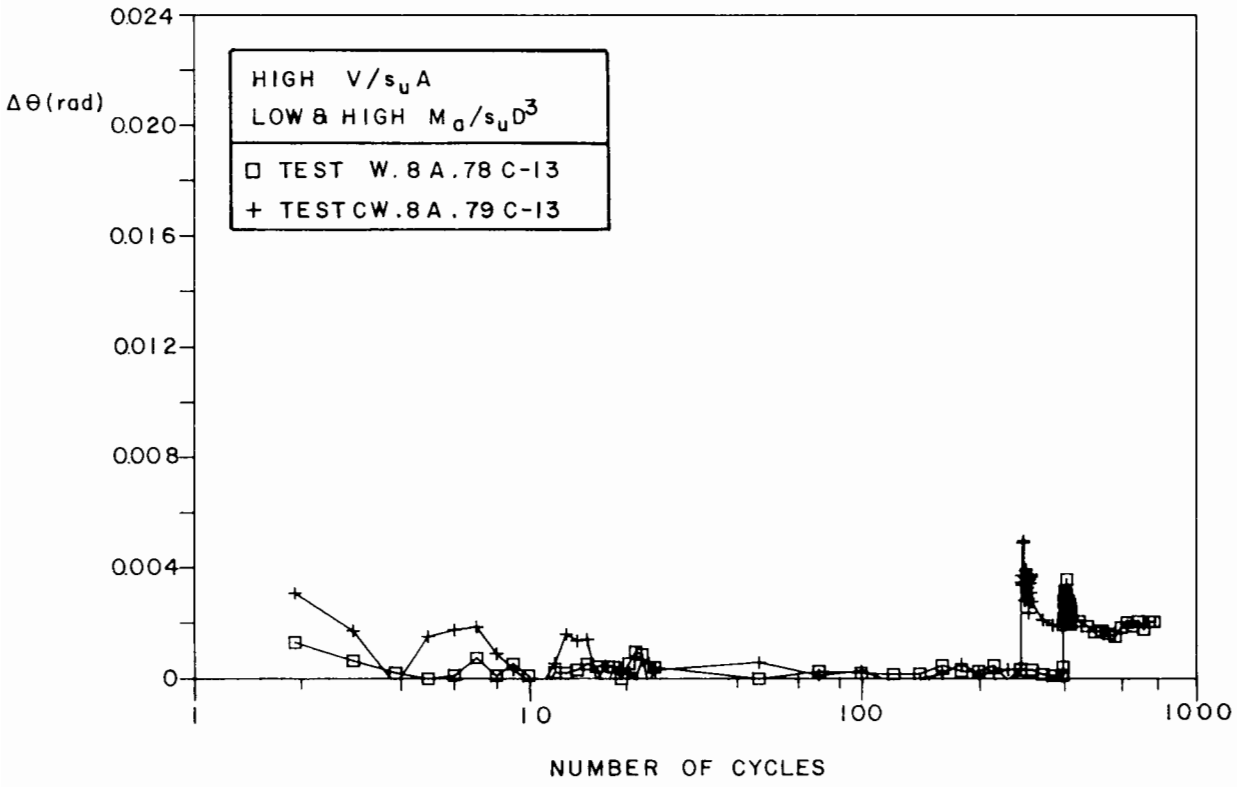

Figure 7.35 Variation of rotation versus number of cycles curves for double amplitude tests

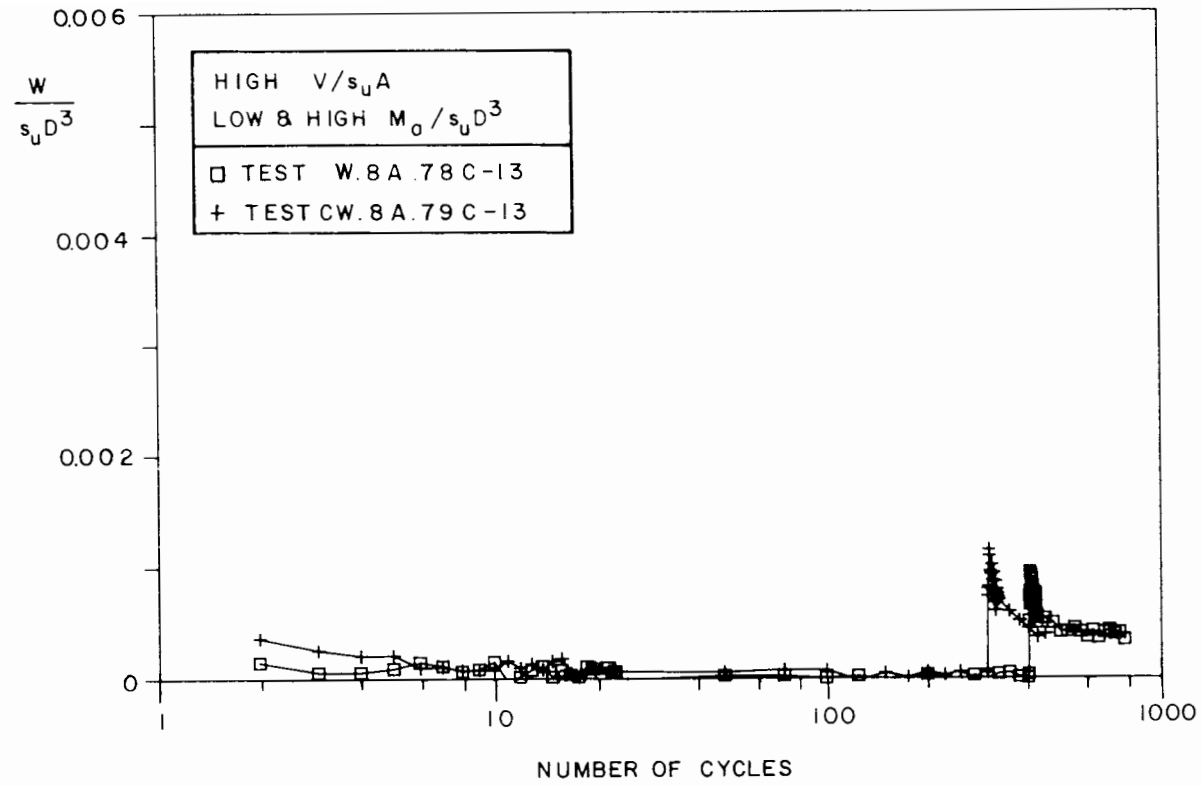

Figure 7.36 Dimensionless energy dissipated per cycle versus number of cycles curves for double amplitude tests

markedly affected by the sudden increase in the amplitude of the moment applied, reaching values very consistent with those obtained at the beginning of similar tests in the main series performed with high amplitude of moment loading.

7.3.2 Bursts of Cycling Tests

Figures 7.37, 7.38 and 7.39 show the relevant results of tests W.8B.80C-13 (represented by squares) and CW.8B.82C-13 (represented by crosses), both carried out with high vertical load, high amplitude of moment and 8 seconds

(a) number of cycles in logarithmic scale

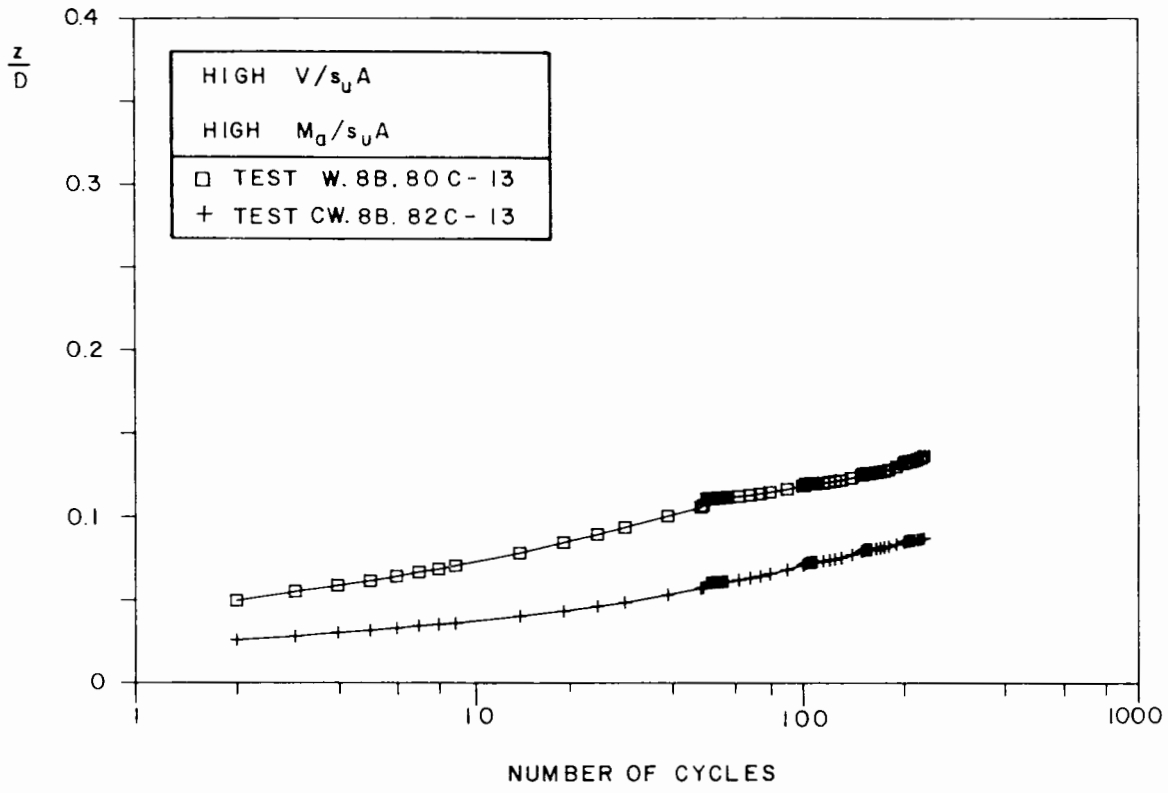

(b) number of cycles in linear scale

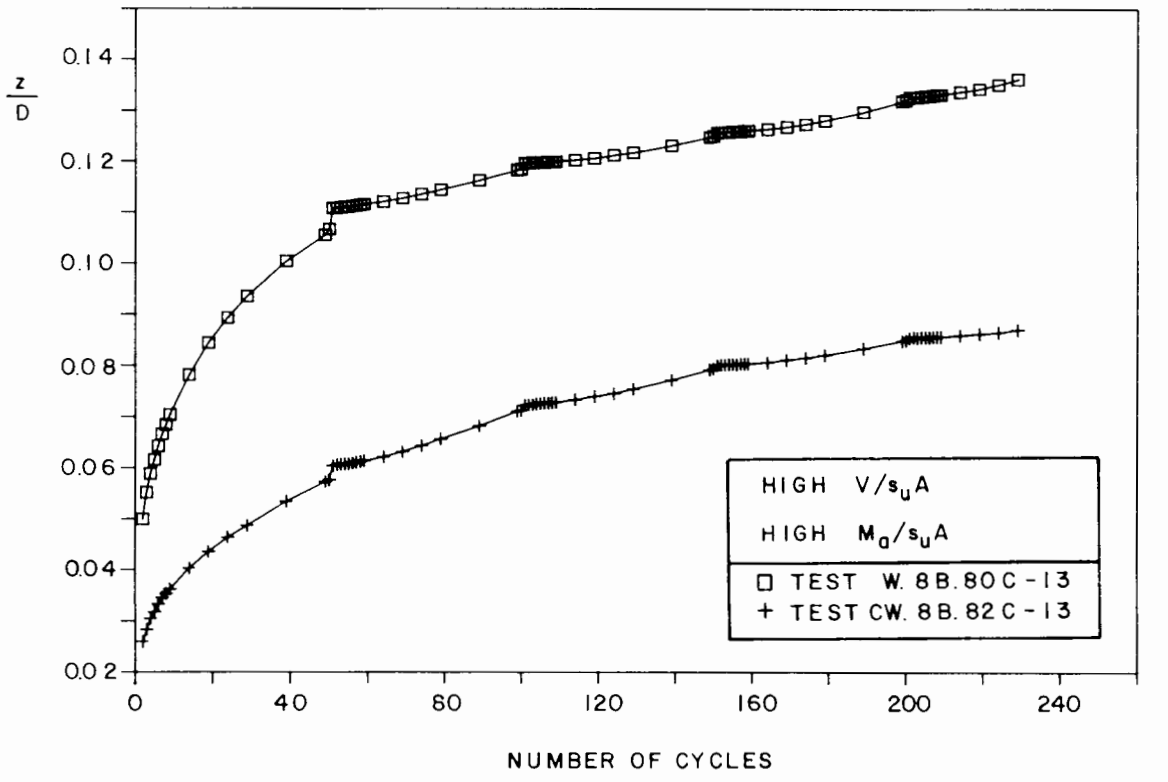

Figure 7.37 Cumulative dimensionless vertical displacement versus number of cycles curves for bursts of cycling tests

(a) number of cycles in logarithmic scale

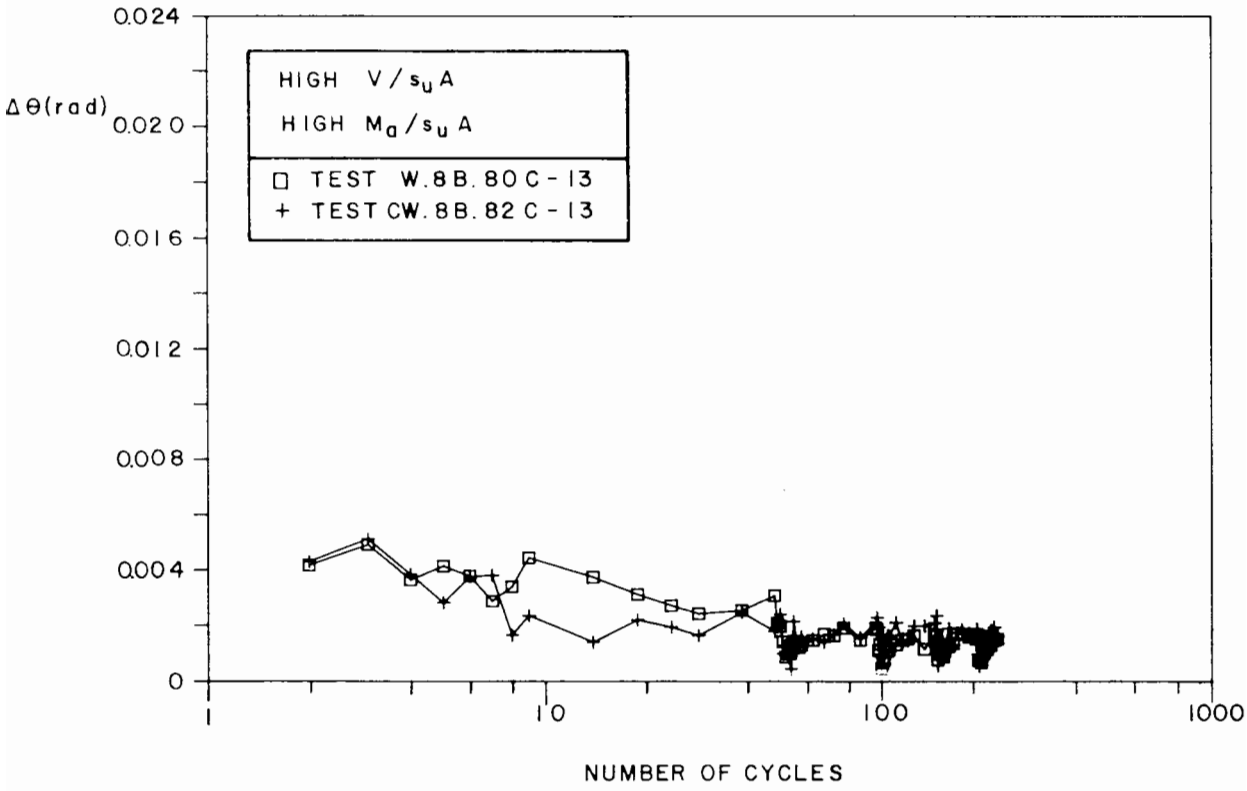

(b) number of cycles in linear scale

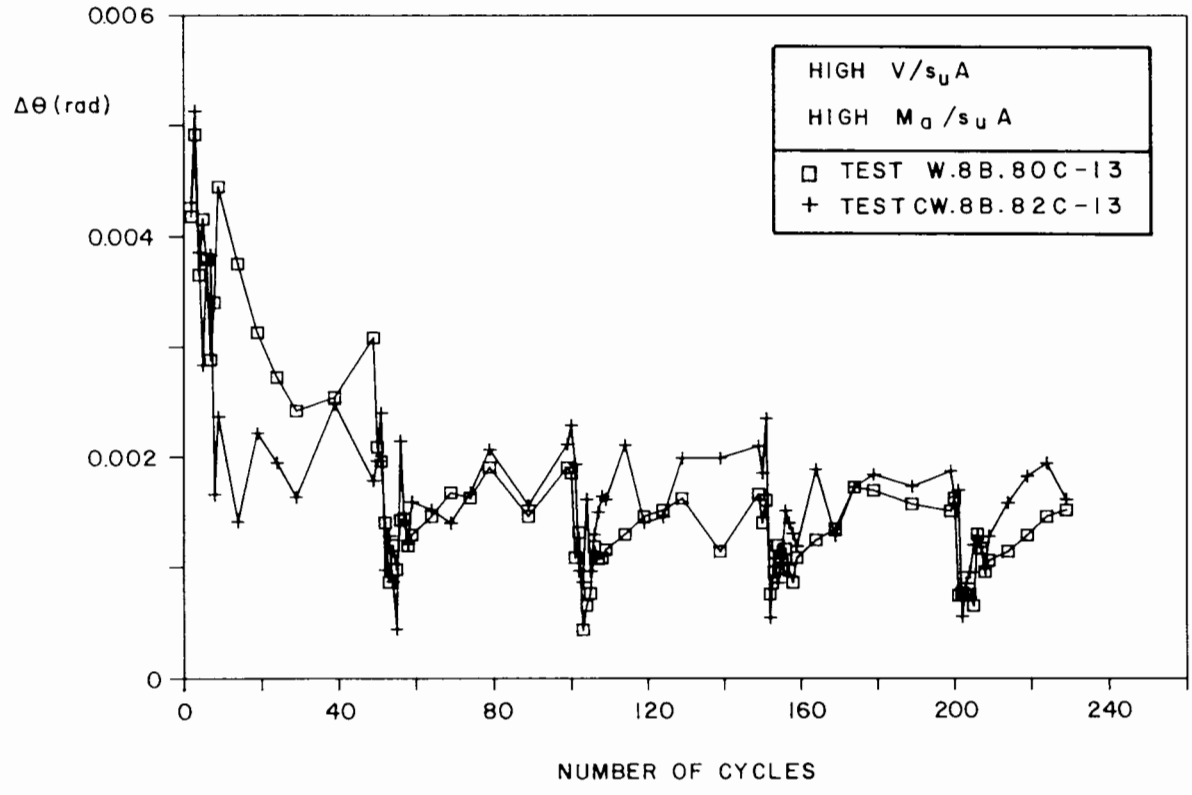

Figure 7.38 Variation of rotation versus number of cycles curves for bursts of cycling tests

(a) number of cycles in logarithmic scale

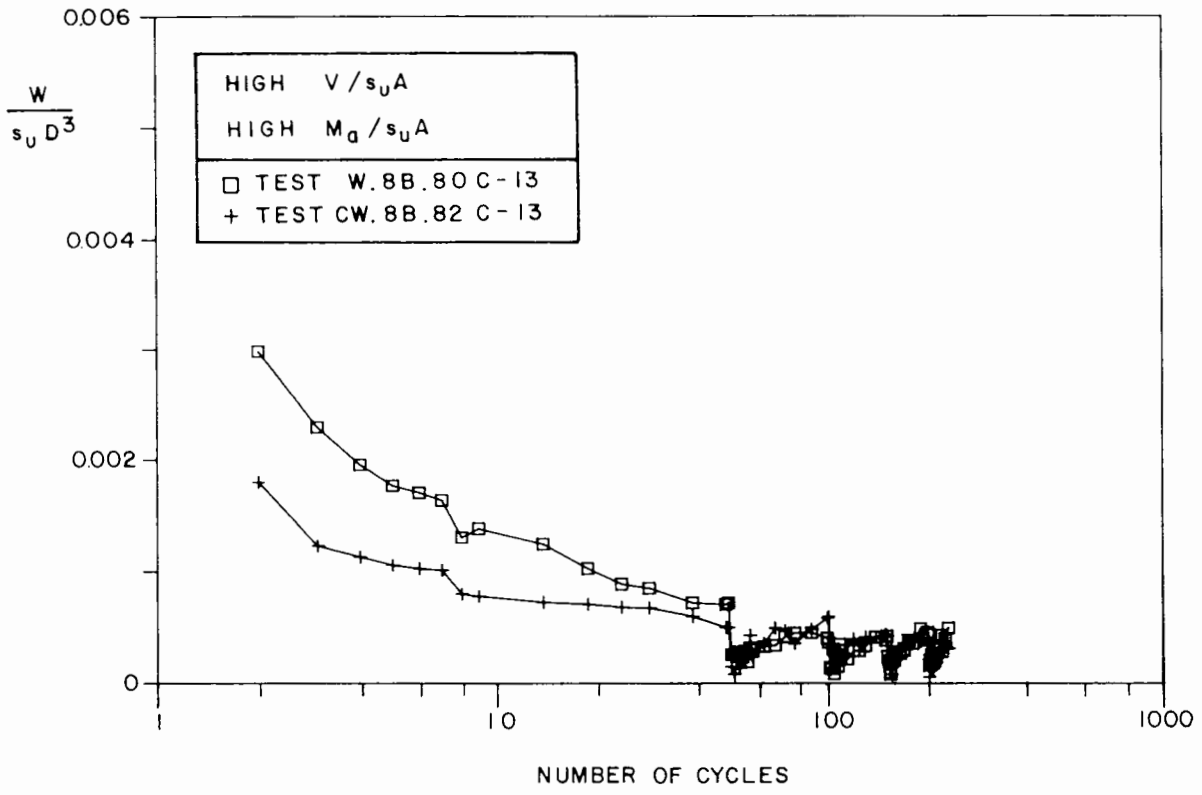

(b) number of cycles in linear scale

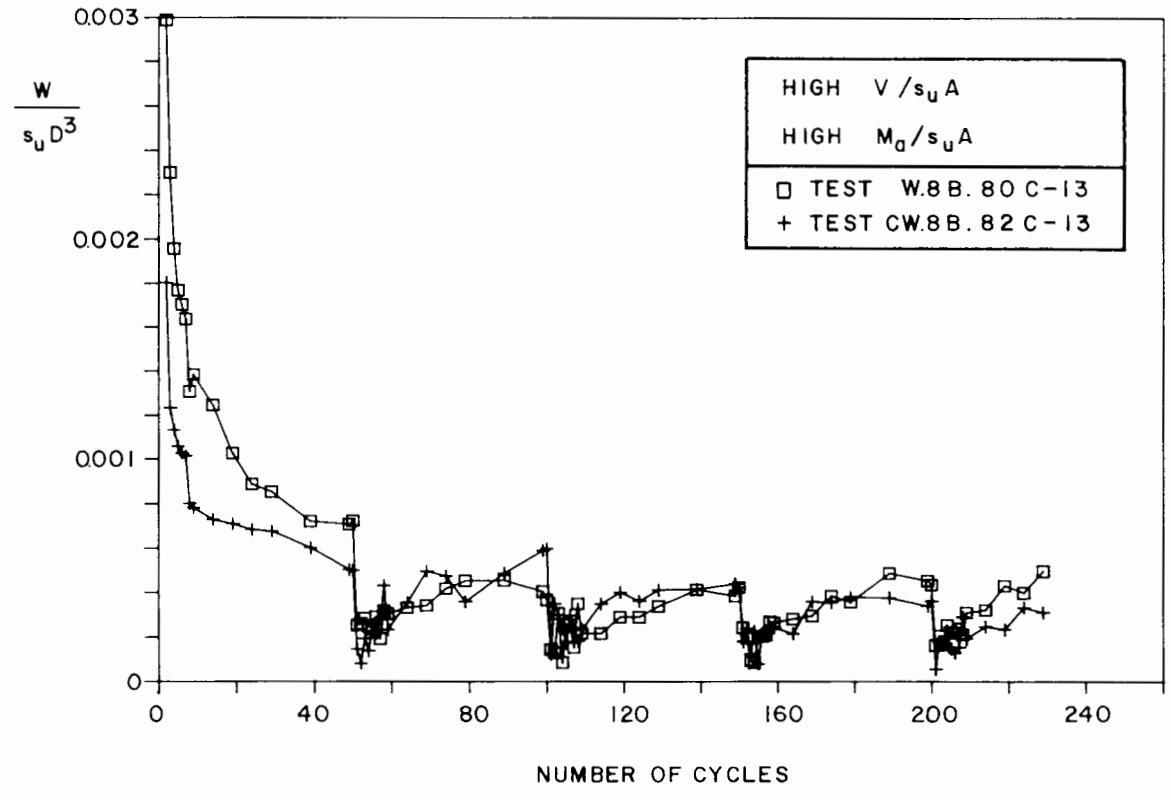

Figure 7.39 Dimensionless energy dissipated per cycle versus number of cycles curves for bursts of cycling tests

period, without and with an offset of moment respectively. In each figure the curves are presented in two ways:

(a) using the same scales as in the corresponding figures of the main series, for comparison purposes;

(b) the scale referring to the parameter in question expanded and the number of cycles represented on a linear scale, to reveal in more detail the pattern of behaviour immediately before and after the resting time.

The steps in the curves of Figure 7.37 (b) represent the settlement of the model footing owing to consolidation of the clay sample during the resting interval. It can be observed that the slope of the curve is reduced drastically immediately after the loading is resumed, gradually increasing thereafter. A similar pattern of behaviour can be noticed in the variation of the rotation angle and energy dissipated per cycle, as illustrated in Figures 7.38 (b) and 7.39 (b). Immediately after the resting time the model footing exhibits a stiffer rotational behaviour with less dissipation than immediately before, reverting then to a steady response in about 20 to 30 cycles. In each case the enveloping curves are quite consistent with the results of equivalent tests of the main series.

CHAPTER 8

ANALYSIS OF THE RESULTS - MONOTONIC LOADING

8.1 Introduction

In this chapter the analysis of the results of the main groups of monotonic loading tests outlined in Chapter 6 are presented. Leg tests are not included in this analysis because the results presented in Chapter 6 already provide satisfactory information about the interaction between footing (spud-can) and leg. Further structural analysis is not within the scope of this research.

The analysis of the results was performed by fitting a three-parameter hyperbola to the initial branch of the curves which is, as far as monotonic loading is concerned, the most important part of the test results. Once the hyperbola was defined, the relevant parameters for the load versus displacement curves were easily obtained through simple algebra, these parameters being the failure load or moment, the initial stiffness and the plastic stiffness (as defined in Sections 8.3.2 and 8.4.2).

Also described and discussed in this chapter is the unloading rotational stiffness of combined loading tests, obtained from the linear segment of the moment versus rotation curve immediately after reversing the direction of the rotation.

8.2 The Hyperbola

The curve which was found to represent best the results of monotonic loading tests is a three-parameter hyperbola

$$y = \frac{x}{\frac{1}{a} + \frac{x}{b + cx}} \qquad [8.1]$$

passing through the origin and having one asymptote parallel to the y axis and the other inclined with a slope k_2 with respect to the x axis, as illustrated in Figure 8.1(a). The vertical asymptote intercepts the x axis at $x = -b/(a + c)$ and the other intercepts the y axis at $y = a^2b/(a + c)^2$. The slope of the tangent at the origin is

$$k_1 = \left(\frac{dy}{dx}\right)_{x=o} = a \ , \qquad [8.2]$$

and at $x \to \infty$ (inclined asymptote)

$$k_2 = \left(\frac{dy}{dx}\right)_{x\to\infty} = \frac{ac}{a + c} \ . \qquad [8.3]$$

The tangent at the origin intercepts the inclined asymptote at the point F, with coordinates

$$x_f = \frac{b}{a + c} \quad \text{and} \quad y_f = \frac{ab}{a + c} \ . \qquad [8.4 \text{ and } 8.5]$$

It is worth noticing that the two-parameter hyperbola employed by Kondner (1963) to describe the stress-strain behaviour of cohesive soils is a

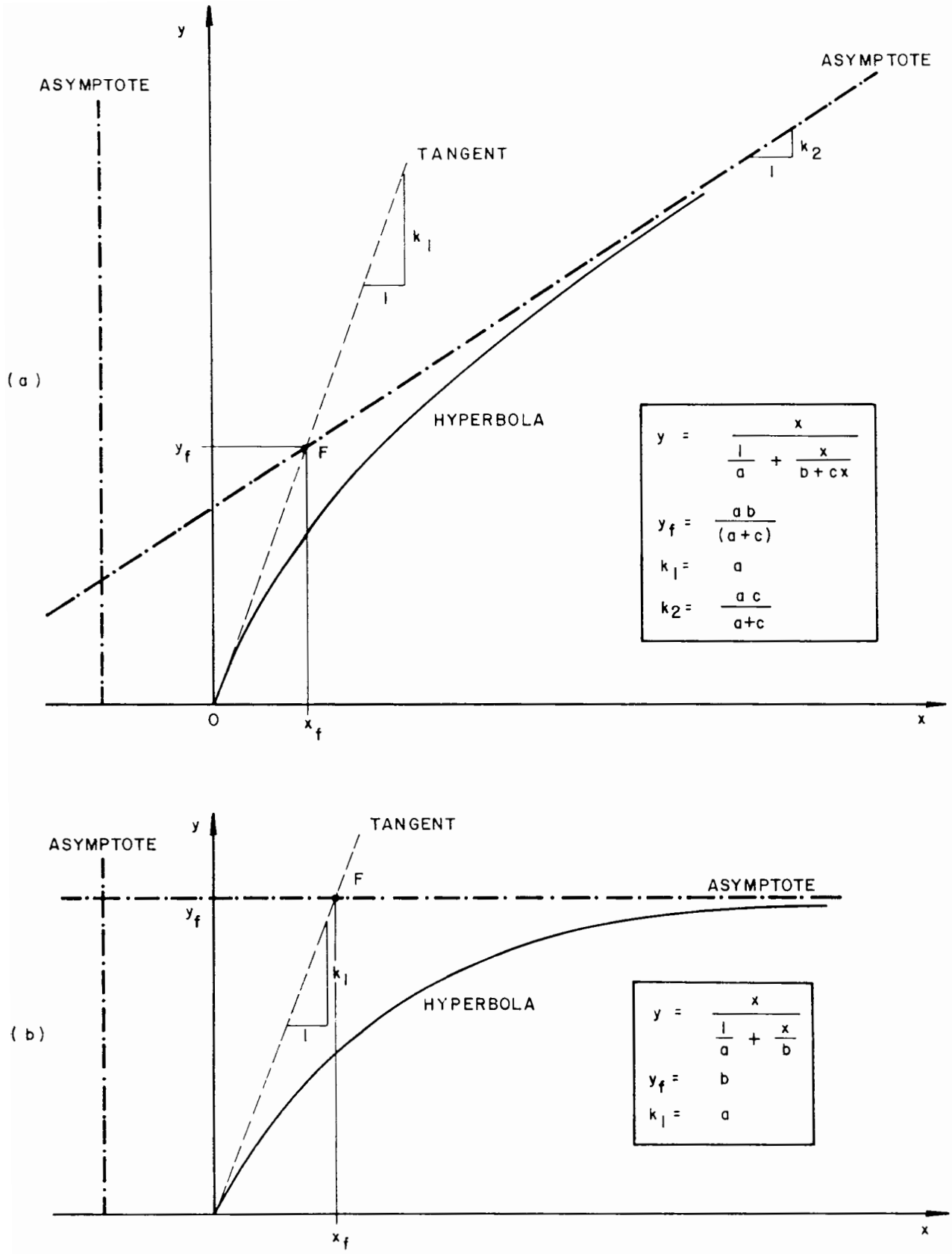

Figure 8.1 Three-parameter (a) and two-parameter (b) hyperbolas

particular case of the three-parameter hyperbola defined here. Equation [8.1] becomes Kondner's hyperbola if c = 0, with $k_1 = a$, $k_2 = 0$, $x_f = b/a$ and $y_f = b$, as shown in Figure 8.1(b).

Stress-strain behaviour of soils often exhibits an ultimate stress represented by a horizontal asymptote and therefore has been conveniently approximated by using the two-parameter hyperbola. Actual foundations, however, usually do not respond with a well defined failure load when subjected to large displacements but, for practical purposes, assume a constantly increasing strength with further displacements (at least within the range considered here) and, consequently, their behaviour is better modelled by a curve featuring an inclined asymptote.

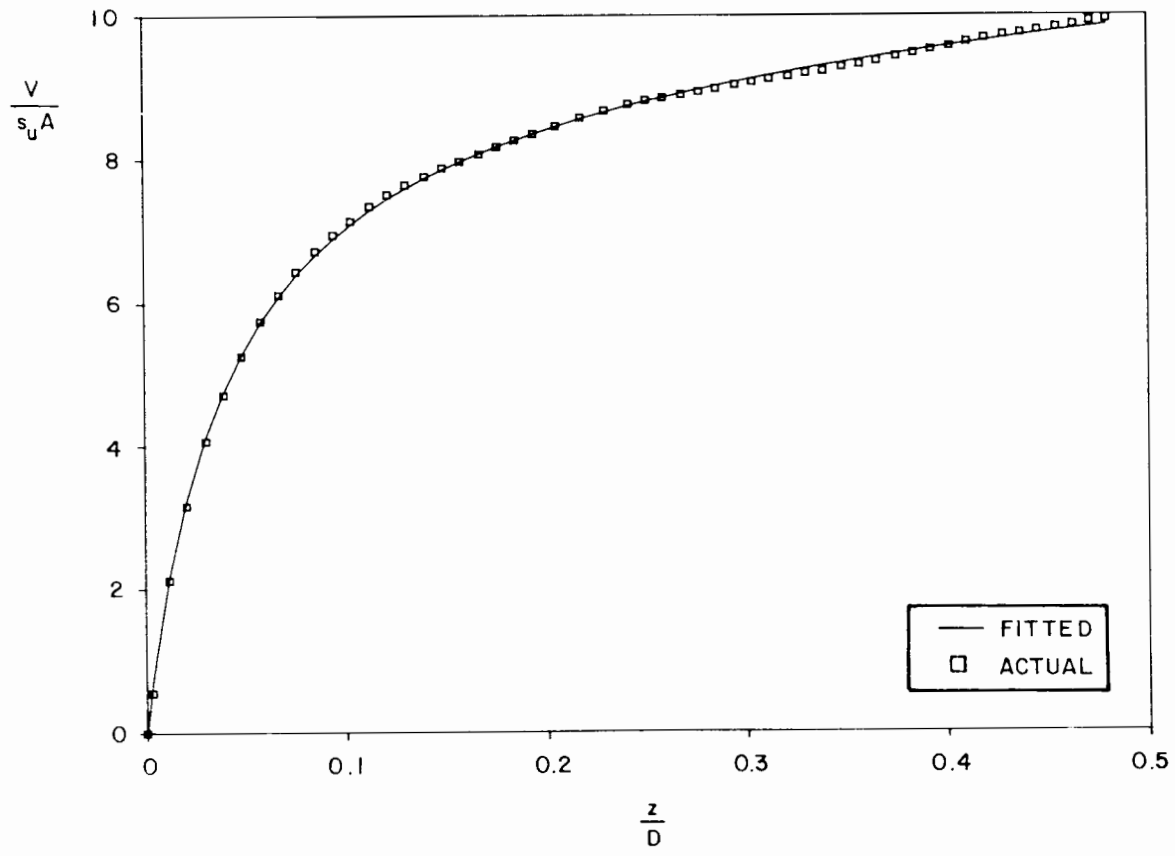

Figure 8.2 Fitted hyperbola compared with actual points obtained from test VC.100F.01-01 (vertical central loading test)

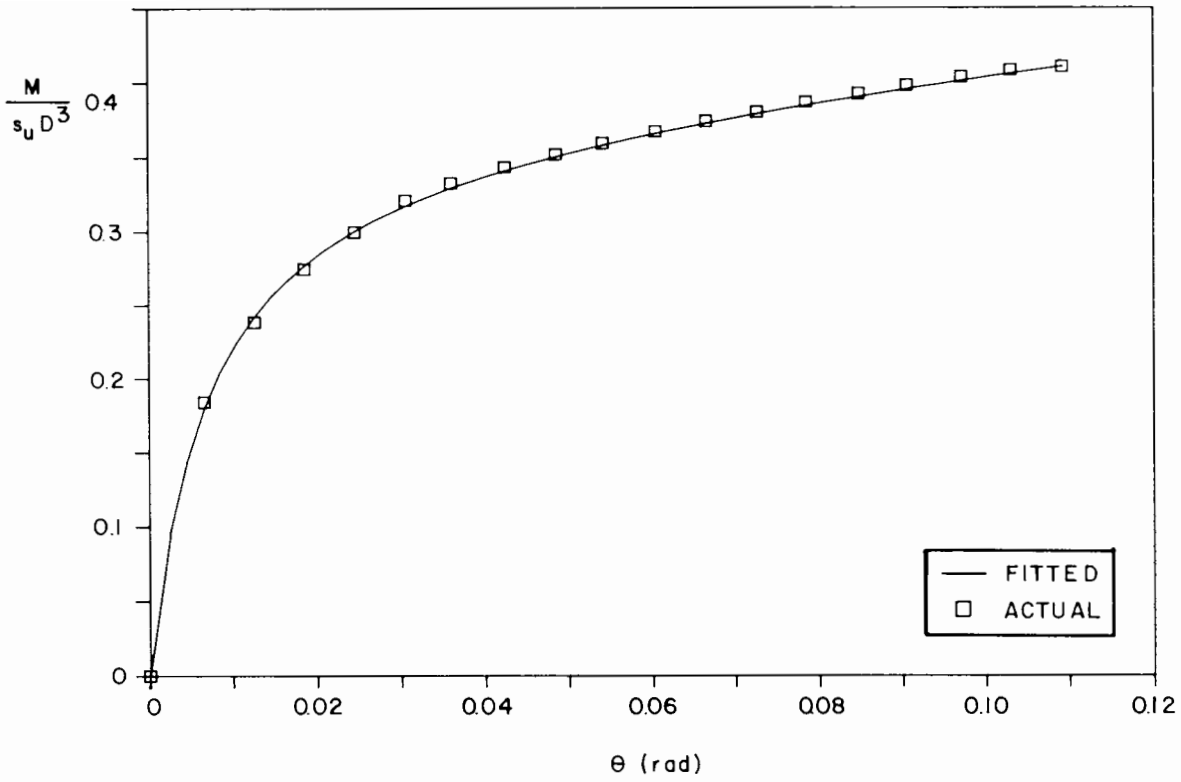

Figure 8.3 Fitted hyperbola compared with actual points obtained from test H.100C.53-08 (combined loading test - best fitting)

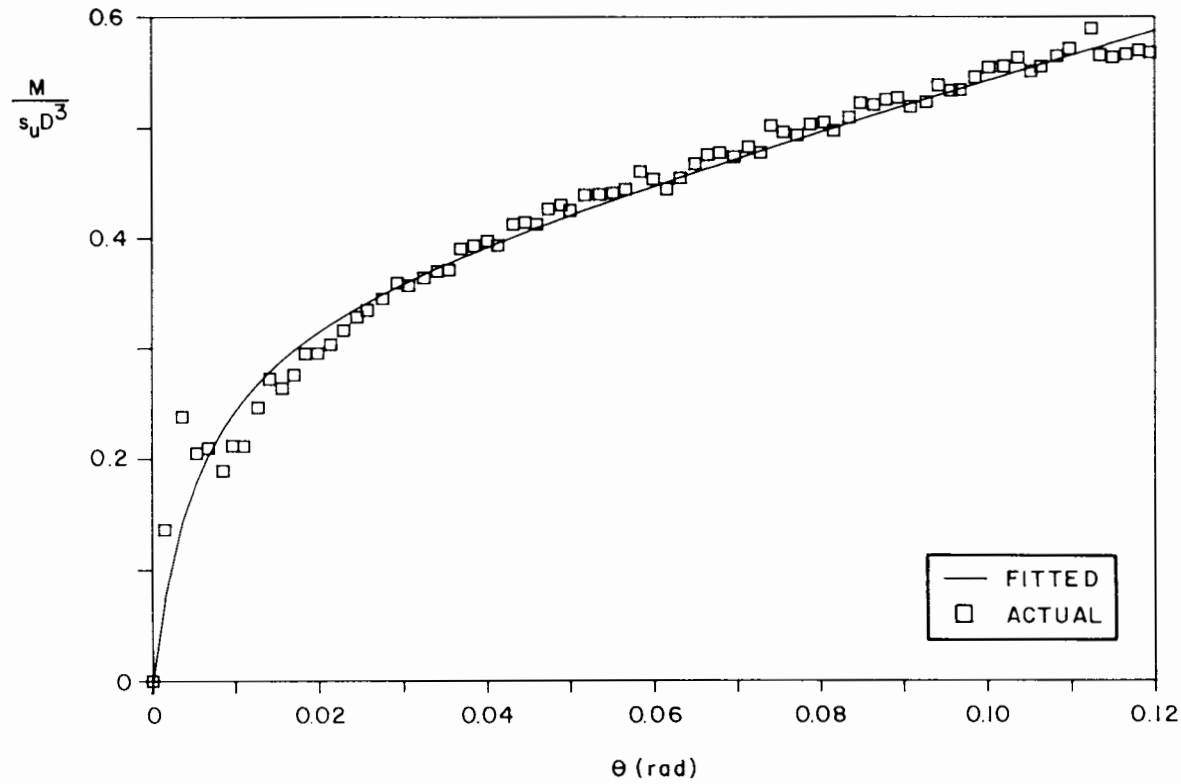

Figure 8.4 Fitted hyperbola compared with actual points obtained from test HD.100S.41-06 (combined loading test - worst fitting)

The curve-fitting was performed using non-linear regression analysis and Figures 8.2, 8.3 and 8.4 show some examples of the fitted curves together with actual points obtained from the tests. Figure 8.2 corresponds to a vertical central loading test (VC.100F.01-01) and Figures 8.3 and 8.4 to combined loading tests (H.100C.53-08 and HD.100S.41-06). These last two tests were chosen to illustrate the best and the worst fitting for moment-rotation data as far as the correlation coefficient is concerned. The values of this coefficient obtained in each regression (see Tables 8.2 and 8.4) indicate that loading-displacement behaviour of monotonic loading tests can be very well represented by the three-parameter hyperbola.

8.3 Vertical Central Loading Tests

Figure 8.5 shows how the failure load V_f/s_uA, the elastic stiffness k_1 (initial stiffness) and the plastic stiffness k_2 are geometrically defined from the load versus displacement curve OA. It is worth mentioning that in case of cones and spud-cans only the upper branch of the curves (O_1A) was considered for curve fitting purposes and therefore the parameter k_1 obtained in these cases does not represent elastic stiffness.

8.3.1 Rigidity Index

The vertical central load applied to a rigid circular plate placed on the surface of a semi-infinite elastic mass is given by equation [2.6] (Section 2.4.1). If the elastic mass is assumed to be a clay soil and undrained behaviour is considered, equation [2.6] can be written as

$$\frac{V}{s_uA} = \frac{16}{\pi}\,\frac{G}{s_u}\,\frac{z}{D} \quad . \qquad [8.6]$$

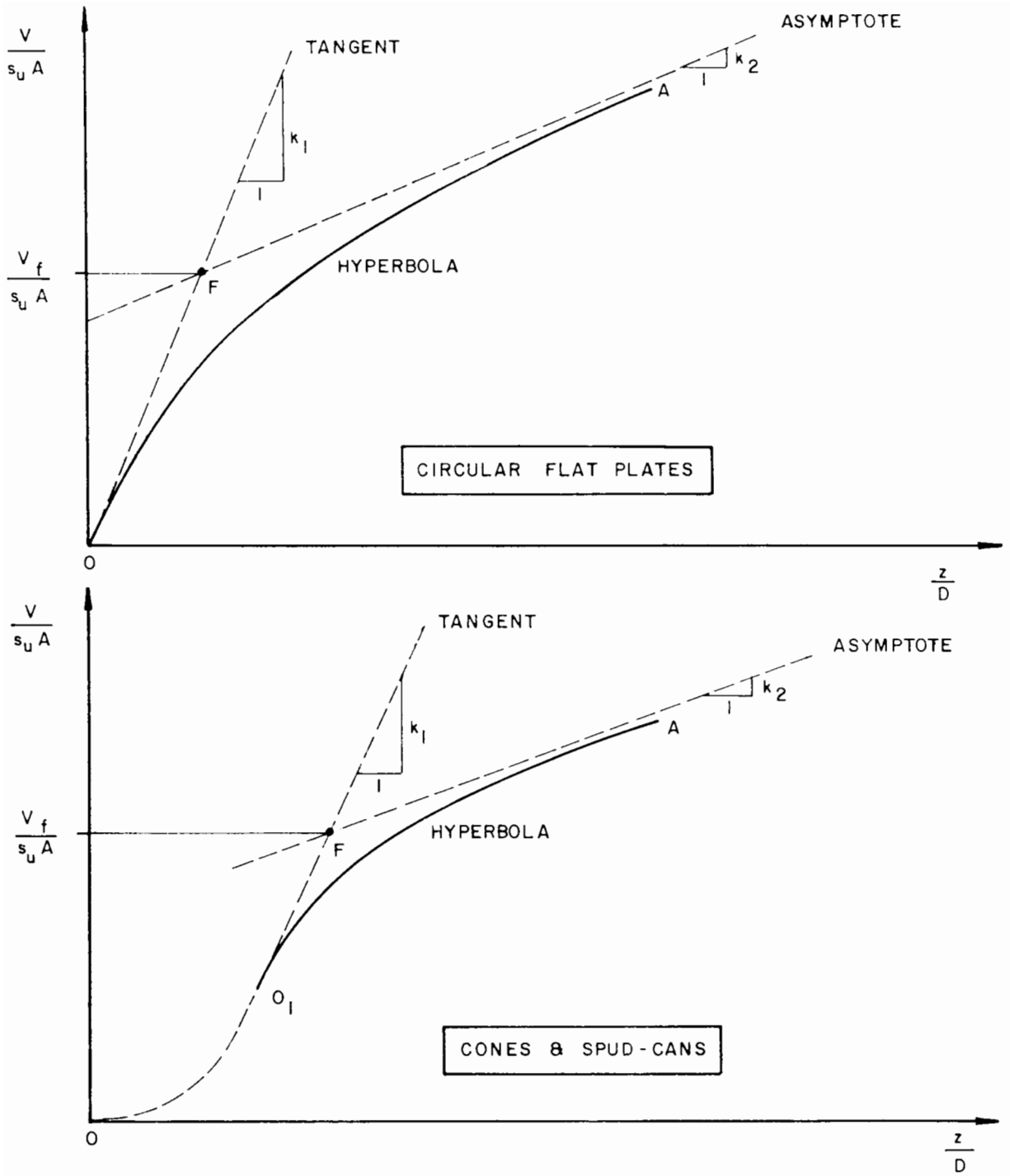

Figure 8.5 Definition of dimensionless failure load and stiffnesses for vertical central loading tests

The initial rigidity index of the kaolin clay sample can be estimated by equating the initial stiffness inferred from test results, k_1, to the theoretical elastic stiffness, $16G/\pi s_u$:

$$\frac{G}{s_u} = \frac{\pi}{16} k_1 \ . \qquad [8.7]$$

Table 8.1 shows the values of the rigidity index obtained by equation [8.7] for the two vertical central loading tests performed on circular plates.

Table 8.1 Initial stiffness and rigidity index (vertical central loading tests)

test	k_1	G/s_u
VC.100F.01-01	233.4	45.8
VC.50F.03-01	196.7	38.6

Note

(1) k_1= initial stiffness

8.3.2 Bearing Capacity and Plastic Stiffness

The values of the hyperbola parameters a, b and c, the correlation coefficient squared r^2 obtained in each fitting, the values of the failure load V_f/s_uA and the stiffnesses k_1 (except for cones and spud-cans) and k_2 for vertical central loading tests are given in Table 8.2. It can be noticed, however, that none of the spud-can vertical loading tests appears in the table and, instead, data obtained from the driving operation of spud-can model footings for deep combined loading tests were adopted. The reason for this is the large amount of data available from deep tests

Table 8.2 Results of the curve-fitting analysis
(vertical central loading tests)

test	a	b	c	r^2	V_f/s_uA	k_1	k_2
VC.100F.01-01	233.37	9.85	2.01	0.99958	9.77	233.37	2.00
VC.50F.03-01	196.66	9.41	3.09	0.99928	9.26	196.66	3.04
VC.50C.04-01	69.30	6.55	2.71	0.99976	9.40	-	2.61
VC.50C.05-01	34.68	4.61	5.72	0.99994	8.22	-	4.91
VC.50C.06-01	29.49	3.56	7.28	0.99943	7.14	-	5.84
VC.50C.07-01	18.36	4.30	2.65	0.99955	9.01	-	2.31
HD.100S.40-06	69.49	4.97	2.63	0.99857	7.10	-	2.53
HD.100S.41-06	81.63	5.45	4.87	0.99913	7.77	-	4.59
HD.100S.42-06	90.17	4.97	1.69	0.99498	7.40	-	1.66
HD.100S.43-06	65.07	4.35	1.83	0.99030	7.84	-	1.78
HD.100S.47-07	72.26	5.96	4.35	0.99953	9.28	-	4.10
HD.100S.48-07	83.98	4.33	4.50	0.99836	7.46	-	4.27

Notes

(1) a,b,c = hyperbola parameters
(2) r^2 = correlation coefficient squared
(3) V_f/s_uA = non-dimensional bearing capacity
(4) k_1 = non-dimensional initial stiffness
(5) k_2 = non-dimensional plastic stiffness

(spud-cans were driven deeper in these tests than in standard vertical central loading ones) allowing the fitting to be more accurately performed.

Figure 8.6 shows how the failure load varies with the cone angle. It must be pointed out that all the cones and one circular plate (50 mm) were tested on the same clay sample, the cones being at 75 mm distance from the wall and the flat circular plate at the centre, as illustrated in Figure 5.3 (see Section 5.2.1).

Except for one circular plate (D = 100 mm) and the spud-cans (D = 100 mm), all the other model footings employed were 50 mm in diameter. Because the spud-can models used in this research are geometrically defined by two conical surfaces of different angles (Figure 3.8, Section 3.5), they are

represented in the cone angle axis by the angle of the cone which has the same volume as the spud-can. For the 130^{o} spud-can this angle is 152.6^{o}.

The variation of the plastic stiffness with the cone angle is represented in Figure 8.7.

The following comments can be made from the analysis of Figures 8.6 and 8.7.

(i) The bearing capacity values obtained experimentally are higher than those predicted by theory. The comparison of the experimental results (Figure 8.6) with the theoretical ones (Figure 2.3, Section 2.4.2) seems to suggest that the model footings behave within an intermediate range of surface roughness α in spite of being made of polished metal. Assuming the shear strength of the clay sample being linearly increasing with the depth in the form

$$s_u = s_o + \rho z \ , \qquad [2.13 \text{ bis}]$$

where s_o is the undrained shear strength at the surface, ρ a constant and z the depth, and using all the site investigation results available it can be concluded that the parameter $\rho D/s_o$ varies approximately from 0.10 to 0.42. In accordance with Houlsby and Wroth (1983) the gain in bearing capacity for $\rho D/s_o = 2.00$ is about 26 % for rough footings and about 18 % for smooth footings. For $\rho D/s_o$ in the range of 0.10 to 0.42 the expected gain would not be very significant and therefore the effect of increasing strength with depth does not account for the high values of bearing capacity observed experimentally.

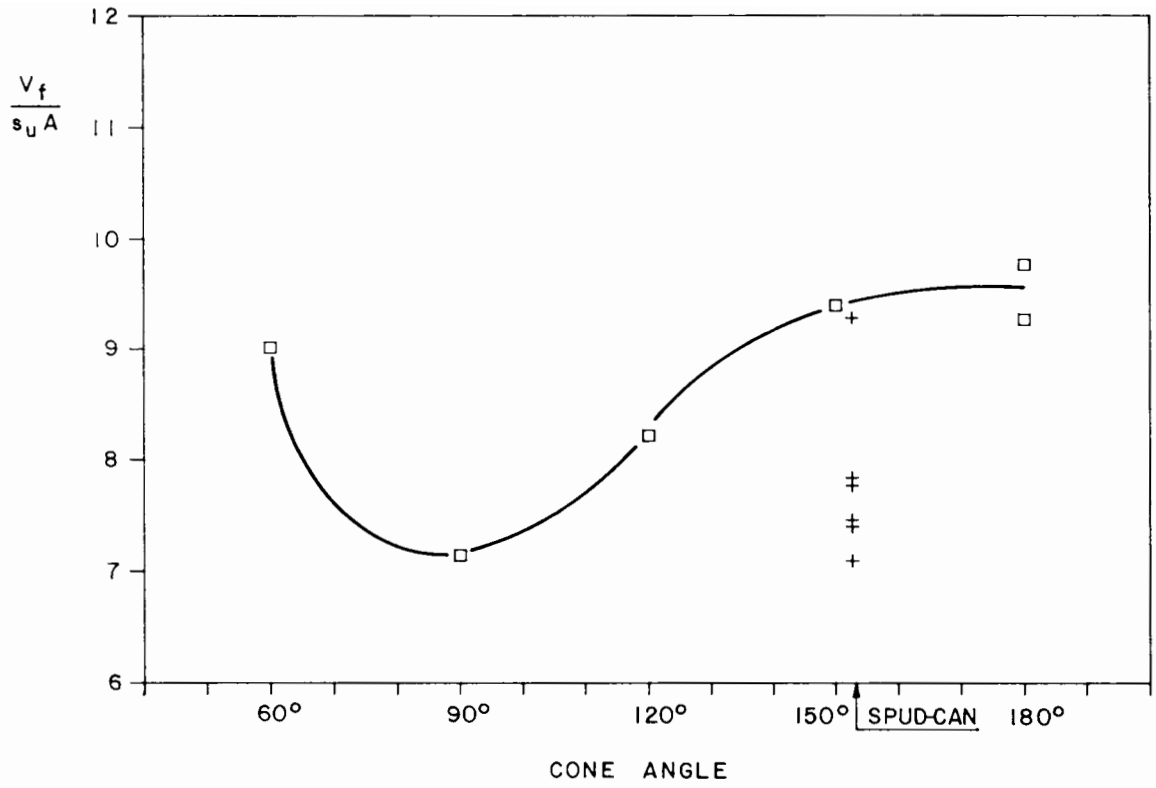

Figure 8.6 Variation of dimensionless vertical central failure load with cone angle

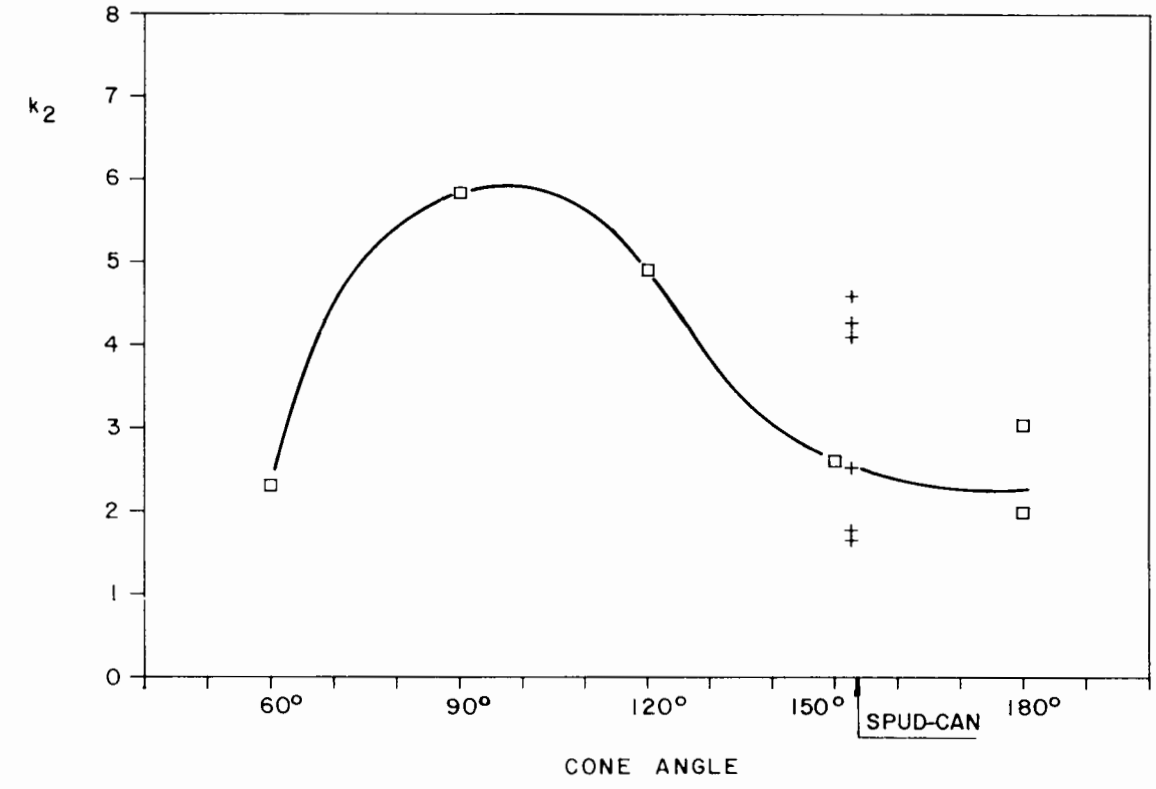

Figure 8.7 Variation of dimensionless plastic stiffness with cone angle

(ii) Although some scatter is observed (with one exceptional point), the results seem to suggest that the spud-can has a lower bearing capacity than the equivalent cone, behaving like a sharper cone with an angle around 90^{o} to 115^{o}.

(iii) Plastic stiffness varies with the cone angle in the opposite way to the bearing capacity, as may be expected bearing in mind the manner in which bearing capacity was geometrically defined in this work. While the bearing capacity exhibits a minimum value for cones of about 90^{o}, the plastic stiffness appears to reach a maximum value at about 90^{o} to 100^{o} cone angle. Because of experimental scatter, no conclusive trend concerning k_2 can be observed from the spud-can results.

8.4 Combined Loading Tests

The geometrical definitions of failure moment M_f/s_uD^3, elastic stiffness k_1 (initial stiffness) and plastic stiffness k_2 for moment versus rotation curves are similar to those of the corresponding parameters for vertical load versus vertical displacement curve and are illustrated in Figure 8.8.

The unloading stiffness k_3 was calculated either for positive or negative moment loading by dividing the variation of the moment $\Delta(M/s_uD^3)$by the variation of the rotation angle $\Delta\theta$ immediately after the direction of the imposed rotation was reversed. The results were plotted against $\Delta\theta$, which varied a little from test to test, and are presented later in Figures 8.23, 8.24 and 8.25 in the form of a band of values obtained.

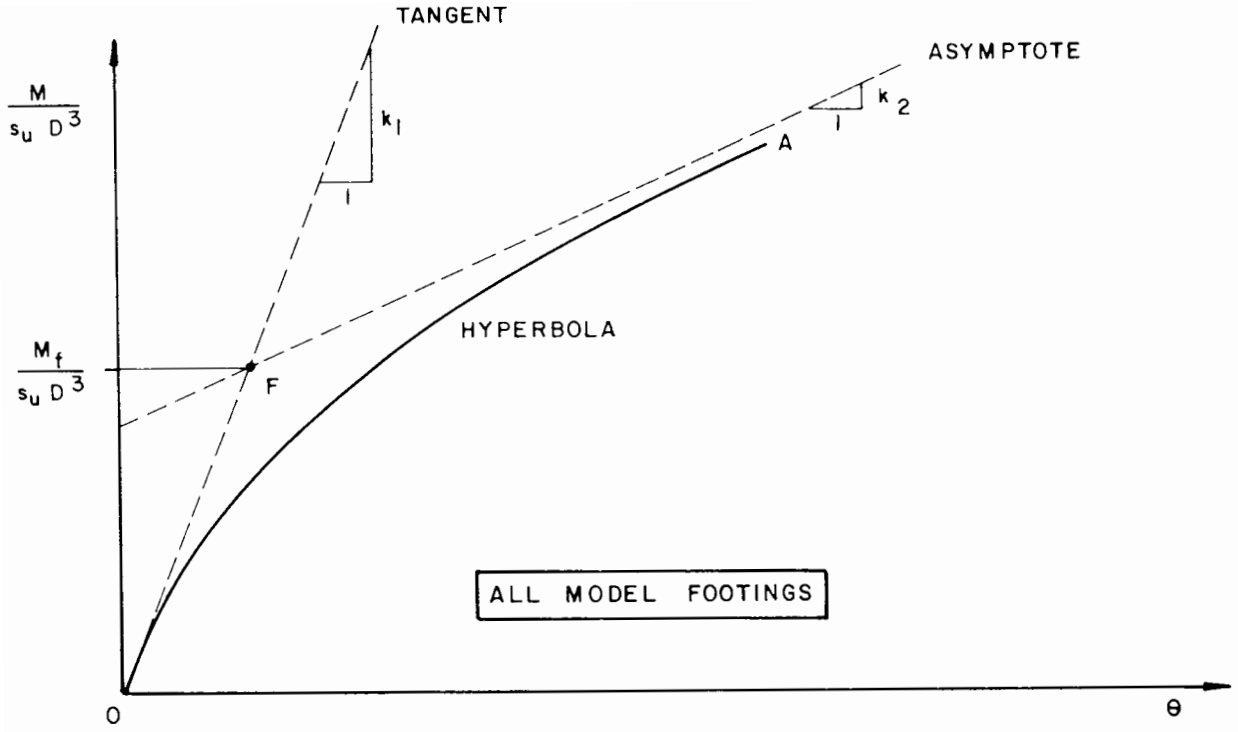

Figure 8.8 Definition of dimensionless failure moment and stiffnesses for combined loading tests

8.4.1 Rigidity Index

Equation [2.9] (Section 2.4.1 (iii)) associates the rotation angle to the moment applied to a circular rigid plate resting on the surface of a semi-infinite elastic mass. Assuming the elastic mass as being a clay soil and the moment loading rate consistent with undrained behaviour, the above equation can be expressed in non-dimensional form:

$$\frac{M}{s_u D^3} = \frac{2}{3} \frac{G}{s_u} \theta \ . \qquad [8.8]$$

An estimation of the initial rigidity index can therefore be made by equating the theoretical elastic stiffness $2G/3s_u$ to the initial stiffness obtained from test results:

$$\frac{G}{s_u} = \frac{3}{2} k_1 \ . \qquad [8.9]$$

The values of the rigidity index thus derived are indicated in Table 8.3 for the four combined loading tests performed on circular flat footings.

Table 8.3 Initial stiffness and rigidity index (combined loading tests)

test	k_1	G/s_u
H.100F.15-02	18.9	28.4
H.100F.16-02	32.0	48.0
H.100F.18-02	20.4	30.7
H.100F.33-05	29.4	44.2

Notes

(1) k_1= initial stiffness

8.4.2 Failure Moment and Stiffnesses

Table 8.4 shows the values of the hyperbola parameters a, b and c, the corresponding correlation coefficient squared, the failure moment M_f/s_uD^3 and the stiffnesses k_1 and k_2 for each test of the representative group of the main series and also for special deep tests.

In order to illustrate better the patterns of behaviour, the figures for the curves of M_f/s_uD^3, k_1 or k_2 versus cone angle were organized into two groups, each one consisting of six figures:

* in the first group each figure displays curves concerning a particular value of h/D for two levels of vertical load (low and high);

* the second group presents curves corresponding to a particular level of vertical load for two values of h/D (0.5 and 1.5).

Deep test results must be treated carefully because they were only performed with h/D = 2.0 for each level of vertical load applied and therefore were

Table 8.4 Results of the curve-fitting analysis (combined loading tests)

test	a	b	c	r^2	M_f/s_uD^3	k_1	k_2
H.100F.15-02	18.93	0.41	0.63	0.99819	0.39	18.93	0.61
H.100F.16-02	31.99	0.26	0.89	0.99784	0.26	31.99	0.87
H.100F.33-05	29.43	0.21	1.72	0.99839	0.21	29.43	1.71
H.100F.18-02	20.44	0.30	1.20	0.99775	0.28	20.44	1.13
H.100C.53-08	51.34	0.38	0.58	0.99961	0.38	51.34	0.58
H.100C.52-08	28.99	0.47	0.41	0.99758	0.46	28.99	0.41
H.100C.23-03	73.60	0.16	2.68	0.99957	0.16	73.60	2.58
H.100C.22-03	34.51	0.20	2.51	0.99902	0.19	34.51	2.34
H.100C.51-08	57.84	0.32	1.24	0.99713	0.31	57.84	1.22
H.100C.50-08	68.61	0.43	1.09	0.99723	0.42	68.61	1.07
H.100C.25-03	47.14	0.29	2.24	0.99887	0.27	47.14	2.14
H.100C.24-03	88.33	0.30	2.37	0.99227	0.29	88.33	2.30
H.100S.29-04	41.85	0.32	0.93	0.98031	0.31	41.85	0.91
H.100S.28-04	45.86	0.29	1.14	0.99329	0.28	45.86	1.11
H.100S.31-04	57.75	0.19	1.63	0.97894	0.19	57.75	1.59
H.100S.49-07	45.59	0.14	2.41	0.99762	0.13	45.59	2.29
HD.100S.47-07	51.39	0.46	1.14	0.99846	0.45	51.39	1.12
HD.100S.48-07	49.22	0.38	2.38	0.99585	0.36	49.22	2.27
HD.100S.42-06	52.22	0.41	1.95	0.98023	0.39	52.22	1.88
HD.100S.41-06	61.71	0.38	2.15	0.97776	0.37	61.71	2.08

Notes

(1) a,b,c = hyperbola parameters
(2) r^2 = correlation coefficient squared
(3) M_f/s_uD^3 = non-dimensional failure moment
(4) k_1 = non-dimensional initial stiffness
(5) k_2 = non-dimensional plastic stiffness

only plotted in the second group of figures.

It is worth mentioning again that a low level of vertical load in combined loading tests means V/s_uA = 1.7 to 2.3 while a high level means V/s_uA = 4.0 to 5.4.

(a) Analysis of the Failure Moment M_f/s_uD^3

(i) Figure 8.9 shows the failure moment obtained from tests performed on circular flat model footings in the M/s_uD^3:H/s_uA space. It also presents contours of V/s_uA (2 to 5) obtained by Brinch Hansen method of calculation applied to circular footings and one curve generated by finite element analysis for the same kind of footing and V/s_uA = 3.6 (see Section 2.4.2). The points corresponding to high vertical load seem to agree fairly well with Hansen's predictions. For low vertical load, however, the value at high horizontal load (h/D = 0.5) is very far from Hansen's result, about 75 % higher and agreeing better with the finite element results, while for low horizontal load (h/D = 1.5) a reasonable agreement can be observed. The anomalous point (V/s_uA = 1.99 and h/D = 0.5) was thoroughly checked and nothing wrong could be detected either in the processing of the raw data or in the curve fitting procedure. Purely for reference, the value of the failure moment calculated by Brinch Hansen method for V/s_uA = 1.99 and h/D = 0.5 is indicated later in Figures 8.11 and 8.13 (showing the variation of the failure moment M_f/s_uD^3 with the cone angle).

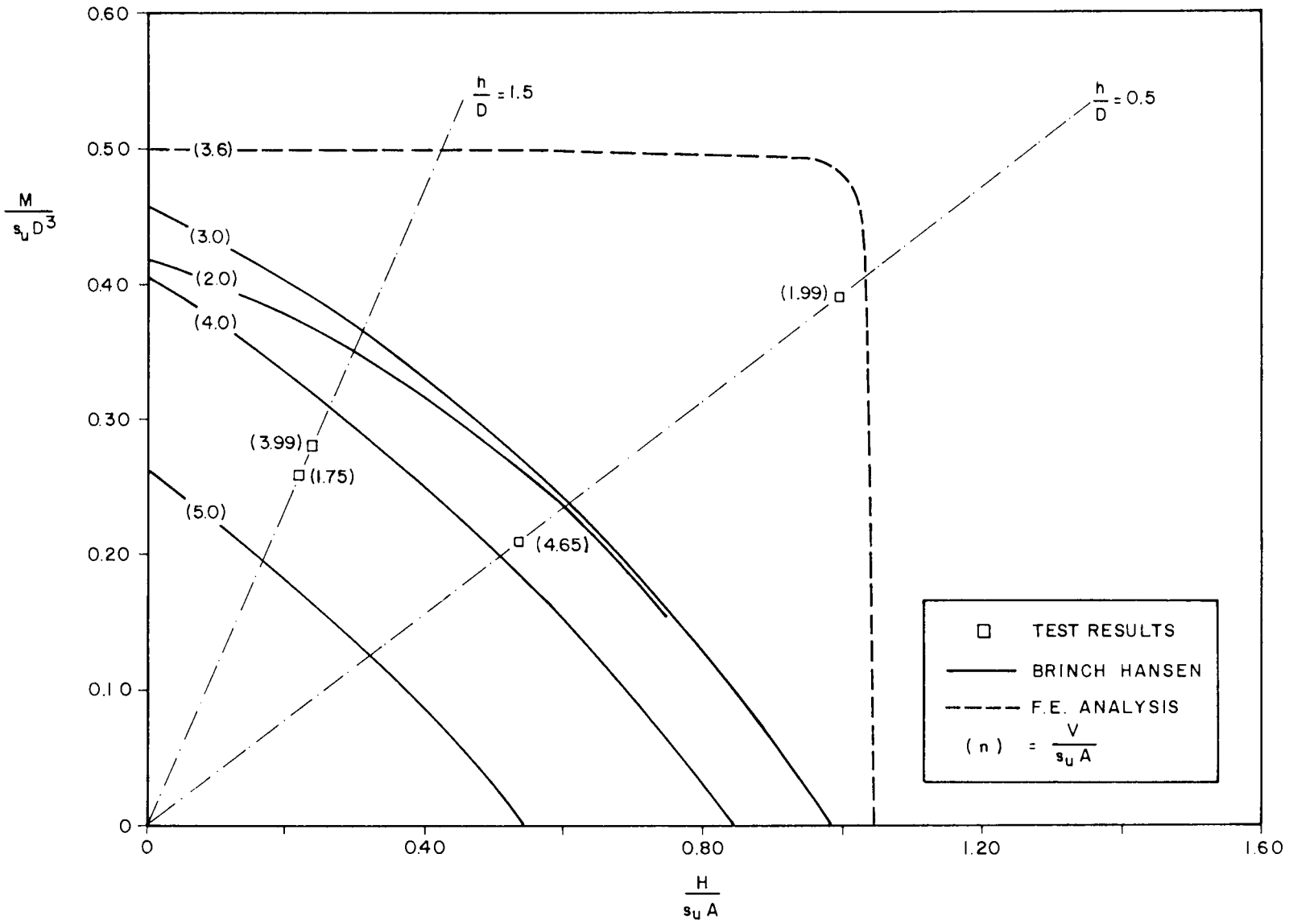

Figure 8.9 Ultimate loads in $M/s_u D^3$:$H/s_u A$ space obtained by Brinch Hansen method, finite element analysis and combined loading tests for flat circular footings

(ii) All the results obtained from the representative group of the main series of tests are presented in the M/s_uD^3:H/s_uA space, in Figure 8.10 together with curves produced by the finite element method carried out for cone angles of 120^o, 150^o and 180^o for $V/s_uA = 3.6$ (Section 2.4.2). The numerical analysis overpredicts the failure moment in almost all the cases, although the shapes of the contours of V/s_uA inferred from experimental results within the sector defined by the lines of slopes $h/D = 0.5$ and $h/D = 1.5$ are generally similar to those from the finite element curves, reflecting small variation in M_f/s_uD^3 with large variation of H/s_uA (also illustrated in Figures 8.13 and 8.14). The contours obtained from spud-can model tests exhibit a rather atypical and interesting pattern, with the higher failure moment M_f/s_uD^3 corresponding to the higher horizontal load ($h/D = 0.5$).

(iii) The pattern of behaviour represented by Figures 8.10, 8.11 and 8.12 reveals clearly that vertical load affects markedly the failure moment M_f/s_uD^3. For the values of vertical load adopted in the tests, the lower tends to produce higher failure moment M_f/s_uD^3 than the high one. Interestingly, the convexity of the curves is also affected by the vertical load, leading to much broader difference at intermediate range of cone angles than at the extreme values employed (60^o and 180^o). This trend was also identified by finite element analysis (see Section 2.4.2), although rather more weakly.

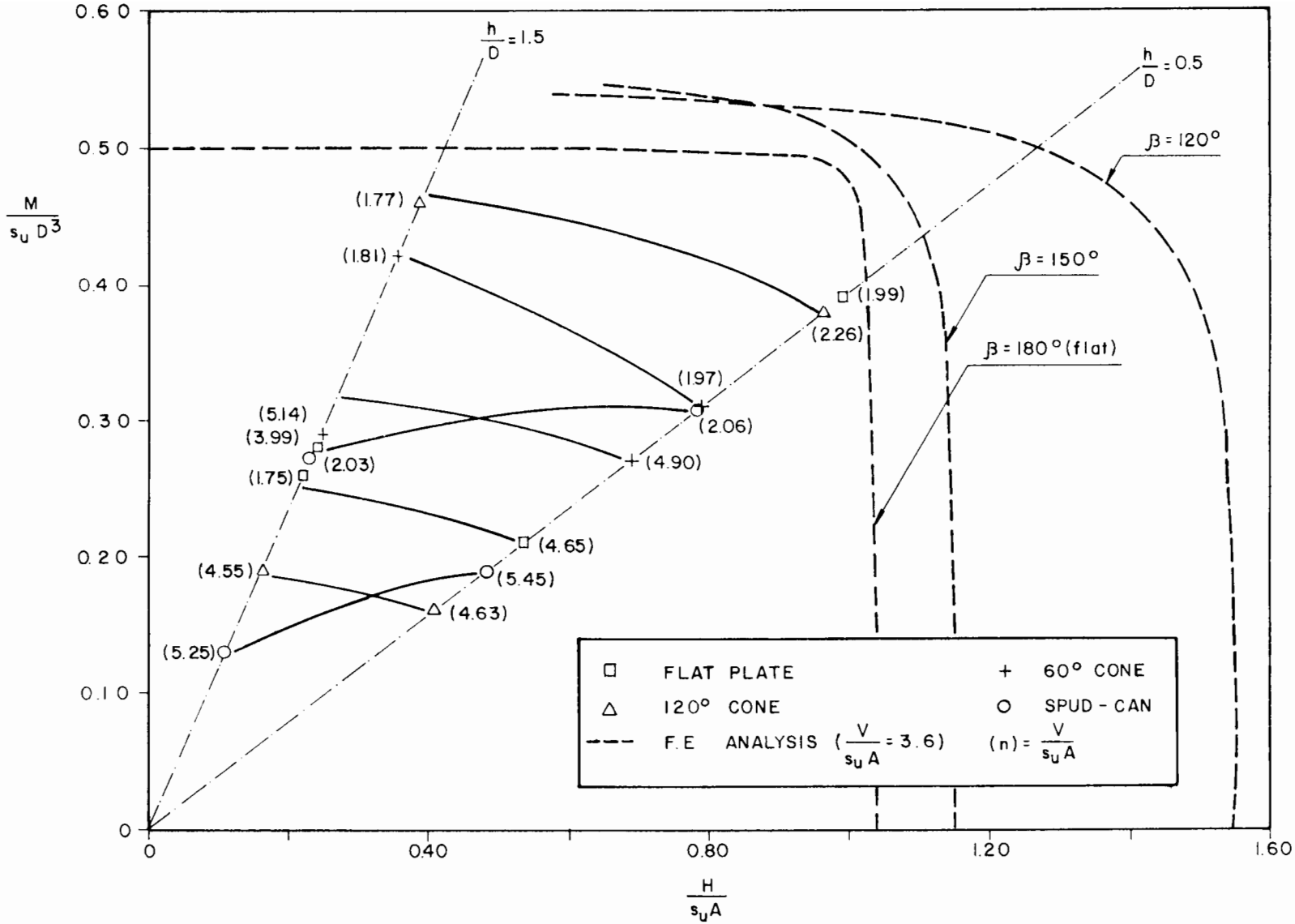

Figure 8.10 Ultimate loads in M/s_uD^3:H/s_uA space obtained by Brinch Hansen method, finite element analysis and combined loading tests for conical footings

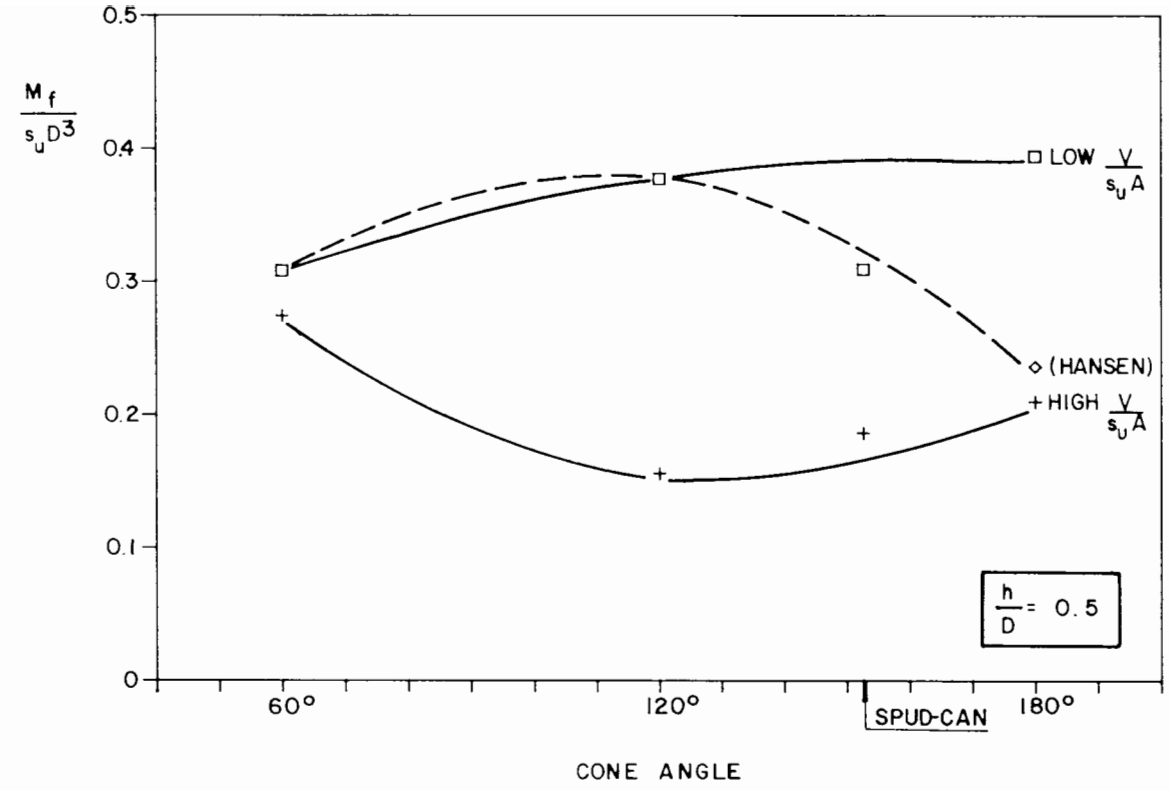

Figure 8.11 Variation of dimensionless failure moment with cone angle for h/D = 0.5

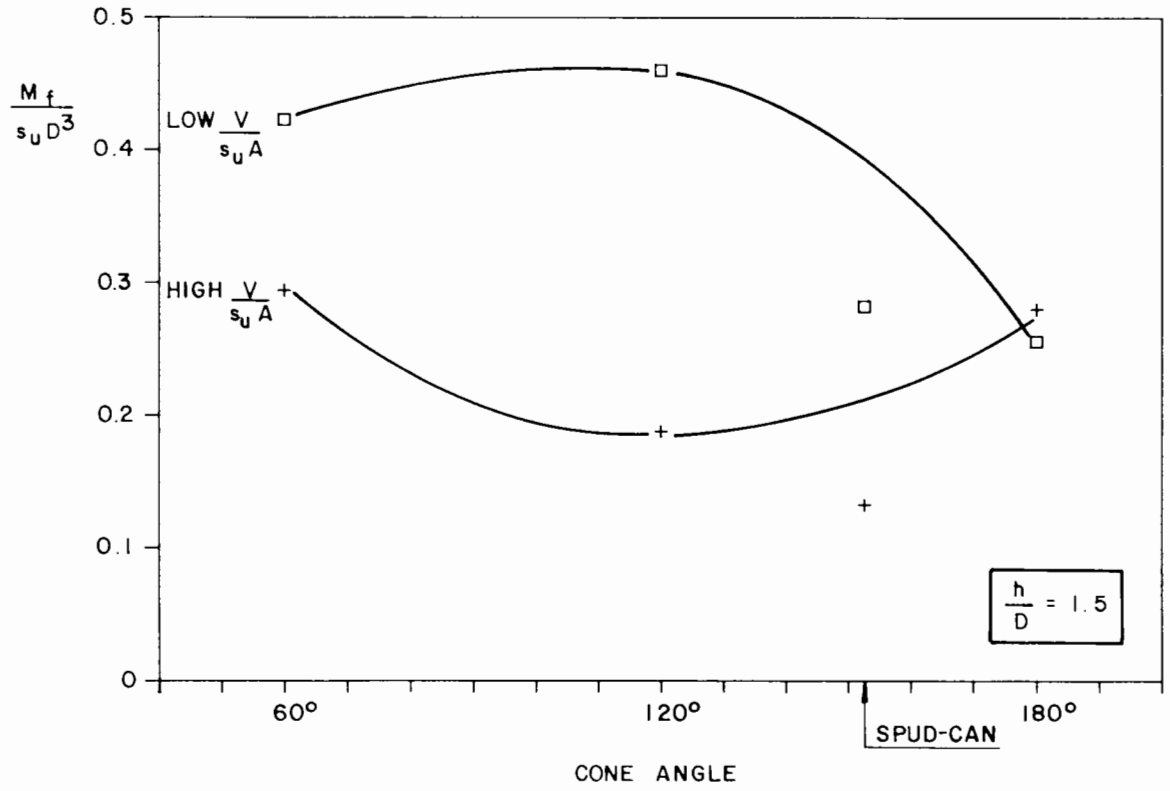

Figure 8.12 Variation of dimensionless failure moment with cone angle for h/D = 1.5

(iv) A spud-can tested at the surface of the clay sample exhibits a failure moment M_f/s_uD^3 of about 70 % of the values corresponding to the equivalent cone, for low horizontal load (h/D = 1.5). For high horizontal load (h/D = 0.5) the spud-can failure moment M_f/s_uD^3 is about 15 % higher when the vertical load is high but no conclusion can be made for low vertical load owing to the anomalous result for the flat circular footing.

(v) Deep tests, performed on spud-can models with h/D = 2.0, should be compared with shallow tests carried out with h/D = 1.5 because, for the same moment, the difference in the horizontal load between these two configurations is relatively small (only 12.5 % of the difference between horizontal loads corresponding to h/D = 0.5 and h/D = 1.5). The embedment in the clay produced an increase in M_f/s_uD^3 of 39 % to 61 % for low vertical load and about 181 % for high vertical load (Figures 8.13 and 8.14), although this increase does not seem to be dependent on the initial depth of installation of the spud-can model (d/D = 0.35 or d/D = 0.70).

(b) Analysis of the Initial Stiffness k_1

(i) Figures 8.15 and 8.16 show that vertical load at the levels adopted in this research does not influence significantly the initial stiffness. The horizontal load, however, has apparently affected the shape of the curves, high horizontal load (h/D = 0.5) displaying upwards convexity (negative curvature) and the opposite for low horizontal load (h/D = 1.5), as illustrated in Figures 8.17 and 8.18.

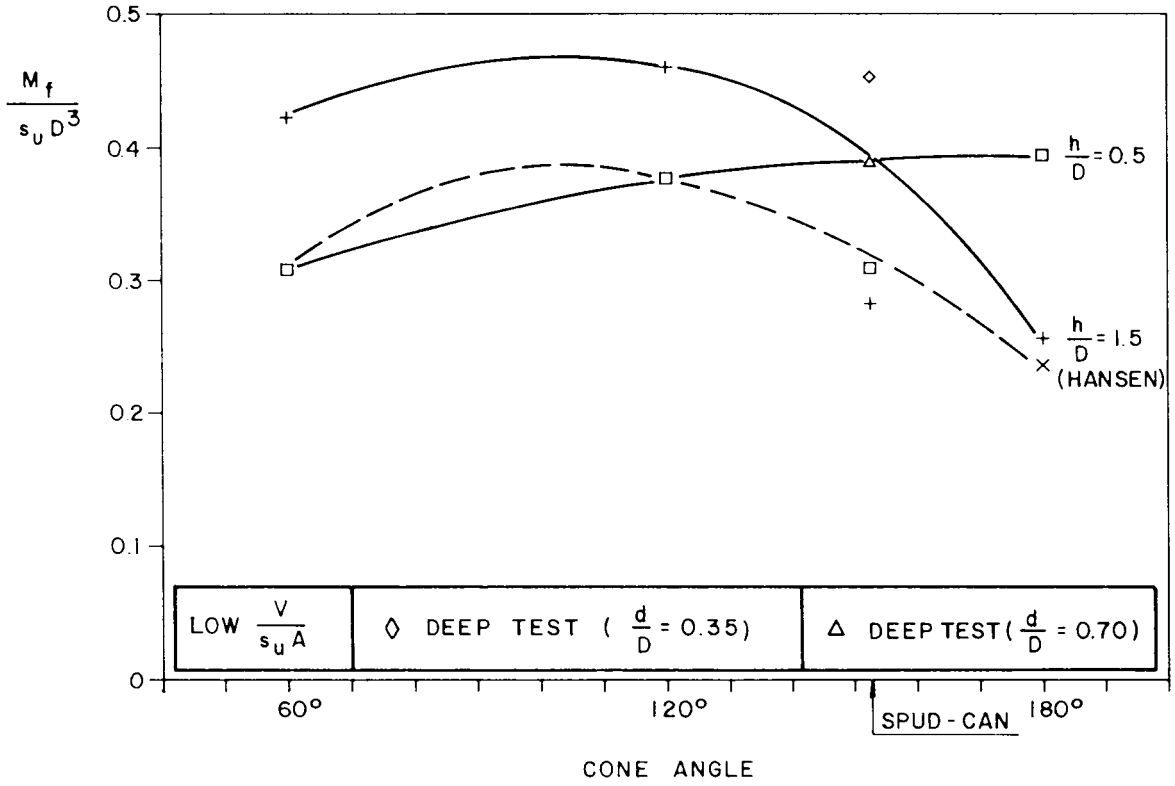

Figure 8.13 Variation of dimensionless failure moment with cone angle for low vertical load

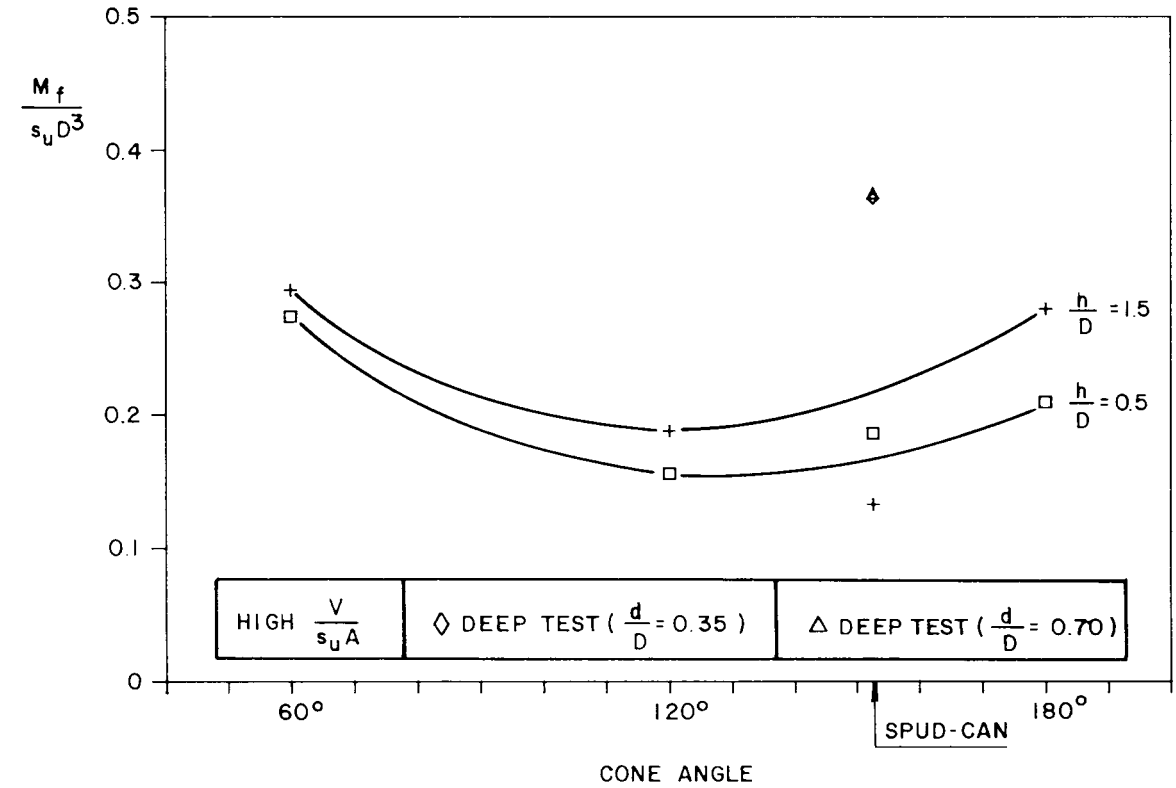

Figure 8.14 Variation of dimensionless failure moment with cone angle for high vertical load

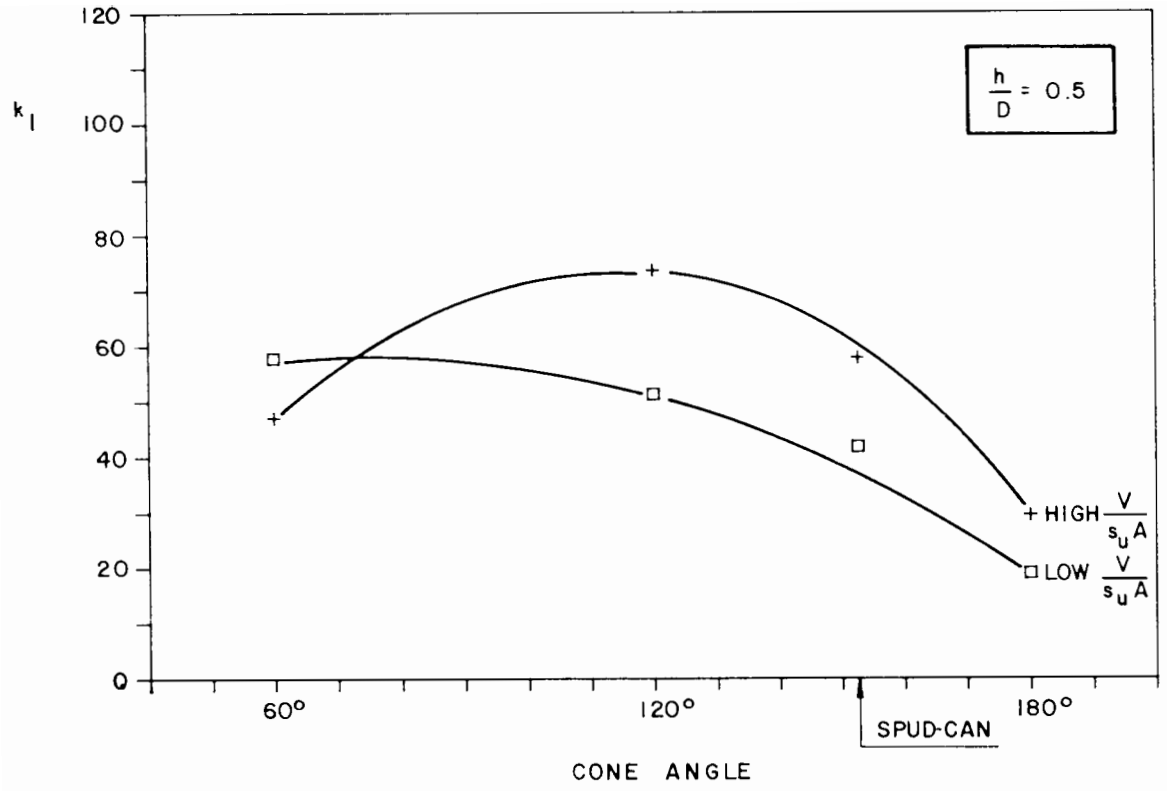

Figure 8.15 Variation of dimensionless initial rotational stiffness with cone angle for h/D = 0.5

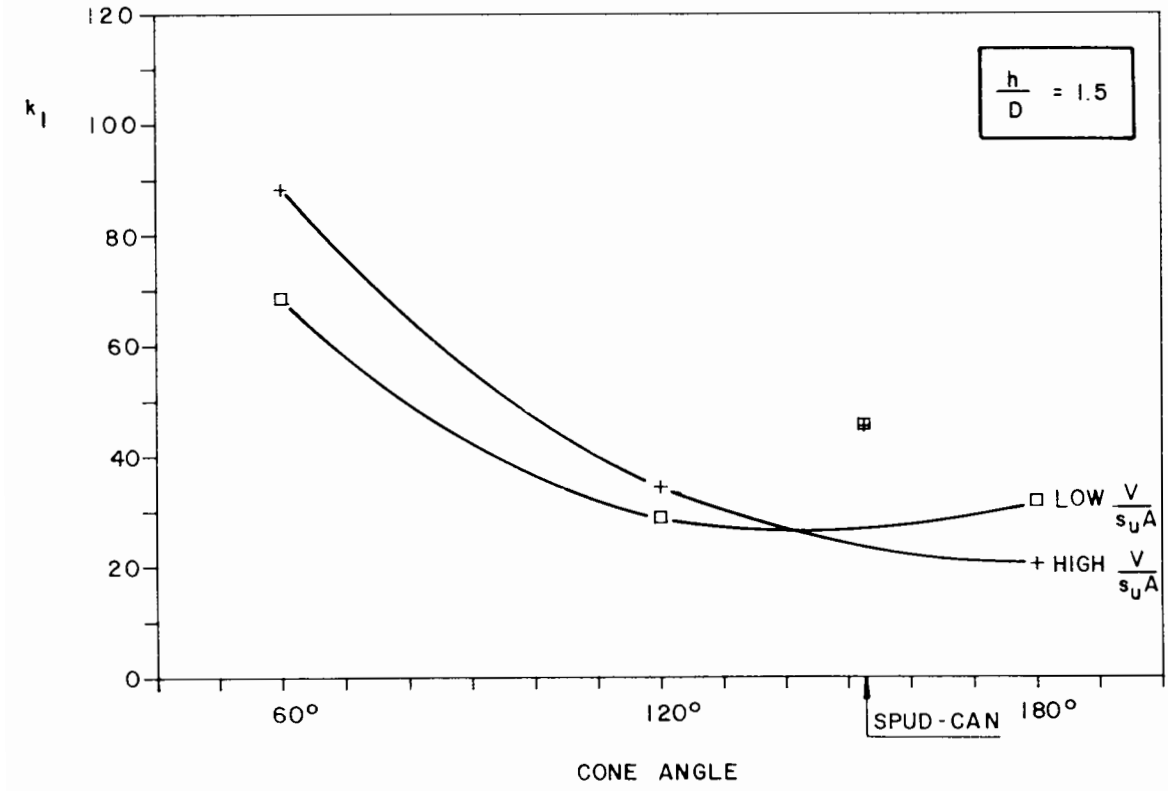

Figure 8.16 Variation of dimensionless initial rotational stiffness with cone angle for h/D = 1.5

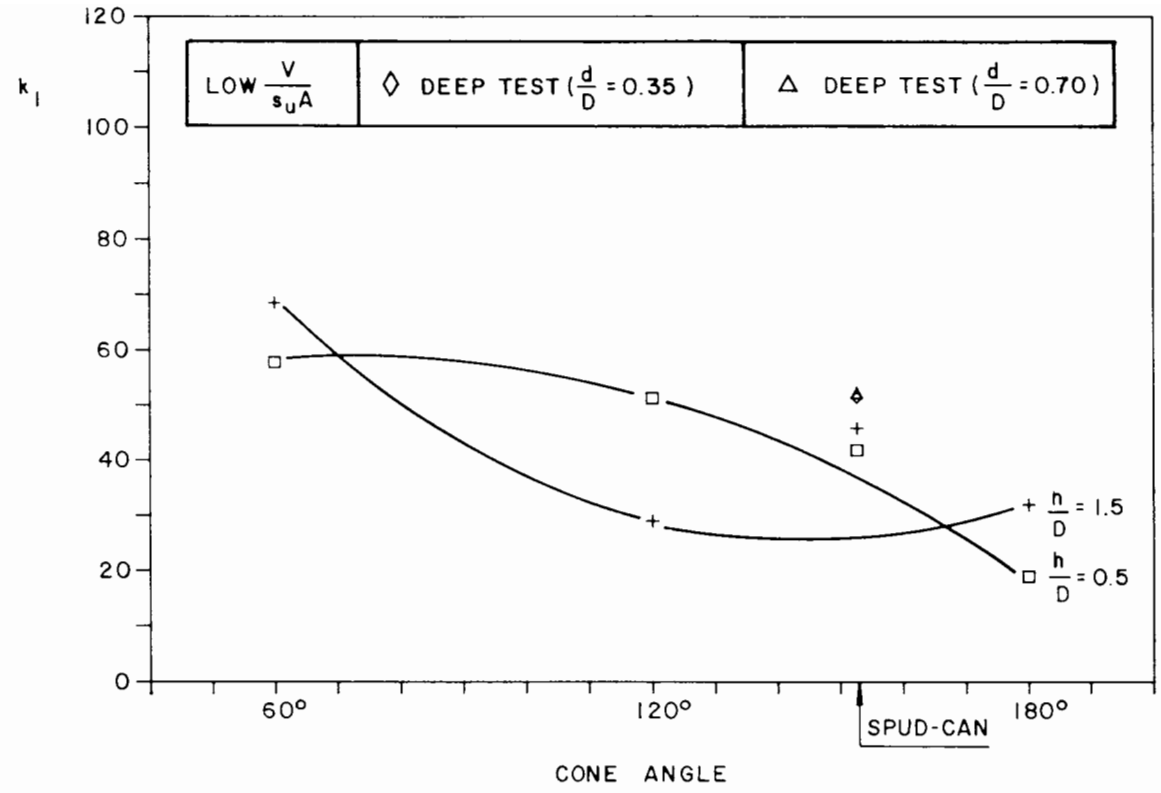

Figure 8.17 Variation of dimensionless initial rotational stiffness with cone angle for low vertical load

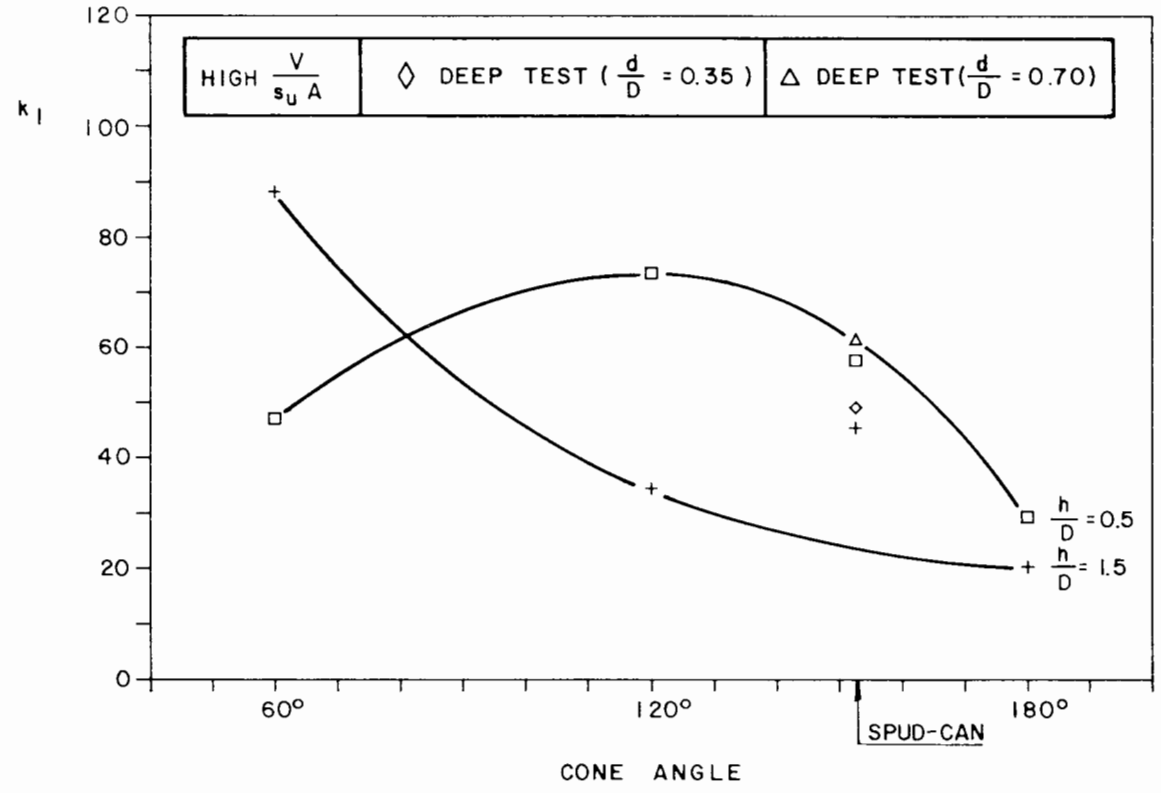

Figure 8.18 Variation of dimensionless initial rotational stiffness with cone angle for high vertical load

(ii) A spud-can under low horizontal load (h/D = 1.5) behaves as about 70 % and 100 % stiffer than an equivalent cone for low and high vertical load respectively. For high horizontal load (h/D = 0.5) a spud-can behaves approximately like the equivalent cone. Deep tests feature stiffer behaviour than shallow ones, the gain being about 13 % for low vertical load and 8 % and 35 % for high vertical load. No trend of stiffening with the embedment could be observed between tests at d/D = 0.35 and d/D = 0.70.

(iii) The pattern of variation of the initial stiffness k_1 with the cone angle for low horizontal load (h/D = 1.5) represented in Figure 8.16 suggests a behaviour more like a rough than a smooth footing when compared with the variation of the elastic rotational stiffness function obtained by finite element analysis for both rough and smooth footings (Figure 2.1, Section 2.4.1). Moreover, the spud-can response 70 % and 100 % stiffer than equivalent cone (Section (ii) above) indicates that this model footing is neither behaving as fully rough nor fully smooth if compared with the results of finite element calculations carried out for similar spud-can footing (Table 2.3, Section 2.4.1).

(c) Analysis of the Plastic Stiffness k_2

(i) As in the vertical central loading test results (Section 8.3.2, item iii), the plastic stiffness k_2 varies in the opposite way to the failure moment $M_f/s_u D^3$, as might be expected. Figures 8.19 and 8.20 indicate that k_2 is strongly dependent on the vertical load, particularly for the intermediate range of cone angles. The plastic

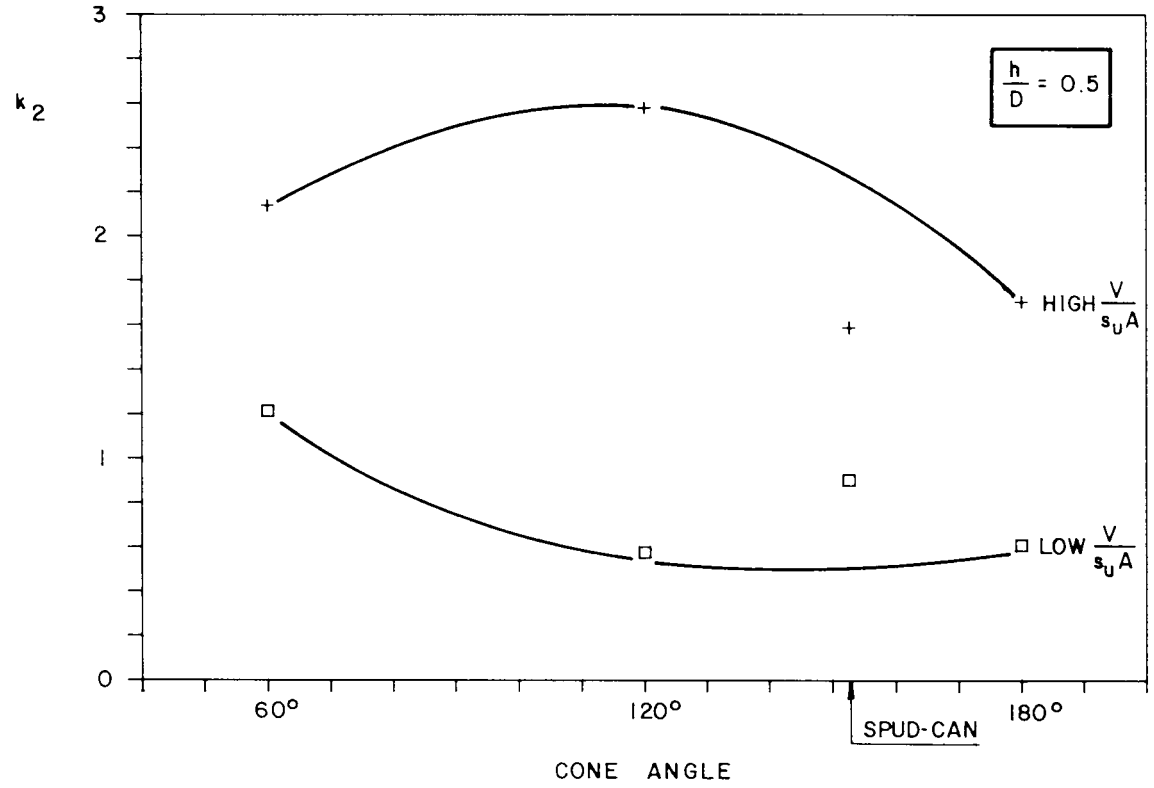

Figure 8.19 Variation of dimensionless plastic rotational stiffness with cone angle for h/D = 0.5

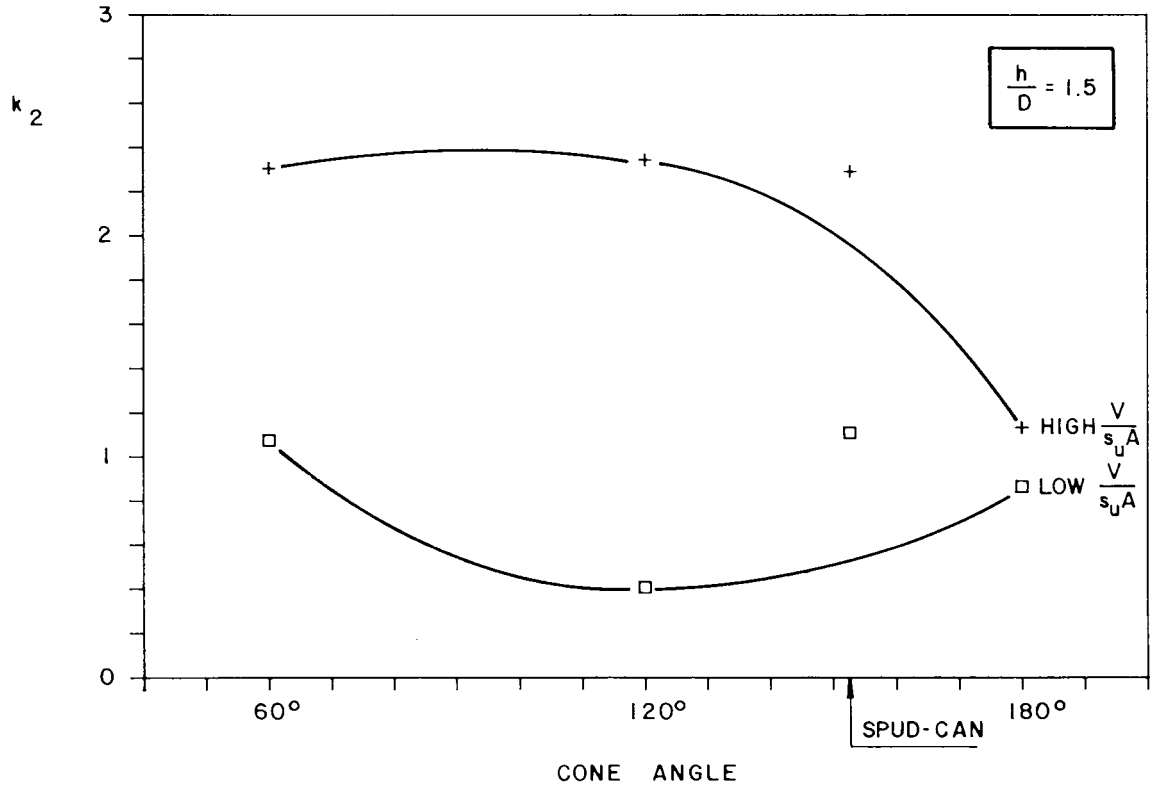

Figure 8.20 Variation of dimensionless plastic rotational stiffness with cone angle for h/D = 1.5

stiffness k_2 for high vertical load is on average 95 %, 408 % and 105 % higher than the values observed for low vertical load for the 60^o cone, 120^o cone and flat circular plate respectively.

(ii) Figures 8.21 and 8.22 show that the intensity of the horizontal load plays no important role in the pattern of behaviour of the plastic stiffness k_2.

(iii) A spud-can in this case also has a stiffer behaviour than the equivalent cone for low horizontal load (h/D = 1.5) and either low or high vertical load (about 100 % and 20 % higher for low and high V/s_uA respectively). When the horizontal load is high (h/D = 0.5) the

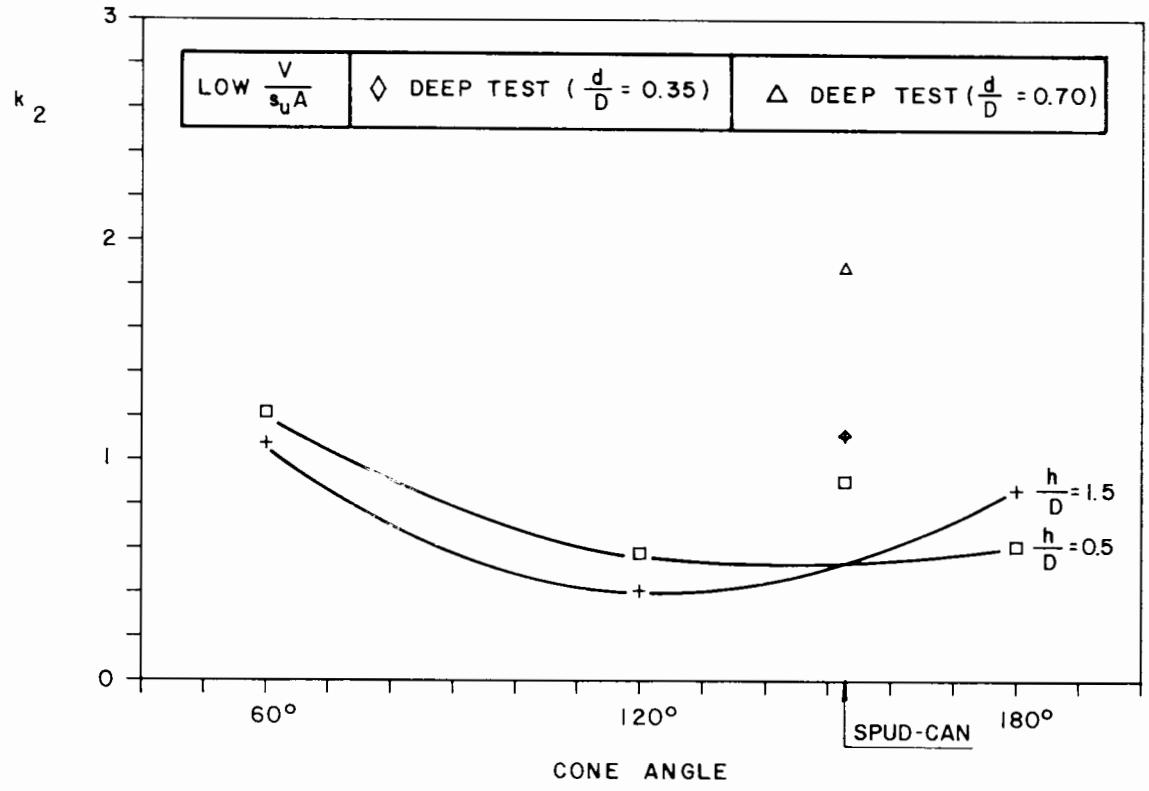

Figure 8.21 Variation of dimensionless plastic rotational stiffness with cone angle for low vertical load

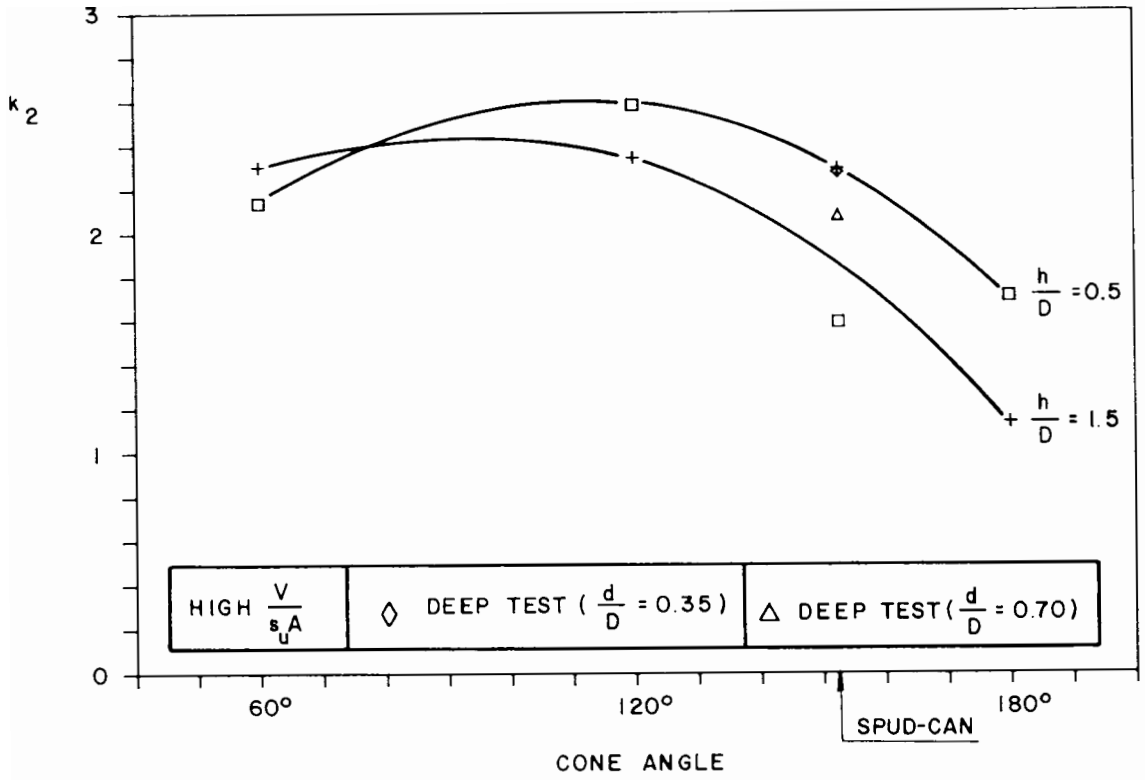

Figure 8.22 Variation of dimensionless rotational stiffness with cone angle for high vertical load

spud-can stiffness k_2 is still higher than the equivalent cone one (by about 70 %) for low vertical load, but is lower (by about 30 %) for high vertical load. Due to the large scatter observed, the results of deep tests are not conclusive in this case.

(d) Analysis of the Unloading Stiffness k_3

(i) In accordance with the results presented in Figures 8.23, 8.24 and 8.25, the first important information concerning the unloading stiffness k_3 is that for small rotation angles $\Delta\theta$ it is much higher than the initial stiffness k_1. Values of k_3 up to approximately three times the maximum value of k_1 are observed.

(ii) Figure 8.23 shows that the value of the vertical load only slightly affects the unloading stiffness k_3. The same average trend is observed in the initial stiffness k_1.

(iii) In a similar way to the initial stiffness k_1 behaviour, the embedment definitely produces an increase in the stiffness k_3, as suggested by the patterns displayed in Figure 8.24.

(iv) No noticeable influence in the unloading stiffness k_3 produced by the intensity of the horizontal load could be identified, as illustrated in Figure 8.25.

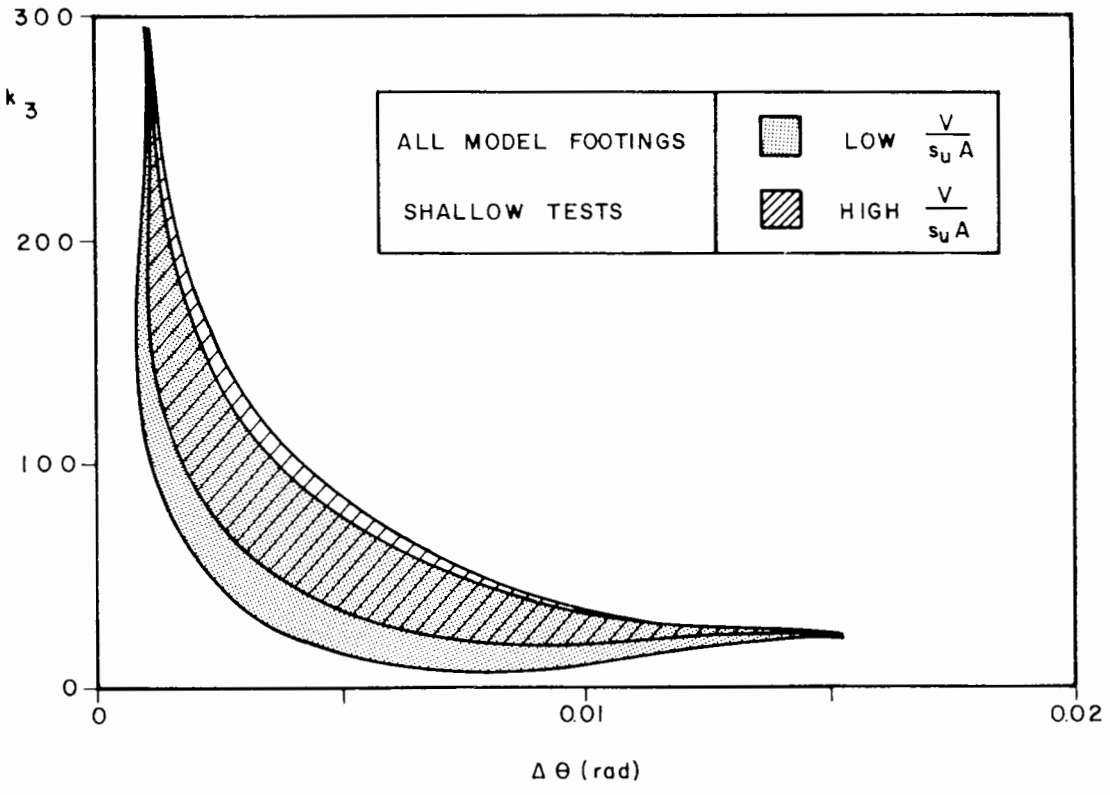

Figure 8.23 Band of values of dimensionless unloading rotational stiffness obtained from all standard (shallow) combined loading tests for low and high vertical load

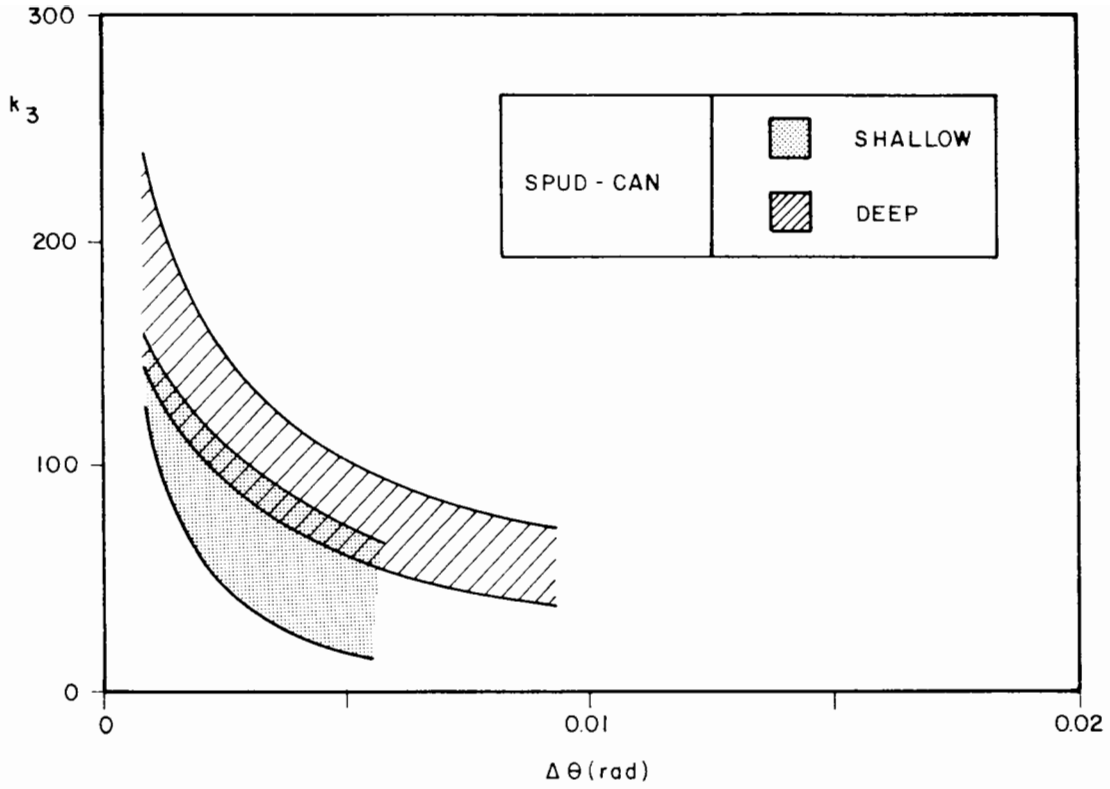

Figure 8.24 Band of values of dimensionless unloading rotational stiffness for shallow and deep spud-can tests

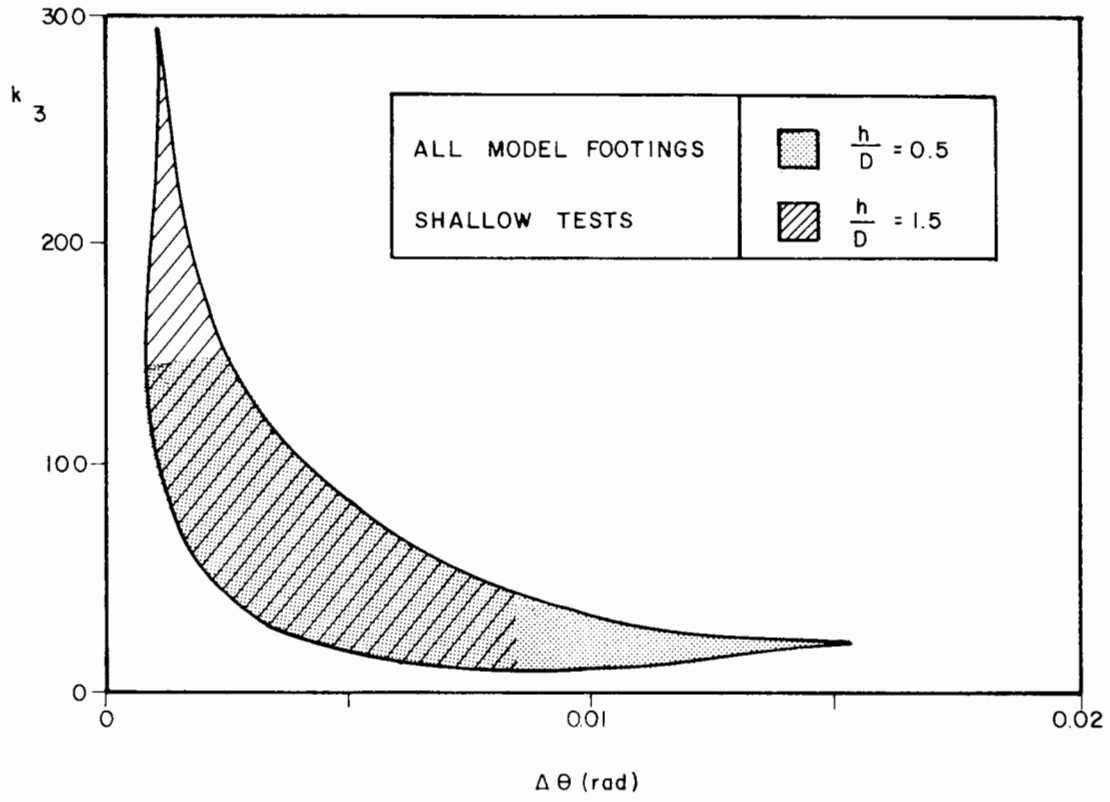

Figure 8.25 Band of values of dimensionless unloading rotational stiffness obtained from all standard (shallow) combined loading tests for h/D = 0.5 and h/D = 1.5

CHAPTER 9

ANALYSIS OF THE RESULTS - CYCLIC LOADING

9.1 Introduction

Because of the difficulty inherent in modelling foundations on clay under cyclic loading, as mentioned in Section 5.3, the results obtained in this stage of the research must be considered very cautiously. Since the behaviour of footings under cyclic loading is directly related to the manner in which pore pressures build up and dissipate, clearly no comprehensive analysis could be made without knowing the variation of pore pressure around the model spud-can during the test. Since no pore pressure measurements were carried out in this work, the analysis of cyclic loading tests is simply limited to identifying patterns of behaviour of a set of relevant parameters.

Although the number of tests carried out was the maximum possible within the time available, it is undeniably limited and is not believed to be enough to allow accurate quantitative conclusions on the behaviour of the model spud-can under sinusoidal moment loading. Nevertheless, some important trends could be identified and are presented in this chapter.

The analysis was performed only for the following group of quantities, believed to be of most relevance for practical purposes in offshore engineering:

* increment of vertical displacement;

* variation of rotation;

* rotational energy dissipated per cycle;

* damping ratio.

Increment of vertical displacement is defined as the component of the vertical displacement observed after cyclic loading has started. Variation of rotation (associated with peak-to-peak moment amplitude) is defined in Section 7.1.

In the context of this analysis, the first three quantities above are always presented and discussed in non-dimensional form and are represented in Figures 9.1 to 9.6 where, for each case of period and offset of loading, they are plotted against the vertical load V/s_uA for the 2nd, 20th, 100th and 400th cycles (in some cases the test was not long enough to provide data point at 400th cycles) and for both low and high amplitude of moment loading M_a/s_uD^3. The second cycle was chosen rather than the first because the first loop, passing through the origin, has one degree of freedom less than the others, featuring consequently an atypical shape.

Since there are only two data points for each case of amplitude of moment, number of cycles, period and offset of loading, a straight line was drawn between them to indicate the trend. A linear variation is by no means suggested by this procedure.

9.2 Increment of Vertical Displacement

Figures 9.1 and 9.2 show the increment of vertical displacement $\Delta z/D$

plotted against the vertical load V/s_uA for the cases mentioned in Section 9.1.

(a) Influence of the Number of Cycles N

As would be expected, the increment of vertical displacement $\Delta z/D$ generally increases with the number of cycles N. In all cases of low amplitude of moment M_a/s_uD^3 and also for the 30 seconds period tests at high amplitude, $\Delta z/D$ increases faster for high vertical load V/s_uA than for low V/s_uA. For 8 seconds period tests at high M_a/s_uD^3 the opposite trend occurs.

(b) Influence of the Vertical Load V/s_uA

The results indicate that the value of the vertical load V/s_uA in the range adopted in this work plays only a secondary role in the variation of the increment of vertical displacement $\Delta z/D$. For low amplitude of moment M_a/s_uD^3 and for the same number of cycles $\Delta z/D$ increases with V/s_uA. For high M_a/s_uD^3 the trend differs for tests at different frequency.

(c) Influence of the Amplitude of Moment Loading M_a/s_uD^3

The value of the amplitude of moment M_a/s_uD^3 affects the increment of vertical displacement $\Delta z/D$ more markedly than the vertical load V/s_uA. For

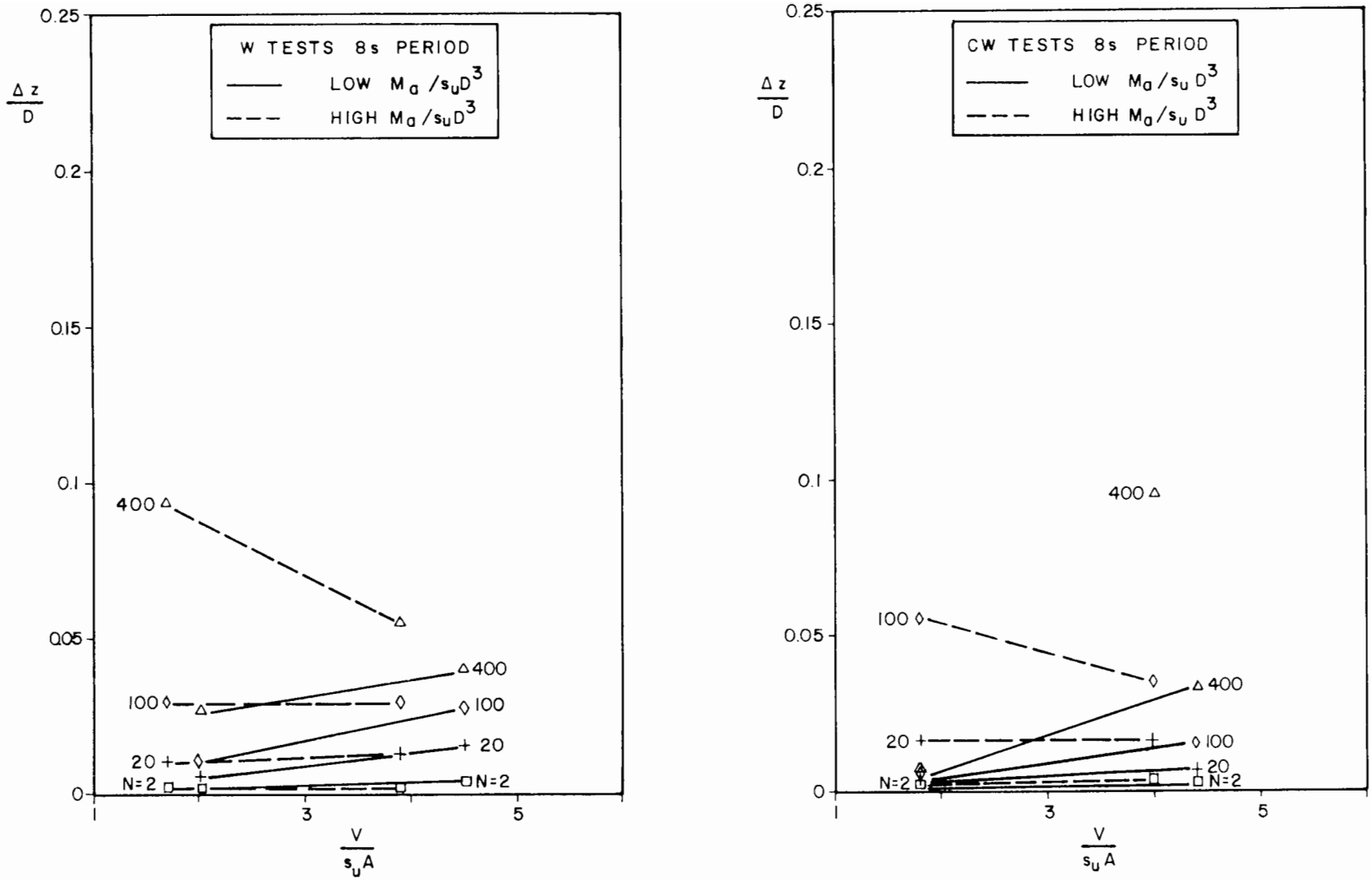

Figure 9.1 Variation of dimensionless increment of vertical displacement with vertical load and number of cycles for fast tests

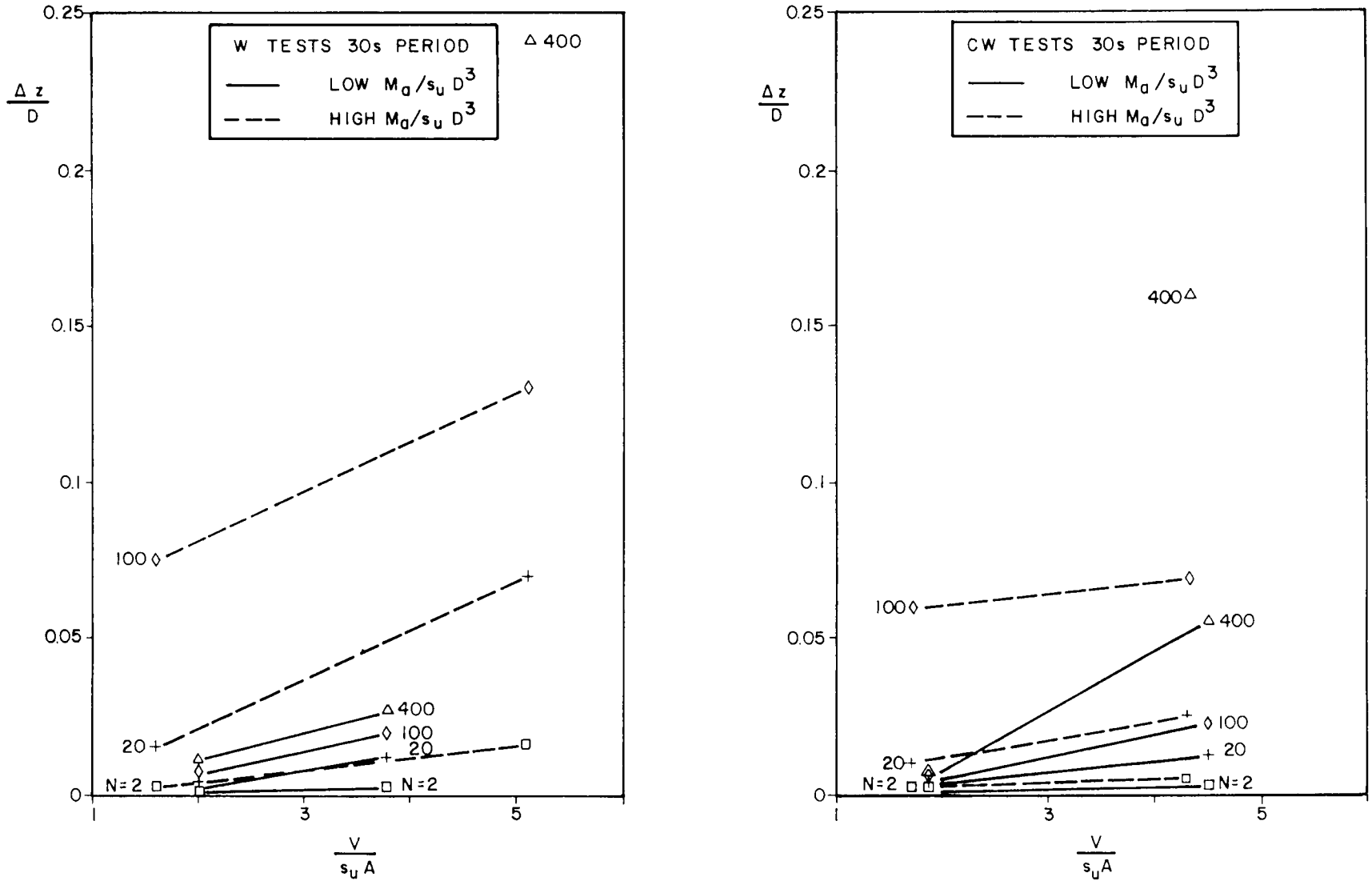

Figure 9.2 Variation of dimensionless increment of vertical displacement with vertical load and number of cycles for slow tests

the same V/s_uA and number of cycles $\Delta z/D$ is higher for high values of M_a/s_uD^3 than for low ones. Special tests performed with double amplitude show clearly the same pattern of behaviour, as illustrated in Figure 7.34 (Section 7.3.1).

(d) Influence of the Offset of Moment Loading M_o/s_uD^3

The results obtained do not indicate any particular trend of behaviour relating the increment of vertical displacement with the offset of moment loading M_o/s_uD^3.

(e) Influence of the Period of Moment Loading

Slow tests (30 seconds period) exhibit larger increment of vertical displacement than fast tests (8 seconds period). The difference may be accounted for by the consolidation associated with the dissipation of pore pressures built up during cyclic loading, bearing in mind that, for the same number of cycles, slow tests are longer by a factor 3.75 than fast tests.

9.3 Variation of Rotation

Because very small variations of rotation $\Delta\theta$ were observed in some tests, a rather large scatter in data points was associated with the measurements, owing to the inability of the data logging system to read small angles (within the magnitude of a thousandth of radian) accurately.

The values of the variation of rotation $\Delta\theta$ displayed in Figures 9.3 and 9.4,

plotted against vertical load V/s_uA for the various parameters adopted in this research, were obtained from curves carefully fitted through the data points in each case.

It is worth mentioning that the variation of rotation $\Delta\theta$ for a fixed amplitude of moment loading M_a/s_uD^3 is inversely proportional to the equivalent non-dimensional rotational stiffness k (Equation [7.1], Section 7.1).

(a) Influence of the Number of Cycles N

In 75 % of the tests performed with low vertical load V/s_uA, the variation of rotation $\Delta\theta$ exhibits a minimum value varying approximately between the 2nd and the 100th cycles, featuring a more flexible response afterwards. For high vertical load $\Delta\theta$ decreases steadily with the number of cycles.

(b) Influence of the Vertical Load V/s_uA

Making allowance for the inaccuracies involved in the determination of small values of variation of rotation $\Delta\theta$, it is obvious that vertical load V/s_uA affects this quantity, the higher the value of V/s_uA the stiffer the behaviour. In that respect, the equivalent stiffness k behaves more like the plastic stiffness k_2 than the elastic stiffness k_1 or the unloading stiffness k_3 in monotonic loading tests, although the magnitude of the stiffness is very different.

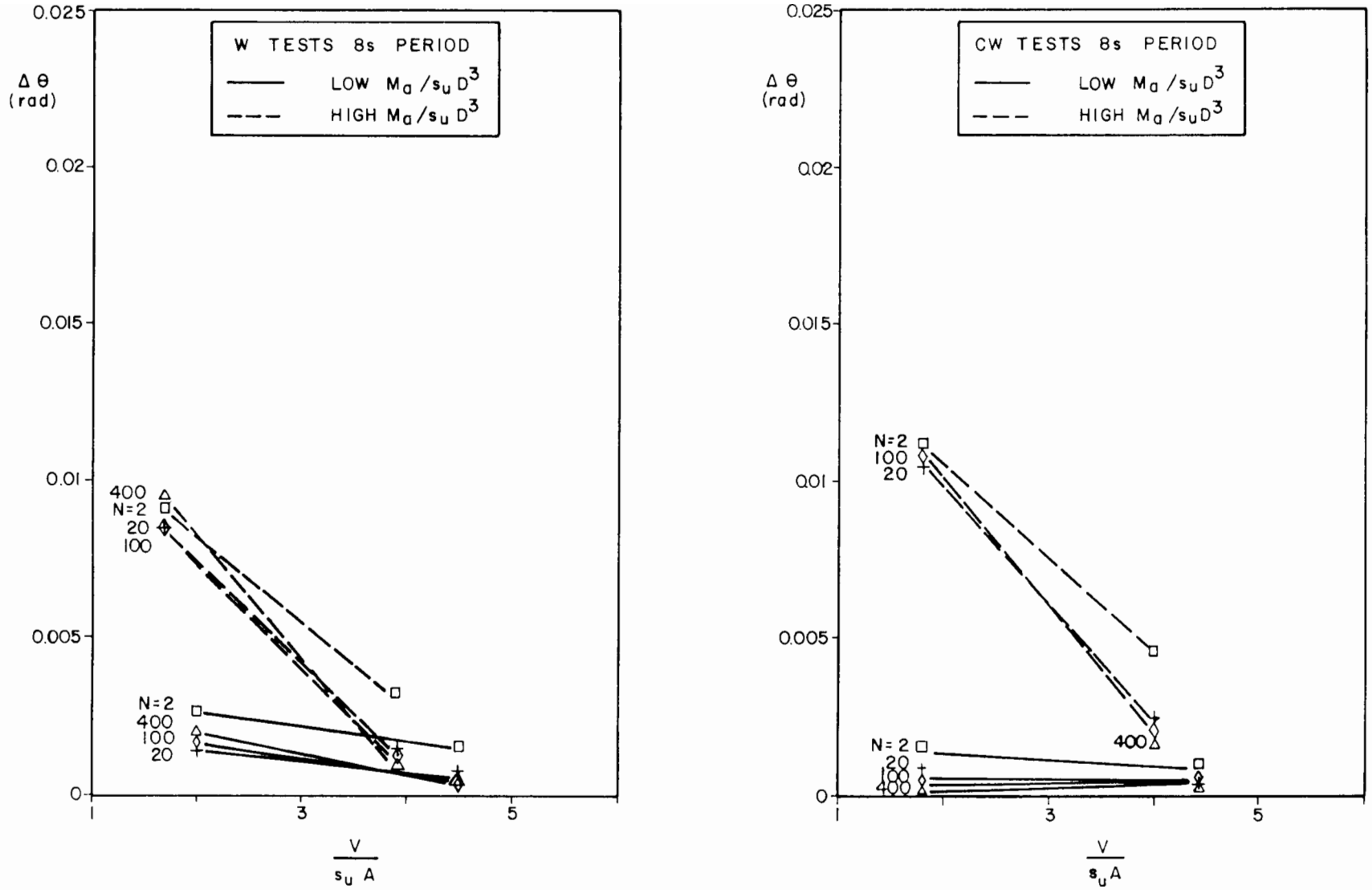

Figure 9.3 Variation of variation of rotation with vertical load and number of cycles for fast tests

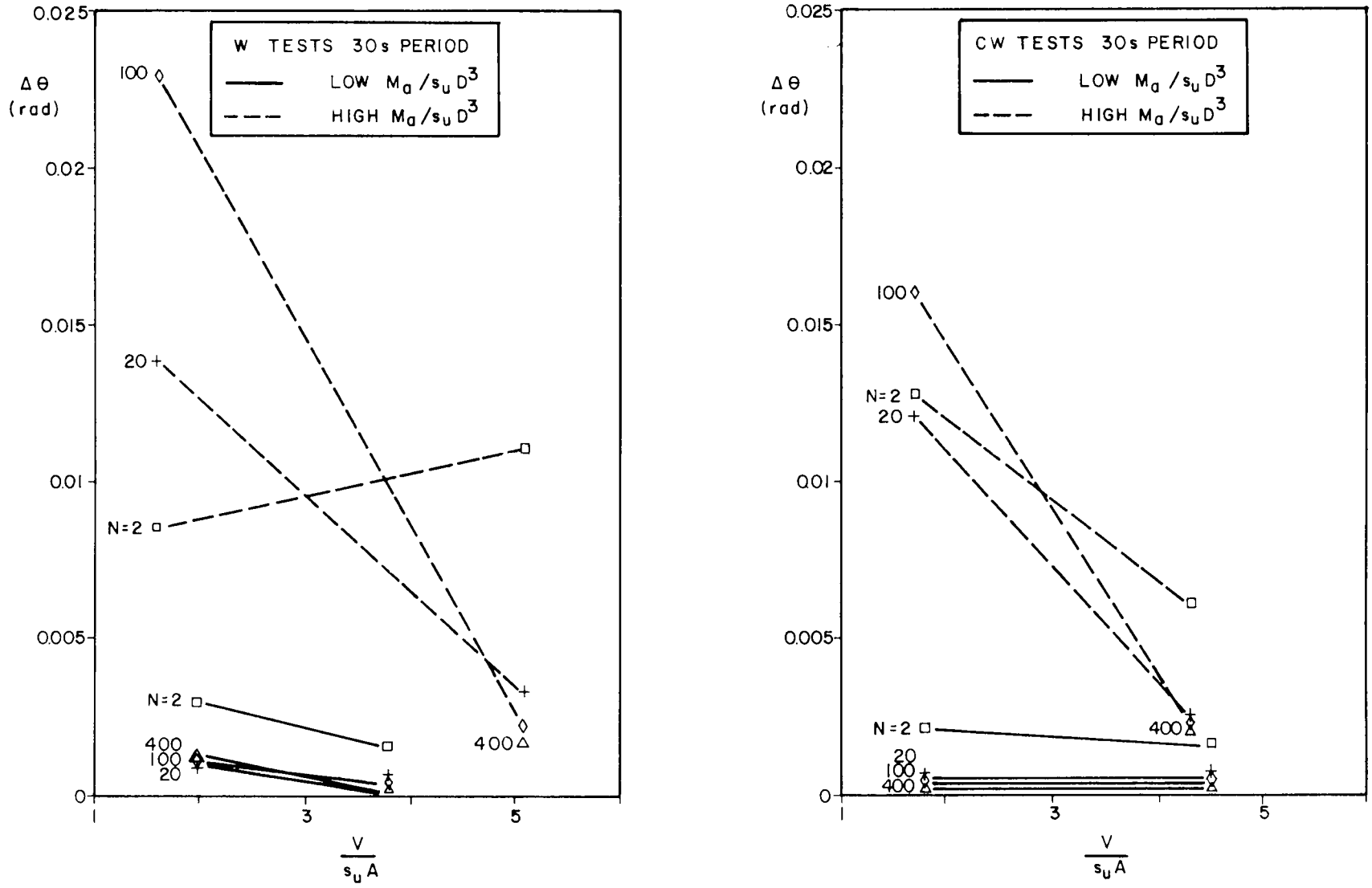

Figure 9.4 Variation of variation of rotation with vertical load and number of cycles for slow tests

(c) Influence of the Amplitude of Moment Loading M_a/s_uD^3

Obviously the variation of rotation $\Delta\theta$ increases with the amplitude of moment M_a/s_oD^3 and consequently this analysis is better expressed in terms of equivalent rotational stiffness k.

For high values of amplitude of moment M_a/s_uD^3 and low values of vertical load V/s_uA the stiffness k varies from 32 to 45 at the 2nd cycle and from 16 to 47 at the 100th cycle (only one observation at 400 cycles corresponding to 30 seconds period and no offset of moment loading: k = 42). For high values of both M_a/s_uD^3 and V/s_uA the stiffness k varies from 44 to 120 at the 2nd cycle and from 195 to 370 at the 400th cycle.

For low values of amplitude of moment M_a/s_uD^3 the stiffness k is much less accurately defined. For low vertical load V/s_uA it varies in the range from 82 to 162 at the 2nd cycle and from 126 to 1050 at the 400th cycle. For high V/s_uA the stiffness k varies from 120 to 263 at the 2nd cycle and from 525 to 3600 at the 400th cycle. It can be concluded therefore that higher stiffness occurs at lower amplitude of moment.

(d) Influence of the Offset of Moment Loading M_o/s_uD^3

No particular pattern of behaviour relating the variation of rotation $\Delta\theta$ with the offset of moment loading M_o/s_uD^3 could be established.

(e) Influence of the Period of Moment Loading

Tests performed with high amplitude of moment M_a/s_uD^3 reveal larger values of variation of rotation $\Delta\theta$ for 30 seconds period than for 8 seconds period when the vertical load V/s_uA is low. When V/s_uA is high, the magnitude of $\Delta\theta$ is approximately the same for either period. For low M_a/s_uD^3 no clear trend can be identified.

9.4 Rotational Energy Dissipated per Cycle

As expected, the overall pattern of behaviour of the non-dimensional rotational energy dissipated per cycle W/s_uD^3 is very similar to the variation of rotation $\Delta\theta$. In this case, however, as this parameter is evaluated by means of numerical integration of a number of points along the loop, the scatter observed is smaller and therefore a better accuracy is achieved.

Figures 9.5 and 9.6 illustrate how the rotational energy dissipated per cycle W/s_uD^3 varies. The following observations apply:

(a) Influence of the Number of Cycles N

In 75 % of the tests with low V/s_uA the energy dissipated per cycle W/s_uD^3 is initially high, decreasing to a minimum value between approximately the 2nd and the 100th cycle and becoming thereafter more dissipative (usually slightly more dissipative, but markedly more dissipative in slow tests performed with high amplitude of moment). Tests with high V/s_uA become

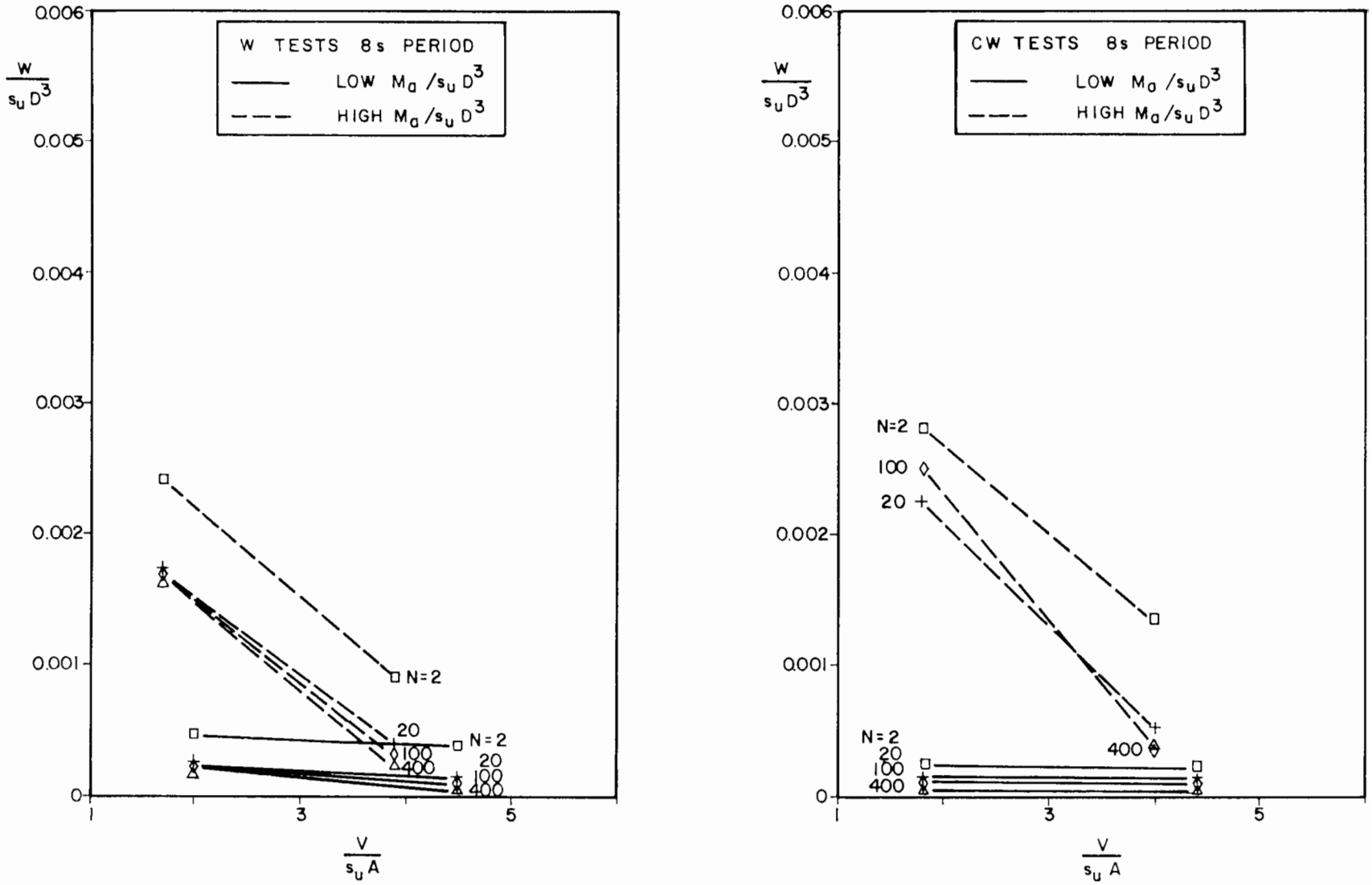

Figure 9.5 Variation of dimensionless rotational energy dissipated per cycle with vertical load and number of cycles for fast tests

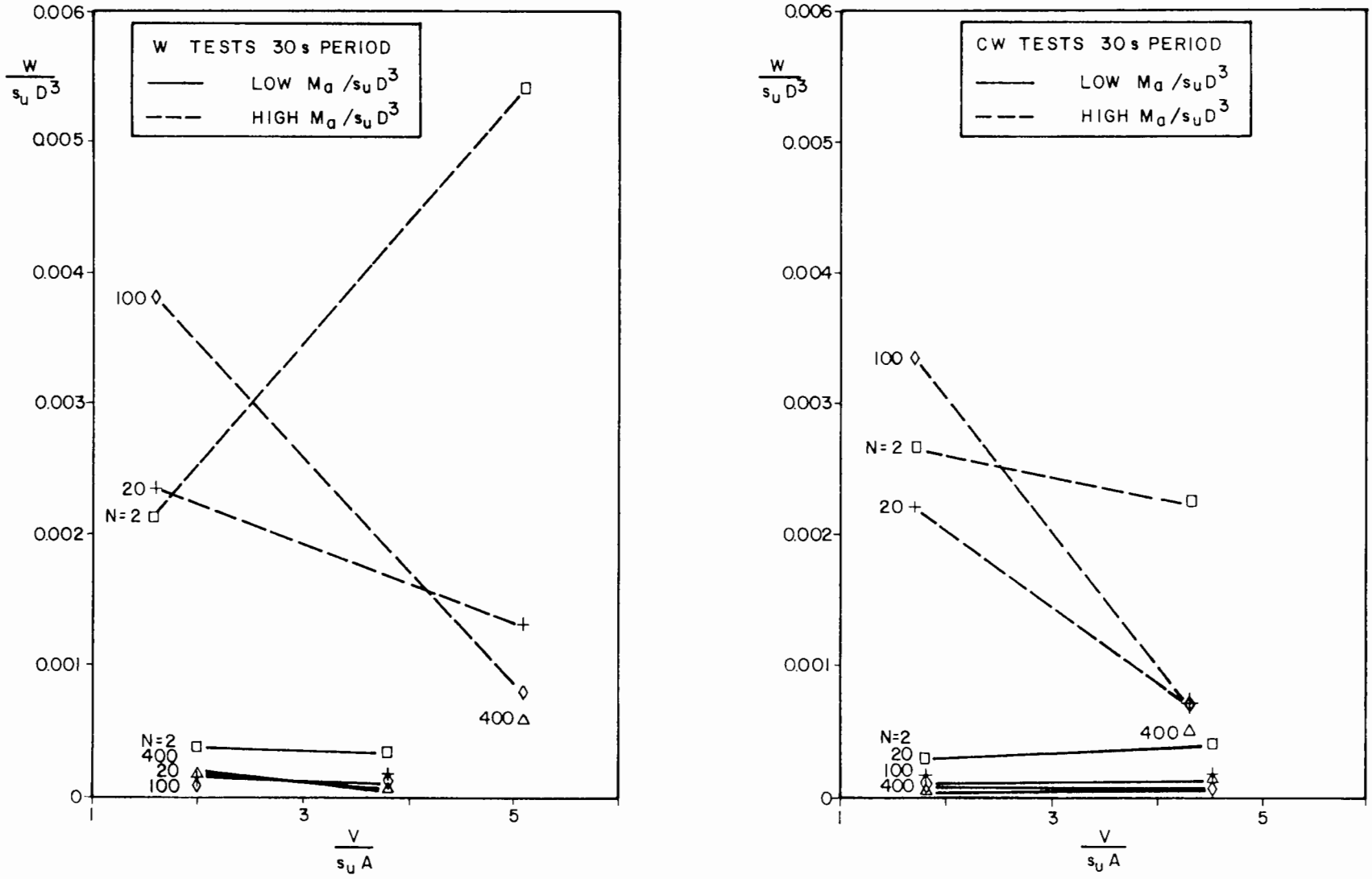

Figure 9.6 Variation of dimensionless rotational energy dissipated per cycle with vertical load and number of cycles for slow tests

less and less dissipative as the number of cycles N increases.

(b) Influence of the Vertical Load V/s_uA

The energy dissipated per cycle W/s_uD^3 tends to be reduced when the vertical load V/s_uA increases, although this is not always true as far as the 2nd cycle is concerned.

(c) Influence of the Amplitude of Moment Loading M_a/s_uD^3

As the energy dissipated per cycle W/s_uD^3 is represented by the area of the moment versus rotation loop, it obviously increases with the amplitude of moment M_a/s_uD^3.

(d) Influence of the Offset of Moment Loading M_o/s_uD^3

The offset of moment loading M_o/s_uD^3 does not appear to have affected the behaviour of the energy dissipated per cycle.

(e) Influence of the Period of Moment Loading

Tests carried out with high amplitude of moment M_a/s_uD^3 show overall a more dissipative pattern at 30 seconds period than at 8 seconds period. Tests with low M_a/s_uD^3 do not exhibit a significant difference in behaviour for the two periods.

9.5 Damping Ratio

The damping ratio η is defined as

$$\eta = \frac{W}{4\pi A} \ , \qquad [9.1]$$

where W is the rotational energy dissipated per cycle and A is defined in Figure 9.7. It can also be written as

$$\eta = \frac{2W}{\pi M_a \Delta\theta} \ , \qquad [9.2]$$

or, in terms of the non-dimensional quantities so far employed,

$$\eta = \frac{2 \dfrac{W}{s_u D^3}}{\pi \dfrac{M_a}{s_u D^3} \Delta\theta} \ . \qquad [9.3]$$

As, for the same value of the amplitude of moment, $W/s_u D^3$ and $\Delta\theta$ vary in the same way, η is not expected to vary significantly with the number of cycles.

Because of the inaccuracies associated with the large scatter observed in the variation of rotation $\Delta\theta$ and, to a lesser extent, in the energy dissipated per cycle $W/s_u D^3$ for low amplitude of moment $M_a/s_u D^3$, it would be unwise to try to evaluate the damping ratio η in this case. For high values of $M_a/s_u D^3$ however, η can be more accurately defined and the values obtained

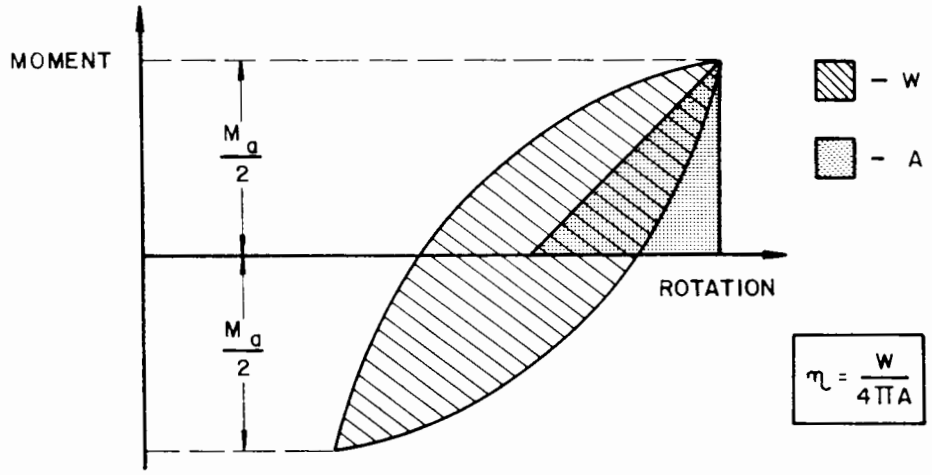

Figure 9.7 Definition of damping ratio

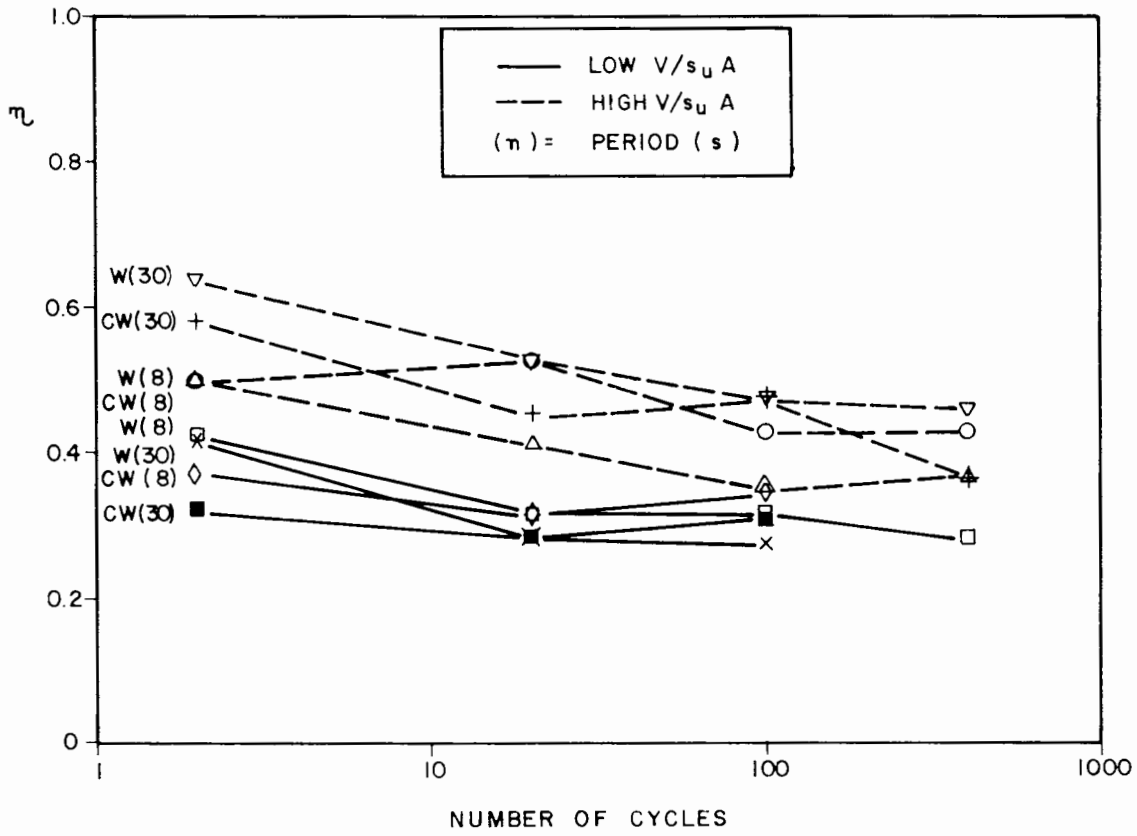

Figure 9.8 Variation of damping ratio with number of cycles for high amplitude of moment loading

are plotted in Figure 9.8 for the 2nd, 20th, 100th and 400th cycles.

The damping ratio η varies only slightly with the number of cycles N and, in most of the cases, its values are situated between 0.3 and 0.6. The general trend seems to be a slight decrease with N, mainly occurring between the 2nd and the 20th cycles. The value of η at 100 cycles varies from 66 % to 100 % of the value at the 2nd cycle while at 400 cycles this ratio ranges from 64 % to 86 %.

There is no clear evidence of either the offset of moment M_o/s_uD^3 or the period of loading influencing the damping ratio η. The vertical load V/s_uA, on the other hand, appears to have affected η, which is on average 44 %, 60 %, 36 % and 43 % higher for high V/s_uA than the corresponding values for low V/s_uA, respectively for the 2nd, 20th, 100th and 400th cycles.

9.6 A Final Remark

It is clear that only under low vertical load and high amplitude of moment is there a significant deterioration of performance in terms of rotational stiffness and dissipation of energy, and this combination of loading must be regarded as potentially dangerous. The cycling period played an important role in this case: slow tests always led to a marked increase of flexibility after a few cycles while fast tests showed a lower degree of degradation or some small increase of stiffness.

CHAPTER 10

CONCLUDING REMARKS

10.1 Model Testing

The understanding of the behaviour of jack-up footings under combined loads is a subject of great relevance for the oil industry around the world. It not only affects the structural design of rigs, but also should be taken into account in the analysis of adequacy of a rig at a specific location to operate at its maximum capacity with the necessary safety. To study this problem a series of model tests have been carried out. Special care has been taken to ensure that the tests are as relevant as possible to field problems, with attention to details of sample preparation, loading arrangements, instrumentation and characterization of the soil used.

The testing equipment and procedures adopted in the present research are appropriate for studying the behaviour of circular footings on clay under combined loads. It allows a variety of parametric studies involving a large number of parameters, providing useful and reliable data for analysis, resulting in a better understanding of several practical problems, including the behaviour of jack-up footings.

10.2 Kaolin Clay

The Speswhite Kaolin clay is convenient for research purposes for a number of reasons, as mentioned in Section 4.2.1. The high permeability, while advantageous in reducing the preparation time of consolidated samples,

results in the drawback that rapid changes in the mean effective stress inside the sample can occur during the test. This is particularly disadvantageous when the samples must be used immediately after the end of consolidation, and the total stresses have to be removed for some practical reason. The high permeability also requires short testing periods when undrained behaviour is desired.

The small inhomogeneity observed in the radial direction of the clay samples, mostly in the lower half samples, can only be explained by the presence of friction between the clay and the inner surface of the tanks in spite of the layer of grease on the surface. Although this inhomogeneity may not be significant in the context of this research, attention must be given to this problem whenever a high degree of homogeneity is imperative in samples prepared by one-dimensional consolidation.

The rigidity index G/s_u derived from back analysis of monotonic loading tests (vertical central loading and combined loading) varied from about 28 to 48, the mean value being approximately 39. Burd (1986), fitting the data from a series of tests carried out on the same clay, obtained a value of 31 for G/s_u, which is within the range observed in this research. The results of triaxial tests, although leading to rather scattered and atypically high undrained shear strength values when compared with vane tests, produced initial rigidity indexes G_{33}/s_u agreeing fairly with the pattern relating this quantity to the overconsolidation ratio presented by Wroth, Randolph, Houlsby and Fahey (1984) and Houlsby and Wroth (1985). For overconsolidation ratio higher than 5, G_{33}/s_u values obtained from triaxial tests either in the present work or by Davidson (1980) are in good agreement with the values inferred from back analysis.

10.3 Monotonic Loading

The three-parameter hyperbola described in Section 8.2 fits remarkably well the data obtained from monotonic loading tests, proving to be a useful and reliable tool in the analysis of test results. Stiffnesses and ultimate loads can be easily and accurately derived from the three parameters defining the hyperbola fitted to the load-displacement data from each test.

The results from vertical central loading tests suggest that the ultimate loads for cones are 30 % to 60 % higher than those predicted by Houlsby and Wroth's solution. However, the assumptions involved in the theoretical analysis lead to "lower bound" or safe solution for collapse loads in the case of undrained behaviour. Nevertheless, the test data are qualitatively in good agreement with the theory.

The spud-can used in this research exhibited bearing capacity values lower than the equivalent cone ($\beta = 152.6^{o}$). It seems to behave similarly to 90^{o} to 115^{o} cones of the same surface roughness.

The results of combined loading tests demonstrate that the horizontal load, in the range adopted in the present study, does not significantly affect the failure moment, confirming a similar trend obtained by numerical analysis. Although the horizontal load slightly reduces the failure moment for the 60^{o} cone, 120^{o} cone and circular plate, surprisingly the opposite is observed for the spud-can model.

The vertical load influences the failure moment of various footing shapes differently. Sharp cones and circular plates seem to be less affected than cones at intermediate angles (e.g., $\beta = 120^{o}$). The spud-can is considerably

affected, although to a lesser extent than the 120^{o} cone. In the range adopted in this work, high vertical loads lead to lower failure moment than low vertical loads.

When the horizontal load is low (h/D = 1.5) the spud-can exhibits a lower failure moment than the equivalent cone. Interestingly the same trend was identified with respect to central vertical loading behaviour (i.e. the spud-can showing a lower collapse load than the equivalent cone).

The initial rotational stiffness of axisymmetric footings is not markedly affected by the value of the vertical load. The horizontal load causes different changes in this quantity depending on the cone angle. The 120^{o} cone showed a stiffer response for high horizontal load while the 60^{o} cone behaved in the opposite manner. In all cases of vertical load and for low horizontal load the spud-can showed a higher initial stiffness than the equivalent cone.

The embedment of the spud-can in the clay improves its performance, increasing both the value of the failure moment and the initial rotational stiffness.

By comparison with theoretical analysis it can be deduced that the model footings (made up of duralumin and having polished finish) behaved neither like fully rough nor fully smooth, but at an intermediate roughness.

The plastic rotational stiffness of axisymmetric footings is markedly altered by the vertical load, whereas the horizontal load does not influence this quantity.

10.4 Cyclic Loading

The study of footings on clay under cyclic loading is extremely complex. In monotonic loading problems a distinction can be drawn between undrained behaviour and drained behaviour for most practical situations. When the loading conditions involve only undrained behaviour, the problem is considerably simplified.

In low frequency cyclic loading problems (offshore structure subjected to wave action), although the same distinction between drained and undrained behaviour can be established for practical purposes, the understanding of the way in which the pore pressures develop and vary during the loading is of paramount importance in deformation and limit analyses. Besides the influence of the pore pressure built up during the repeated loading, a degradation in the mechanical behaviour of soils has been observed. The latter phenomenon, producing a weakening effect and being difficult to assess, introduces an enormous complexity to the problem.

The results of cyclic loading tests reveal that the increment of vertical displacement of the spud-can with the number of cycles is more strongly related to the amplitude of moment loading than to the intensity of the vertical load.

The equivalent rotational stiffness obtained from cyclic loading of the spud-can model clearly increases with the value of the vertical load. In most of the cases corresponding to low vertical load a degradation effect is observed as the stiffness declines with the number of cycles after reaching a maximum value. This degradation is far more accentuated when the period and the amplitude of the moment loading are high. For high vertical load a steady increase in this quantity is always observed.

The lowest values of equivalent rotational stiffness, observed at high amplitude of moment and low vertical load, are in the same order of magnitude as the initial rotational stiffness of the spud-can under monotonic loading.

The damping ratio corresponding to high amplitude of cyclic moment loading slightly decreases with the number of cycles, most of this variation occurring before the 20th cycle. This parameter is typically in the range 0.3 to 0.6 and is dependent on the vertical load (lower vertical load leading to lower damping ratio).

As far as the conditions and results of this study are concerned, the offset of the moment has no significant influence in the mechanical behaviour of the spud-can model footing subjected to cyclic loading.

10.5 Closing Remarks

The purpose of the research has been to clarify aspects of a practical design problem. The work reported in this thesis was part of a more extensive research programme. Although all the questions have not been answered fully, the programme has shed some light on many aspects of the problem. In particular the role of small scale model testing in engineering design has been demonstrated.

REFERENCES

American Institute of Steel Construction (1980). Manual of steel construction, 8th Edition, Chicago, I11.

American Petroleum Institute (1984). Recommended practice for planning, designing and constructing fixed offshore platforms, API RP2A, 15th Edition.

Andersen, K.H. (1976).Behaviour of clay subjected to undrained cyclic loading. Proc. 1st Int. Conf. Behaviour of Offshore Structures (BOSS '76), Trondheim, 392-403.

Atkinson, J.H. & Bransby, P.L. (1978). The mechanics of soils - an introduction to critical state soil mechanics. London:McGraw-Hill.

Atkinson, J.H. (1981). Foundations and slopes - an introduction to applications of critical state soil mechanics. London:McGraw-Hill.

Bass, H.G. (1971). Introduction to engineering measurements. London:McGraw-Hill.

Bishop, A.W. & Henkel, D.J. (1962). The measurement of soil properties in the triaxial test. London:Arnold.

Bishop, R.E.D. & Price, W.G. (1979). Hydroelasticity of ships. Cambridge University Press.

Blake, A. (ed) (1985). Handbook of mechanics, materials and structures. New York:John Wiley.

Bowen, L.P. (1966). Structural design in aluminium.London:Hutchinson.

Bowles, J.E. (1982). Foundation analysis and design. Singapore:McGraw-Hill.

Brinch Hansen, J. (1961). A general formula for bearing capacity. Bulletin No. 11, Danish Geotechnical Institute, Copenhagen, 38-46.

Brinch Hansen, J. (1970). A revised and extended formula for bearing capacity. Bulletin No. 28, Danish Geotechnical Institute, Copenhagen, 5-11.

British Standards Institution (1975). Methods of test for soils for civil engineering purposes. BS 1377. London:British Standards Institution.

Burd, H.J. (1986). Large displacement finite element analysis of a reinforced unpaved road. D.Phil. Thesis, University of Oxford.

Butterfield, R. (1979). A natural compression law for soils (an advance on e-log p'). Geotechnique Vol 29, No. 4, 469-480.

Calladine, C.R. (1985). Plasticity for engineers. Chichester:Ellis Horwood.

Capper, P.L. & Cassie, W.F. (1978). The mechanics of engineering soils. London:Spon.

Carlsen, C.A., Kjeoy, H. & Eriksson, K. (1986). Structural behaviour of harsh environment jack-ups. The jack-up drilling platform - design and operation (Boswell, L.F., ed), 90-136. London:Collins.

Carter, J.P., Booker, J.R. & Wroth, C.P. (1982). A critical state soil model for cyclic loading. Soil Mechanics - Transient and Cyclic Loads (G.N. Pande & O.C. Zienkiewicz, eds), 219-252. London:John Wiley.

Chiba, S., Onuki, T. & Sao, K. (1986). Static and dynamic measurement of bottom fixity. The jack-up drilling platform - design and operation (Boswell, L.F., ed), 307-327. London:Collins.

Cottrell, A.H. (1964). The mechanical properties of matter. New York:John Wiley.

Cox, A.D., Eason, G. & Hopkins, H.G. (1961). Axially symmetric plastic deformations in soils. Phil. Trans. Roy. Soc. London, Series A, 254, 1-45.

Craig, W.H. & Higham M.D. (1985). The applications of centrifugal modelling to the design of jack-up rig foundations. Proc. Int. Conf. on Offshore Site Investigation.

D'Appolonia, D.J., Poulos, H.G., & Ladd, C.C. (1971). Initial settlement of structures on clay. J. Soil Mech. Found. Div. ASCE Vol 97, SM10, 1359-1377.

Davidson, C.S. (1980). The shear modulus of clays. Part II project, University of Cambridge.

Davis, E.H. & Booker, J.R. (1973). The effect of increasing strength with depth on the bearing capacity of clays. Geotechnique Vol 23, No. 4, 551-563.

Davis, E.H. (1968). Theories of plasticity and the failure of soil masses. Soil Mechanics - Selected Topics (I.K. Lee, ed). London:Butterworths.

Du Thinh, K. & Hansbo, S. (1985). The rotational stiffness of strip footings in sand. Proc. 11th Int. Conf. Soil Mech. Found. Eng., San Francisco Vol 4, 2191-2194.

Dwight, H.B. (1961). Tables of integrals and other mathematical data. New York:Macmillan.

Etter, D.M. (1983). Structural Fortran 77 for engineers and scientists. Menlo Park:Benjamin-Cummings.

Fannin, R.J. (1986). Geogrid reinforcement of granular layers on soft clay - a study at model and full scale. D.Phil. Thesis, University of Oxford.

Gemenhardt, J.P. & Focht, J.A., Jr. (1970). Theoretical and observed performance of mobile rig footings on clay. Proc. 2nd Offshore Technology Conf., Houston. OTC 1201.

Gue, S.S. (1984). Ground heave around driven piles in clay. D.Phil. Thesis, University of Oxford.

Hambly, E.C. (1985). Punch-through instability of jack-up on seabed. J. Geotech. Eng. Div. ASCE Vol 111, No. 4, 545-550.

Hardin, B.O. & Drnevich, V.P. (1972). Shear modulus and damping in soils: design equations and curves. J. Soil Mech. Found. Div. ASCE Vol 98, SM7, 667-692.

Hardin, B.O. & Drnevich, V.P. (1972). Shear modulus and damping in soils: measurement and parameter effects. J. Soil Mech. Found. Div. ASCE Vol 98, SM6, 603-624.

Hardin, B.O. (1965). The nature of damping in sands. J. Soil Mech. Found. Eng. Div. ASCE Vol 91, SM1, 63-97.

Hattori, Y., Ushio, M., Ishihama, T. & Kawamura, T. (1986). Experimental study of foundation stability of jack-up rigs. The jack-up drilling platform - design and operation (Boswell, L.F., ed), 280-306. London:Collins.

Head, K.H. (1982). Manual of soil laboratory testing - volume 2: permeability, shear strength and compressibility tests. London:Pentech Press.

Hedges, T.S. (1983). Effects of currents on wave drag and inertia loads. Proc. Coastal Structures '83, Arlington, 461-473.

Hossdorf, H. (1974). Model analysis of structures. New York:Van Nostrand.

Houlsby, G.T. & Santa Maria, P.E.L. (1987). Model studies of cyclic combined loading of jack-up foundations. Report on cyclic loading to the Joint Industry Study on the subject of foundation fixity of jack-up units, University of Oxford.

Houlsby, G.T. & Wroth, C.P. (1982). Direct solution of plasticity problems in soils by the method of characteristics. Proc. 4th Int. Conf. Numerical Methods in Geomechanics, Edmonton Vol 3, 1059-1071.

Houlsby, G.T. & Wroth, C.P. (1983). Calculation of stresses on shallow penetrometers and footings. Proc. IUTAM Symp. on Seabed Mechanics, Newcastle, 107-112.

Houlsby, G.T. & Wroth, C.P. (1985). The variation of shear modulus of a clay with pressure and overconsolidation ratio. OUEL Report No. 1591/85, Department of Engineering Science, University of Oxford.

Houlsby, G.T. (1982). Theoretical analysis of the fall cone test. Geotechnique Vol 32, No. 2, 111-118.

Hsu, T.H. (1984). Applied offshore structural engineering. Houston:Gulf.

Idriss, I.M., Dobry, R. (1978). Nonlinear behaviour of soft clays during cyclic loading. J. Geotech. Eng. Div. ASCE Vol 104, GT12, 1427-1447.

Jacobsen, L.S. (1930). Motion of a soil subjected to a simple harmonic ground vibration. Bull. Seism. Soc. Am. 20, 160-195.

Janbu, N. (1985). Soil models in offshore engineering, 25th Rankine Lecture. Geotechnique Vol 35, No. 3, 241-281.

Kondner, R.L. (1963). Hyperbolic stress-strain response: cohesive soils. J. Soil Mech. Found. Eng. Div. ASCE Vol 89, SM1, 115-143.

Langhaar, H.L. (1964). Dimensional analysis and theory of models. New York:John Wiley.

Lazan, B.J. (1968). Damping of materials and members in structural mechanics. Oxford:Pergamon Press.

Leeming, J.J. (1963). Statistical methods for engineers. London:Blackie.

Loudon, P.A. (1967). Some deformation characteristics of kaolin. Ph.D. Thesis, University of Cambridge.

Love, J.P. (1984). Model testing of geogrids in unpaved roads. D.Phil. Thesis, University of Oxford.

Mair, R.J. (1979). Centrifugal modelling of tunnel construction in soft clay. Ph.D. Thesis, University of Cambridge.

Martins, J.P. (1983). Shaft resistance of axially loaded piles in clay. Ph.D. Thesis, Imperial College, London.

May, R.E. (1987). A study of the piezocone penetrometer in normally consolidated clay. D.Phil. Thesis, University of Oxford.

Meimon, Y. & Lassoudiere, F. (1985). Application to design of marine foundations of a complete model for cyclic behaviour of soils. Proc. 4th Int. Conf. Behaviour of Offshore Structures (BOSS '85), Delft, 785-796.

Mendelson, A. (1968). Plasticity: theory and application. New York:Macmillan.

Menezes Cortes, H.V., Adeodato, H.V.F. & Machado, C.F.D. (1985). Brazilian experience on prediction of jack-up rig leg penetration. Symp. Brazil Offshore 85, Rio de Janeiro.

Meyerhof, G.G. (1951). The ultimate bearing capacity of foundations. Geotechnique Vol 2, 301-332.

Meyerhof, G.G. (1953). The bearing capacity of foundations under eccentric and inclined loads. Proc. 3rd Int. Conf. Soil Mech. Found. Eng., Zurich Vol 1, 440-445.

Meyerhof, G.G. (1961). The ultimate bearing capacity of wedge-shaped foundations. Proc. 5th Int. Conf. Soil Mech. Found. Eng., Paris Vol 2, 105-109.

Meyerhof, G.G. (1963). Some recent research on the bearing capacity of foundations. Can. Geotech. J. Vol 1, No. 1, 16-26.

Noble Denton & Associates (1987). Foundation fixity of jack-up units, Vols. I and II, 10th March 1987 (confidential).

Offshore engineer (1985). Down amongst the spud cans something is stirring. October, 24-40.

Pande, G.N. (1982). Shakedown of foundations subjected to cyclic loads. Soil Mechanics - Transient and Cyclic Loads (G.N. Pande & O.C. Zienkiewicz, eds), 469-489. London:John Wiley.

Potts, D.M., Windle, D. (1985). A numerical study of the foundation behaviour of a proposed north sea gravity platform. Proc. 4th Int. Conf. Behaviour of Offshore Structures (BOSS '85), Delft, 665-672.

Poulos, H.G. & Davis, E.H. (1974). Elastic solutions for soil and rock mechanics. New York:John Wiley.

Richart, F.E., Jr. (1975). Some effects of dynamic soil properties on soil-structure interaction. J. Geotech. Eng. Div. ASCE Vol 101, GT12, 1197-1240.

Richart, F.E., Jr., Hall, J.R., Jr. & Woods, R.D. (1970). Vibrations of soils and foundations. Englewood Cliffs, N.J.:Prentice-Hall.

Rowe, P.W., Craig, W.H. & Procter, D.C. (1976). Model studies of offshore gravity structures founded on clay. Proc. 1st Int. Conf. Behaviour of Offshore Structures (BOSS '76), Trondheim, 439-448.

Rowe, P.W., Smith, I.M. (1982). Comments on the use of physical and analytical models. Soil Mechanics - Transient and Cyclic Loads (G.N. Pande & O.C. Zienkiewicz, eds), 491-512. London:John Wiley.

Santa Maria, P.E.L. & Houlsby, G.T. (1988). Model tests for offshore foundations under combined loads. Proc. Symp. on New Concepts in Site and Laboratory Tests in Geotechnical Engineering, Rio de Janeiro.

Santa Maria, P.E.L. (1985). Behaviour of footings on clay under combined loads. First Year Report, University of Oxford.

Schofield, A.N. & Wroth, C.P. (1968). Critical state soil mechanics. London:McGraw-Hill.

Scott, R.F. (1963). Principles of soil mechanics. Reading, Massachusetts:Addison-Wesley.

Scott, R.F. (1981). Foundation analysis. Englewood Cliffs, N.J.:Prentice-Hall.

Selvadurai, A.P.S. (1979). Elastic analysis of soil-foundation interaction. Amsterdam:Elsevier.

Skempton, A.W. (1951). The bearing capacity of clays. Proc. Building Research Congress, London Vol 1, 180-189.

Sneddon, I.N. (1965). The relation between load and penetration in the axisymmetric Boussinesq problem for a punch of arbitrary profile. Int. J. Eng. Sci. Vol 3, No. 1, 47-57.

Steenfelt, J.S., Randolph, M.F. & Wroth, C.P. (1981). Instrumented model piles jacked into clay. Proc. 10th Int. Conf. Soil Mech. Found. Eng., Stockholm Vol 2, 857-864.

Taylor, D.W. (1948). Fundamentals of soil mechanics. New York:John Wiley.

Taylor, E.S. (1974). Dimensional analysis for engineers. Oxford:Clarendon Press.

Terzaghi, K. (1943). Theoretical soil mechanics. New York:John Wiley.

Thiers, G.R., Seed, H.B. (1968). Cyclic stress-strain characteristics of clay. J. Soil Mech. Found. Div. ASCE Vol 94, SM2, 555-569.

Verruijt, A. (1985). The influence of soil properties on the behaviour of offshore structures. Proc. 4th Int. Conf. Behaviour of Offshore Structures (BOSS '85), Delft, 7-19.

Vesic, A. (1973). Analysis of ultimate loads of shallow foundations. J. Soil Mech. Found. Eng. Div. ASCE Vol 99, SM1, 45-73.

Vesic, A.S. (1975). Bearing capacity of shallow foundations. Foundation Engineering Handbook (H.F. Winterkorn & H.Y. Fang, eds), 121-147. New York:Van Nostrand.

Winkworth, W.J. & Bennett, R. (1986). Design considerations for deep water jack-ups. The jack-up drilling platform - design and operation (Boswell, L.F., ed), 72-89. London:Collins.

Wroth, C.P. & Houlsby, G.T. (1985). Soil mechanics - property characterization and analysis procedures. Proc. 11th Int. Conf. Soil Mech. Found. Eng., San Francisco Vol 1, 1-55.

Wroth, C.P. (1984). The interpretation of in situ soil tests, 24th Rankine Lecture. Geotechnique Vol 34, No. 4, 449-489.

Wroth, C.P., Randolph, M.F., Houlsby, G.T. & Fahey, M. (1979). A review of the engineering properties of soils with particular reference to the shear modulus. Technical Report Soils TR75, University of Cambridge.

Wu, T.H. (1966). Soil mechanics. Boston:Allyn & Bacon.